The Role of CO Cores in Star Formation

in the Dwarf Irregular Galaxy WLM

by

Haylee Archer

A Dissertation Presented in Partial Fulfillment
of the Requirements for the Degree
Doctor of Philosophy

Approved March 2025 by the
Graduate Supervisory Committee:

Rogier Windhorst, Chair
Deidre Hunter
Rolf Jansen
Sanch Borthakur
Molly Simon

ARIZONA STATE UNIVERSITY

May 2025

ABSTRACT

Star formation shapes the evolution of galaxies, yet many of its core processes remain poorly understood, especially in low-metallicity galaxies. In this dissertation, I explore how stars form in environments lacking heavy elements, specifically focusing on the dwarf irregular galaxy WLM. By leveraging ALMA CO observations, I investigate the role of CO cores and determine their influence on star formation processes in WLM. I further utilize JWST and HST imaging to look for correlations between young stellar populations, molecular gas properties, and the local environment in regions both with and without CO cores. These findings reveal crucial insights into how low metallicity environments affect CO core formation, the relationship between CO and embedded star formation, and the role of CO dark gas in star-forming regions in low-metallicity dwarf galaxies.

Additionally, I bridge astrophysics research with astronomy education by analyzing the effectiveness of translating established lecture-tutorials about planet formation into an online teaching environment. I assess student learning gains, address common misconceptions, and explore how interactive, online resources can meaningfully enhance undergraduate astronomy education.

Collectively, these studies enhance the understanding of star formation in low-metallicity environments and provide valuable strategies for effectively engaging students with complex astronomical concepts.

DEDICATION

To my dad, who first taught me to look up and wonder, who encouraged every dream, every question, and every discovery, and whose support proved to me, time and again, that the sky was never the limit.

ACKNOWLEDGMENTS

To my advisors, Dr. Deidre Hunter and Dr. Rogier Windhorst: Thank you for taking a chance on me and making our usual advising situation work. Your expertise, patience, and encouragement have been instrumental in shaping both my research and personal growth as a scientist. I am deeply appreciative to have had you as both as my advisors and am incredibly lucky to have you in my corner.

To my secondary project advisor, Dr. Molly Simon: Thank you for taking me on for my secondary project and helping me see it through to publication. Thanks to you, I was able to incorporate my love of education into this dissertation.

To my dissertation committee, Dr. Rolf Jansen and Dr. Sanch Borthakur: Whether it was in class, group meetings, or informally, thank you both for the invaluable feedback you've provided me over the years for both my science and my career.

To the Windhorst Research Group: Thank you for your constant support and advice, even when most of our interactions happened over Zoom. I especially appreciate your excitement whenever I managed to appear in person at lab group meetings and you could finally confirm my corporeal existence.

To the Lowell Observatory Science Staff: I feel extremely fortunate to have spent the past several years surrounded by such a welcoming and supportive group of people. Your kindness, guidance, and encouragement have had a profound impact on my science, my career, and my life. I'm immensely grateful to each of you.

To Rosalia O'Brien: I'm incredibly thankful that we both joined the group at the same time. Whether it was reading my proposals, helping me reduce HST data, or spending the week with my cat, I'm lucky to have you as a colleague and friend.

To Ashley Heida: I am so grateful for your constant support and friendship throughout our journey from UND to ASU, especially the year you housed me down in Tempe while I took classes. Your enthusiasm and constant encouragement made every challenge feel manageable.

To Elijah Mathews: From the late night Zoom sessions learning Cosmology during the pandemic to the SED fitting code of Chapter 4, your friendship and content knowledge is woven into the very fabric of this dissertation, and I could never thank you enough.

To my family: To my parents, David and Jodi Archer: thank you for every sacrifice you've made so I could pursue my dreams, and for always believing in me without hesitation. Our near-daily calls and FaceTimes kept me going–I truly couldn't have done this without you. To my sister, Alli Roller, thank you for ensuring that you taught me everything you were learning growing up despite our four year age gap. Your willingness to share your knowledge and excitement inspired my own curiosity and shaped who I am today. I'm endlessly grateful for you. To my nieces, Haven and Brynn Roller, thank you both for filling my life with joy, laughter, and curiosity. Watching you grow into such smart and creative people inspires me every day.

To my husband, Mike Gowanlock: Thank you for being my greatest source of support, patience, and love. Your understanding of the grad school journey made mine easier in countless ways. I'm incredibly grateful to have you beside me.

And finally, to my cat, Slippers: Thank you for being my loudest cheerleader and most persistent distraction. Your perfectly timed yells, relentless demands for treats, and affectionate interruptions for snuggles made this journey infinitely better. I couldn't have done this without your chaos, and I wouldn't have wanted to.

TABLE OF CONTENTS

CHAPTER Page

CHAPTER Page

LIST OF FIGURES

Figure Page

Figure Page

Figure Page

Figure Page

Figure Page

Figure Page

Figure Page

Figure Page

Figure Page

Figure Page

Figure Page

Figure Page

Figure | Page

Figure Page

Chapter 1

INTRODUCTION

1.1 Background and Motivation

1.1.1 The Importance of Star Formation in Galaxy Evolution

Star formation is a fundamental process that shapes galaxies and influences their structure, evolution, and chemical enrichment over time. By converting cold molecular gas into stars, this process defines the stellar populations of a galaxy and plays a critical role in regulating the interstellar medium (ISM) through stellar feedback mechanisms (e.g. Hopkins *et al.* 2010; Chevance *et al.* 2023; Schinnerer and Leroy 2024). Star formation, however, does not occur uniformly across different local environments. The efficiency with which galaxies convert molecular gas into stars depends on several factors such as gas density, turbulence, metallicity, and feedback processes, which vary across different local galactic environments (e.g. Elmegreen 1989; Brosch *et al.* 1998; Hunter *et al.* 1998; Scalo and Elmegreen 2004; Leroy *et al.* 2008; Kennicutt and Evans 2012; Krumholz *et al.* 2012; Chevance *et al.* 2020a; Hunter *et al.* 2024). As stars form, they emit radiation that drives stellar winds, and some ultimately end their lives in powerful supernova explosions. These feedback processes disrupt molecular clouds, regulating star formation by either dispersing gas and inhibiting further collapse or triggering new star formation (e.g. Tenorio-Tagle *et al.* 1992; Krumholz and Tan 2007; McKee and Ostriker 2007; Ostriker *et al.* 2010). The complex interplay between gas inflows, star formation, and feedback ultimately regulates the life cycle of galaxies.

The morphology and dynamics of a galaxy influence how stars form within it. In galaxies like the Milky Way, star formation largely takes place in the spiral arms where gravitational instabilities and differential rotation cause the accumulation of dense gas clouds (e.g. Ostriker *et al.* 2010; Kennicutt and Evans 2012; Elmegreen *et al.* 2018; Elmegreen and Elmegreen 2019, 2020). These regions host giant molecular clouds (GMCs), the primary birthplaces of stars, where cold gas collapses under gravity to form stars and star clusters. The energy released by young, massive stars in the form of ultraviolet (UV) radiation and stellar winds disrupts molecular clouds, which regulates further star formation and shapes the ISM (e.g. Kennicutt 1998; Fukui and Kawamura 2010; Kennicutt and Evans 2012; Saintonge and Catinella 2022; Schinnerer and Leroy 2024, and references therein). This feedback cycle plays a crucial role in maintaining a balance between gas inflow, molecular cloud formation, and star formation efficiency (SFE).

In dwarf galaxies like the Small Magellanic Cloud (SMC) and Large Magellanic Cloud (LMC), however, star formation takes place differently. Dwarf irregulars (dIrrs), which are gas-rich, metal poor galaxies, exhibit star formation that is more stochastic and bursty compared to larger spirals, often forming stars in regions where molecular gas is not easily detected (e.g. Elmegreen 1989; Brosch *et al.* 1998; Fukui and Kawamura 2010; Kennicutt and Evans 2012; Schruba *et al.* 2012; Madden *et al.* 2020; Hunter *et al.* 2024). Unlike spirals, which have well-defined spiral structure that channel gas into dense star-forming regions, star formation in dIrrs is less organized. Their lower metallicities and weaker gravitational potentials make them more susceptible to stellar feedback, which can disrupt molecular clouds and eject gas from the system, potentially quenching future star formation (e.g. Tenorio-Tagle and Bodenheimer 1988;

Bolatto *et al.* 1999; Vorobyov and Basu 2005; Grisdale *et al.* 2017; El-Badry *et al.* 2018).

One of the most significant ways star formation shapes galaxies is through stellar feedback. In regions of intense star formation, stellar winds, ionizing radiation and supernova explosions inject energy into the ISM, driving turbulence that influences the formation, evolution, and dispersal of molecular clouds (e.g. Efremov and Elmegreen 1998; Williams *et al.* 2000; Leroy *et al.* 2008; Kim *et al.* 2018; Kruijssen *et al.* 2019; Chevance *et al.* 2020a; Schinnerer and Leroy 2024). Observations of dwarf galaxies suggest that many exhibit lower star formation rates (SFRs) despite their significant gas reservoirs, likely a consequence of intermittent feedback-driven suppression of star-formation (Tolstoy *et al.* 2009; Kennicutt and Evans 2012; Hunter *et al.* 2024). Ultimately, the balance between gas accretion, star formation, and feedback dictates whether a galaxy continues to actively form stars or transitions into a quiescent state over time.

Star formation not only determines the structure of galaxies but also plays a crucial role in their chemical evolution. As stars evolve and explode as supernovae, they release heavy elements such as carbon, oxygen, and iron into the ISM, enriching their surrounding environment and future generations of stars (e.g. Elmegreen *et al.* 1980; Bolatto *et al.* 1999; Tolstoy *et al.* 2009). This process is critical in shaping galaxy metallicities.

At the heart of the star formation process is the ISM, a multi-phase component of galaxies that acts as the primary reservoir of cold gas available for new star formation. The ISM is composed of atomic gas, primarily in the form of neutral hyrogen (H I), molecular gas dominated by molecular hydrogen (H_2), ionized gas, dust, and cosmic rays, all of which interact under the influence of gravity, turbulence, and feedback.

Spanning six orders of magnitude in temperature and density, the ISM exists in three phases: a cold, dense component or Cold Neutral Medium (CNM), a warm, diffuse component that includes the Warm Neutral Medium (WNM) and Warm Ionized Medium (WIM), and the Hot Ionized Medium (HIM; Radhakrishnan *et al.* 1972; Mebold 1972; McKee and Ostriker 1977; Kalberla *et al.* 1985; Heiles 1989). In metal-poor galaxies, the conversion from atomic to molecular gas is less efficient due to reduced cooling and shielding capabilities, making the CNM particularly important (Bialy and Sternberg 2019). The ability of a galaxy to sustain ongoing star formation depends on its capacity to retain and replenish its ISM over cosmic timescales, from either the intergalactic medium (IGM) or circumgalactic medium (CGM; Saintonge and Catinella 2022).

1.1.2 Molecular Gas as the Fuel for Star Formation

Star formation occurs primarily in dense molecular clouds, where temperatures are low enough for gravitational collapse to initiate the formation of stars. The prominence of H_2 in molecular clouds stems from the fundamental physics of gas cooling and fragmentation. For a cloud to collapse and form stars, it must cool efficiently to counteract thermal pressure and turbulence. H I alone cannot cool effectively at the low temperatures required for collapse, but when H I transitions into H_2, the gas condenses into dense, self-shielding structures, where it is protected from external radiation that could otherwise disrupt molecular formation (Schinnerer and Leroy 2024, and references therein). Once a molecular cloud reaches sufficient density, its internal turbulence weakens, leading to gravitational collapse and the formation of protostellar cores (McKee and Ostriker 2007, and refererences therein).

Despite being the most abundant molecule in molecular clouds, H_2 is notoriously difficult to detect directly because it lacks a permanent dipole moment, meaning it does not emit efficiently in radio or infrared (IR) wavelengths under the cold conditions of star-forming clouds. Instead, direct detection of H_2 is limited to warm gas phases, such as shocked regions or photo-dissociation regions (PDRs), where rotational or vibrational transitions in the UV or IR can be observed. However, these emissions only trace a small fraction of the total H_2 content, making them unreliable indicators of the bulk of H_2 in molecular clouds (Bolatto *et al.* 2013).

In metal-rich galaxies, astronomers rely on carbon monoxide (CO)–the second most abundant molecule in molecular clouds–as a tracer of H_2. CO emits strong rotational transitions in the millimeter and submillimeter regimes, making it an accessible observational proxy for molecular hydrogen. The intensity of CO emission is used to estimate the total molecular gas content via the CO-to-H_2 conversion factor, X_{CO}, which relates CO line intensity, I_{CO}, to H_2 column density, $N(\mathrm{H_2})$:

$$N(\mathrm{H_2}) = X_{CO}\ I_{CO}. \tag{1.1}$$

For the Milky Way, a widely adopted value is:

$$X_{CO,MW} \approx 2 \times 10^{20}\ \mathrm{cm^{-2}(K\ km\ s^{-1})^{-1}}. \tag{1.2}$$

Since CO forms in molecular clouds where H_2 is abundant, it is often assumed that the CO-to-H_2 ratio is relatively stable, allowing astronomers to estimate the total molecular gas mass based on CO emission. However, the reliability of CO as a tracer depends on the physical conditions of the ISM. In metal-rich galaxies, CO emission is generally well correlated with H_2 mass because dust and other heavy elements provide sufficient shielding against photodissociation.

However, variations in gas density, turbulence, and shielding properties complicate the CO-H_2 relationship, requiring metallicity-dependent corrections to CO-based gas mass estimates (Bolatto *et al.* 2013). In low-metallicity environments, the altered ISM conditions significantly impact the survival of CO and the structure of molecular clouds. Observations of dwarf galaxies such as the SMC, WLM, NGC 6822, and Sextans B indicate that CO emission is frequently weak or entirely absent, even in regions with ongoing star formation (Hunter *et al.* 2024). Observations indicate that X_{CO} increases sharply with decreasing metallicity (Bolatto *et al.* 2013).

Turbulence further complicates CO detectability, as it can disperse CO molecules more readily, resulting in a patchy distribution of CO even within dense molecular clouds. In high-density gas regions, X_{CO} tends to be lower due to the increased shielding and localized CO stability, whereas more diffuse clouds exhibit higher X_{CO} values, reflecting the role of cloud structure in regulating CO survival. Additionally, galaxies with intense UV radiation fields—such as starburst galaxies—experience enhanced CO photodissociation leading to higher X_{CO} values (Bolatto *et al.* 2013; Madden *et al.* 2020).

The study of molecular gas properties in different galactic environments is crucial for understanding star formation efficiency and cloud evolution. The variations in X_{CO} highlight the need for multi-wavelength approaches to accurately estimate the molecular gas content in galaxies. By refining CO-to-H_2 conversion factors, exploring alternative tracers, and improving molecular cloud modeling, astronomers can develop a more comprehensive understanding of star formation across different galactic environments, particularly in low-metallicity galaxies.

1.1.3 WLM

Wolf–Lundmark–Melotte (WLM), also designated as DDO 221, is a low-metallicity dIrr galaxy in the Local Group. It was first discovered by Max Wolf on October 15, 1909, through photographic plates (Wolf 1909). However, at the time, its true nature remained uncertain. It was not until 1926 that Knut Lundmark and P.J. Melotte independently identified WLM as an extragalactic system, thereby recognizing it as a galaxy rather than a faint nebular object (Melotte 1926). At a distance of approximately 980 kpc, WLM's distance from the Milky Way and M31 is far enough to suggest a low probability of previously interacting with either (Leaman *et al.* 2012; Teyssier *et al.* 2012; Albers *et al.* 2019). This relative isolation means that its evolution has been largely unaffected by gravitational interactions with massive galaxies, making it an important subject for understanding star formation in low-density environments.

WLM is classified as a dwarf irregular galaxy of type Irr IV-V. Its structural properties, including a lack of a well-defined bulge and a prominent bar, have been noted in various studies (e.g. Dolphin 2000; Weisz 2014; Weisz *et al.* 2023). The galaxy's stellar population exhibits a radial gradient, with older stars predominantly in the outer regions and younger stars concentrated in the inner disk (Albers *et al.* 2019; Weisz *et al.* 2023; Boyer *et al.* 2024; McQuinn *et al.* 2024; Cohen *et al.* 2025). These findings suggest a history of inside-out star formation.

The SFH of WLM has been extensively studied through resolved stellar populations. Early analyses by Dolphin (2000) indicated that WLM's star formation began approximately 12 Gyr ago, with roughly half of its stellar mass forming before 9 Gyr ago. More recent studies using HST imaging (Albers *et al.* 2019) and JWST observations (Boyer *et al.* 2024; McQuinn *et al.* 2024; Cohen *et al.* 2025) confirm a rising SFH, with significant star formation occurring in the last 5 Gyr.

Metallicity studies reveal a low metal content typical of dwarf irregular galaxies. Spectroscopic studies of red giant branch stars indicate a mean metallicity of [Fe/H] = -1.28 ± 0.02 (Leaman *et al.* 2012).

The ISM of WLM is dominated by H I, with a total H I gas mass of approximately $7.1 \times 10^7 M_\odot$ (Hunter *et al.* 2012). Despite active star formation, molecular gas, as traced by CO emission, has been notoriously difficult to detect in WLM due to its low metallicity (Taylor and Klein 2001). However, Elmegreen *et al.* (2013) and Rubio *et al.* (2015) successfully detected CO in dense cloud cores using ALMA, revealing that CO exists in small, high-density clumps. With a metallicity of just 0.13Z⊙, lower than that of the SMC (Z = 0.2Z⊙) and the LMC ($Z = 0.5Z_\odot$), it represented the lowest metallicity environment in which CO cores had been detected.

WLM's relative isolation makes it an invaluable subject for studying star formation and chemical evolution in a low-density environment. Unlike satellite galaxies that have been influenced by interactions with the Milky Way or M31, WLM appears to have evolved largely independently, though recent observations of stellar age gradients, H I morphology, and kinematics in WLM find evidence of ram-pressure stripping, suggesting the galaxy may be less isolated than previously thought (Yang *et al.* 2022; Cohen *et al.* 2025). This provides crucial insights into the internal mechanisms governing star formation, metal enrichment, and gas dynamics in small galaxies.

Furthermore, WLM serves as a local analog for high-redshift dwarf galaxies in the early universe, where low metallicity environments were more common, though the early universe was more chaotic. The insights gained from WLM continue to shape our understanding of galaxy formation and evolution in a broader cosmological context.

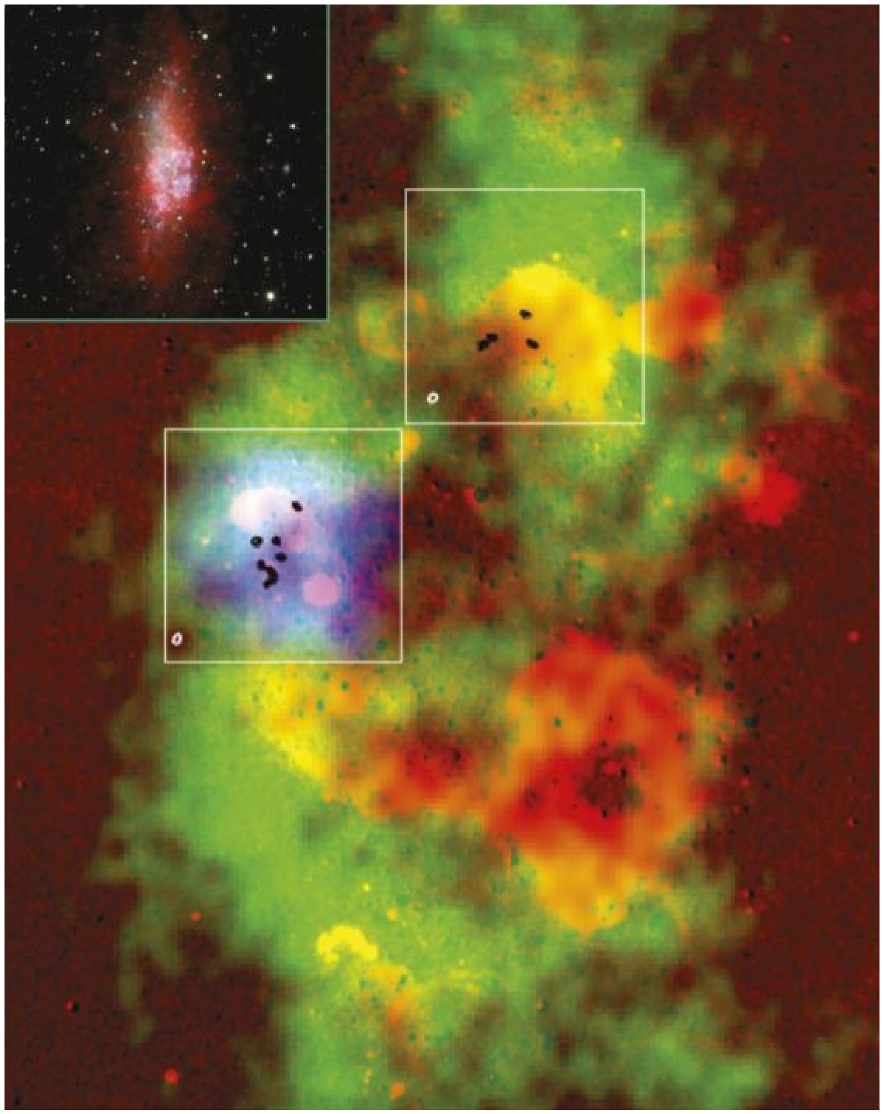

Figure 1. Figure 1 from Rubio *et al.* (2015), a three-color composite detailing the gas phases in WLM: Hα in red (Massey *et al.* 2007), H I in green (Hunter *et al.* 2012), and [CII]λ158μm in blue (Cigan *et al.* 2016). The black contours inside the 1'×1' white squares are the original 10 detected CO cores from ALMA CO(1-0) Cycle 1 observations from Rubio et al. 2015. The top left corner shows the full view of WLM obtained by combining H I (red, Hunter *et al.* 2012), V band (green, Hunter and Elmegreen 2006), and GALEX FUV (blue, Zhang *et al.* 2012) data.

1.1.4 Star Formation in Low-Metallicity Galaxies

WLM is an excellent case study for examining star formation in low-metallicity environments. Dwarf irregular galaxies provide crucial insights into star formation under low-metallicity conditions, serving as local analogs for early-universe galaxies. In the first few billion years after the Big Bang, galaxies formed in environments with low dust content and reduced metal abundances, conditions that are mirrored in present-day dIrrs (Tolstoy *et al.* 2009). Unlike the Milky Way, where molecular clouds are well-traced by CO emission, WLM and other dIrrs often exhibit weak or absent CO detections, despite ongoing star formation.

Located at a distance of ∼980 kpc, WLM's proximity makes it an ideal laboratory for studying star formation in detail. Though it was previously believed that a metallicity of 13% solar like in WLM would result in CO being fully photodissociated, the ALMA observations by Elmegreen *et al.* (2013) and Rubio *et al.* (2015) have revealed a complex CO structure in WLM (Taylor and Klein 2001; Lee *et al.* 2005). A three-color composite of WLM from Rubio *et al.* (2015) showing ancillary Hα (red, Massey *et al.* 2007), H I (green, Hunter *et al.* 1998), and [C II] (blue, Cigan *et al.* 2016) observations, along with the 10 CO cores detected by Rubio *et al.* (2015) is shown in Figure 1. The top left corner of the figure also includes a three-color composite of WLM combing H I (red, Hunter *et al.* 2012), V-band (green, Hunter and Elmegreen 2006), and GALEX FUV (blue, Zhang *et al.* 2012) observations of the full galaxy. Rubio et al. (in preparation) detected an additional 35 CO cores in WLM with ALMA Cycle 6. Though the detected CO cores are small, with an average radius of ∼2.3 parsecs, their properties such as CO linewidths (σ_v), luminosities (L_{CO}), and virial masses (M_{vir}) are typical for parsec-size molecular cloud cores in the solar neighborhood. That is, the CO cores detected in WLM still abide by the Larson size-linewidth relation, which describes the correlation between the velocity dispersion (σ_v) and the radius (R) of molecular cloud structures:

$$\sigma_v \propto R^\gamma \tag{1.3}$$

where γ is typically found to be around 0.5 in Galactic molecular clouds (Larson 1981). One analogy for this relation is city traffic patterns: smaller cities generally have fewer major roads, resulting in more uniform and typically slower traffic speeds. Conversely, larger cities have a broader range of road types, such as freeways and neighborhood streets, producing significantly greater variations in vehicle speeds. In other words, velocity dispersion increases disproportionately with the size of the system, reflecting greater turbulence in larger molecular clouds, similar to the increasingly complex and varied traffic patterns in larger cities.

The Larson size-linewidth relation suggests that larger molecular cloud structures exhibit greater turbulent velocity dispersions, consistent with a turbulence-driven ISM. The physical interpretation of this scaling law is linked to the turbulent cascade, where energy is injected at large scales and transferred to smaller scales, leading to observed self-similar properties of clouds, which extends to the CO cores found in WLM (Larson 1981; Heyer *et al.* 2009; Rubio *et al.* 2015). The linewidth versus radius of the 10 CO cores in WLM, along with other CO clouds found in the SMC, LMC, M31, M33, and other dwarf galaxies is shown in Figure 2. In Chapter 2, we examine the star-forming regions and surrounding environment where the the CO cores detected in WLM formed compared to other star-forming regions in the galaxy where no CO cores were detected.

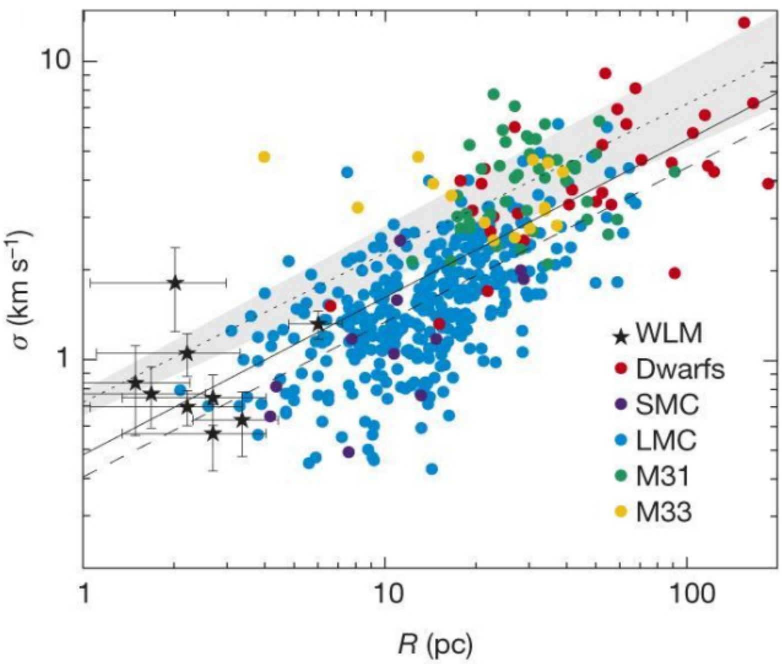

Figure 2. Figure 3a from Rubio *et al.* (2015), CO linewidth (σ_v) versus radius (R) for CO clouds in Local Group galaxies, where the solid line is a fit to WLM, the SMC, and dwarf galaxies, the dashed line also includes LMC's CO clouds in the fit, and the black short dashed line and the grey area indicate the standard relation for the Milky Way

1.2 Research Context

1.2.1 The Challenge of CO-Dark Molecular Gas

A key assumption in star formation studies is that CO emission traces molecular gas, providing an indirect measure of the total H_2 content in galaxies. However, observations have shown that CO emission does not always coincide with active star formation, particularly in low-metallicity galaxies (e.g., Schruba *et al.* 2012; Bolatto *et al.* 2013; Madden *et al.* 2020). In Chapter 3, we examine the relationship between CO cores in WLM and early star formation. Many low-metallicity dwarf galaxies exhibit weak or undetectable CO emission despite ongoing star formation, challenging the standard model of star formation in which CO-rich molecular clouds serve as the primary star-forming regions (Elmegreen *et al.* 1980). If CO-based estimates of H_2 mass are applied using standard X_{CO} conversion factors for more massive galaxies, the inferred SFEs appear anomalously high relative to the Schmidt-Kennicutt relation, which describes how the the star formation rate (SFR) surface density (Σ_{SFR}) scales as some positive power (n) of the local gas surface density (Σ_{gas}) (Kennicutt 1998; Madden and Cormier 2019):

$$\Sigma_{SFR} \propto (\Sigma_{gas})^n. \tag{1.4}$$

The Schmidt-Kennicutt relation is similar to how the growth rate of plants depends on the richness of soil. In a garden, the more fertile the soil, the more plants can grow. Similarly, in galaxies, the more gas there is in a given area, the more stars can form. If a section of a garden has nutrient-rich soil, plants will grow faster. In the same way, regions in a galaxy with high gas density experience more rapid star formation. If you double the nutrients in the soil, plant growth does not necessarily double–it often increases at a steeper rate due to compounding benefits. The Schmidt-Kennicutt relation similarly follows a power-law. For star forming galaxies, $n \approx 1.4$.

The discrepancy in the Schmidt-Kennicutt relation for low metallicity dwarfs suggests that a substantial fraction of molecular gas exists in a CO-dark state, where H_2 is present but remains undetected due to insufficient CO emission (Wolfire *et al.* 2010; Madden *et al.* 2020). Consequently, CO-based methods likely underestimate the total molecular gas mass available for star formation in low-metallicity environments. The existence of CO-dark molecular gas can be attributed to the unique ISM conditions in low-metallicity galaxies. In metal-rich galaxies like the Milky Way, CO survives within molecular clouds due to dust shielding, which protects CO molecules from photodissociation by UV radiation. Elmegreen (1989) suggests that at low metallicity, the extended CO formation timescale allows H_2 to be disrupted and dissociated before CO can form, except in the densest cloud cores. This delay is partly due to the lower dust abundance at low metallicity, which reduces shielding against FUV radiation, enabling CO photodissociation while leaving behind smaller CO cores (Elmegreen *et al.* 1980; Taylor *et al.* 1998; Schruba *et al.* 2012). In contrast, H_2 is self-shielded and can persist in PDRs. This results in a situation where large reservoirs of molecular gas exist but remain invisible to CO surveys, making CO an unreliable tracer of H_2 in these galaxies (Wolfire *et al.* 2010; Pineda *et al.* 2014; Cormier *et al.* 2017; Madden *et al.* 2020).

Given this limitation, alternative tracers are required to accurately measure the molecular gas content in low-metallicity galaxies. One promising approach is dust-based gas tracers, where the total gas mass is estimated by measuring far-infrared (FIR) dust emission and calibrating it with known dust-to-gas ratios (Rémy-Ruyer *et al.* 2014; Madden *et al.* 2020; Hu *et al.* 2023). Since dust is mixed with both atomic and molecular gas, this method provides a more complete picture of total gas content, though it still relies on assumptions about dust properties in different galactic environments. Another important tracer is the [C II] 158μm fine-structure line, which is emitted from CO-dark molecular regions where carbon exists in the form of [C II] rather than CO. Observations have shown that [C II] emission is strongly correlated with star formation activity, making it a valuable alternative tracer in CO-poor galaxies (Requena-Torres *et al.* 2016; Madden *et al.* 2020; Ramambason *et al.* 2024).

In Chapter 4, we measure the physical properties of stellar populations within and surrounding a star-forming region in WLM and measure the total gas content within the [C II]-defined PDR. If CO-dark gas dominates molecular reservoirs in low-metallicity galaxies, the initial conditions for star formation in the early universe may have differed significantly from those observed in the Milky Way today. Studying the CO-dark fraction in WLM and similar dIrrs provides crucial insights into star formation under these conditions, ultimately refining models of galaxy evolution across cosmic time.

1.2.2 Implications for Star Formation Theories

The presence of CO-dark gas necessitates a revised understanding of molecular cloud evolution in metal-poor galaxies. Unlike metal-rich environments where molecular clouds are long-lived, CO-bright structures, low-metallicity galaxies may host transient, CO-poor clouds in which star formation occurs in more diffuse and turbulent gas reservoirs (Scalo and Elmegreen 2004; El-Badry *et al.* 2018; Hunter *et al.* 2021, 2024). These findings suggest that the classical model of star formation occurring predominantly in CO-rich molecular clouds may not be universally applicable, particularly in dwarf irregular galaxies and early-universe systems. If a substantial fraction of molecular gas is CO-dark, then the total available gas mass is likely underestimated when using CO-based methods alone. This, in turn, affects our understanding of SFE, which is typically defined as the ratio of the SFR to the molecular gas mass (Krumholz *et al.* 2012).

In low-metallicity galaxies dominated by CO-dark gas, current SFE estimates may be artificially high, as they are based on an incomplete accounting of molecular gas. The actual molecular gas reservoir could be much larger than inferred from CO alone, suggesting that intrinsic SFEs may be lower than previously thought. This has profound implications for galaxy evolution models, particularly for dwarf galaxies, which serve as analogs for early-universe systems. The first galaxies likely formed in environments with low metallicity and weak dust shielding, conditions in which CO-dark gas may have played a central role in fueling early star formation. Understanding these environments is essential for constructing accurate models of early galaxy formation and evolution.

Observations of nearby dwarf galaxies, including WLM, provide an opportunity to refine theoretical models of early star formation by constraining the role of CO-dark gas. If molecular clouds in metal-poor environments evolve differently from those in metal-rich galaxies, models must be adjusted to account for the influence of CO-dark gas on the total molecular content. A deeper understanding of these processes will improve the interpretation of low-metallicity galaxy observations and enhance models of star formation across cosmic time.

1.3 Bridging Science and Education

Scientific discoveries in astrophysics not only expand our understanding of the universe but also present challenges in effectively communicating these complex ideas to students and the general public. One of the most significant challenges in astronomy education is ensuring that students develop a correct conceptual understanding of fundamental processes such as star and planet formation. Preconceptions about these topics can persist even among students who have taken formal courses in astronomy, highlighting the need for effective teaching strategies that address these misunderstandings. By bridging the gap between research in astrophysics and educational methodologies, we can enhance student learning and improve science literacy.

1.3.1 Common Student Preconceptions About Planet Formation

Research in astronomy education has demonstrated that students frequently struggle with fundamental concepts in star and planet formation, often confusing these processes with broader cosmological evolution. One preconception is the belief that planetary systems, including the Solar System, formed at the same time as the universe itself, despite the events being separated by more than nine billion years (Simon *et al.* 2018). In addition to this large-scale misunderstanding, Simon *et al.* (2018) also find that students struggle with key details about planet formation, such as the differentiation between gas giants and terrestrial planets, as well as concepts like planetary migration, which explain the existence of hot Jupiters.

These preconceptions in education often parallel scientific uncertainties in astrophysics. While scientists have developed a well-established framework for planet formation, significant questions remain regarding the diversity of exoplanetary architectures and the factors influencing planetary habitability. For example, while the nebular theory provides a foundational model for solar system formation, the discovery of hot Jupiters and compact planetary systems like TRAPPIST-1 challenges traditional expectations of planet formation and migration, much like how students struggle to reconcile theoretical models with observational data. The difficulty in understanding how planetary systems evolve—both for students and scientists—highlights the importance of addressing preconceptions in education. Addressing student preconceptions, therefore, not only improves education but also mirrors the iterative process of scientific discovery (Simon *et al.* 2018).

1.3.2 Lecture-Tutorials as a Solution

To address these common preconceptions and improve student understanding, astronomy educators have increasingly adopted active learning strategies that engage students in structured reasoning and guided inquiry. One such approach is the use of lecture-tutorials, a type of interactive worksheet designed to guide students through conceptual reasoning using carefully scaffolded questions and peer discussion. Studies have shown that active learning strategies, including lecture-tutorials, significantly enhance student comprehension and retention of scientific concepts (Chi and Wylie 2014; Freeman *et al.* 2014; Lombardi *et al.* 2021). By requiring students to work through reasoning exercises rather than passively receiving information, these approaches help students confront and correct their preconceptions in real time.

Lecture-tutorials have been successfully implemented in in-person astronomy courses, showing measurable improvements in student learning outcomes (Prather *et al.* 2004; Wallace *et al.* 2012; LoPresto and Slater 2016). By guiding students through step-by-step conceptual questions, these materials help learners construct a more accurate understanding of the content, moving beyond memorization to deeper comprehension.

With the increasing shift to online education, a key question remains: Can online or digital adaptations of lecture-tutorials achieve comparable learning gains? The effectiveness of active learning depends not only on content delivery but also on student engagement and interaction, which may be more challenging to replicate in an online format. Evaluating online lecture-tutorials requires assessing whether students experience similar improvements in conceptual understanding and whether interactive features can enhance the learning experience. Can online instructional tools be just as effective as traditional methods, provided they incorporate elements of active learning? As astronomy education continues to evolve, integrating research-based instructional strategies into digital platforms will be essential for ensuring that students develop a robust understanding of planet formation. In Chapter 5, we discuss our development and assessment of an online lecture-tutorial to teach planet formation in a more interactive way.

1.4 Research Objectives

This dissertation addresses two key areas of research: the astrophysical study of star formation in low-metallicity environments and the development of effective educational strategies for teaching planet formation. The first component focuses on characterizing the molecular gas properties of the dwarf irregular galaxy WLM, particularly the distribution and role of CO-bright and CO-dark molecular gas in the star formation process. The second component evaluates active learning methodologies in astronomy education, aiming to improve student understanding of planet formation through online interactive tools.

1.4.1 Astrophysical Research Objectives

One of the primary goals of this dissertation is to investigate the molecular gas conditions in WLM, a low-metallicity dwarf irregular galaxy that serves as an analog for early-universe galaxies. WLM is still forming stars, though the detected CO cores are small, suggesting that the CO emission is not representative of the total molecular gas reservoir. To address this, the astrophysical research objectives include:

- **Characterizing CO cores in WLM and examining their environmental conditions:** This involves analyzing the spatial distribution and physical properties of star-forming regions with and without CO cores in WLM. Understanding the environmental factors that lead to CO core formation and survival in low-metallicity ISM conditions will provide key insights into the molecular cloud lifecycle.
- **Investigating the relationship between CO cores and young stellar populations:** By comparing the locations of CO core detections with JWST observations of young stellar populations, this work aims to determine role of the CO cores in star formation.
- **Analyzing the stellar populations in WLM and evaluating molecular gas composition:** Understanding the stellar populations and molecular gas content within a star-forming region of WLM is crucial for determining the contributions of both CO-bright and CO-dark gas to star formation within the photodissociation region (PDR).

1.4.2 Astronomy Education Research Objectives

The second component of this dissertation focuses on improving astronomy education by evaluating effectiveness of online lecture-tutorials. Research in science education has shown that preconceptions about astronomical processes are common and that interactive learning strategies can help students develop a deeper conceptual understanding. To address these challenges, the educational research objective is:

- **Assessing the effectiveness of online lecture-tutorials in teaching planet formation:** Lecture-tutorials have been shown to improve conceptual understanding in traditional classroom settings, but their effectiveness in online or digital formats remains less well understood. This study aims to determine whether online adaptations of lecture-tutorials produce comparable learning gains and whether online interactive tools enhance student engagement.

By integrating astrophysical research with education studies, this dissertation aims to advance both scientific knowledge of star formation in low-metallicity galaxies and best practices in astronomy education. The findings from this work will contribute to a broader understanding of how galaxies evolve and how students develop accurate scientific reasoning in astronomy.

1.5 Dissertation Statement

This dissertation explores two key questions in astrophysics and education: (1) What is the role of CO cores in star formation in low-metallicity galaxies? and (2) How can astronomy education effectively convey complex astrophysical concepts in online learning environments? The astrophysical component investigates CO cores in the low-metallicity dwarf galaxy WLM, assessing their relationship to the surrounding stars and gas. The educational component evaluates the effectiveness of online lecture-tutorials in improving student understanding of planet formation. By integrating these studies, this work advances both our knowledge of star formation in metal-poor environments and best practices in online science education.

1.6 Dissertation Structure

Each chapter builds upon the previous one, transitioning from astronomical research to education research:

- *Chapter 2*: The Environments of CO Cores in WLM
  - Examines the physical properties such as H I surface density, stellar mass surface density, and pressure of the star-forming regions in WLM with and without CO cores, as well as their surrounding environments.
- *Chapter 3*: The Relationship Between CO and Young Stellar Populations
  - Investigates the role of CO cores in young star formation.
- *Chapter 4*: Molecular Gas Composition and Star Formation Efficiency
  - Explores stellar populations in and surrounding a star-forming region of WLM and evaluates the true molecular gas content within the PDR.
- *Chapter 5*: Online lecture-tutorials for Astronomy Education
  - Evaluates the impact of digital active learning on student comprehension of planet formation.
- *Chapter 6*: Conclusion and Future Directions
  - Summarizes key findings and their implications for both low-metallicity star formation and astronomy education.

Chapter 2

THE ENVIRONMENTS OF CO CORES AND STAR FORMATION IN THE DWARF IRREGULAR GALAXY WLM

[1,2]Haylee N. Archer, [2]Deidre A. Hunter, [3]Bruce G. Elmegreen, [4]Phil Cigan, [1]Rolf A. Jansen, [1]Rogier A. Windorst, [5]Leslie K. Hunt, [6]Monica Rubio

[1]School of Earth and Space Exploration, Arizona State University, Tempe, AZ, USA
[2]Lowell Observatory, Flagstaff, AZ, USA
[3]IBM T. J. Watson Research Center, Yorktown Heights, NY, USA
[4]George Mason University, Fairfax, VA, USA
[5]INAF, Osservatorio Astrofisico di Arcetri, Firenze, Italy
[6]Departamento de Astronomía, Universidad de Chile, Santiago, Chile

Published in the Astronomical Journal at doi.org/10.3847/1538-3881/ac4e88 (Archer *et al.* 2022b)

Abstract: The low metallicities of dwarf irregular galaxies (dIrr) greatly influence the formation and structure of molecular clouds. These clouds, which consist primarily of H_2, are typically traced by CO, but low metallicity galaxies are found to have little CO despite ongoing star formation. In order to probe the conditions necessary for CO core formation in dwarf galaxies, we have used the catalog of Rubio et al. (2022, in preparation) for CO cores in WLM, a Local Group dwarf with an oxygen abundance that is 13% of solar. Here we aim to characterize the galactic environments in which

these 57 CO cores formed. We grouped the cores together based on proximity to each other and strong FUV emission, examining properties of the star forming region enveloping the cores and the surrounding environment where the cores formed. We find that high H I surface density does not necessarily correspond to higher total CO mass, but regions with higher CO mass have higher H I surface densities. We also find the cores in star forming regions spanning a wide range of ages show no correlation between age and CO core mass, suggesting that the small size of the cores is not due to fragmentation of the clouds with age. The presence of CO cores in a variety of different local environments, along with the similar properties between star forming regions with and without CO cores, leads us to conclude that there are no obvious environmental characteristics that drive the formation of these CO cores.

2.1 Introduction

Wolf-Lundmark-Melotte (WLM) is a Local Group, dwarf irregular (dIrr) galaxy at a distance of 985 ± 33 kiloparsecs (kpc) (Leaman *et al.* 2012). Like other dwarf galaxies, the mass and metallicity of WLM are low, with a total stellar mass of $1.62 \times 10^7 M_\odot$ (Zhang *et al.* 2012) and metallicity of 12+log(O/H)=7.8 (Lee *et al.* 2005). WLM is an isolated galaxy, and the large spatial distances between it and both the Milky Way and M31 indicate a low probability of past interaction with either (Teyssier *et al.* 2012; Albers *et al.* 2019). The low mass, low metallicity, distance, and isolation of WLM make it an ideal laboratory for understanding star formation in undisturbed dwarf galaxies.

Star formation in galaxies is believed to be mostly regulated by molecular gas found in giant molecular clouds (GMCs) in the interstellar medium (ISM) (Kennicutt

1998; McKee and Ostriker 2007). The most abundant species in these molecular clouds is molecular hydrogen (H_2), which is nearly impossible to observe in the typical conditions of the cold ISM because it does not possess a permanent dipole moment and thus no dipolar rotational transitions (Bolatto *et al.* 2013). As such, H_2 is traced using indirect methods, the most common of which is through the measurement of low rotational lines of carbon monoxide (CO). Despite being much less abundant than H_2 in molecular clouds, CO is easily excited even in the cold ISM.

Many low-metallicity dwarf galaxies are found to have little CO despite ongoing star formation (Elmegreen *et al.* 1980), which disputes the standard model of star formation in CO-rich molecular clouds. If the small amount of detected CO is translated to the total H_2 of the cloud using the standard conversion factor, X_{CO}, of more massive galaxies, the high inferred star formation efficiency of the dwarfs would make them outliers on the Schmidt-Kennicutt relation (Kennicutt 1998; Madden and Cormier 2019). Elmegreen (1989) finds that the increase in CO formation time at lower metallicity could result in the disruption and dissociation of H_2 before CO can form anywhere but in the cores of larger clouds. This longer CO formation time is partly because lower metallicity also corresponds to lower dust abundance, which allows far-ultraviolet (FUV) photons to photodissociate CO molecules in the molecular cloud and leave behind smaller CO cores (Elmegreen *et al.* 1980; Taylor *et al.* 1998; Schruba *et al.* 2012). H_2 is self-shielded from the FUV photons and can survive in the photodissociation region (PDR). This H_2 gas that is not traced by the CO cores is referred to as “dark" gas (Wolfire *et al.* 2010). There is strong evidence that the observed lack of CO at low metallicities is a natural consequence of the lower carbon and oxygen abundances as metallicity decreases, with the result that the H_2 is primarily associated with the so-called CO-dark molecular gas (Wolfire *et al.* 2010; Pineda *et al.* 2014; Cormier *et al.* 2017).

Following the discovery by Elmegreen *et al.* (2013) of CO(3–2) in two star forming regions of WLM using the APEX telescope, Rubio *et al.* (2015) used pointed CO(1–0) of these regions with the the Atacama Large Millimeter Array (ALMA) to map 10 CO cores for the first time at an oxygen abundance that is 13% of the solar value (Lee *et al.* 2005; Asplund *et al.* 2009). The PDR region as traced by the C II observations surrounding six of the discovered cores is five times wider than the cluster of cores. This indicates that molecular cloud structure at lower metallicities consists of thicker H_2 shells and smaller CO cores compared to those seen in the Milky Way (Rubio *et al.* 2015; Cigan *et al.* 2016). An FUV image of the region with that PDR and the six detected CO cores overlaid as contours is shown in Figure 3. Rubio et al. (2022, in preparation) has since mapped most of the star forming area of WLM with pointed ALMA CO(2–1) observations and detected an additional 47 cores.

This paper seeks to characterize the galactic environments in which these star forming CO cores formed in WLM to determine (1) if the CO cores have the same properties in different local environments, (2) if areas where CO has formed have different properties from star forming regions without detected CO, (3) the nature of the stellar populations surrounding the molecular clouds, and (4) the relationship between CO and star formation. The paper is organized as follows. In Section 2.2 we introduce our multi-wavelength data and describe our region selection and definitions of their environment, along with our methods for determining the region age, stellar mass surface density, and CO-dark gas. We present our results in Section 2.3 and discuss our findings in Section 2.4.

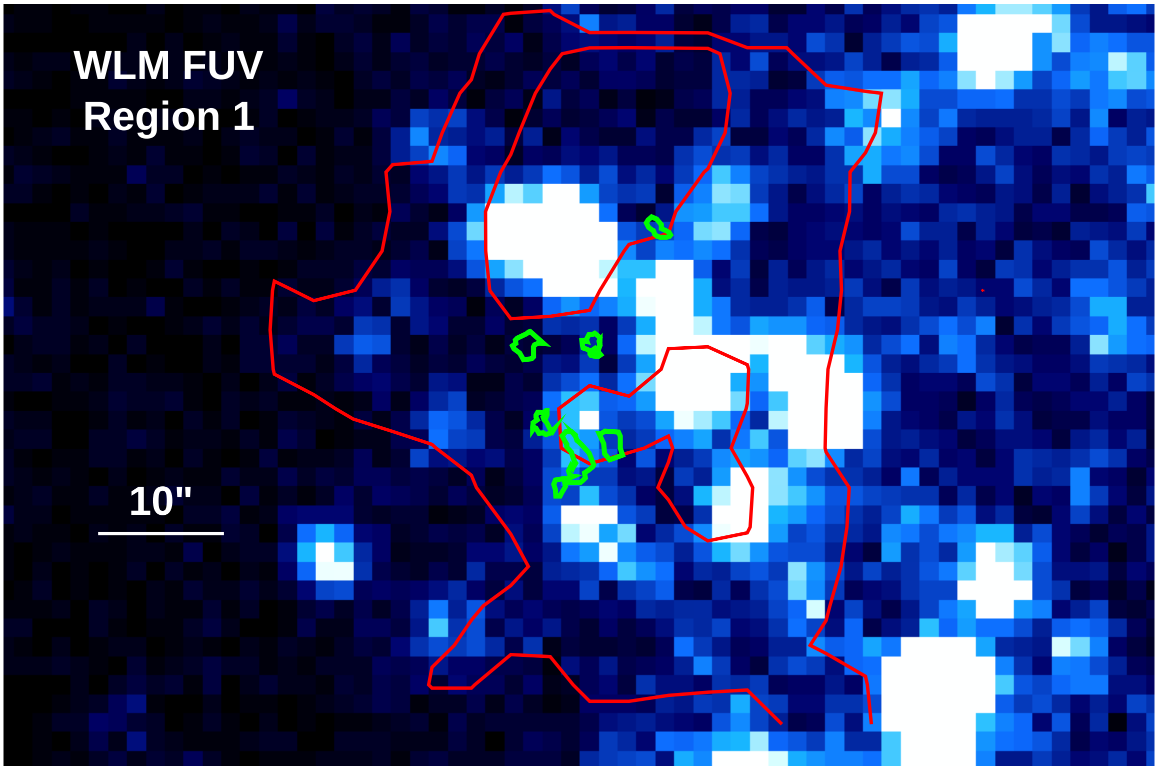

Figure 3. FUV image of a WLM star forming region (region 1 in this paper, as in Figures 5–8) overlaid with the PDR indicated by [C II]$\lambda 158\mu$m contours (red) of 2.5×10^{-19} and 4.6×10^{-19} W m^{-2} pix^{-1}, for pixels of 3.13″ per side, from Cigan *et al.* (2016) and 6 CO core contours (green) from Rubio *et al.* (2015).

2.2 Data

Two star-forming regions of WLM were imaged in CO(1–0) with ALMA in Cycle 1 by Rubio *et al.* (2015) where 10 CO cores were detected with an average radius of 2 pc and average virial mass of $2 \times 10^3\ M_\odot$. Another 47 CO cores were discovered in WLM from Cycle 6 ALMA CO(2–1) observations over much of the star-forming area of the galaxy, which included one of the two regions observed in Cycle 1 (Rubio et al., 2022, in preparation). The beam size of these observations were $0.6'' \times 0.5''$. These two resulting catalogues provide characteristics of the CO cores including locations, virial masses, and surfaces densities. We use the sum of the virial masses of the individual

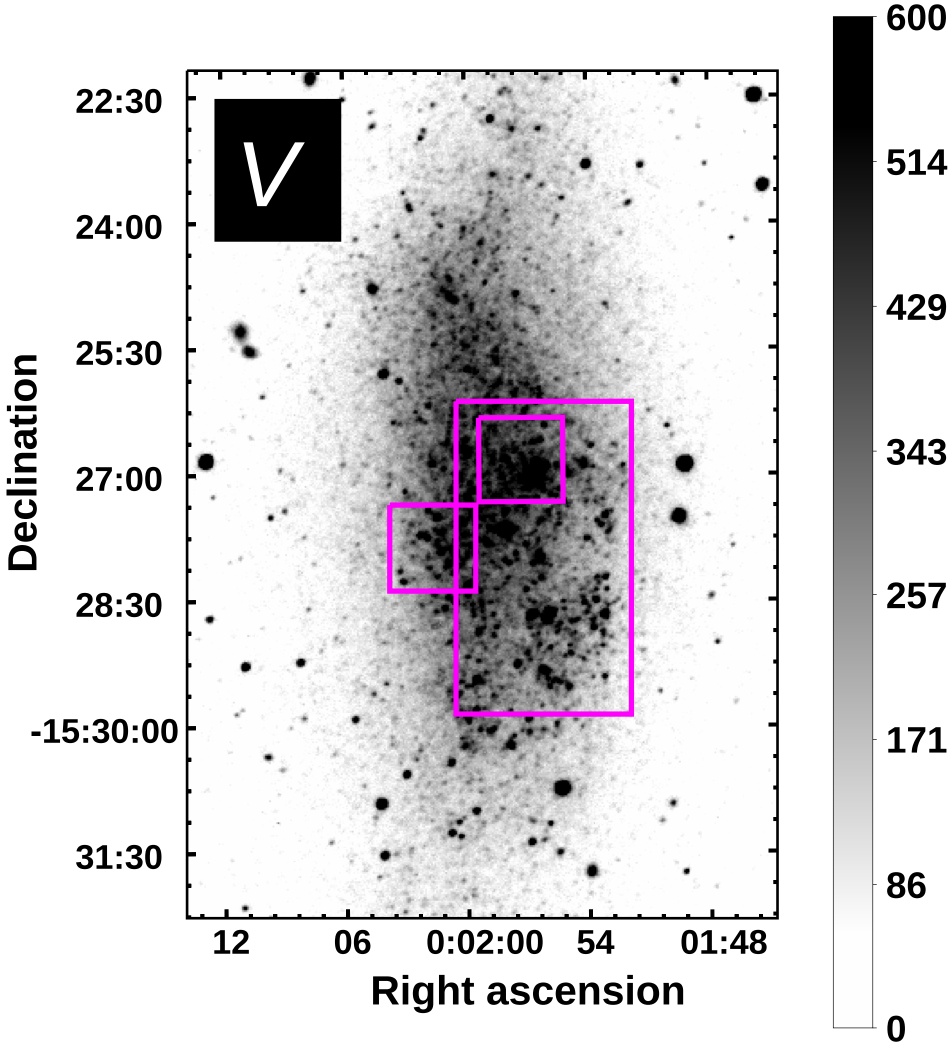

Figure 4. V band image of WLM showing the ALMA field of view (FOV) from Rubio *et al.* (2015) (smaller magenta squares) and Rubio et al. (2022, in preparation) (larger magenta rectangle). The orientation of the image is such that North is up and East is to the left. Colorbar values can be converted from counts in one pixel (DN/pixel) to Johnson magnitudes with the equation: $V_{Johnson} = 0.0157(B - V)_{Johnson} - 2.5 \log V_{counts} + 29.41$.

CO cores for each region ($M_{\mathrm{CO},vir}$) and the median surface density of the individual CO cores in each region (Σ_{CO}) to examine any relationships with other star forming and environmental properties. Figure 4 shows the V band image of WLM overlaid with an outline of the total field of view observed by Rubio *et al.* (2015) and Rubio et al. (2022, in preparation).

UBV images of WLM came from observations using the Lowell Observatory Hall 1.07-m Telescope. Further information on the acquisition and reduction of these images are described by Hunter and Elmegreen (2006). H I surface density ($\Sigma_{\rm H\,I}$) maps and H I surface density radial profiles were acquired by Hunter *et al.* (2012) with the Very Large Array (VLA[1]) for the Local Irregulars That Trace Luminosity Extremes, The H I Nearby Galaxy Survey (LITTLE THINGS), a multi-wavelength survey of 37 nearby dIrr galaxies and 4 nearby Blue Compact Dwarf (BCD) galaxies. The authors created robust-weighted and natural-weighted H I maps, and we chose to use the robust-weighted maps due to the higher resolution (6″). The FUV and near-ultraviolet (NUV) images came from the NASA Galaxy Evolution Explorer (GALEX[2]) satellite (Martin *et al.* 2005a) GR4/5 pipeline, and were further reduced by Zhang *et al.* (2012). We also used stellar mass surface density (Σ_*) and pressure maps created by Hunter *et al.* (2018). The stellar mass surface density image was determined on a pixel-by-pixel basis based on $B - V$ (Herrmann *et al.* 2016), and the pressure map was calculated with the equation

$$\mathrm{P} = 2.934 \times 10^{-55} \times \Sigma_{gas}(\Sigma_{gas} + (\frac{\sigma_{gas}}{\sigma_*})\Sigma_*)\ [\mathrm{g}/(\mathrm{s}^2\ \mathrm{cm})] \tag{2.1}$$

where Σ is a surface density and σ is a velocity dispersion (Elmegreen 1989). The Σ_{gas} in the pressure map comes from the robust-weighted H I map from Hunter *et al.* (2012). Further details on the creation of these images are described by Hunter *et al.* (2018). To gain insight into the formation of the CO cores, we used the pressure,

[1]The VLA, now the Karl G. Jansky Very Large Array, is a facility of the National Radio Astronomy Observatory. The National Radio Astronomy Observatory is a facility of the National Science Foundation operated under cooperative agreement by Associated Universities, Inc. Observations were made during the transition from the Very Large Array to the Karl G. Jansky Very Large Array.

[2]GALEX was operated for NASA by the California Institute of Technology under NASA contract NAS5-98034.

H I surface density, and stellar mass surface density data to characterize the regions within which the CO cores formed and the environment surrounding the regions. We also used the *UBV*, FUV, and NUV data for determining ages of the young stars in the star-forming regions of the CO cores.

2.2.1 Regions

We grouped the CO cores into regions based on apparent proximity to FUV knots and each other. The size and clustering of region 1 was chosen using both the ALMA mapped CO cores of Rubio *et al.* (2015) and their [C II]λ158 micron image from the Herschel Space Observatory indicating the PDR that surrounds those cores (Figure 3). The other regions were chosen by eye based on the following criteria: 1) apparent distance to nearby FUV emission within the plane of the galaxy and 2) apparent distance to other CO cores, with the size of the region determined by grouping CO cores that appeared to be closest to the same FUV knots. We then used SExtractor (Bertin and Arnouts 1996) with a detection and analysis threshold of 3 sigma, a minimum of 10 pixels above the threshold for detection, and a background mesh and filter size of 50 and 7 respectively to objectively identify the brighter FUV knots. We then computed the distances between the center of the CO cores and the center of the detected FUV sources to determine how far each CO core in a region is from its closest detected FUV knot.

We attempted to cluster the CO cores using the clustering algorithm DBSCAN (Density-Based Spatial Clustering of Applications with Noise) (Ester *et al.* 1996).

We found that we could not reproduce the known clustering in region 1 with this algorithm. Depending on the parameters chosen, the algorithm would either include most CO cores across the galaxy in the same cluster or leave each core as an outlier.

Instead, we grouped the cores into 22 regions, several of which only include one CO core. Four additional regions (regions 23, 24, 25, and 26) were selected as regions including strong FUV emission without any CO cores. These regions were used as comparisons to the regions containing CO cores. The regions, along with the CO

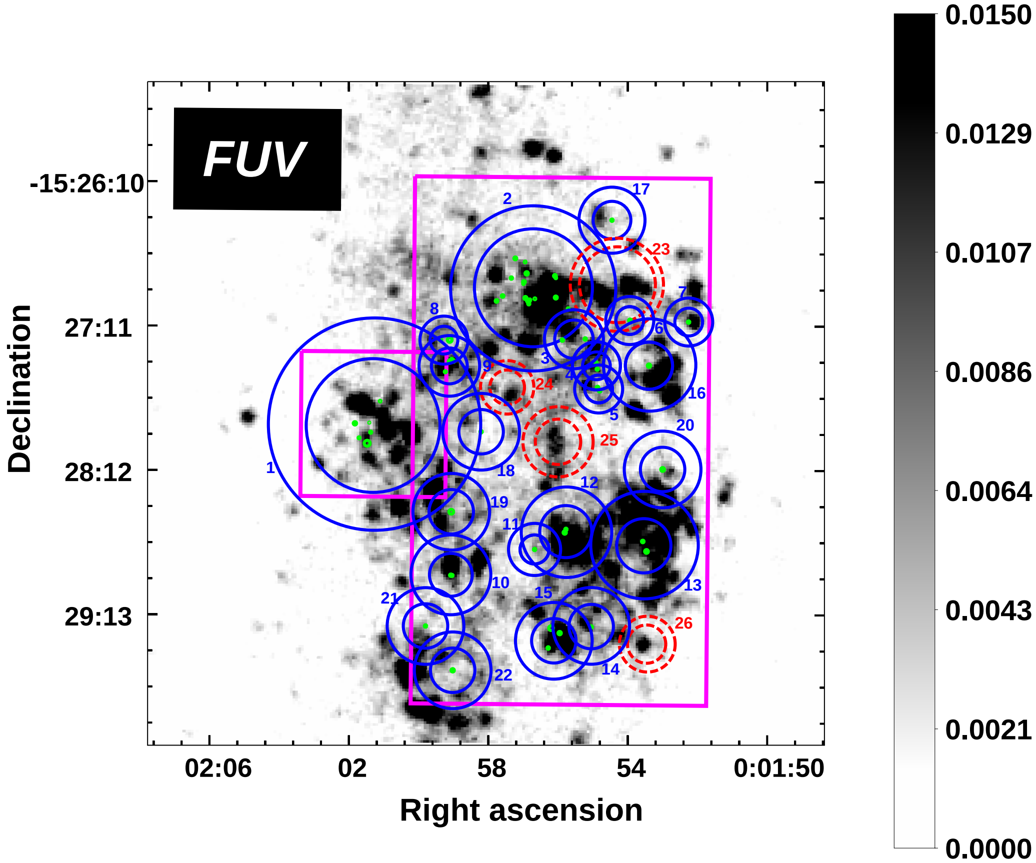

Figure 5. FUV image of WLM showing the ALMA FOV of region 1 from Rubio *et al.* (2015) (smaller magenta square) and of the Rubio et al. (2022, in preparation) survey (larger magenta rectangle), regions and annuli defined here (blue circles for regions with CO cores and red dashed circles for the regions without CO cores), and the CO cores (tiny green circles). Colorbar values can be converted from counts to calibrated AB magnitudes with the equation: $\mathrm{FUV}_{AB} = -2.5\log_{10}(\mathrm{FUV}_{counts}) + 18.82$.

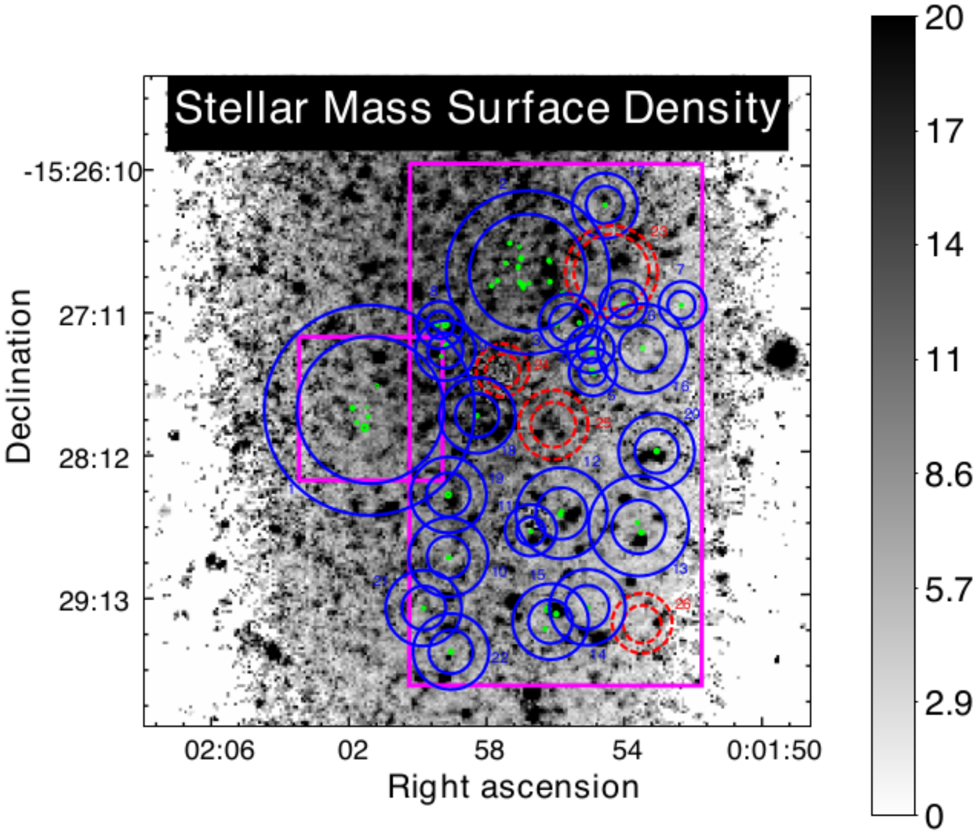

Figure 6. As in Figure 5, but for stellar mass surface density. The colorbar values are in units of $M_{\odot}$ pc^{-2}.

cores and ALMA FOV from both Rubio *et al.* (2015) and Rubio et al. (2022, in preparation), are overlaid and labeled on the FUV, stellar mass surface density, H I surface density, and pressure maps in Figures 5, 6, 7, and 8, respectively. We list the region IDs, coordinates, and sizes in the table in Figure 9.

2.2.2 Environments

Each region consists of a circular inner region representing the CO cores and the star-forming region in which they currently sit, along with an outer annulus which represents the projected environment in which the star-forming region formed. We will

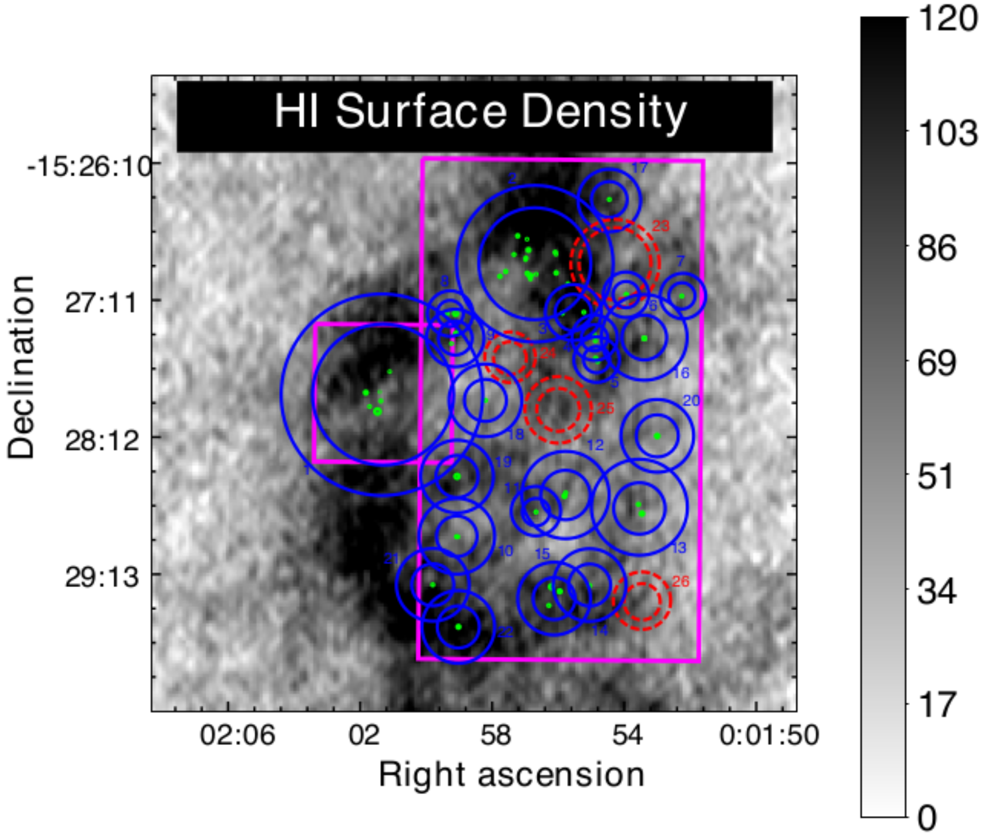

Figure 7. As in Figure 5, but for H I, with a beam size of 7.6″ × 5.1″. The colorbar values can be multiplied by 0.231 to convert from J bm^{-1} m s^{-1} to $M_\odot$ pc^{-2} (see §2.2.2).

refer to the star forming regions as the *inner regions* and the surrounding environments as the *annuli*. For region 1, we chose the inner region to be about the size of the PDR. The outer annuli widths used in measuring the environmental characteristics ranged from 3.7 to 14.2 arcseconds depending on the location of the CO cores in the galaxy and their surrounding to minimize contamination from other regions. The annuli are also overlaid on the FUV, stellar mass surface density, H I surface density, and presssure maps in Figures 5, 6, 7, and 8, respectively and can be found in the table in Figure 9.

We used the Image Reduction and Analysis Facility (IRAF) (Tody 1986) routine

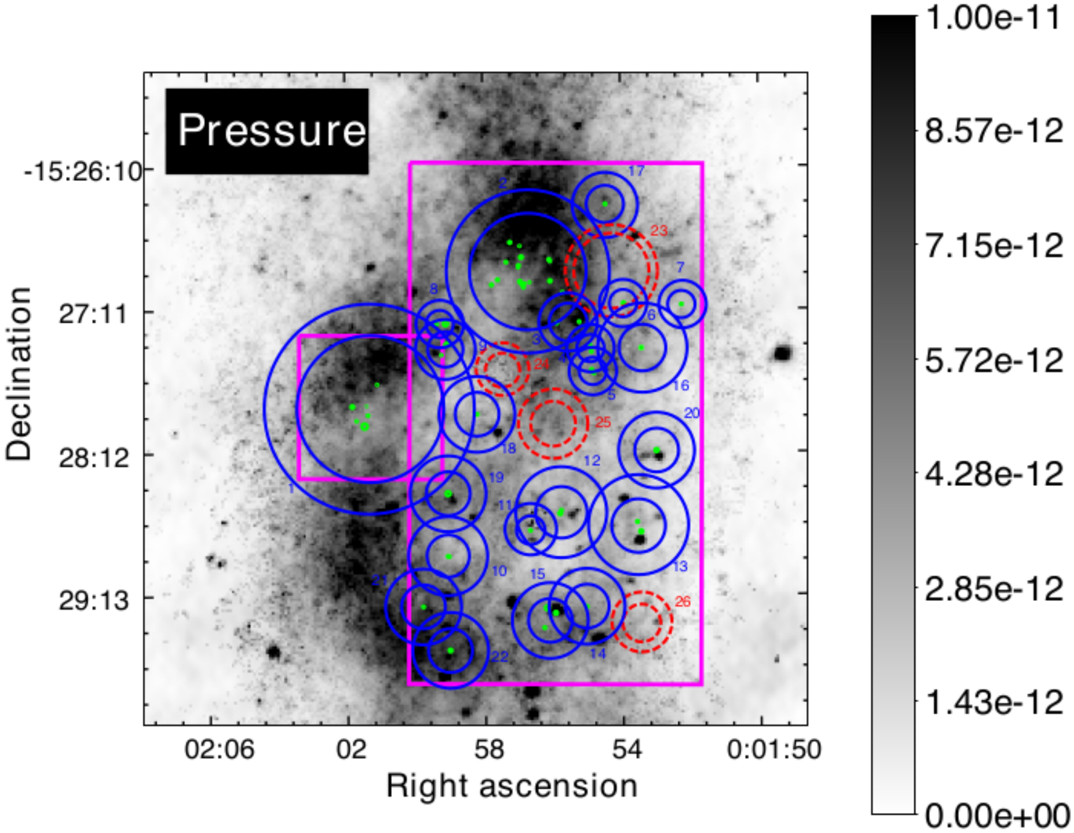

Figure 8. As in Figure 5, but for pressure with a beam size of $7.6'' \times 5.1''$. The pressure is dominated by the gas, as is evident from a comparison with Figure 7. The colorbar values are in units of g s^{-2} cm^{-1}.

Apphot to measure the fluxes in the H I surface density, stellar mass surface density, pressure map, U, B, V, FUV, and NUV images. We found the average pixel value for each inner region and the modal pixel value each outer annulus. The modal pixel value was chosen for the annulus to minimize contamination from the environmental annulus overlapping other regions. We converted the pixel values for the UBV images to Johnson magnitudes for each region and the FUV and NUV image values for each region to AB magnitudes. We also converted the H I surface density values from Jy·m beam^{-1} s^{-1} to $M_{\odot}$ pc^{-2} using the equation

$$M_{HI} = 235.6\ D^2 \sum_i S_i \Delta V \tag{2.2}$$

where D is the distance to the object in Mpc, S_i is the flux in Jy, ΔV is the velocity resolution in m s^{-1}, and M_{HI} is in units of $M_\odot$ (Brinks, private communication). The Robust-weighted H I moment 0 map ($S_i \Delta V$) is in units of Jy·m beam^{-1} s^{-1} per pixel, so we divide this by the number of pixels per beam

$$M_{HI} = 235.6\ D^2 \sum_i S_i \Delta V\ \times \frac{pixel\ size^2}{1.13\ \Delta\alpha\Delta\delta} = 208.5\ D^2 \sum_i S_i \Delta V\ \times \frac{pixel\ size^2}{\Delta\alpha\Delta\delta} \quad (2.3)$$

where the distance to WLM is 1 Mpc, the pixel size is 1.5″ and $\Delta\alpha$ and $\Delta\delta$ are the beam semi-major and semi-minor axis, which are 7.6″ and 5.1″ respectively. This makes the M$_{HI}$ in one pixel

$$M_{HI} = 12.21\ S[Jy/beam \cdot m/s/pixel]\ M_\odot. \quad (2.4)$$

One pixel is 52.93 pc^2, so the H I surface density becomes

$$\Sigma_{HI} = 0.231\ S[Jy/beam \cdot m/s/pixel]\ \ M_\odot/pc^2. \quad (2.5)$$

The stellar mass density and pressure map images were already in units of $M_\odot$ pc^{-2} and g s^{-2} cm^{-1} respectively. We list the center coordinates, radius of star forming region, and width of annulus of each region, along with the background subtracted and extinction corrected colors described in §2.2.3 for each inner region can be found in the table in Figure 9, while the inner region H I surface densities and stellar mass surface densities can be found in the table in Figure 10. The extinction corrected colors, H I surface densities, stellar mass surface densities, and pressures for each region's corresponding annulus can be found in the table in Figure 11. The quantities are averaged over regions or annuli that are larger than the 6″ resolution of the H I and pressure maps except for a few annuli widths, as can be seen in the table in Figure 9.

Table 1. Region centers & background subtracted photometry of star forming regions

Region (1)	RA *(J2000)* (2)	Dec *(J2000)* (3)	Inner Radius (″) (4)	Annulus Width (″) (5)	*FUV* *(mag)* (6)	*FUV − NUV* *(mag)* (7)	*V* *(mag)* (8)	*U − B* *(mag)* (9)	*B − V* *(mag)* (10)
1	0:02:01.7	−15:27:53.0	23.4	10.2	22.61 ± 0.01	−0.32 ± 0.01	23.88 ± 0.06	−0.32 ± 0.14	−0.17 ± 0.08
2	0:01:57.0	−15:26:55.5	25.0	10.0	23.27 ± 0.01	−0.01 ± 0.01	23.66 ± 0.04	−0.51 ± 0.09	−0.06 ± 0.06
3	0:01:55.8	−15:27:16.2	8.2	4.4	23.35 ± 0.01	0.23 ± 0.01	23.60 ± 0.04	−0.45 ± 0.09	−0.11 ± 0.05
4	0:01:55.1	−15:27:27.5	5.9	4.3	24.54 ± 0.01	0.10 ± 0.01	25.41 ± 0.10	−0.78 ± 0.29	−0.41 ± 0.12
5	0:01:55.1	−15:27:37.3	5.9	4.3	24.73 ± 0.01	0.10 ± 0.01	24.72 ± 0.07	−0.20 ± 0.20	0.16 ± 0.10
6	0:01:54.2	−15:27:08.3	5.9	4.3	22.70 ± 0.01	−0.08 ± 0.01	23.84 ± 0.08	0.73 ± 0.29	−0.30 ± 0.11
7	0:01:52.5	−15:27:08.9	5.9	4.3	23.88 ± 0.01	−0.56 ± 0.01	26.77 ± 0.18	−0.62 ± 0.23	−1.11 ± 0.20
8	0:01:59.6	−15:27:16.7	5.9	4.3	17.04 ± 0.01	−0.22 ± 0.01	21.69 ± 0.08	−0.09 ± 0.33	−0.01 ± 0.13
9	0:01:59.5	−15:27:27.7	7.6	5.2	22.73 ± 0.01	−0.51 ± 0.01	23.97 ± 0.06	−0.46 ± 0.14	−0.18 ± 0.08
10	0:01:59.4	−15:28:56.2	9.1	7.8	23.62 ± 0.01	−0.27 ± 0.01	24.70 ± 0.07	−0.55 ± 0.14	−0.18 ± 0.09
11	0:01:56.0	−15:28:45.4	6.1	4.9	25.34 ± 0.01	0.56 ± 0.01	24.69 ± 0.07	−0.80 ± 0.14	−0.04 ± 0.09
12	0:01:56.1	−15:28:37.8	11.0	9.2	22.17 ± 0.01	−0.24 ± 0.01	23.20 ± 0.04	−0.55 ± 0.08	−0.08 ± 0.05
13	0:01:53.8	−15:28:43.8	11.5	11.3	24.00 ± 0.01	0.19 ± 0.01	23.48 ± 0.04	−0.07 ± 0.11	0.05 ± 0.05
14	0:01:55.3	−15:29:18.1	9.4	6.8	25.22 ± 0.01	−0.68 ± 0.01	26.15 ± 0.14	−1.15 ± 0.22	−0.31 ± 0.18
15	0:01:56.4	−15:29:24.1	9.4	6.8	22.68 ± 0.01	−0.05 ± 0.01	23.29 ± 0.04	−0.53 ± 0.10	0.19 ± 0.05
16	0:01:53.6	−15:27:27.4	10.0	10.0	23.13 ± 0.01	−0.09 ± 0.01	23.19 ± 0.04	−0.49 ± 0.09	0.16 ± 0.05
17	0:01:54.7	−15:26:25.8	8.0	6.0	24.60 ± 0.01	−0.01 ± 0.01	24.75 ± 0.07	−0.03 ± 0.18	−0.12 ± 0.09
18	0:01:58.5	−15:27:55.5	9.4	6.8	19.77 ± 0.01	… [1]	22.80 ± 0.11	0.53 ± 0.36	−0.31 ± 0.18
19	0:01:59.4	−15:28:29.5	9.4	6.8	23.20 ± 0.01	−0.18 ± 0.01	23.99 ± 0.06	−0.20 ± 0.16	0.05 ± 0.08
20	0:01:53.2	−15:28:11.4	9.4	6.8	17.90 ± 0.01	−0.47 ± 0.01	21.81 ± 0.05	−0.23 ± 0.19	0.07 ± 0.08
21	0:02:00.2	−15:29:17.9	9.4	6.8	24.66 ± 0.01	−0.35 ± 0.01	25.28 ± 0.09	−0.07 ± 0.21	−0.29 ± 0.12
22	0:01:59.4	−15:29:36.7	9.4	6.8	… [2]	… [2]	23.98 ± 0.08	1.06 ± 0.37	−0.28 ± 0.12
23	0:01:54.5	−15:26:54.4	16.0	14.2	23.08 ± 0.01	−0.27 ± 0.01	24.11 ± 0.06	−0.71 ± 0.13	−0.12 ± 0.08
24	0:01:57.8	−15:27:36.7	7.4	4.0	24.90 ± 0.01	−0.07 ± 0.01	28.97 ± 0.50	−4.94 ± 0.25	1.45 ± 0.55
25	0:01:56.3	−15:27:59.8	9.6	5.3	22.48 ± 0.01	−0.08 ± 0.01	22.97 ± 0.04	−0.18 ± 0.14	−0.08 ± 0.06
26	0:01:53.7	−15:29:25.4	8.1	3.7	20.62 ± 0.01	−0.40 ± 0.01	23.58 ± 0.06	−0.06 ± 0.23	−0.23 ± 0.11

[1] NUV background counts were higher than measured inside the region.

[2] *FUV* background counts were higher than measured inside the region.

Note—Magnitudes and colors are background subtracted and corrected for Galactic foreground and internal extinction.

Figure 9. Table 1 from The Environments of CO Cores and Star Formation in the Dwarf Irregular Galaxy WLM by Archer *et al.* (2022b) published in the Astronomical Journal.

2.2.3 Age

To calculate the age of each inner region, we used the colors in the region and iterated on reddening to find the best fit with cluster evolutionary models. First, to determine the region colors, we subtracted the background stellar disk from each region. To do so, we subtracted the mode of the pixel values of the outer annulus, measured using Apphot, from the average pixel value in the inner region. We chose to use the

Table 2. Characteristics of star forming regions

Region (1)	$\Sigma_{*,\mathrm{SF}}$ $(M_\odot\ pc^{-2})$ (2)	$\Sigma_{\mathrm{H\,I,SF}}$ $(M_\odot\ pc^{-2})$ (3)	$\Sigma_{\mathrm{H\,I,SF}} - \Sigma_{\mathrm{H\,I,rad}}$ [1] $(M_\odot\ pc^{-2})$ (4)	$M_{\mathrm{CO},\ vir}$ [2] $(M_\odot)$ (5)	Σ_{CO} [3] $(M_\odot\ pc^{-2})$ (6)	$M_{Dark\ \mathrm{H_2}}/M_{MC}$ [4] (%) (7)	$E(B-V)$ (Chabrier IMF) (8)	Log Age (Chabrier IMF) (*years*) (9)
1	$0.06^{+0.74}_{0.00}$	21.33±0.01	15.30±0.01	21700±6440	$106.4^{+421.6}_{67.6}$	$82.1^{+17.2}_{0.0}$	0.21	$6.62^{+1.19}_{0.02}$
2	$0.91^{+0.03}_{-0.39}$	24.05±0.01	17.96±0.01	33900±5260	$106.7^{+682.5}_{-80.0}$	$98.4^{+0.8}_{-0.0}$	0.06	$7.74^{+0.02}_{-0.42}$
3	$1.18^{+0.24}_{-0.19}$	21.91±0.01	16.13±0.01	4300±2550	$101.4^{+54.1}_{-54.1}$	$98.5^{+0.9}_{-0.0}$	0.06	$7.91^{+0.15}_{-0.15}$
4	$0.56^{+0.05}_{-0.21}$	20.11±0.01	14.54±0.01	1790±888	$74.3^{+50.8}_{-50.8}$	$97.5^{+1.4}_{-0.0}$	0.06	$8.56^{+0.05}_{-0.30}$
5	$0.55^{+0.16}_{-0.21}$	19.63±0.01	14.61±0.01	4160±2000	$145.1^{+105.8}_{-106.0}$	$94.2^{+3.6}_{-0.0}$	0.08	$8.16^{+0.20}_{-0.40}$
6	$1.46^{+0.39}_{-0.29}$	16.15±0.01	11.63±0.01	2140±1130	61.5^{+0}_{-0}	$98.9^{+0.7}_{-0.0}$	0.42	$8.26^{+0.20}_{-0.15}$
7	$0.02^{+0.00}_{-0.01}$	16.90±0.01	13.80±0.01	571±1050	32.70^{+0}_{-0}	$71.4^{+14.3}_{-17.1}$	0.06	$6.40^{+0.10}_{-0.00}$
8	$2.05^{+2.60}_{-0.00}$	18.61±0.01	15.26±0.01	2800±1960	$121.1^{+61.1}_{-61.1}$	$98.9^{+0.8}_{-0.0}$	1.10	$7.10^{+0.53}_{-0.08}$
9	$0.06^{+0.00}_{-0.01}$	20.45±0.01	16.73±0.01	16800±2170	$138.4^{+56.1}_{-77.6}$	$0.0^{+38.7}_{-0.0}$	0.20	$6.50^{+0.02}_{-0.00}$
10	$0.03^{+0.02}_{-0.00}$	15.48±0.01	11.32±0.01	3050±1900	$100.3^{+34.7}_{-34.7}$	$67.1^{+23.7}_{-0.0}$	0.06	$6.64^{+0.02}_{-0.12}$
11	$0.21^{+0.46}_{-0.02}$	17.44±0.01	12.70±0.01	935±586	114.6^{+0}_{-0}	$96.8^{+0.2}_{-0.0}$	0.06	$7.34^{+0.92}_{-0.16}$
12	$0.11^{+0.01}_{-0.00}$	15.62±0.01	10.70±0.01	6010±1820	$85.4^{+31.5}_{-31.5}$	$87.7^{+6.6}_{-0.0}$	0.08	$6.62^{+0.00}_{-0.02}$
13	$2.05^{+0.33}_{-0.18}$	14.92±0.01	11.63±0.01	3960±2330	$146.9^{+3.1}_{-6.1}$	$99.6^{+0.2}_{-0.0}$	0.06	$8.26^{+0.15}_{-0.05}$
14	$0.03^{+0.00}_{-0.01}$	19.05±0.01	15.58±0.01	701±565	33.3^{+0}_{-0}	$92.2^{+3.9}_{-0.0}$	0.08	$6.40^{+0.06}_{-0.00}$
15	$1.03^{+0.00}_{-0.01}$	22.03±0.01	18.16±0.01	10100±5020	$182.5^{+232.9}_{-97.6}$	$97.0^{+1.6}_{-0.0}$	0.11	$7.59^{+0.06}_{-0.15}$
16	$1.17^{+0.08}_{-0.25}$	17.84±0.01	13.09±0.01	543±1130	34.6^{+0}_{-0}	$99.9^{+0.1}_{-0.0}$	0.08	$7.63^{+0.05}_{-0.17}$
17	$0.46^{+0.12}_{-0.05}$	21.02±0.01	16.13±0.01	1760±2780	64.4^{+0}_{-0}	$98.4^{+1.0}_{-0.0}$	0.06	$8.01^{+0.20}_{-0.10}$
18	$0.60^{+0.19}_{-0.05}$	12.71±0.01	8.51±0.01	469±1090	30.3^{+0}_{-0}	$99.8^{+0.3}_{-0.0}$	1.03	$6.40^{+0.72}_{-0.00}$
19	$0.73^{+0.14}_{-0.05}$	20.98±0.01	17.09±0.01	1020±1680	102.4^{+0}_{-0}	$99.6^{+0.2}_{-0.0}$	0.16	$8.01^{+0.20}_{-0.10}$
20	$0.47^{+0.66}_{-0.00}$	12.78±0.01	9.69±0.01	518±1010	146.5^{+0}_{-0}	$99.7^{+0.3}_{-0.0}$	0.81	$6.50^{+0.48}_{-0.02}$
21	$0.25^{+0.01}_{-0.23}$	24.15±0.01	19.58±0.01	447±634	43.8^{+0}_{-0}	$99.5^{+0.3}_{-3.7}$	0.06	$7.91^{+0.05}_{-1.29}$
22	$2.68^{+0.00}_{-0.00}$	26.71±0.01	22.06±0.01	665±1000	94^{+0}_{-0}	$99.9^{+0.0}_{-0.0}$	0.43	$8.71^{+0.00}_{-0.00}$
23	$0.09^{+0.02}_{-0.00}$	18.73±0.01	13.02±0.01	0	0	100	0.17	$6.76^{+0.08}_{-0.04}$
24	$0.002^{+0.000}_{-0.000}$	15.22±0.01	10.54±0.01	0	0	100	0.06	$6.40^{+0.00}_{-0.00}$
25	$2.32^{+1.43}_{-0.00}$	7.52±0.01	1.67±0.01	0	0	100	0.30	$8.01^{+0.40}_{-0.15}$
26	$0.08^{+1.42}_{-0.00}$	15.64±0.01	12.86±0.01	0	0	100	0.51	$6.62^{+1.49}_{-1.19}$

[1] Average star forming region $\Sigma_{\mathrm{H\,I,SF}}$ above radial average $\Sigma_{\mathrm{H\,I,rad}}$. Uncertainties are carried over from the $\Sigma_{\mathrm{H\,I,SF}}$ of the region.

[2] Sum of CO core virial masses given by Rubio et al. (2015) and Rubio et al. (2022, in preparation)

[3] Rubio et al. (2015) and Rubio et al. (2022, in preparation) calculated the Σ_{CO} of the individual CO cores from their $M_{\mathrm{CO},vir}$. For each ensemble of individual Σ_{CO} in a given region, we adopt the median Σ_{CO} value. The Σ_{CO} ± uncertainties represent the range of Σ_{CO} for each region containing multiple CO cores.

[4] Percentage of original total molecular cloud mass in dark H_2.

Figure 10. Table 2 from The Environments of CO Cores and Star Formation in the Dwarf Irregular Galaxy WLM by Archer *et al.* (2022b) published in the Astronomical Journal.

mode of the surroundings rather than the average in order minimize contamination from other star-forming regions (partially) sampled by the annulus.

To find the extinction toward each region, we computed $FUV - NUV$, $U - B$, and $B - V$ colors using a series of $E(B-V)$ values ranging from 0.06–1.5 in steps of 0.01. The lower $E(B-V)$ limit of 0.06 was selected from adding the Milky Way foreground reddening and a minimal (0.05 mag) internal reddening for stars (Schlafly

Table 3. Colors and characteristics of environments

Region (1)	*FUV* (*mag*) (2)	*FUV − NUV* (*mag*) (3)	*V* (*mag*) (4)	*U − B* (*mag*) (5)	*B − V* (*mag*) (6)	$\Sigma_{*,\mathrm{env}}$ ($M_\odot$ pc^{-2}) (7)	Pressure ($\times10^{-12}$) (g s^{-2} cm^{-1}) (8)	$\Sigma_{\mathrm{H\,I,env}}$ ($M_\odot$ pc^{-2}) (9)	Log Age (Chabrier IMF) (*years*) (10)
1	24.87±0.01	0.58±0.01	22.86±0.03	−0.04±0.10	0.36±0.04	10.30±0.28	3.86±4.29	19.50±0.01	$8.81^{+0.00}_{-0.05}$
2	24.43±0.01	0.26±0.01	22.65±0.03	0.09±0.09	0.37±0.04	12.02±0.29	5.66±4.67	21.22±0.01	$8.61^{+0.05}_{-0.15}$
3	23.69±0.01	0.01±0.01	22.52±0.03	−0.08±0.08	0.28±0.04	12.38±0.28	5.68±4.02	18.27±0.01	$8.31^{+0.05}_{-0.20}$
4	23.84±0.01	0.03±0.01	22.87±0.03	−0.17±0.09	0.32±0.04	9.10±0.25	5.33±4.80	21.81±0.01	$8.16^{+0.05}_{-0.20}$
5	24.09±0.01	−0.02±0.01	23.10±0.03	0.04±0.11	0.31±0.05	8.79±0.27	4.78±4.17	18.92±0.01	$8.36^{+0.05}_{-0.20}$
6	24.16±0.01	0.18±0.01	23.00±0.03	−0.002±0.10	0.33±0.05	8.25±0.24	3.59±3.67	16.66±0.01	$8.46^{+0.00}_{-0.05}$
7	24.74±0.01	0.29±0.01	23.31±0.04	0.06±0.12	0.30±0.05	5.89±0.19	2.81±3.42	15.56±0.01	$8.61^{+0.05}_{-0.10}$
8	23.85±0.01	0.15±0.01	22.46±0.02	0.08±0.08	0.25±0.04	13.83±0.31	5.56±4.19	19.05±0.01	$8.46^{+0.00}_{-0.05}$
9	23.94±0.01	0.31±0.01	22.45±0.02	0.02±0.08	0.35±0.04	13.65±0.31	5.07±4.13	18.78±0.01	$8.61^{+0.05}_{-0.10}$
10	24.44±0.01	0.09±0.01	22.87±0.03	−0.02±0.10	0.36±0.04	10.11±0.27	4.38±3.94	17.90±0.01	$8.41^{+0.05}_{-0.05}$
11	24.53±0.01	0.04±0.01	22.87±0.03	−0.03±0.10	0.50±0.05	8.68±0.23	3.65±4.08	18.56±0.01	$8.41^{+0.05}_{-0.05}$
12	24.18±0.01	0.18±0.01	22.88±0.03	−0.09±0.09	0.31±0.04	7.67±0.21	2.48±3.01	13.71±0.01	$8.41^{+0.05}_{-0.05}$
13	23.12±0.01	−0.08±0.01	23.05±0.03	−0.36±0.08	0.18±0.05	5.04±0.15	1.93±2.75	12.50±0.01	$7.72^{+0.09}_{-0.02}$
14	23.77±0.01	0.14±0.01	23.01±0.03	−0.14±0.09	0.22±0.05	6.98±0.20	3.39±4.16	18.89±0.01	$8.31^{+0.10}_{-0.10}$
15	24.91±0.01	0.14±0.01	23.01±0.03	−0.21±0.09	0.28±0.05	7.64±0.22	4.97±4.58	20.80±0.01	$8.31^{+0.10}_{-0.10}$
16	24.48±0.01	0.19±0.01	23.25±0.04	−0.15±0.11	0.36±0.05	6.40±0.20	2.86±3.21	14.61±0.01	$8.41^{+0.05}_{-0.05}$
17	25.51±0.01	0.11±0.01	23.13±0.03	0.18±0.12	0.49±0.05	9.24±0.28	4.97±4.39	19.97±0.01	$8.46^{+0.00}_{-0.00}$
18	24.46±0.01	0.39±0.01	22.60±0.03	0.19±0.09	0.41±0.04	13.33±0.32	2.96±2.84	12.90±0.01	$8.71^{+0.05}_{-0.05}$
19	23.96±0.01	0.19±0.01	22.71±0.03	−0.06±0.09	0.32±0.04	10.54±0.26	4.48±4.00	18.17±0.01	$8.41^{+0.05}_{-0.05}$
20	25.33±0.01	0.37±0.01	23.63±0.04	0.11±0.14	0.38±0.06	6.18±0.24	1.71±2.55	11.58±0.01	$8.66^{+0.10}_{-0.00}$
21	24.83±0.01	0.37±0.01	22.99±0.03	0.004±0.10	0.41±0.05	8.66±0.25	7.54±5.09	23.11±0.01	$8.66^{+0.05}_{-0.05}$
22	23.89±0.01	0.09±0.01	22.92±0.03	−0.17±0.09	0.28±0.04	7.92±0.22	7.25±5.33	24.21±0.01	$8.31^{+0.05}_{-0.20}$
23	24.64±0.01	0.36±0.01	22.98±0.03	0.22±0.11	0.39±0.05	8.74±0.30	3.40±4.36	19.81±0.01	$8.71^{+0.00}_{-0.05}$
24	20.79±0.01	0.12±0.01	22.57±0.03	0.10±0.09	0.36±0.04	11.89±0.21	4.35±3.60	16.37±0.01	$8.46^{+0.00}_{-0.05}$
25	21.02±0.01	0.29±0.01	22.89±0.03	−0.07±0.09	0.31±0.04	10.03±0.27	3.77±3.71	16.84±0.01	$8.51^{+0.10}_{-0.00}$
26	21.83±0.01	0.45±0.01	21.57±0.03	0.10±0.09	0.36±0.04	4.68±0.12	2.79±3.36	15.26±0.01	$8.76^{+0.00}_{-0.05}$

NOTE—Magnitudes and colors have been corrected for extinction.

Figure 11. Table 3 from The Environments of CO Cores and Star Formation in the Dwarf Irregular Galaxy WLM by Archer *et al.* (2022b) published in the Astronomical Journal.

and Finkbeiner 2011; Cardelli *et al.* 1989). We used an upper limit $E(B-V)$ of 1.5 in our model search as it is higher than the estimates of reddening necessary to form CO molecules in the Milky Way (Glover and Clark 2012; Lee *et al.* 2018).

We then compared the background-subtracted $FUV-NUV$, $U-B$, and $B-V$ colors to evolutionary stellar population synthesis models from GALEXEV (Bruzual and Charlot 2003). The single stellar population (SSP) models used were computed using the Bertelli *et al.* (1994) Padova evolutionary tracks with a metallicity of 0.004, as this was closest of the models to the WLM metallicity of ∼0.003. We compared models computed using both the Chabrier (2003) initial mass function (IMF) and the

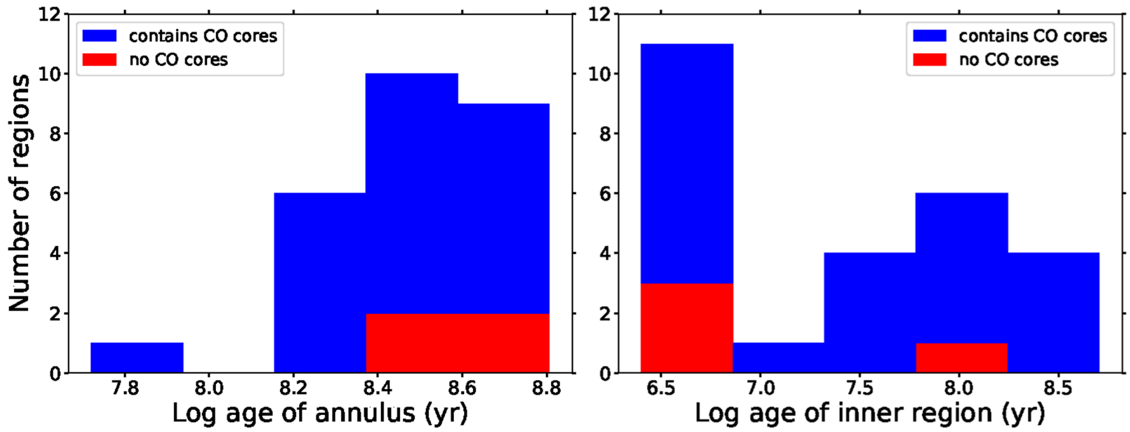

Figure 12. Left: Histogram of ages of the environment where CO cores formed (blue) and environment surrounding the star forming regions without any CO cores (red). Right: Histogram of ages of star forming regions with CO cores (blue) and the star forming regions without any CO cores (red). Ages were computed using the Chabrier IMF.

Salpeter (1955) IMF with the aforementioned evolutionary tracks and metallicity. We then compared the observed and modeled $FUV-NUV$, $U-B$, and $B-V$ colors to find the age that corresponded to the closest fit for each $E(B-V)$ value. For each region, we adopt the combination of age and $E(B-V)$ that minimizes the residuals between observed and modeled colors. Using this extinction, we then compared the $FUV-NUV$, $U-B$, and $B-V$ colors with their respective upper and lower uncertainty limits and the model colors, and selected these as the worst case scenario upper and lower age uncertainties of that region. Both IMFs produced similar results, so we report only $E(B-V)$ and ages calculated using the Chabrier IMF in the table in Figure 10. Figure 12 shows a histogram of the ages of the inner regions.

Grasha *et al.* (2018, 2019) find a strong correlation between the age of star clusters and distance from their GMCs, with the age distribution increasing as the cluster-GMC distance increases. For star forming regions that contained multiple FUV knots, we used the method described above to explore the ages of the individual knots compared to the age we computed for the entire region. We selected the photometry aperture size for each knot based on the FUV and V images to encompass as much as was likely to be part of the same star forming knot. We used a larger aperture size around multiple knots that could not be individually resolved. For each star forming region, the individual knots have the same or similar ages as that of the entire region. For example, individual knots in region 1 range from 3.2 to 4.4 Myr, with 10 out of 13 regions having the same age as we calculated for the entire region – 4.2 Myr. Similarly, the average $E(B-V)$ of the individual knots in region 1 is 0.23, while that of the entire region is 0.21. Figure 13 shows the star forming regions with multiple knots and the photometry apertures we selected for the individual knots in each region. We note that the ages and reddening of the knots are sensitive to aperture size and background subtraction selection due to the crowding of knots within the regions.

The projected distance from the CO core to the nearest FUV knot in regions 22 and especially 18 is greater than for most other regions (Figure 14) and the NUV or FUV background measured in their annuli exceeded the corresponding average of their inner region. One reason for this may be that the inner star forming region actually extends into the annulus we adopted for the environment. This prevented us from placing meaningful constraints on the $FUV-NUV$ colors of these regions. We see in Figure 14 that there are possibly two relationships showing the age of a region increasing with distance from its nearest FUV knot (one above log(age) $\simeq 7.25$ and one below), but there is no clear explanation for why the regions would separate into these two sequences. As such, only the $U-B$ and $B-V$ colors were used in the age calculation for these two regions. We mark these regions with an $(\times)$ when showing

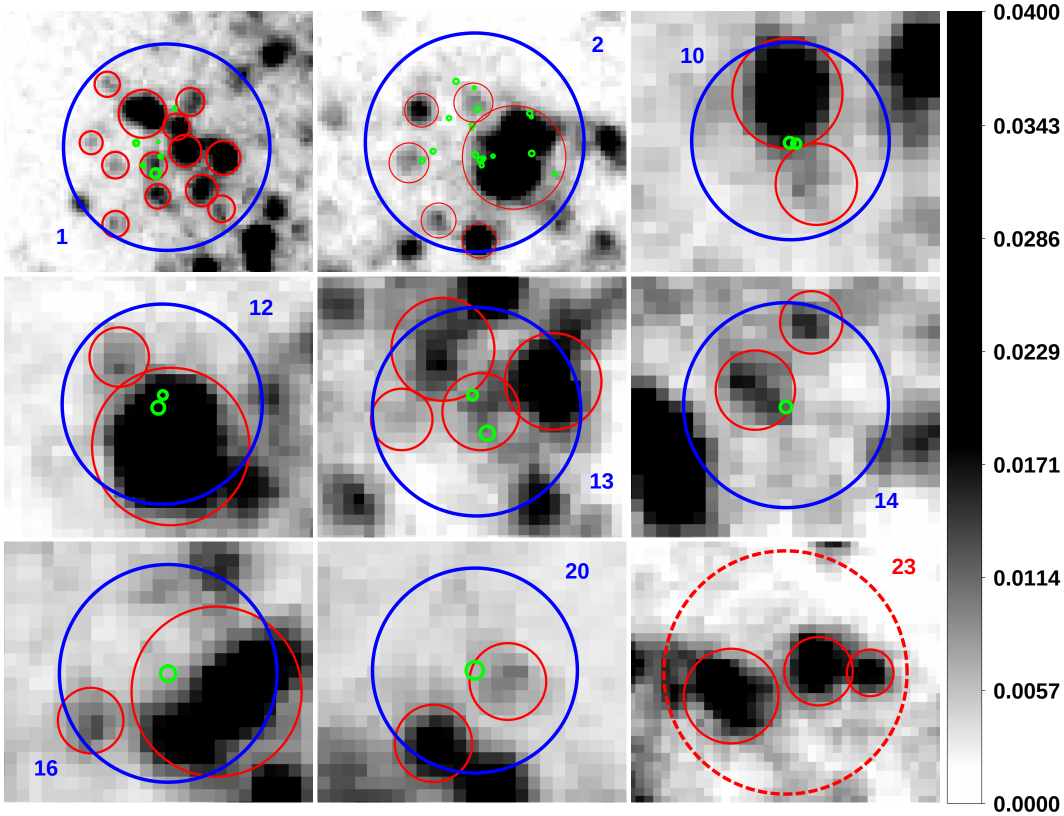

Figure 13. FUV image of star forming regions (blue solid or red dashed circles), star forming knots (red circles), and CO cores (green circles) for which we compared the average of the ages of the individual knots to the calculated age of the entire region. We find that the individual knot ages are the same or similar to the age of the region comprising the knots.

the region ages (Figures 20 and 25). We also examined subtracting the background colors instead of the background fluxes to find the color excess before iterating on reddening, which allowed us to use the $FUV - NUV$, $U - B$, and $B - V$ colors in the age calculation of all regions. We compare the two methods in Figure 15, where we see a trade-off between the extinction and the age. Subtracting the background colors typically finds regions to have lower $E(B-V)$ extinction and higher ages compared to subtracting the background fluxes. We chose to use the ages computed with the

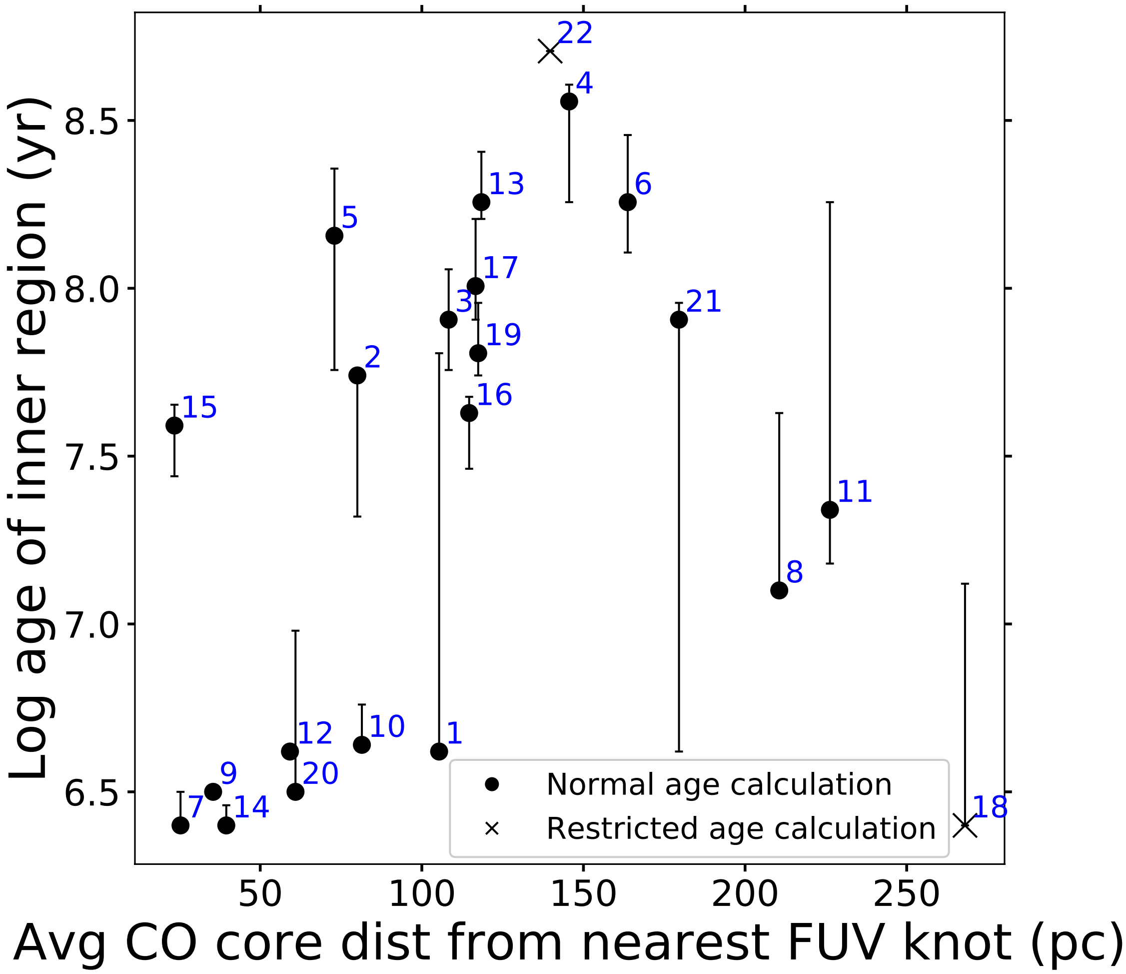

Figure 14. The age of the inner region plotted against the average distance of the CO cores in that region to its nearest FUV knot in parsecs. Age error bars that appear one-sided are the result of the upper or lower color uncertainties finding the same age in the model. Regions 18 and 22 are marked with an ($\times$) as the age was determined from UBV alone.

background flux subtracted photometry throughout this analysis in order to avoid unphysically old ages for star forming regions.

To account for the stochastic effects of red supergiants (RSGs), which could skew the colors of small young clusters (Krumholz *et al.* 2015), we looked at the location of catalogued RSGs in WLM from Levesque and Massey (2012). We found three RSGs in four regions (regions 11, 12, 18, and 20), with one RSG located in the overlap of

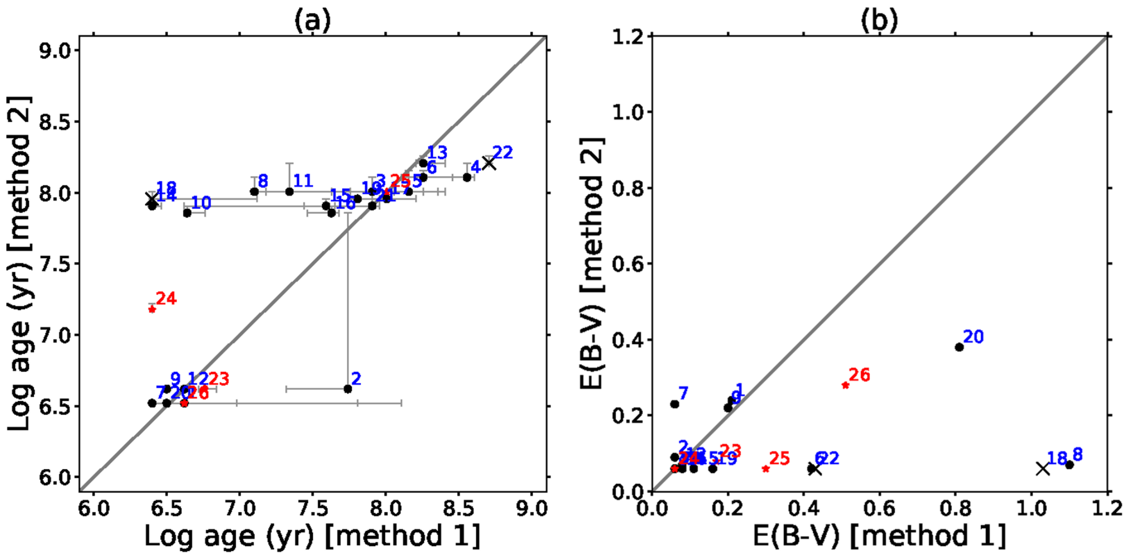

Figure 15. Comparison of (a) inferred ages, log(age), and (b) color excesses, $E(B-V)$, of the inner regions, computed using either background subtracted fluxes (method 1; horizontal axes) or background subtracted colors (method 2; vertical axes). Age error bars that appear one-sided are the result of the upper or lower color uncertainties finding the same age in the model. The gray line represents where both methods return the same age or $E(B-V)$. Regions 18 and 22 are marked with an ($\times$) as the age from the background flux subtraction was determined from UBV alone. The regions without CO (regions 23, 24, 25, and 26) are marked with a red star ($\star$).

regions 11 and 12. The ages of regions 11, 12, 18, and 20 are rather young at 22, 4, 2, and 3 Myr respectively. With the age of these regions well within the range of all other regions, it is not clear that RSGs have made a noticeable impact on our age calculations.

To find the age of the annulus representing the environment where the star-forming region formed, we did not subtract any background since the age we were measuring was that of the background disk surrounding each region. Likewise, we only computed our measured $FUV-NUV$, $U-B$, and $B-V$ colors with the $E(B-V)$ of 0.068 since the annuli are not likely to be heavily reddened. As for the inner regions, our measured colors were fit to the BC03 model colors for each region, where we selected the best fit as the age for that region. The table in Figure 11 contains the age of each annulus computed with the Chabrier IMF, and Figure 12 shows a histogram of the annuli ages.

2.2.4 Stellar mass surface density

After finding the age of the inner region using BC03, we took the ratio between the V flux corresponding to the model age of each region and measured the integrated V flux, which was corrected for the extinction we determined from the colors. This ratio was used to scale the model mass and find the mass of young stars ($M_{*,\mathrm{SF}}$) for each inner region.

The young star mass was then divided by the area of each region in parsecs to find the corresponding average Σ_* in $M_\odot$ pc^{-2}. We note that this method of determining the stellar mass surface density does not take into account the dispersal of stars over time. The model V values corresponding to the upper and lower age uncertainties for each region were used for the model V uncertainties, which were used to compute the uncertainties for the M_* and Σ_* for each region. These stellar mass surface densities and uncertainties for the star forming regions can be found in the table in Figure 10. Since the ages were used in calculating the Σ_* of the inner regions, regions 18 and 22, where the ages were calculated from UBV alone, have their Σ_* marked with an $(\times)$ in relevant figures.

2.2.5 CO-dark H_2 gas

We also wanted to examine any potential relationship of CO-dark H_2 gas with the small CO cores. In order to find the percentage of the original molecular cloud mass M_{MC} in CO-dark H_2 ($M_{Dark\ \mathrm{H_2}}/M_{MC}$), we assumed that the percentage of the original total molecular cloud gas that was converted into stars was roughly 2% (Krumholz *et al.* 2012). We used M_* and 2% efficiency to find the total molecular cloud gas mass for each inner region. Then, given that the molecular gas mass of the cloud is a combination of the CO-dark gas mass and the mass contained in CO cores, we found the percentage of the molecular cloud that is CO and that is CO-dark. For region 1, we also looked at how much the mass of carbon in the PDR contributes to the mass of the molecular cloud. The [C II]$\lambda 158\mu$m flux measurements from Cigan *et al.* (2016) correspond to $40 - 170 M_\odot$ of free carbon atoms. As this is only $0.03 - 0.14\%$ of the original total mass of the molecular cloud, we choose to ignore it in our analysis. We note that the M_{MC} is the original mass of the molecular cloud, which would break up and dissociate with time. Without information on the status of the cloud itself, our estimates do not take into account the current structure of the molecular cloud. The uncertainties in the CO-dark H_2 mass were found by computing the dark H_2 mass percentage using the uncertainties in the M_* for each region as previously described, although the uncertainty is most likely dominated by the assumption of a star formation efficiency. The $M_{Dark\ \mathrm{H_2}}/M_{MC}$ and associated uncertainties can be found in the table in Figure 10. Since the M_* for each region is determined by the V value corresponding to the model age found, regions 18 and 22, for which their age was calculated from UBV alone, have their dark H_2 mass denoted with an ($\times$) in relevant figures.

In summary, the star forming region properties include the H I surface density ($\Sigma_{\mathrm{H\,I,SF}}$), stellar mass surface density ($\Sigma_{*,\mathrm{SF}}$), sum of individual CO core virial masses in a region ($M_{\mathrm{CO},vir}$), median individual CO core surface density (Σ_{CO}) in a region, stellar age, and dark molecular hydrogen to original molecular cloud mass ratio ($M_{Dark\ \mathrm{H_2}}/M_{MC}$). The environmental properties include the H I surface density ($\Sigma_{\mathrm{H\,I,env}}$), pressure, stellar mass, and age. In Section 2.3 we compare and contrast these properties.

2.3 Results

2.3.1 Characteristics of Star-Forming Regions

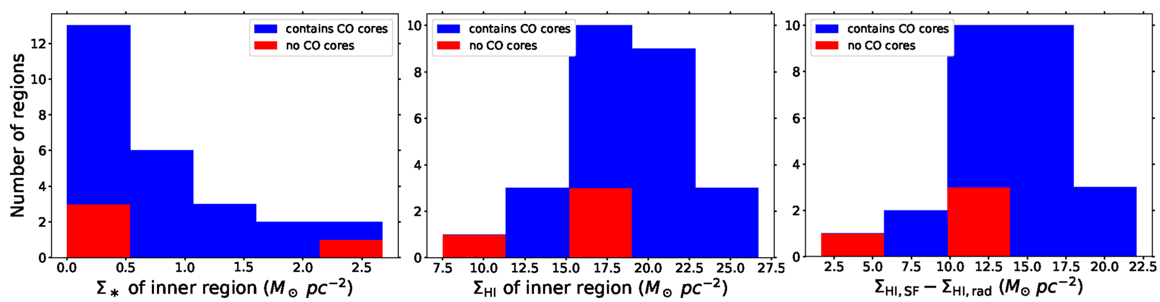

Figure 16. Histograms of properties of inner regions where CO cores currently sit (blue) and the inner regions without any CO cores (red). Left: Average stellar mass surface density. Center: Average H I surface density. Right: Difference between the average $\Sigma_{\mathrm{H\,I,SF}}$ and the corresponding azimuthally-averaged radial profile $\Sigma_{\mathrm{H\,I,rad}}$ at the region ($\Sigma_{\mathrm{H\,I,SF}} - \Sigma_{\mathrm{H\,I,rad}}$).

In Figure 16 we plot histograms for the star-forming region properties of stellar mass surface density $\Sigma_{*,\mathrm{SF}}$ and H I surface density $\Sigma_{\mathrm{H\,I,SF}}$. We also plot a histogram of the difference between the average $\Sigma_{\mathrm{H\,I,SF}}$ and the corresponding azimuthally-averaged radial profile $\Sigma_{\mathrm{H\,I,rad}}$ at the region ($\Sigma_{\mathrm{H\,I,SF}} - \Sigma_{\mathrm{H\,I,rad}}$). While the regions without CO cores typically have $\Sigma_{*,\mathrm{SF}}$, $\Sigma_{\mathrm{H\,I,SF}}$, and $\Sigma_{\mathrm{H\,I,SF}} - \Sigma_{\mathrm{H\,I,rad}}$ values within the range of values for the regions with CO, the $\Sigma_{\mathrm{H\,I,SF}}$ and $\Sigma_{\mathrm{H\,I,SF}} - \Sigma_{\mathrm{H\,I,rad}}$ tend to fall at lower end of that range.

2.3.1.1 CO Core Mass and Surface Density

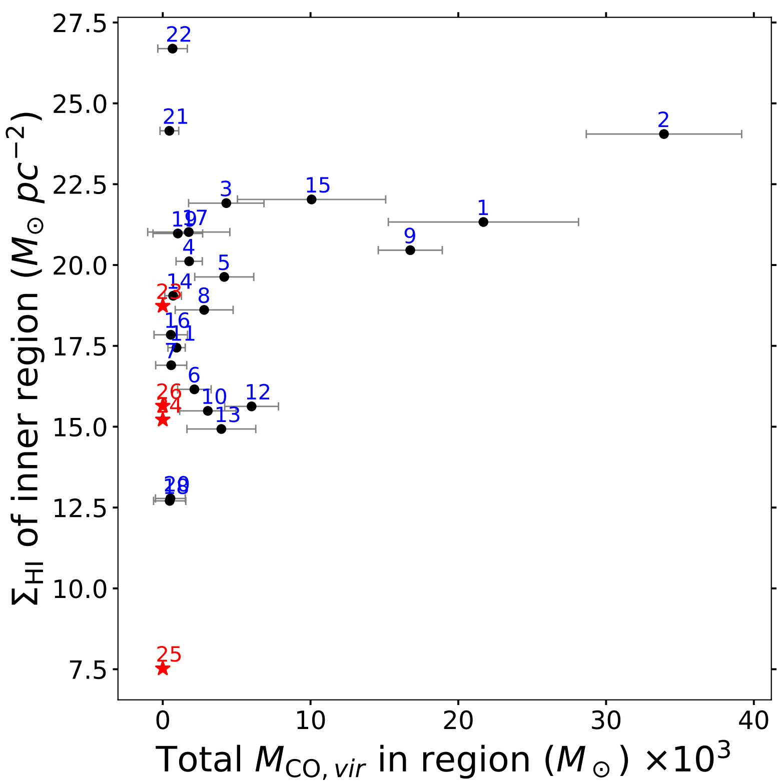

Figure 17. H I surface density of each inner region versus the total mass of CO cores of that region, where the H I uncertainties are smaller than the size of the plot markers. We find that a higher H I surface density is found in regions with a higher total CO core mass (regions 1, 2, 9, and 15), while a high H I surface density does not necessarily correspond to a higher total CO core mass (regions 3, 4, 17, 19, 21, and 22).

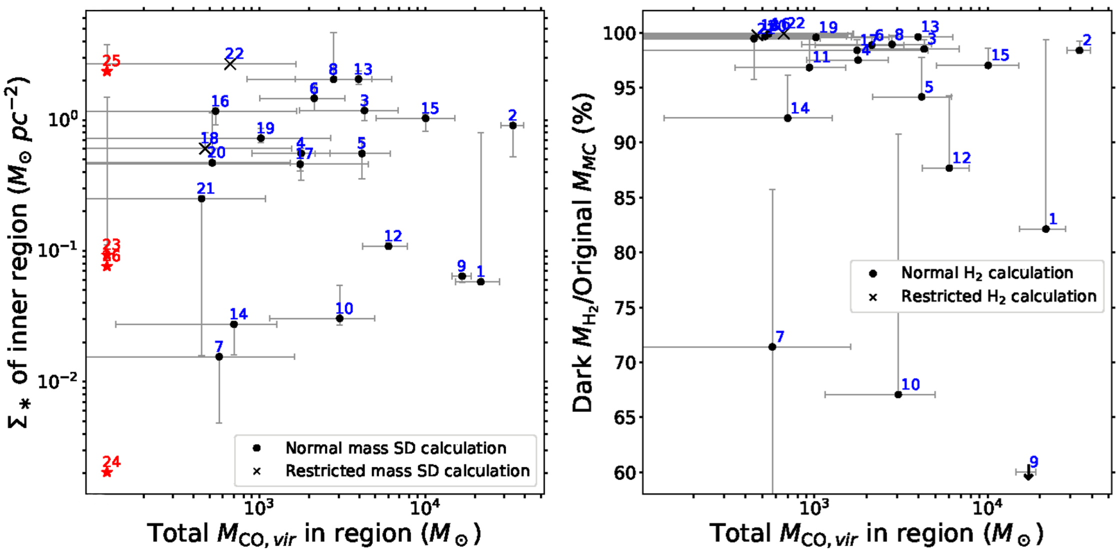

Figure 18. Left: Stellar mass surface density of each inner region plotted against the total mass of CO cores of that region. The regions without CO cores (region 23, 24, 25, and 26) are marked with a red star ($\star$) and have a total $M_{\mathrm{CO},vir}$ of zero, but have been placed at a total $M_{\mathrm{CO},vir}$ of 1.2×10^2 $M_\odot$ to show their corresponding Σ_*. Right: Percentage of original total molecular cloud mass that is dark $\mathrm{H_2}$ gas of each inner region plotted against the total mass of CO cores in that region. We do not show the $M_{Dark\ \mathrm{H_2}}/M_{MC}$ against the total $M_{\mathrm{CO},vir}$ of regions without detected CO as they all have a total $M_{\mathrm{CO},vir}$ of zero and thus a dark $\mathrm{H_2}$ mass percentage of 100%. Region 9 is displayed with arrow marker to indicate that the actual dark $\mathrm{H_2}$ mass ratio value is 0% but has been shifted up to better show the distribution of the dark $\mathrm{H_2}$ mass ratios of the other regions. The correct dark $\mathrm{H_2}$ mass percentages are listed in the table in Figure 10. Regions 18 and 22 are marked with an ($\times$) as the stellar mass surface density and dark $\mathrm{H_2}$ were determined from UBV alone.

Next, we look at whether the sum of individual CO virial masses, $M_{\mathrm{CO},vir}$, and median surface density, Σ_{CO}, of the individual CO cores in a region have any relationship with the star forming region where they now sit. To do this, we plot the $\Sigma_{\mathrm{H\,I,SF}}$, $\Sigma_{*,\mathrm{SF}}$, and $M_{Dark\ \mathrm{H_2}}/M_{MC}$ against the total mass of the CO cores in each region. In Figure 17 we see that regions with a higher total $M_{\mathrm{CO},vir}$ also show a higher $\Sigma_{\mathrm{H\,I,SF}}$ (regions 1, 2, 9, and 15), while a region with a higher $\Sigma_{\mathrm{H\,I,SF}}$ does not necessarily correspond to a higher total $M_{\mathrm{CO},vir}$ (regions 3, 4, 17, 19, 21, and 22). The correlation

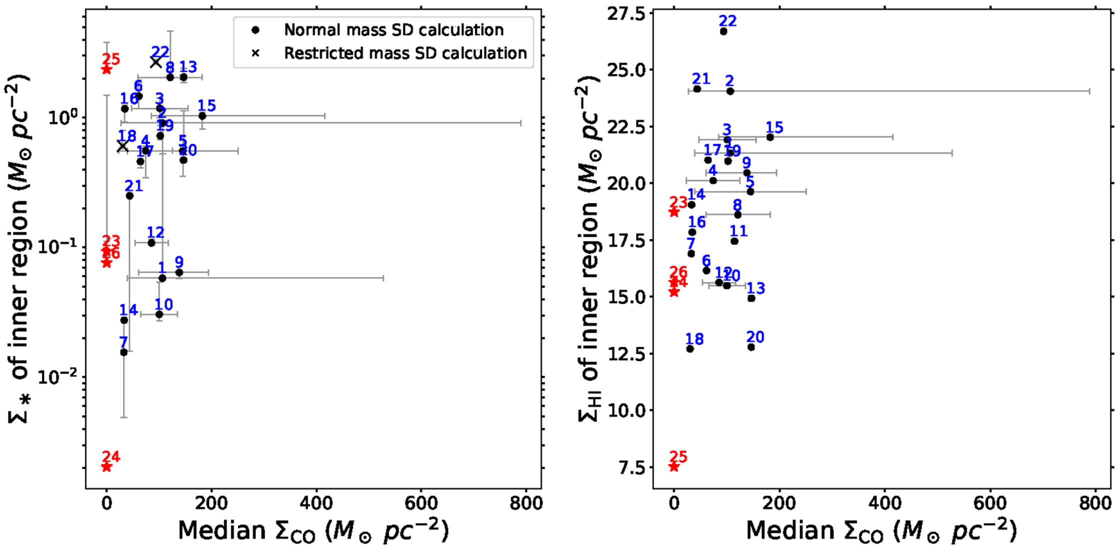

Figure 19. Left: Stellar mass surface density of each inner region plotted against the median individual CO core surface density of that region. Regions 18 and 22 are marked with an (×) as the stellar mass surface density was determined from *UBV* alone. Right: H I surface density of each inner region plotted against the median individual CO core surface density of that region, where the H I uncertainties are smaller than the size of the plot markers. The x-axis error bars are not uncertainties, but instead represent the range of CO core surface densities for that region, with some being smaller than the size of the marker, especially if the region only has one CO core. The regions without CO cores (region 23, 24, 25, and 26) are marked with a red star ($\star$) and have a CO core surface density of zero.

between higher $M_{\mathrm{CO},vir}$ and $\Sigma_{\mathrm{H\,I,SF}}$ suggests that considerable amounts of H I are needed to create large quantities of molecules, and that large molecular clouds are difficult or impossible to make at low $\Sigma_{\mathrm{H\,I}}$. Figure 18 shows Σ_* and $M_{Dark\ \mathrm{H_2}}/M_{MC}$ plotted against the total $M_{\mathrm{CO},vir}$ of each region, where we see no relationship in either.

In Figure 19 we plot $\Sigma_{*,\mathrm{SF}}$ and $\Sigma_{\mathrm{H\,I,SF}}$ with the median individual Σ_{CO} in each region. Here, the error bars given for the Σ_{CO} are the minimum and maximum Σ_{CO} in that region for regions with more than one CO core. We do not find any relation between the Σ_{CO} in a region and the $\Sigma_{*,\mathrm{SF}}$ or $\Sigma_{\mathrm{H\,I,SF}}$ of that region.

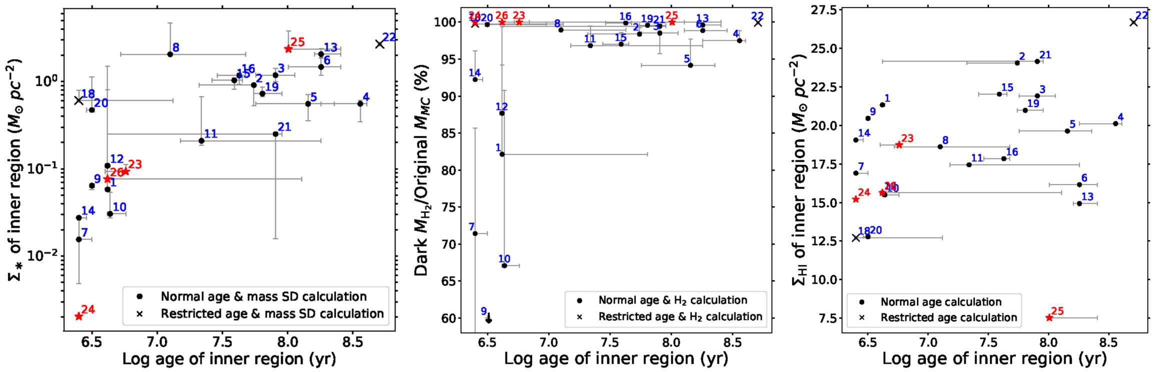

Figure 20. Left: Stellar mass surface density of each inner region plotted against the age of that region. Center: ratio (%) of dark H_2 mass to original total molecular cloud mass of each inner region plotted against the age of that region. Region 9 is displayed with an arrow marker to indicate that the actual dark H_2 mass ratio value is 0% but has been shifted up to better show the distribution of the dark H_2 mass ratios of the other regions. Right: H I surface density of each inner region plotted against the age of that region, where the H I uncertainties are smaller than the size of the plot markers. Age error bars that appear one-sided are the result of the upper or lower color uncertainties finding the same age in the model. Regions 18 and 22 are marked with an ($\times$) as the age and stellar mass were determined from UBV alone. The regions without CO (region 23, 24, 25, and 26) are marked with a red star ($\star$) and are assumed to have a dark H_2 mass percentage of 100%. Neither the stellar mass surface densities nor dark H_2 mass percentages take into account the current structure of the molecular cloud, which would break up and dissociate with time.

2.3.1.2 Age

In Figure 20 we plot the $\Sigma_{*,\mathrm{SF}}$, $M_{Dark\ \mathrm{H_2}}/M_{MC}$, and $\Sigma_{\mathrm{H\,I,SF}}$ against the age of the region to examine any relationships between the star forming region properties and the age of the regions where we find CO cores. We find that both the $\Sigma_{*,\mathrm{SF}}$ and $M_{Dark\ \mathrm{H_2}}/M_{MC}$ appear to increase with age. Both quantities are computed from the age of the region but do not take into account the disruption of the molecular cloud by stars with time, which may affect any apparent correlation seen between the $\Sigma_{*,\mathrm{SF}}$, $M_{Dark\ \mathrm{H_2}}/M_{MC}$, and age.

2.3.1.3 Dark H_2 Mass to Total Molecular Cloud Mass Ratio

In Figure 21 we plot the $\Sigma_{*,\mathrm{SF}}$ and $\Sigma_{\mathrm{H\,I},\mathrm{SF}}$ of the inner region against the percentage of the original molecular cloud mass that is in dark H_2 to determine if the amount of CO-dark H_2 where we find CO cores correlates to other star forming region properties. We find that most regions have a dark H_2 mass that is between 90 and 100% of the original total molecular cloud mass, and that higher $M_{Dark\,\mathrm{H_2}}/M_{MC}$ tends to corresponds to higher $\Sigma_{*,\mathrm{SF}}$. Both of these quantities are derived from the age of the region, while neither take into account dispersal of the molecular cloud over time which may affect any apparent correlation. The HI surface density of the inner regions varies independently of the percentage of dark gas in the molecular cloud.

2.3.2 Environments of Star-Forming Regions

To compare the environment where CO cores formed against regions where we do not detect any CO cores, we plot histograms for the environmental properties of $\Sigma_{*,\mathrm{env}}$, pressure, and $\Sigma_{\mathrm{H\,I},\mathrm{env}}$ for the outer annulus of all 26 regions. We again find that the annuli surrounding the star forming regions with CO cores fall within the same range of environmental property values as the annuli surrounding regions where no CO cores reside. These histograms are shown in Figure 22.

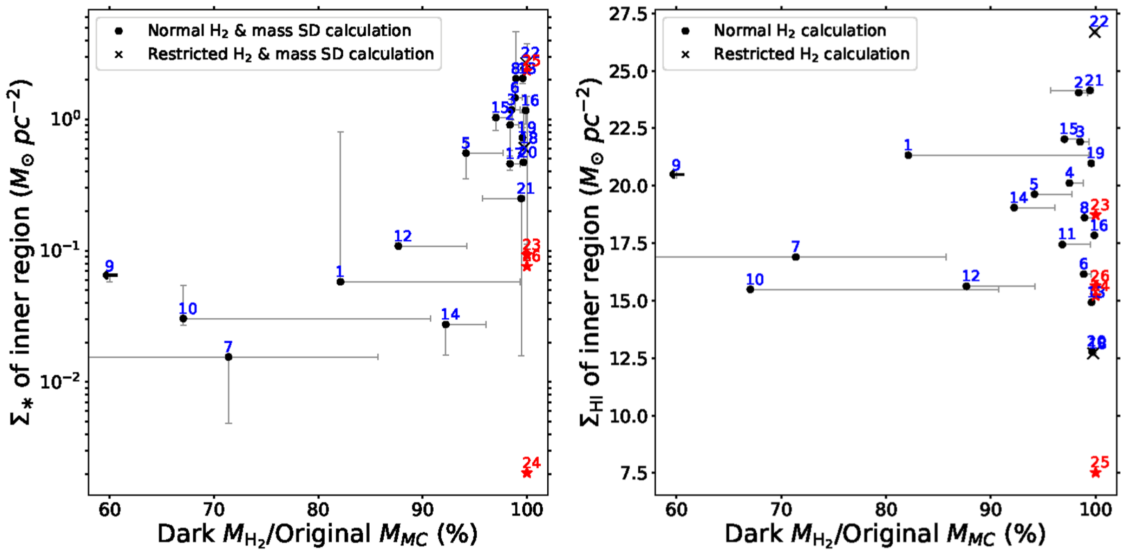

Figure 21. Left: Stellar mass surface density of each inner region plotted against the ratio of dark H_2 mass to total molecular cloud mass of that region. Right: H I surface density of each inner region plotted against the ratio of dark H_2 mass to total molecular cloud mass of that region, where the H I uncertainties are smaller than the size of the plot markers. Region 9 is displayed with a left-pointing arrow marker to indicate that the actual dark H_2 mass ratio value is 0% but has been shifted right to better show the distribution of the other dark H_2 mass ratios. Regions 18 and 22 are marked with an ($\times$) as the stellar mass surface density and dark H_2 were determined from UBV alone. The regions without CO (region 23, 24, 25, and 26) are marked with a red star ($\star$) and are assumed to have a dark H_2 mass percentage of 100%. Neither the original molecular cloud mass nor the $\Sigma_{*,\mathrm{SF}}$ account for the dispersal of the molecular cloud over time, which may affect any correlation seen between the two quantities. The correct stellar mass surface densities and dark H_2 mass percentages are listed in the table in Figure 10.

2.3.2.1 CO Core Mass and Surface Density

Another way of examining the environment where the CO cores formed is to look at the relationship between the sum of individual CO core virial masses $M_{\mathrm{CO},vir}$ of a region with the corresponding $\Sigma_{\mathrm{H\,I,env}}$, pressure, and $\Sigma_{*,\mathrm{env}}$ of the annulus of that

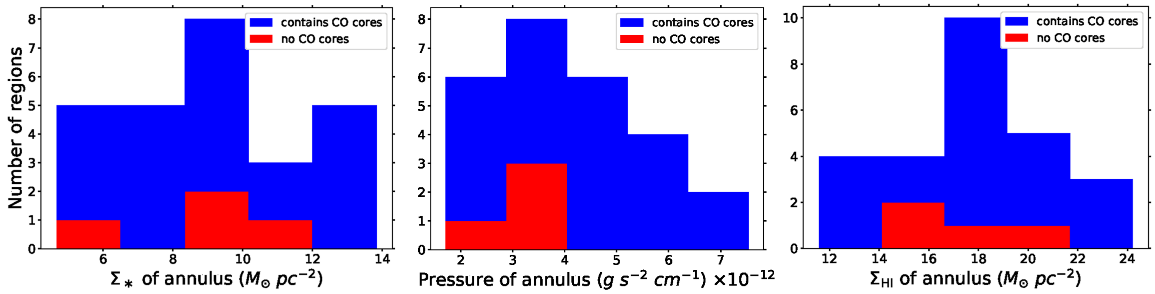

Figure 22. Histogram of average stellar mass surface density (left), pressure (center), and H I surface density (right) of annuli representing the environment where CO cores formed (blue) and the annuli of the star forming regions without any CO cores (red).

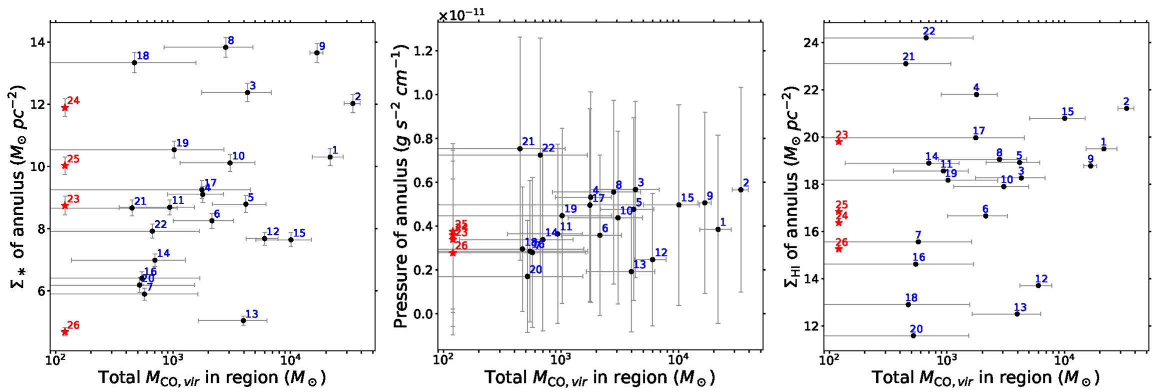

Figure 23. Stellar mass surface density (left), pressure (center), and H I surface density (right) of each annulus plotted against the log of the total CO core mass of that region. H I uncertainties are smaller than the size of the plot markers. The regions without CO cores (regions 23, 24, 25, and 26) are marked with a red star ($\star$) and have a total $M_{\mathrm{CO},vir}$ of zero, but have been placed at a $M_{\mathrm{CO},vir}$ of 1.2×10^2 $M_\odot$ to show their corresponding $\Sigma_{*,\mathrm{env}}$, pressure, and $\Sigma_{\mathrm{H\,I},\mathrm{env}}$.

region. We show these in Figure 23. We find that regions with a higher total $M_{\mathrm{CO},vir}$ tend to have a higher $\Sigma_{\mathrm{H\,I},\mathrm{env}}$, as we found in the star forming regions themselves, while again showing that a higher H I does not necessarily lead to a higher total $M_{\mathrm{CO},vir}$. This correlation between the $\Sigma_{\mathrm{H\,I}}$ and total $M_{\mathrm{CO},vir}$ is not as pronounced in the annuli as the inner regions. The three regions with highest $M_{\mathrm{CO},vir}$ also have relatively high $\Sigma_{*,\mathrm{env}}$, but we find no relationship between the total $M_{\mathrm{CO},vir}$ and the

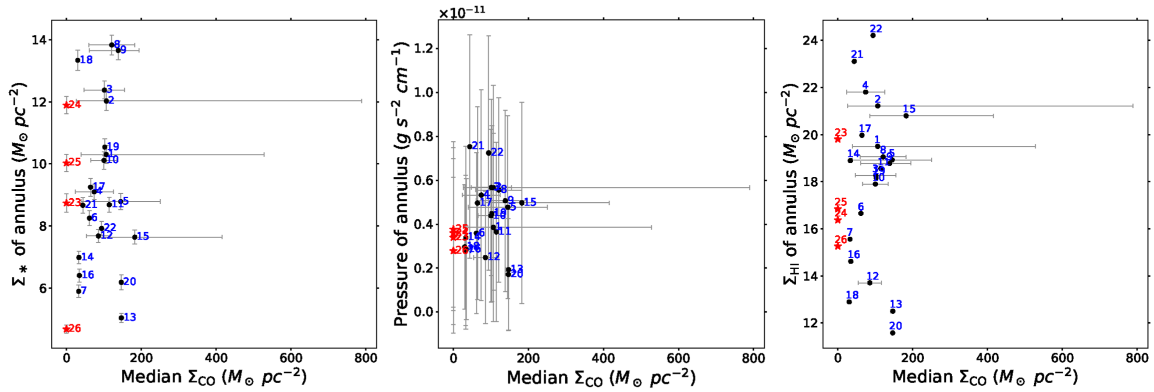

Figure 24. Stellar mass surface density (left), pressure (center), and H I surface density (right) of each annulus plotted against the median individual CO core surface density of that region. H I uncertainties are smaller than the size of the plot markers. The x-axis error bars are not uncertainties, but instead represent the range of CO core surface densities for that region, with some being smaller than the size of the marker. The regions without CO cores (regions 23, 24, 25, and 26) are marked with a red star ($\star$) and have a CO core surface density of zero.

pressure. We also compare the pressure, $\Sigma_{\mathrm{H\,I,env}}$, and $\Sigma_{*,\mathrm{env}}$ of the annuli with the median individual Σ_{CO} of the regions in Figure 24 and find no relationship.

2.3.2.2 Age

To examine any relationships between the environmental properties and the age of both the environment where the CO cores formed and the star forming region where we now find the CO cores, we plot the environmental pressure, $\Sigma_{\mathrm{H\,I,env}}$, and $\Sigma_{*,\mathrm{env}}$ against the age of the annuli and the age of the inner region in Figure 25. Not surprisingly we find that the age of the annuli are older than inner regions. The annuli ages of the regions fall between ~50 and 650 Myr, with most around 250 Myr. The age of inner regions spans a much larger range between ~2 and 500 Myr, with most regions less than 100 My. We do not find any correlation between the environment where the CO cores formed and either the current age of that environment or the age of the star-forming region in which the CO cores sit.

2.3.2.3 Dark H_2 Mass to Original Total Molecular Cloud Mass Ratio

In Figure 26 we plot the $\Sigma_{*,\mathrm{env}}$, pressure, and $\Sigma_{\mathrm{H\,I,env}}$ of the annulus of each region against the $M_{Dark\ \mathrm{H_2}}/M_{MC}$ for that region to determine if the amount of CO-dark H_2 in the star forming regions where the CO cores sit have any relationship with the environmental properties where the CO cores formed. We find no correlations between the percentage of original molecular cloud mass in dark H_2 and the $\Sigma_{*,\mathrm{env}}$, pressure, or $\Sigma_{\mathrm{H\,I,env}}$ of the annuli where the CO cores formed.

2.3.3 Summary of Results

Rubio *et al.* (2015) and Rubio et al. (2022, in preparation) discovered CO cores in the dIrr galaxy WLM, which has a metallicity 13% of solar. The detection of this CO is important for understanding star formation in the most numerous type of galaxy, as CO is used to trace the molecular hydrogen thought to be responsible for star formation. This study is aimed at understanding the environments in which these small CO cores form at low mass and metallicities. In this work, we have examined the properties of CO-detected regions in WLM and explored relationships between the CO and the environments where they formed and the star-forming regions where they currently reside. We grouped the cores into 22 regions based on proximity to FUV knots, along with four regions containing FUV emission that don't have any detected CO cores.

We looked at the $\Sigma_{*,\mathrm{SF}}$, $\Sigma_{\mathrm{H\,I,SF}}$, total $M_{\mathrm{CO},vir}$, median individual Σ_{CO}, age, and $M_{Dark\ \mathrm{H}_2}/M_{MC}$ of the star forming regions and the $\Sigma_{*,\mathrm{env}}$, pressure, $\Sigma_{\mathrm{H\,I,env}}$, and age of the environments measured in annuli around the star-forming regions. We do not see any difference between the star forming region properties where we find CO cores and the star forming region properties where we do not find CO cores, nor do we see a difference between environmental region properties where we find CO cores and environmental region properties where we do not. We do not see any correlations among the star forming region properties or environmental region properties except between the $\Sigma_{\mathrm{H\,I}}$ and total $M_{\mathrm{CO},vir}$ and, to a lesser extent, the pressure and total $M_{\mathrm{CO},vir}$. We find that regions with a higher total $M_{\mathrm{CO},vir}$ have higher H I surface densities, and this relationship is more pronounced in the star forming regions than in the surrounding environment.

2.4 Discussion and Conclusions

Regions 1, 2, 9, and 15 have the highest number of CO cores (6, 17, 4, and 3 cores respectively) and, as expected, the highest total $M_{\mathrm{CO},vir}$ of the regions. We calculate the amount of dark H_2 in a region using the assumption that 2% of the total molecular gas (dark H_2 plus $M_{\mathrm{CO},vir}$) is turned into stars, and find that the percentage of CO-dark H_2 of regions 1, 2, and 15 agree with that of the other regions. Region 9, however, has a $M_{Dark\ \mathrm{H}_2}/M_{MC}$ of 0%. The total $M_{\mathrm{CO},vir}$ of the region is higher than what the total molecular cloud gas mass is expected to be with a 2% star formation efficiency. One possible reason for this is embedded star formation. To look for potential embedded star formation, we show the regions and their CO cores overlaid on the Spitzer 8μm image of WLM in Figure 27. Here we see 8μm peaks near several CO cores, including those in region 9. This may suggest that region 9 has yet to convert 2% of its molecular gas to stars.

In Figure 28 we plot the ratio of the young stellar mass to the observed CO virial mass ($M_*/M_{\mathrm{CO},vir}$) of the inner regions against the age of the inner regions. Because we made the assumption that $M_* = 0.02(M_{CO,vir} + M_{Dark\ H_2})$, we mark with a gray dashed line where the $M_*/M_{\mathrm{CO},vir}$ is 2% to examine what the excess mass above our estimated star formation efficiency is in dark CO. For young regions (1, 7, 10, 11, 14) we find that the excess of $M_*/M_{\mathrm{CO},vir}$ above 2% is

$$\left(1 + \frac{M_{Dark\ H_2}}{M_{CO,vir}}\right) \approx 5, \tag{2.6}$$

which yields

$$\frac{M_{Dark\ H_2}}{M_{CO,vir}} \approx 4. \tag{2.7}$$

This value agrees with that found in larger scale regions in recent papers (Hunter *et al.* 2019, 2021). When the ratio $M_*/M_{\mathrm{CO},vir}$ is much larger than ∼4, as we see it is for mostly old regions, the molecular gas has likely been destroyed. We see this transition at an age of about 5 Myr which is reasonable for the time it takes for young star formation to break apart its GMC (Williams *et al.* 2000; Kim *et al.* 2018; Kruijssen *et al.* 2019).

Looking at the scale of the whole galaxy, we see in Figure 7 a ridge or shell surrounding a depression of H I. Star formation, shown in Figure 5, is found within and along the ridge as well as further into the hole. A possible scenario is that past star formation within the hole pushed the H I gas outward and created the ridge we see today (Heiles 1979; Meaburn 1980; Hunter *et al.* 2001; Kepley *et al.* 2007). However, we would then expect to see an age gradient, with the oldest regions closer to the center of the hole, but in fact we do not see any systematic pattern of ages.

The wide range of ages for our star forming regions and their lack of correlation with total $M_{\mathrm{CO},vir}$ also suggests that the extremely small size of the individual CO cores is not due only to fragmentation of aging clouds. Instead, tiny CO cores are all that can be formed in a galaxy with this gas density and metallicity without some galaxy-scale compression.

Hunter *et al.* (2001) find star formation is located where $\Sigma_{\mathrm{H\,I}}$ is locally higher in the dIrr galaxy NGC 2366 which, like WLM, has a ring of H I surrounding most of the star formation in the galaxy. In Figure 16 we see that star forming regions with CO cores have an average $\Sigma_{\mathrm{H\,I}}$ higher than the radial average by amounts of 8-22 $M_{\odot}$, which is consistent with the need for a higher $\Sigma_{\mathrm{H\,I}}$ than the average in dIrrs to form stars. This, along with the relationship between higher $\Sigma_{\mathrm{H\,I}}$ and higher total $M_{\mathrm{CO},vir}$ suggests that $\Sigma_{\mathrm{H\,I}}$ may play a role in the formation of these CO cores. However, the presence of star forming regions with lower $M_{\mathrm{CO},vir}$ along this H I ridge suggests that a higher $\Sigma_{\mathrm{H\,I}}$ does not guarantee their formation. We also find star forming regions with CO cores that are not on this high density H I ridge, which we would not expect to see if higher $\Sigma_{\mathrm{H\,I}}$ or pressure were needed to form CO cores. This could mean that the ridge of H I that we see is actually a “bubble" that we are only seeing in two dimensions. Additionally, there are portions of the H I ridge without any star formation associated with it, particularly to the southeast, that do not show any obvious difference from the rest of the ridge. This portion of the ridge may contain CO cores, but was not surveyed due to lack of time. However, the area surveyed is still representative of the star forming area of the galaxy. The presence of CO cores in a variety of different local environments, along with the similar properties between star forming regions containing CO cores and those without CO cores, leads us to conclude that we do not find clear characteristics to form star forming regions with CO cores.

2.5 Acknowledgements

We are grateful for funding for this work, which was provided by the National Science Foundation through grant AST-1907492 to D.H. M.R. wishes to acknowledge support from ANID(CHILE) through FONDECYT grant No1190684.

This paper makes use of the following ALMA data: ADS/JAO.ALMA#2012.1.00208.S and ADS/JAO.ALMA#2018.1.00337.S. ALMA is a partnership of ESO (representing its member states), NSF (USA) and NINS (Japan), together with NRC (Canada), MOST and ASIAA (Taiwan), and KASI (Republic of Korea), in cooperation with the Republic of Chile. The Joint ALMA Observatory is operated by ESO, AUI/NRAO and NAOJ. The National Radio Astronomy Observatory is a facility of the National Science Foundation operated under cooperative agreement by Associated Universities, Inc.

Lowell Observatory sits at the base of mountains sacred to tribes throughout the region. We honor their past, present, and future generations, who have lived here for millennia and will forever call this place home.

*Facilities:*ALMA, VLA, GALEX, Lowell Observatory:1.1m

*Software:*IRAF (Tody 1986), SExtractor (Bertin and Arnouts 1996)

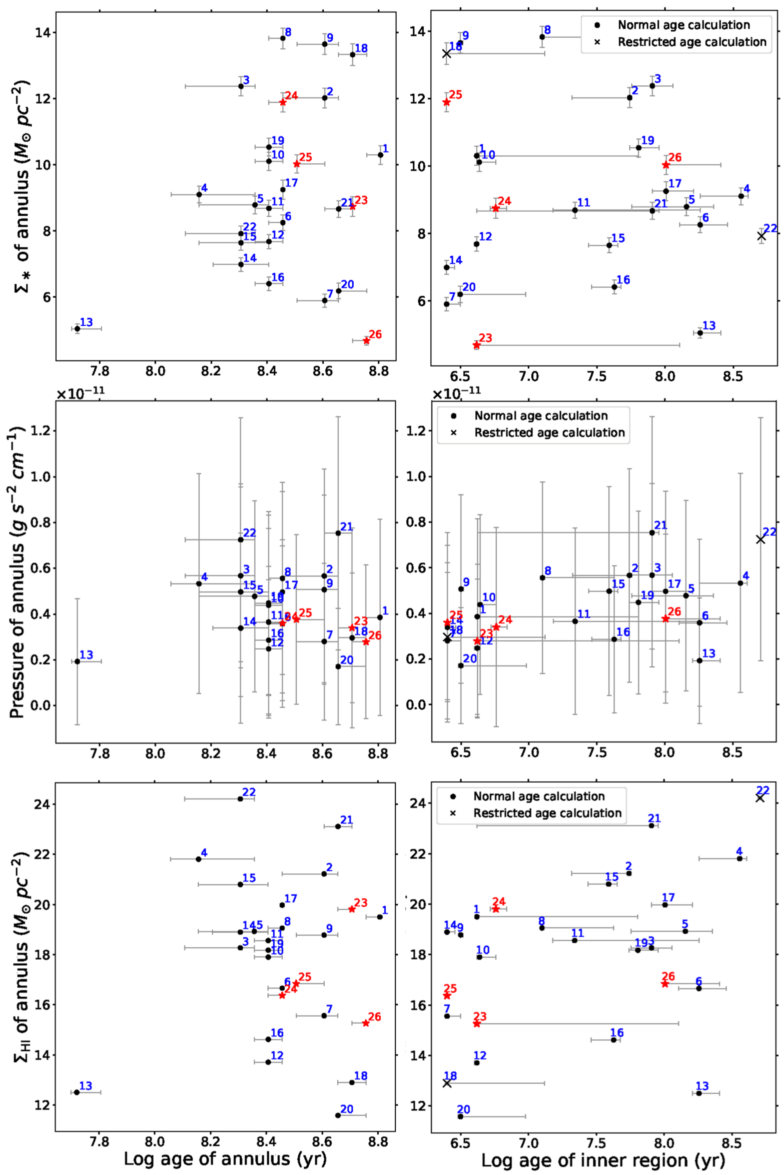

Figure 25. Left column: Stellar mass surface density (top), pressure (center), and H I surface density (bottom) of each annulus plotted against the age of that annulus. Right column: Stellar mass surface density (top), pressure (center), and H I surface density (bottom) of each annulus plotted against the age of the corresponding inner region. The age of inner regions spans a much larger range than the age of the annuli, however most star forming regions are less than 100 Myr while the ages of the environment are mostly older than 100 Myr. The H I uncertainties are smaller than the size of the plot markers. Age error bars that appear one-sided are the result of the upper or lower color uncertainties finding the same age in the model. Regions 18 and 22 are marked with an ($\times$) as the age and stellar mass were determined from UBV alone. The regions without CO (regions 23, 24, 25, and 26) are marked with a red star ($\star$).

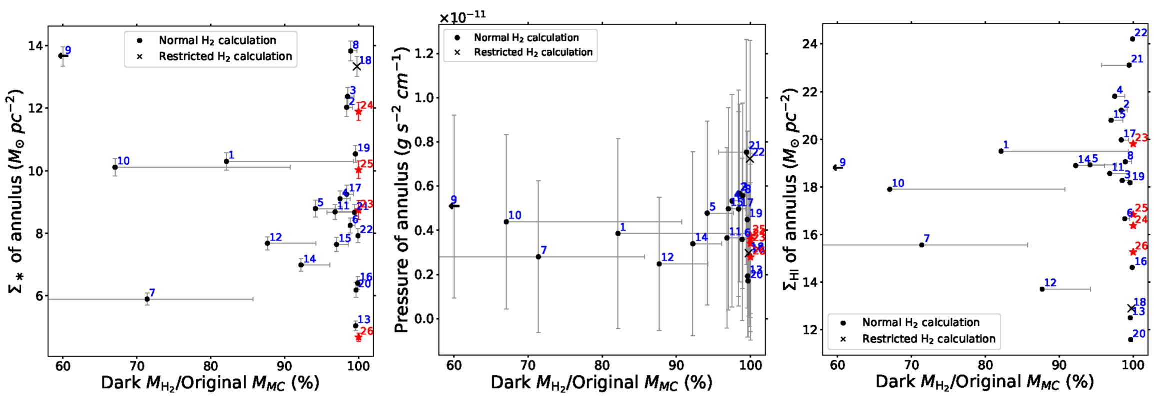

Figure 26. Stellar mass surface density (left), pressure (center), and H I surface density of each annulus plotted against the dark H_2 mass to original total molecular cloud mass ratio of that region. H I uncertainties are smaller than the size of the plot markers. Region 9 is displayed with a left-pointing arrow marker to indicate that the actual dark H_2 mass ratio is 0% but has been shifted right to better show the distribution of the other dark H_2 mass ratios. The total molecular cloud mass is the original mass of the cloud and does not take into account the dissociation of the cloud over time. Regions 18 and 22 are marked with an ($\times$) as the dark H_2 were determined from the stellar mass that was derived from UBV alone. The regions without CO (regions 23, 24, 25, and 26) are marked with a red star ($\star$) and assumed to have a dark H_2 mass percentage of 100%.

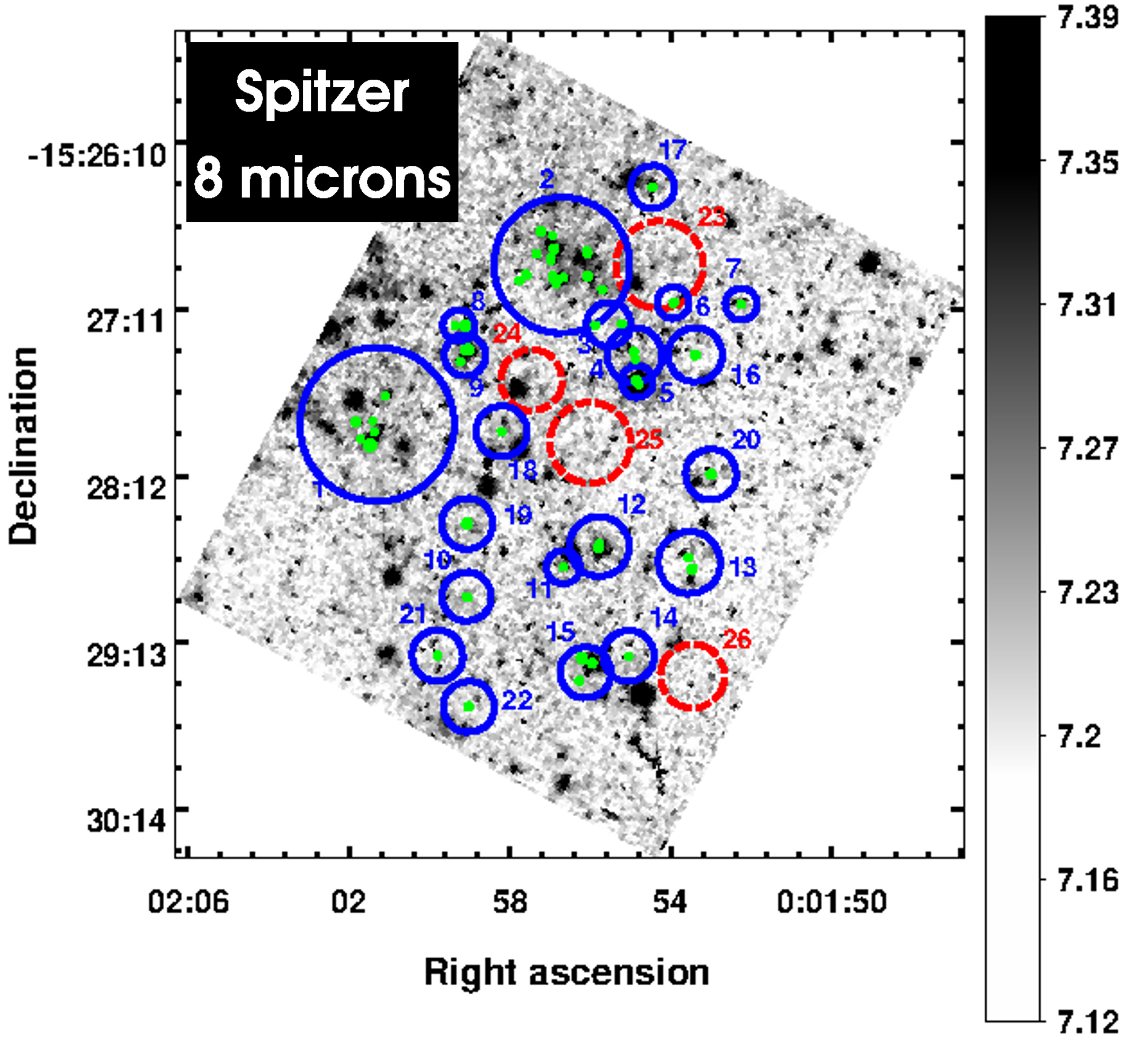

Figure 27. Spitzer 8μm image of WLM showing the regions defined here (larger blue and red dashed circles) and the CO cores (tiny green circles). Colorbar values are in units of MJy sr^{-1}.

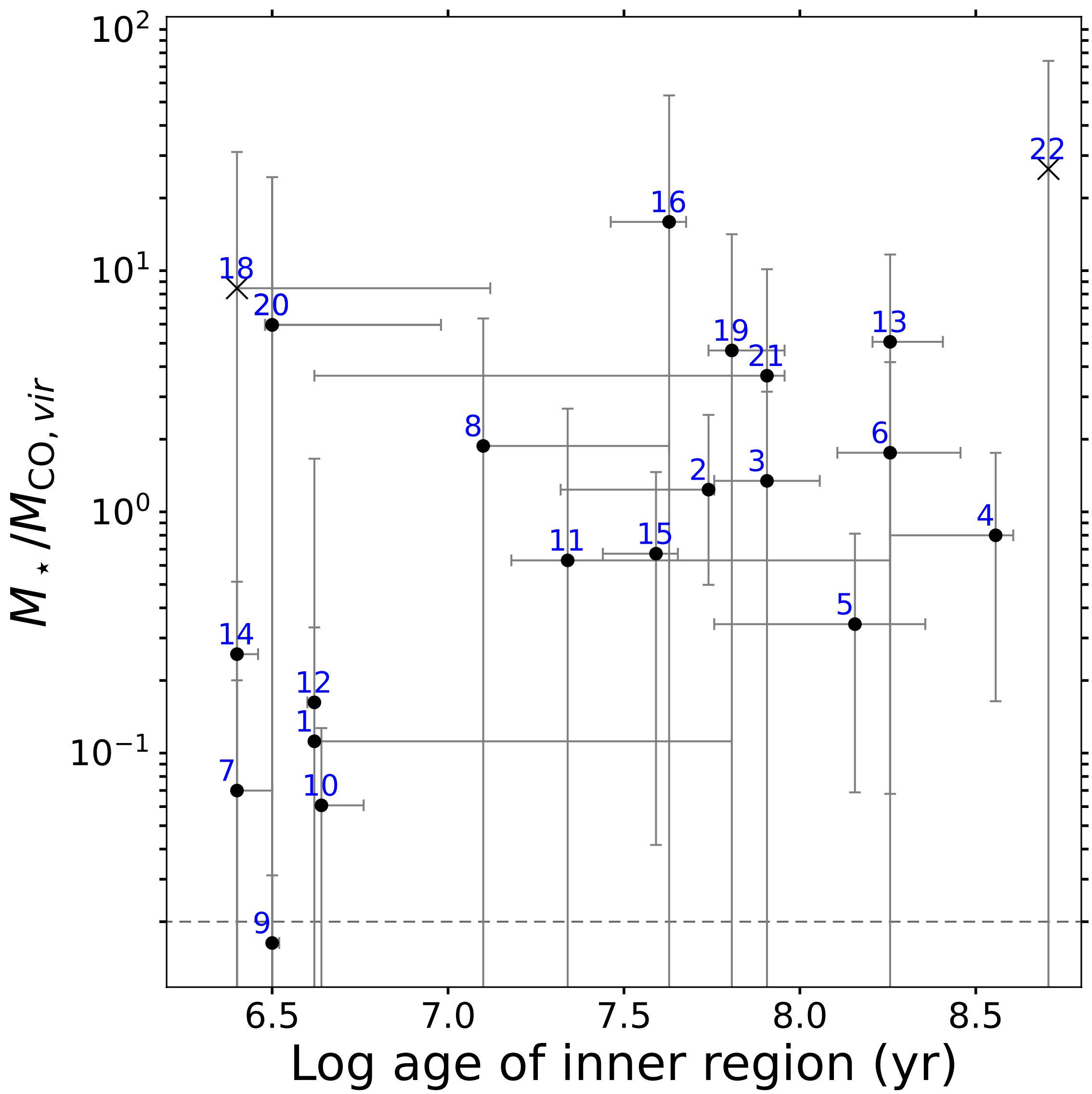

Figure 28. Ratio of young stellar mass to observed CO virial mass in the inner region ($M_*/M_{\mathrm{CO},vir}$) against the age of the inner region. The gray dashed line at $M_*/M_{\mathrm{CO},vir}$= 2% shows where $M_*/M_{\mathrm{CO},vir}$ is equal to the star formation efficiency of 2%.

Chapter 3

PROBING THE RELATIONSHIP BETWEEN EARLY STAR FORMATION AND CO IN THE DWARF IRREGULAR GALAXY WLM WITH JWST

[1,2]Haylee N. Archer, [2]Deidre A. Hunter, [3]Bruce G. Elmegreen, [4]Monica Rubio, [5]Phil Cigan, [1]Rogier A. Windorst, [6,7]Juan R. Cortés, [1]Rolf A. Jansen

[1]School of Earth and Space Exploration, Arizona State University, Tempe, AZ, USA

[2]Lowell Observatory, Flagstaff, AZ, USA

[3]IBM T. J. Watson Research Center, Yorktown Heights, NY, USA

[4]Departamento de Astronomía, Universidad de Chile, Santiago, Chile

[5]United States Naval Observatory, Washington, DC, USA

[6]Joint ALMA Observatory, Vitacura, Santiago, Chile

[7]National Radio Astronomy Observatory, Santiago, Chile

Published in the Astronomical Journal at doi.org/10.3847/1538-3881/ad3f18 (Archer *et al.* 2024a)

Abstract: Wolf-Lundmark-Melotte (WLM) is a Local Group dwarf irregular (dIrr) galaxy with a metallicity 13% of solar. At 1 Mpc, the relative isolation of WLM provides a unique opportunity to investigate the internal mechanisms of star formation at low metallicities. The earliest stages of star formation in larger spirals occur in embedded clusters within molecular clouds, but dIrrs lack the dust, heavy metals, and organized structure of spirals believed necessary to collapse the molecular clouds into stars. Despite actively forming stars, the early stages of star formation in dIrrs is not well understood. We examine the relationship between early star formation and molecular clouds at low metallicities. We utilize ALMA-detected CO cores, *JWST* near-infrared (NIR) images (F090W, F150W, F250M, and F430M), and *GALEX* far-ultraviolet (FUV) images of WLM to trace molecular clouds, early star formation, and longer star formation timescales respectively. We compare clumps of NIR-bright sources (referred to as objects) categorized into three types based on their proximity to FUV sources and CO cores. We find objects, independent of their location, have similar colors and magnitudes and no discernible difference in temperature. However, we find that objects near CO have higher masses than objects away from CO, independent of proximity to FUV. Additionally, objects near CO are coincident with Spitzer 8μm sources at a higher frequency than objects elsewhere in WLM. This suggests objects near CO may be embedded star clusters at an earlier stage of star formation, but accurate age estimates for all objects are required for confirmation.

3.1 Introduction

Wolf-Lundmark-Melotte (WLM) is a nearby dwarf irregular galaxy (dIrr) in the Local Group at a distance of approximately 980 kpc (Leaman *et al.* 2012; Lee *et al.* 2021). WLM is a relatively isolated galaxy, with distances far enough from both the Milky Way and M31 to indicate a low probability of previously interacting with either (Teyssier *et al.* 2012; Albers *et al.* 2019). However, recent observations of H I morphology and kinematics in WLM find evidence of ram-pressure stripping, suggesting the galaxy may be less isolated than previously thought (Yang *et al.* 2022). Studying star formation in WLM's potentially less perturbed environment can provide insights into the internal mechanisms of star-forming regions and the impact of the surrounding environment on the process. Like other nearby dIrrs, the proximity and low metal content of WLM at $12 + \log(O/H) = 7.8$ (Lee *et al.* 2005), which is ∼13% of solar metallicity, allow us to probe the details of star formation at low metallicity.

Star formation occurs in molecular clouds that are primarily composed of H_2, which is typically traced with low rotational transitions of CO (e.g. Kennicutt 1998; Bigiel *et al.* 2011; Glover and Mac Low 2011; Bolatto *et al.* 2013). In larger spirals like the Milky Way, Giant Molecular Clouds (GMCs) account for nearly all star formation, but in dwarf galaxies there is little CO to trace the molecular clouds despite ongoing star formation. In environments with low metal content, molecular clouds have altered properties compared to those in metal-rich environments (e.g. Elmegreen 1989; Hunter *et al.* 1998; Brosch *et al.* 1998; Bolatto *et al.* 1999; Leroy *et al.* 2008; Chevance *et al.* 2020b). For instance, scarcity of heavy elements limits the formation of dust grains, which play a crucial role in shielding and cooling molecular clouds (e.g. Draine and Li 2007; Fukui and Kawamura 2010; Wakelam *et al.* 2017a; Osman *et al.* 2020). Additionally, lower amounts of carbon and dust necessary for cooling result in larger photodissociation regions, longer CO formation time, and smaller CO clouds that are typically used to trace the molecular clouds (Elmegreen *et al.* 1980; Israel *et al.* 1986; Taylor *et al.* 1998; Leroy *et al.* 2009; Schruba *et al.* 2012).

The earliest stages of star formation in larger spiral galaxies occur within embedded clusters in GMCs (e.g. Lada and Lada 2003; Bastian and Goodwin 2006; Dale *et al.* 2015). Elmegreen *et al.* (2018) find embedded star clusters occurring at regular intervals within the main spiral arms of nearby spiral galaxies, suggesting that star formation likely originated from the collapse of dense gas, which was then compressed into narrow dust lanes due to the impact of stellar spiral arm shocks (Elmegreen and

Elmegreen 2019, 2020). Without the organized structures of spiral arms, however, star formation in dwarf galaxies tends to be more irregular and sporadic, and the early stages of star formation in these low metallicity environments are not well understood.

Following the discovery of CO(3–2) emission in two star-forming regions of WLM by Elmegreen *et al.* (2013) using the APEX telescope, Rubio *et al.* (2015) targeted these regions with CO(1–0) and mapped 10 CO cores with the Atacama Large Millimeter Array (ALMA). Archer *et al.* (2022b) then examined the relation between these 10 – plus an additional 35 (Rubio et al. in preparation) – CO cores in WLM and FUV used to define star-forming regions, along with the H I reservoir out of which the star-forming clouds formed, and found no obvious characteristics driving the formation of the CO cores. Recently, the *JWST* Resolved Stellar Populations ERS program (PID 1334) imaged a large portion of the star-forming area of WLM in the near infrared (NIR) at 0.9 μm, 1.5 μm, 2.5 μm, and 4.3 μm with the Near Infrared Camera (NIRCam) (Weisz *et al.* 2023). The NIR images now provide a clearer view of the young, embedded star-forming regions to explore the role of the CO cores in these regions and better understand early star formation at low metallicities.

Gaining insights into the role of CO in the initial stages of star formation in dwarf galaxies not only sheds light on how stars form at low metallicities but also provides insights into the fundamental physical processes of star formation and the interplay between stars and their environments. In this paper we investigate young star-forming regions in WLM to determine (1) if early star-forming regions have the same properties in different local environments and (2) the relationship between early star formation and CO in low metallicity environments. We use NIR images as tracers of young, embedded star formation (<5 Myr, Lada and Lada 2003), the CO cores to trace the

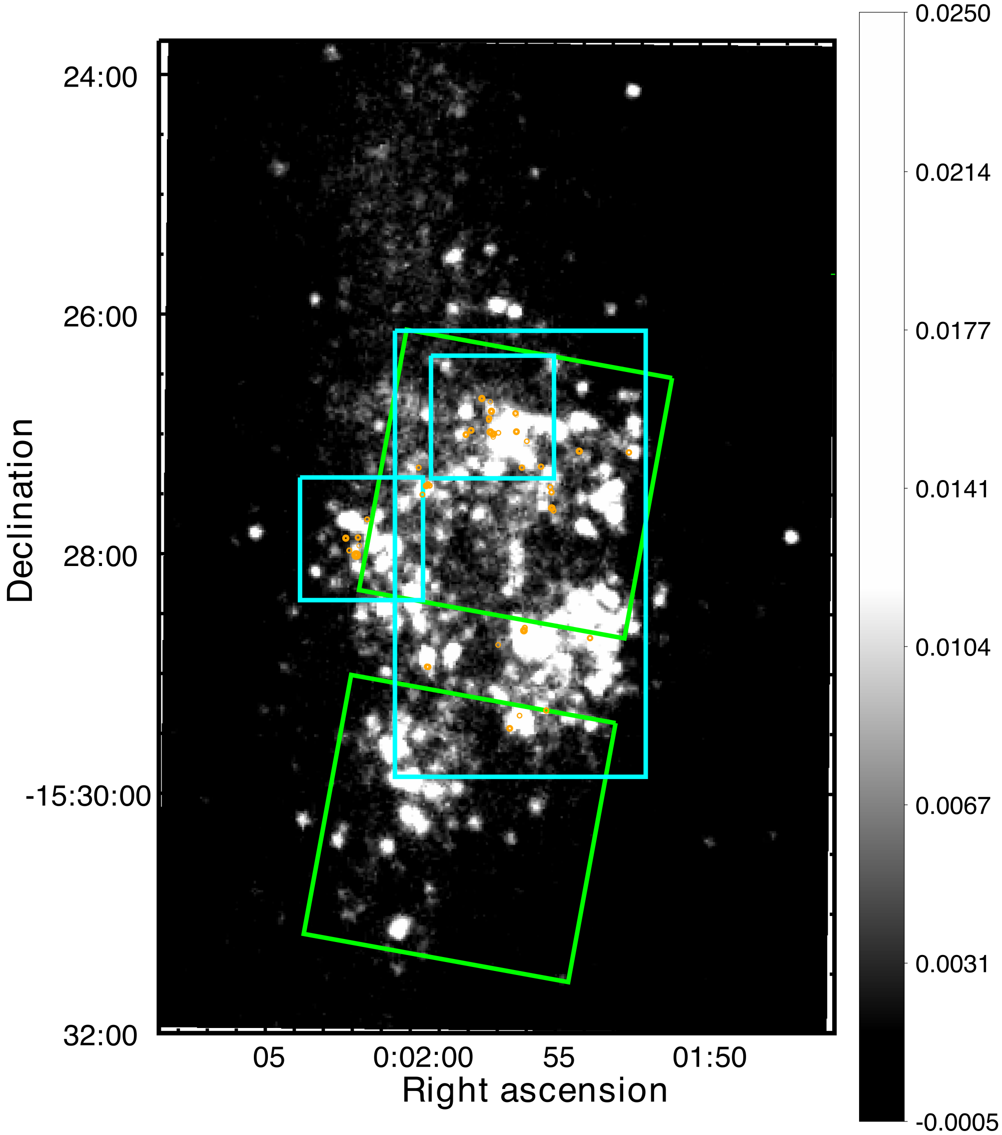

Figure 29. *FUV* image of WLM showing the field of view from ALMA Cycle 1 (smaller cyan squares, Rubio *et al.* 2015) and Cycle 6 (larger cyan rectangle, Rubio et al. in preparation) and the 45 detected CO cores (tiny orange circles), along with the field of view from *JWST* ERS PID 1334 (green squares, Weisz *et al.* 2023). The ERS fields will be referred to as the North field and the South field. The orientation of the image is such that North is up and East is to the left. Colorbar values can be converted from counts/second to calibrated AB magnitudes with the equation: $\mathrm{FUV}_{AB} = -2.5\log_{10}(\mathrm{FUV}_{counts/s}) + 18.82$.

molecular clouds from which stars form, and FUV to trace star formation on longer time scales (up to ~100 Myr, Calzetti 2013).

The paper is organized as follows. In Section 3.2 we introduce our data and describe our object selection and definitions of the object types, along with our methods for determining the blackbody temperature, luminosity, and mass of the objects. We present our results in Section 3.3 and discuss our findings in Section 3.4. Finally, we summarize our conclusions in Section 3.5.

3.2 Data

3.2.1 CO Cores

Rubio *et al.* (2015) imaged two star-forming regions of WLM in CO(1–0) with ALMA Cycle 1 and detected 10 CO cores, with an additional 35 cores detected from CO(2–1) ALMA Cycle 6 observations (Rubio et al., in preparation). The beam size was $0.9'' \times 1.3''$ for Cycle 1 and $0.6'' \times 0.5''$ for Cycle 6, and the observations covered most of the star-forming area of WLM. Further details on the CO(1–0) detection are described by Rubio *et al.* (2015).

Rubio et al. (in preparation) used the CPROPS algorithm (Rosolowsky and Leroy 2006) in the ALMA CO(2–1) data-cube to identify the molecular clouds. They considered as true clouds those with sizes larger than the beam size spatial resolution, a velocity width (FWHM) greater than 3 channels (>0.5 km s^{-1}), and a noise level

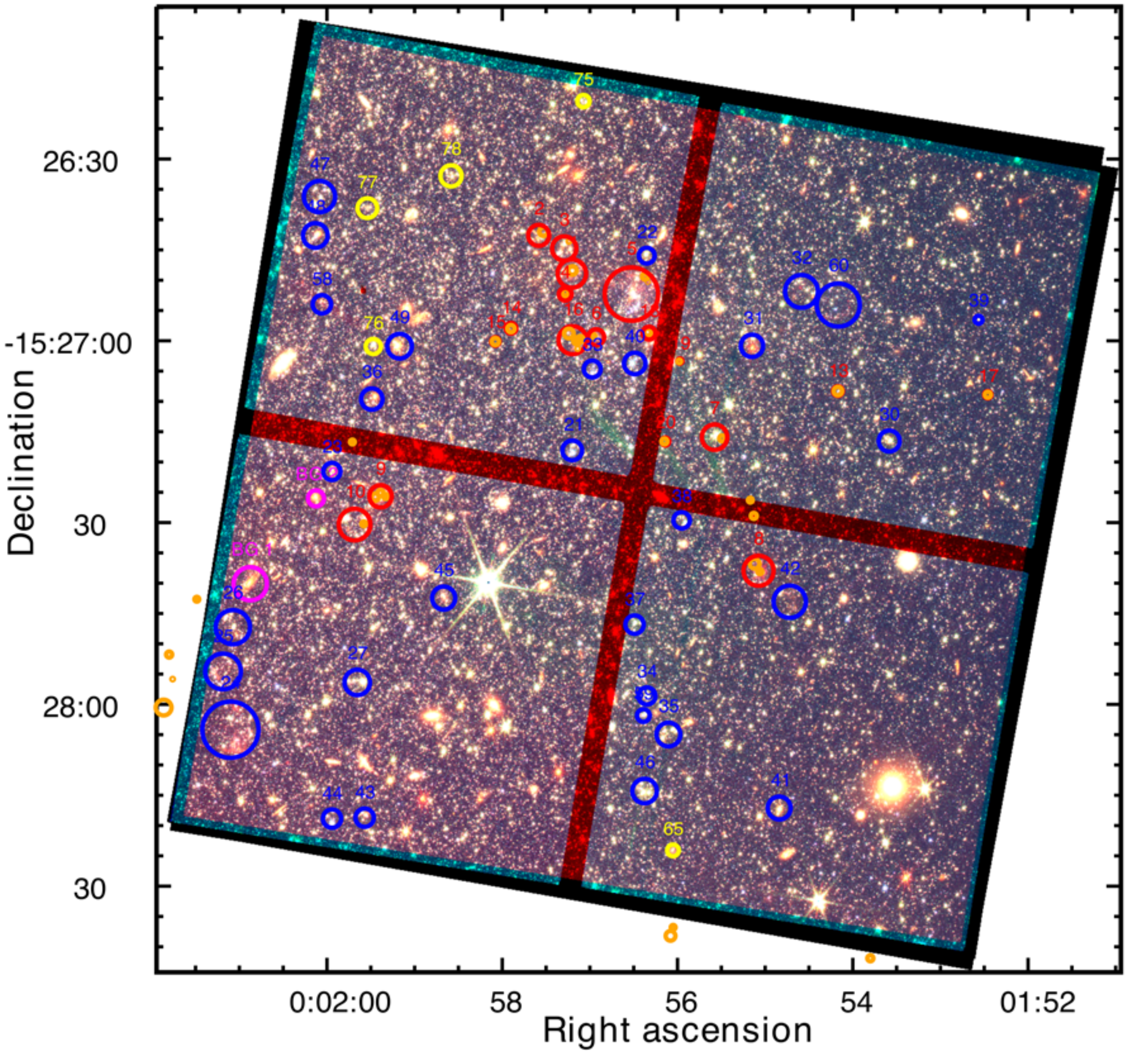

Figure 30. F250M (red), F150W (green), F090W (blue) three-color image of *JWST* ERS north field overlaid with type 1 objects (in FUV and near CO, red circles), type 2 objects (in FUV and away from CO, blue circles), type 3 objects (away from FUV and away from CO, yellow), resolved background galaxies (magenta circles), and CO cores (orange circles). The orientation of the image is such that North is up and East is to the left.

above 3 sigma rms. With these criteria 35 clouds were identified and their properties derived. All these clouds have signal-to-noise (S/N) ratios larger than 5 and V_{lsr} between -150 and -110 km s^{-1}.

The properties of the CO(2–1) clouds such as the radius (R), velocity dispersion

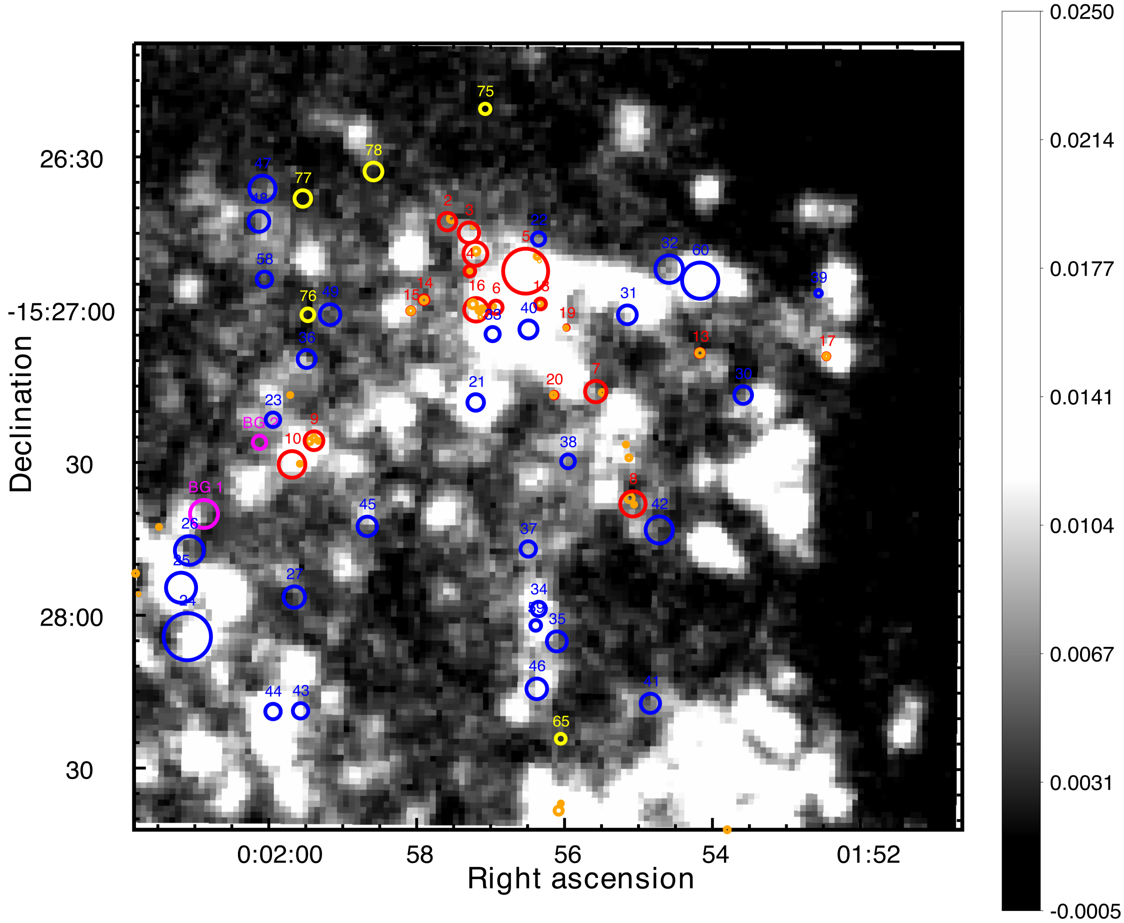

Figure 31. FUV image of *JWST* ERS north field overlaid with type 1 objects (in FUV and near CO, red circles), type 2 objects (in FUV and away from CO, blue circles), type 3 objects (away from FUV and away from CO, yellow), resolved background galaxies (magenta circles), and CO cores (orange circles). The orientation of the image is such that North is up and East is to the left. Colorbar values can be converted from counts/second to calibrated AB magnitudes with the equation: $\mathrm{FUV}_{AB} = -2.5\log_{10}(\mathrm{FUV}_{counts/s}) + 18.82$.

(σ_v), CO flux (F_{CO}) were calculated by CPROPS using the moment method in the position-position-velocity data cube. For the calculation of the radius R, CPROPS uses the Solomon *et al.* (1987) definition for spherical clouds assuming a factor of 1.91 to convert the second moments of the emission along the major and minor axes of clouds (σ_r) to R. For unresolved clouds along the minor axis, Rubio et al. obtained

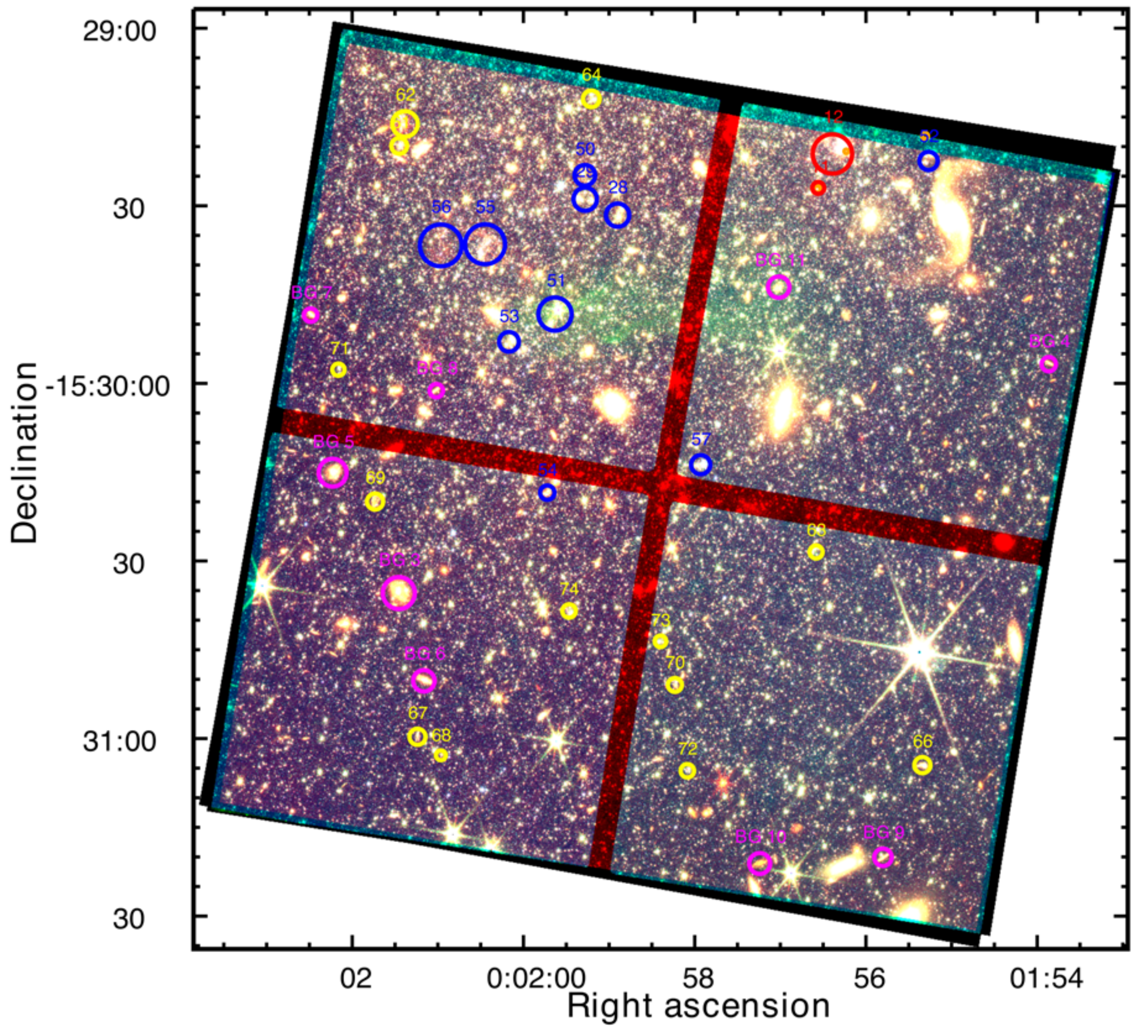

Figure 32. F250M (red), F150W (green), F090W (blue) three-color image of *JWST* ERS south field overlaid with type 1 objects (in FUV and near CO, red circles), type 2 objects (in FUV and away from CO, blue circles), type 3 objects (away from FUV and away from CO, yellow), resolved background galaxies (magenta circles), and CO cores (orange circles). The orientation of the image is such that North is up and East is to the left.

the radii following the Saldaño *et al.* (2023) calculation, in which the radii were recalculated assuming that the minor axis is equal to the minor beam axis size.

They found that the WLM clouds are tiny with sizes between 0.6 pc to 3.8 pc. The velocity dispersion of the clouds is quite small ranging form 0.4 $\mathrm{km\,s^{-1}}$ to 1.3

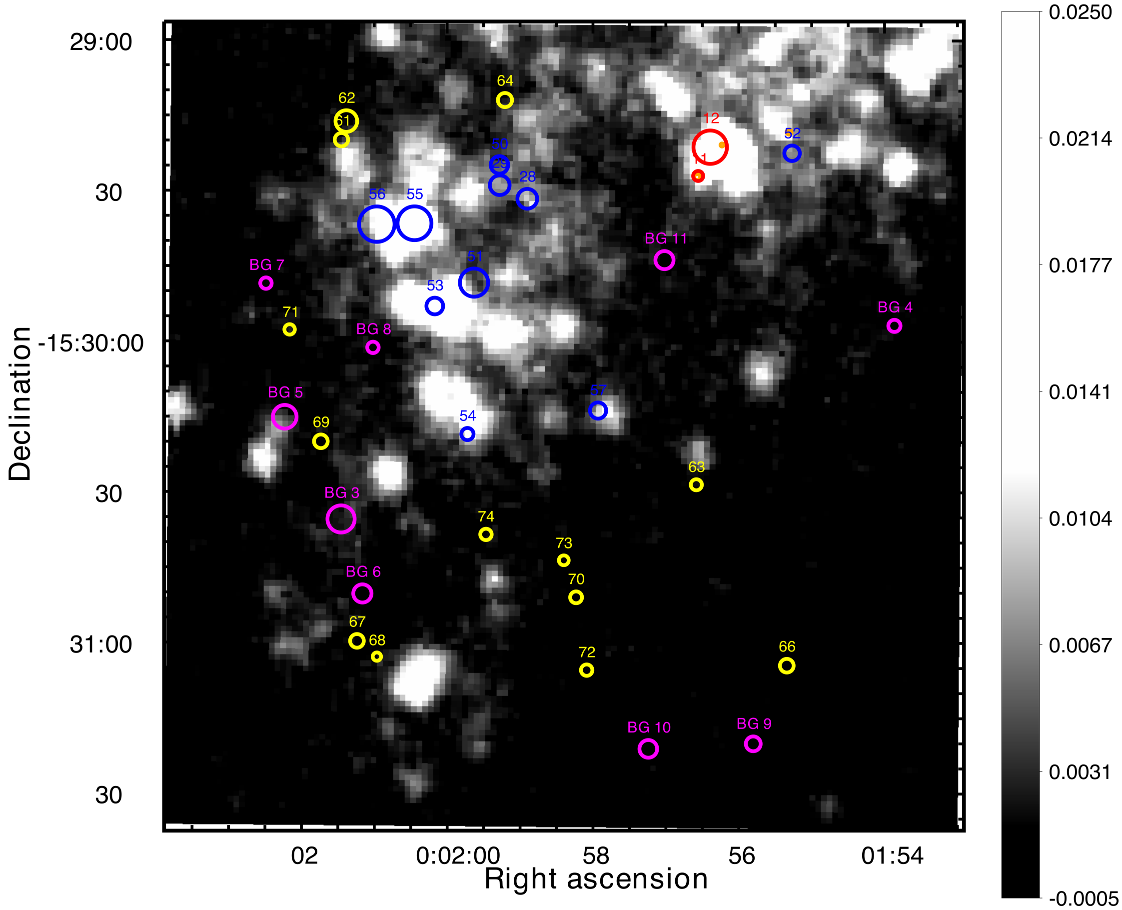

Figure 33. FUV image of *JWST* ERS south field overlaid with type 1 objects (in FUV and near CO, red circles), type 2 objects (in FUV and away from CO, blue circles), type 3 objects (away from FUV and away from CO, yellow), resolved background galaxies (magenta circles), and CO cores (orange circles). The orientation of the image is such that North is up and East is to the left. Colorbar values can be converted from counts/second to calibrated AB magnitudes with the equation: $\mathrm{FUV}_{AB} = -2.5\log_{10}(\mathrm{FUV}_{counts/s}) + 18.82$.

$\mathrm{km\,s^{-1}}$. The CO luminosity ranges from 2.5×10^2 K $\mathrm{km\,s^{-1}}$ to 15.2×10^2 K $\mathrm{km\,s^{-1}}$. The derived virial mass of the clouds ranges between 0.4×10^3 $\mathrm{M_\odot}$ to 7.6×10^3 $\mathrm{M_\odot}$.

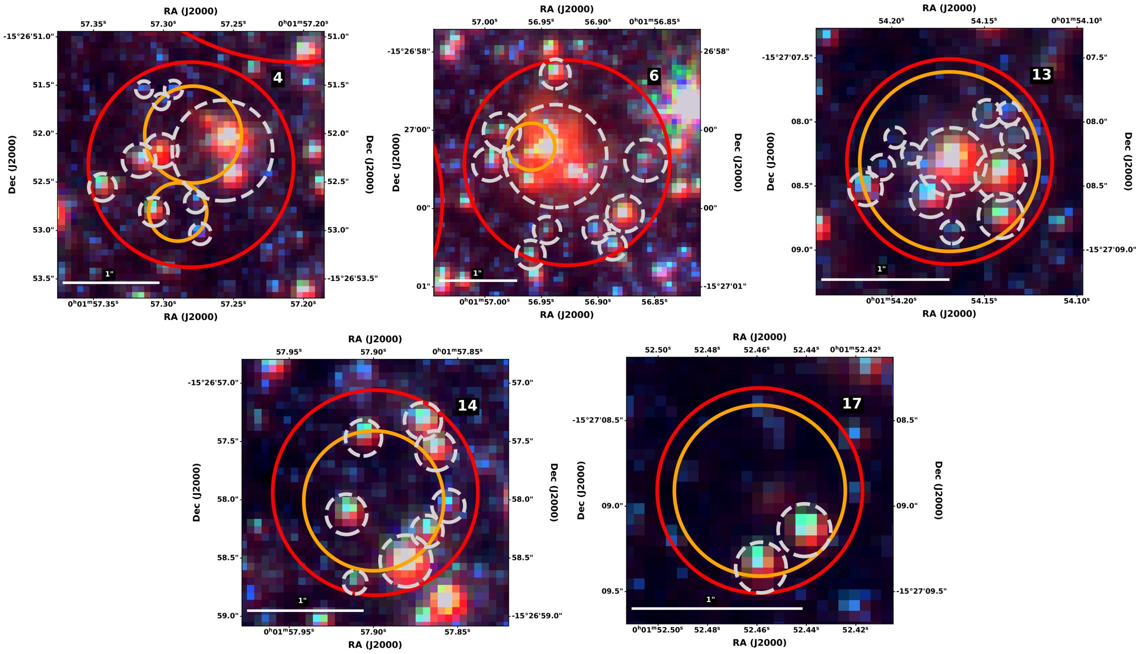

Figure 34. F250M (red), F150W (green), F090W (blue) three-color image postage stamps of select type 1 objects (red circles) and the individual NIR sources within (gray, dashed circles) that we used to compare photometry between our larger objects and the smaller, individual sources within. We also overlay the CO cores (orange circles) inside the type 1 objects. The orientation of the image is such that North is up and East is to the left.

3.2.2 JWST ERS #1334

The F090W ($\lambda = 0.9\ \mu m$), F150W ($\lambda = 1.5\ \mu m$), F250M ($\lambda = 2.5\ \mu m$), and F430M ($\lambda = 4.3\ \mu m$) NIRCam images come from the *JWST* Resolved Stellar Populations ERS program (PID 1334). All the *JWST* data used in this paper can be found in MAST: https://doi.org/10.17909/wq6j-x975https://doi.org/10.17909/wq6j-x975. The exposure time was 30492 seconds for each of the F090W and F430M filters and 23707 seconds for each of the F150W and F250M filters. Further information on the ERS program and acquired images can be found in Weisz *et al.* (2023).

Table 1. Object type, definition based on location, and color used for the clumps of NIR sources (referred to as objects) examined in this work.

Object Type	Location	Color
Type 1	In FUV knots, near CO cores	Red
Type 2	In FUV knots, away from CO cores	Blue
Type 3	Away from FUV knots, away from CO cores	Yellow

Figure 35. Table 1 from Probing the Relationship Between Early Star Formation and CO in the Dwarf Irregular Galaxy WLM with JWST by Archer *et al.* (2024a) published in the Astronomical Journal.

Table 2. Object number, right ascension, declination, radius, F090W AB magnitude, F090W–F150W color, F250M AB magnitude, F250M–F430M color, blackbody temperature corresponding to the F090W–F150W and F250M–F430M colors, and total mass for type 1 objects. A full table including all objects is available in the online materials.

Object (1)	RA [*J2000*] (2)	Dec [*J2000*] (3)	Radius [$''$] (4)	F090W [*AB mag*] (5)	F090W–F150W (6)	F250M [*AB mag*] (7)	F250M–F430M (8)	$T_{090-150}$ [K] (9)	$T_{250-430}$ [K] (10)	Mass [$M_\odot$] (11)
Object Type 1 (red)										
1	00:01:57.20	−15:26:48.9	2.34	19.84 ± 0.02	0.20 ± 0.03	20.10 ± 0.03	-0.65 ± 0.05	3910 ± 70	1420 ± 310	1134 ± 1118
2	00:01:57.58	−15:26:42.6	1.73	19.89 ± 0.02	0.38 ± 0.03	20.18 ± 0.03	-0.75 ± 0.05	3520 ± 60	1280 ± 530	555 ± 540
3	00:01:57.29	−15:26:44.7	2.00	19.73 ± 0.02	0.32 ± 0.03	19.87 ± 0.03	-0.60 ± 0.04	3640 ± 60	1320 ± 230	878 ± 859
4	00:01:57.28	−15:26:52.3	1.06	22.05 ± 0.03	0.01 ± 0.05	22.35 ± 0.07	-0.02 ± 0.10	4450 ± 160	1610 ± 120	1961 ± 1959
5	00:01:56.52	−15:26:52.2	4.41	18.15 ± 0.02	-0.07 ± 0.03	18.92 ± 0.02	-0.73 ± 0.03	4750 ± 100	1720 ± 310	2355 ± 2285
6	00:01:56.92	−15:26:59.4	1.31	21.32 ± 0.03	0.29 ± 0.04	21.36 ± 0.04	-0.62 ± 0.07	3710 ± 80	1350 ± 450	821 ± 817
7	00:01:55.57	−15:27:15.9	2.10	18.91 ± 0.02	-0.13 ± 0.03	19.44 ± 0.02	-0.52 ± 0.04	4980 ± 110	1800 ± 150	3388 ± 3348
8	00:01:55.07	−15:27:37.9	2.48	19.87 ± 0.02	0.36 ± 0.03	18.71 ± 0.02	1.38 ± 0.03	3560 ± 60	1300 ± 10	1012 ± 941
9	00:01:59.38	−15:27:25.6	1.84	20.05 ± 0.02	-0.06 ± 0.03	20.31 ± 0.03	-0.45 ± 0.05	4680 ± 120	1700 ± 150	2644 ± 2629
10	00:01:59.68	−15:27:30.3	2.61	18.82 ± 0.02	0.28 ± 0.03	19.22 ± 0.02	-0.87 ± 0.04	3730 ± 60	1360 ± 900	589 ± 553
11	00:01:56.55	−15:29:26.9	1.00	21.65 ± 0.03	0.01 ± 0.04	21.99 ± 0.06	-0.90 ± 0.10	4450 ± 130	1610 ± 2990	357 ± 354
12	00:01:56.39	−15:29:21.2	3.33	18.81 ± 0.02	-0.27 ± 0.03	19.20 ± 0.02	-0.08 ± 0.03	5650 ± 150	2040 ± 50	5930 ± 5875
13	00:01:54.16	−15:27:08.3	0.80	22.39 ± 0.04	0.09 ± 0.05	22.83 ± 0.08	0.24 ± 0.11	4210 ± 160	1530 ± 100	1303 ± 1301
14	00:01:57.90	−15:26:57.9	0.88	21.99 ± 0.03	0.31 ± 0.04	22.68 ± 0.08	-1.04 ± 0.15	3660 ± 90	1330 ± 3280	92 ± 91
15	00:01:58.07	−15:27:00.1	0.70	23.12 ± 0.05	-0.42 ± 0.08	24.74 ± 0.20	-1.25 ± 0.40	6640 ± 680	2380 ± 4150	1867 ± 1866
16	00:01:57.19	−15:26:59.8	2.31	19.72 ± 0.02	0.24 ± 0.03	20.22 ± 0.03	-0.60 ± 0.05	3830 ± 70	1390 ± 260	883 ± 867
17	00:01:52.45	−15:27:08.8	0.60	24.10 ± 0.07	0.12 ± 0.10	25.06 ± 0.23	-1.28 ± 0.47	4110 ± 300	1490 ± 4770	4 ± 4
18	00:01:56.32	−15:26:58.7	1.07	21.17 ± 0.03	-0.07 ± 0.04	21.94 ± 0.06	-0.85 ± 0.10	4720 ± 160	1710 ± 2800	381 ± 378
19	00:01:55.97	−15:27:03.3	0.44	22.96 ± 0.05	0.31 ± 0.06	22.62 ± 0.08	0.15 ± 0.10	3660 ± 130	1330 ± 100	937 ± 936
20	00:01:56.14	−15:27:16.6	0.66	24.03 ± 0.07	0.07 ± 0.10	24.93 ± 0.22	-0.55 ± 0.35	4280 ± 320	1550 ± 3670	1 ± 1

NOTE—Table 2 is published in its entirety in the supplemental materials in machine-readable format.

Figure 36. Table 2 from Probing the Relationship Between Early Star Formation and CO in the Dwarf Irregular Galaxy WLM with JWST by Archer *et al.* (2024a) published in the Astronomical Journal.

Table 3. CO core number, right ascension, declination, and radius for the 28 CO cores used in this work.

Object (1)	RA [$J2000$] (2)	Dec [$J2000$] (3)	Radius [$''$] (4)	M_{vir} [$M_\odot$] (5)
1	00:01:57.29	−15:26:52.8	0.31	1087 ± 919
2	00:01:57.90	−15:26:58.0	0.56	1561 ± 985
3	00:01:58.08	−15:27:00.1	0.56	894 ± 637
4	00:01:52.46	−15:27:08.9	0.10	600 ± 1100
5	00:01:54.17	−15:27:08.3	0.15	2100 ± 1000
6	00:01:55.06	−15:27:38.1	0.08	2400 ± 1200
7	00:01:55.12	−15:27:36.8	0.17	1800 ± 1600
8	00:01:55.49	−15:27:16.1	0.10	1000 ± 700
9	00:01:55.98	−15:27:03.4	0.06	3600 ± 2700
10	00:01:56.15	−15:27:16.6	0.10	3300 ± 2400
11	00:01:56.23	−15:29:20.8	0.06	3100 ± 2700
12	00:01:56.34	−15:26:50.3	0.02	300 ± 400
13	00:01:56.34	−15:26:58.6	0.13	2800 ± 1600
14	00:01:56.37	−15:26:49.4	0.10	900 ± 600
15	00:01:56.57	−15:29:27.2	0.13	5600 ± 4100
16	00:01:56.96	−15:26:59.2	0.06	800 ± 700
17	00:01:57.11	−15:26:59.7	0.10	1400 ± 1100
18	00:01:57.14	−15:27:01.3	0.04	400 ± 300
19	00:01:57.15	−15:27:00.0	0.13	3400 ± 1200
20	00:01:57.20	−15:26:48.4	0.15	7600 ± 2300
21	00:01:57.24	−15:26:58.8	0.17	1200 ± 1100
22	00:01:57.24	−15:26:43.6	0.04	700 ± 400
23	00:01:57.28	−15:26:52.0	0.10	3100 ± 1200
24	00:01:57.53	−15:26:42.0	0.15	1400 ± 1000
25	00:01:59.33	−15:27:25.7	0.08	900 ± 600
26	00:01:59.39	−15:27:25.1	0.10	3900 ± 1300
27	00:01:59.45	−15:27:25.8	0.13	1800 ± 1000
28	00:01:59.58	−15:27:30.2	0.08	1600 ± 1200

Figure 37. Table 3 from Probing the Relationship Between Early Star Formation and CO in the Dwarf Irregular Galaxy WLM with JWST by Archer *et al.* (2024a) published in the Astronomical Journal.

3.2.3 FUV

The FUV image comes from the NASA Galaxy Evolution Explorer (*GALEX*[1]) satellite (Martin *et al.* 2005b) GR4/5 pipeline, and were further reduced by Zhang *et al.* (2012). Figure 29 shows the *FUV* image of WLM overlaid with the detected CO cores and the ALMA field of view (FOV) for both Cycle 1 and Cycle 6, along with the two FOVs from the *JWST* Resolved Stellar Populations ERS program (PID 1334). The colorbar values can be converted from counts per second to calibrated AB magnitudes with the equation:

$$FUV_{AB} = -2.5\log_{10}(FUV_{counts/s}) + 18.82. \tag{3.1}$$

Table 4. Individual source number, host object number, right ascension, declination, radius, F090W AB magnitude, F090W–F150W color, F250M AB magnitude, and F250M–F430M color for 10 individual sources within Type 1 Objects. A full table including all measured individual sources is available in the online materials.

Individual Source (1)	Host Object (2)	RA [*J2000*] (3)	Dec [*J2000*] (4)	Radius [″] (5)	F090W [*AB mag*] (6)	F090W–F150W (7)	F250M [*AB mag*] (8)	F250M–F430M
1	14	00:01:57.87	−15:26:57.3	0.16	24.48 ± 0.09	0.43 ± 0.11	25.74 ± 0.31	-0.81 ± 0.54
2	14	00:01:57.86	−15:26:57.5	0.17	24.65 ± 0.09	0.40 ± 0.12	25.10 ± 0.23	-0.93 ± 0.42
3	14	00:01:57.88	−15:26:58.5	0.22	23.00 ± 0.05	0.57 ± 0.06	23.35 ± 0.10	-0.96 ± 0.19
4	14	00:01:57.86	−15:26:58.2	0.14	25.25 ± 0.12	0.24 ± 0.16	26.17 ± 0.38	-1.68 ± 0.91
5	14	00:01:57.85	−15:26:58.0	0.14	25.01 ± 0.11	-0.84 ± 0.20	27.09 ± 0.58	-1.14 ± 1.13
6	14	00:01:57.91	−15:26:58.1	0.17	25.05 ± 0.11	0.39 ± 0.15	25.90 ± 0.33	-0.91 ± 0.61
7	14	00:01:57.90	−15:26:57.4	0.15	25.47 ± 0.13	0.36 ± 0.18	26.41 ± 0.42	-0.83 ± 0.75
8	14	00:01:57.91	−15:26:58.6	0.10	26.83 ± 0.25	0.27 ± 0.33	28.49 ± 1.10	-1.26 ± 2.24
9	4	00:01:57.25	−15:26:52.1	0.52	22.67 ± 0.04	0.12 ± 0.06	22.80 ± 0.08	-0.11 ± 0.12
10	4	00:01:57.30	−15:26:52.7	0.15	25.46 ± 0.13	0.18 ± 0.18	26.45 ± 0.43	-1.22 ± 0.86

Note—Table 4 is published in its entirety in the supplemental materials in machine-readable format.

Figure 38. Table 4 from Probing the Relationship Between Early Star Formation and CO in the Dwarf Irregular Galaxy WLM with JWST by Archer *et al.* (2024a) published in the Astronomical Journal.

[1] *GALEX* was operated for NASA by the California Institute of Technology under NASA contract NAS5-98034.

3.2.4 Object Types

We used a three-color image combining the *JWST* NIRCam F250M (red), F150W (green), and F090W (blue) images to identify and define three types of objects: those in FUV knots and near CO cores (object **type 1**), those in FUV knots and away from CO cores (object **type 2**), and those away from FUV knots and away from CO cores (object **type 3**). We focus on clumps of NIR sources in this work, which we refer to as "objects". The table in Figure 35 details each object type, location, and color used in figures and plots for reference as the reader proceeds.

We refer to the CO sources as "CO cores" and the FUV sources as "FUV knots". We consider the FUV knots to be the visible parts of star forming regions. The determination of whether a NIR object is near or away from a CO core is made visually; nearby objects encompass the CO core. Figures 30, 31, 32, and 33 show the three object types overlaid on the *JWST* three-color and FUV images for each of the two *JWST* pointings. The table in Figure 36 lists the RA, Dec, object radius in arcseconds, F090W AB magnitude, and F250M AB magnitude for type 1 objects. A full list for objects of all three types is available in the online materials. We also present the locations, radii, and masses of the 28 CO cores included in this work in the table in Figure 37. All of the CO cores are inside FUV knots, which is why there is no object type "outside FUV knots and near CO cores". Additionally, we include four type 2 objects and 12 type 3 objects further south than was mapped with ALMA. The type 2 objects south of the ALMA FOV may contain unobserved CO, and removing them from the sample changes the ratio of type 1 to type 2 objects from 50% to 56%. Because the CO cores are all near FUV knots, we do not expect any type 3 objects to be near unobserved CO. A *JWST* three-color postage stamp for each object is included in the appendix.

We then performed aperture photometry on the objects using the Image Reduction and Analysis Facility (IRAF) (Tody 1986) routine APPHOT to measure the fluxes of the objects in the F090W, F150W, F250M, and F430M images. The size of the aperture for each object corresponded to the size of the object, shown in Figures 30, 31, 32, and 33. We calculated our uncertainties using photon statistics convolved with the known 4% NIRCam zeropoint uncertainty (Windhorst *et al.* 2023). We converted the fluxes of the objects in each image to AB magnitudes using the conversions:

$$\mathrm{F090W}_{AB} = -2.5\log_{10}(\mathrm{F090W}_{MJy/sr} \times 2.2 \times 10^{-8}) + 8.90 \tag{3.2}$$

$$\mathrm{F150W}_{AB} = -2.5\log_{10}(\mathrm{F150W}_{MJy/sr} \times 2.3 \times 10^{-8}) + 8.90 \tag{3.3}$$

$$\mathrm{F250M}_{AB} = -2.5\log_{10}(\mathrm{F250M}_{MJy/sr} \times 9.3 \times 10^{-8}) + 8.90 \tag{3.4}$$

$$\mathrm{F430M}_{AB} = -2.5\log_{10}(\mathrm{F430M}_{MJy/sr} \times 9.3 \times 10^{-8}) + 8.90. \tag{3.5}$$

We chose to look at larger clumps instead of individual NIR sources to include extended sources that appeared to be part of the same system. As a test case, we also measured the colors of the individual NIR sources inside a subset of the larger type 1 objects (Figure 34). We include the right ascension (RA), declination (Dec), radius in arcseconds, F090W AB mag, F090W–F150W color, F250M AB mag, and F250M–F430M color for 10 of the individual sources within Type 1 Objects used in our test case in the table in Figure 38, with the full table included in the online materials. We find that the individual sources have similar colors to the larger objects. As such, we chose to stick with the larger objects for the purpose of this paper.

To determine whether our objects are contaminated by unresolved background galaxies, we use Windhorst *et al.* (2023, Section 4 and Figures 6-8) to estimate the surface density of faint galaxies at our AB magnitude flux limit of ∼25 to be approximately 0.02 background galaxies per square arcsecond in all four NIRCam filters. For a typical object with a radius of 1.5 arcseconds, this equates to about 0.14 unresolved background galaxies within each object.

Table 5. Object number, right ascension, declination, radius, F090W AB magnitude, F090W–F150W color, F250M AB magnitude, and F250M–F430M color for our sample of resolved background galaxies.

Object (1)	RA [*J2000*] (2)	Dec [*J2000*] (3)	Radius [″] (4)	F090W [*AB mag*] (5)	F090W–F150W (6)	F250M [*AB mag*] (7)	F250M–F430M (8)
BG 1	00:02:00.87	−15:27:40.0	2.74	19.99 ± 0.02	0.44 ± 0.03	19.55 ± 0.02	-0.02 ± 0.04
BG 2	00:02:00.12	−15:27:26.0	1.32	20.95 ± 0.02	0.66 ± 0.03	20.33 ± 0.03	0.27 ± 0.04
BG 3	00:02:01.45	−15:30:35.4	2.70	20.09 ± 0.02	0.85 ± 0.03	18.72 ± 0.02	0.89 ± 0.03
BG 4	00:01:53.86	−15:29:56.7	1.21	22.61 ± 0.04	0.44 ± 0.05	21.89 ± 0.06	-0.38 ± 0.09
BG 5	00:02:02.22	−15:30:15.0	2.35	20.65 ± 0.02	0.57 ± 0.03	19.84 ± 0.03	0.05 ± 0.04
BG 6	00:02:01.16	−15:30:50.2	1.81	21.37 ± 0.03	0.53 ± 0.04	20.56 ± 0.03	-0.54 ± 0.05
BG 7	00:02:02.48	−15:29:48.4	1.13	21.99 ± 0.03	0.63 ± 0.04	20.90 ± 0.04	-0.36 ± 0.06
BG 8	00:02:01.01	−15:30:01.2	1.13	22.39 ± 0.04	0.45 ± 0.05	21.63 ± 0.05	0.35 ± 0.07
BG 9	00:01:55.80	−15:31:20.0	1.47	21.76 ± 0.03	0.50 ± 0.04	21.50 ± 0.05	-0.49 ± 0.07
BG 10	00:01:57.24	−15:31:21.1	1.76	23.05 ± 0.05	0.99 ± 0.06	21.44 ± 0.05	0.73 ± 0.06
BG 11	00:01:57.01	−15:29:43.7	1.80	20.90 ± 0.02	0.22 ± 0.03	20.97 ± 0.04	-0.08 ± 0.06

Figure 39. Table 5 from Probing the Relationship Between Early Star Formation and CO in the Dwarf Irregular Galaxy WLM with JWST by Archer *et al.* (2024a) published in the Astronomical Journal.

3.2.5 Blackbody Temperature, Luminosity, and Mass Estimates

We calculated the blackbody temperatures corresponding to the color for the given filters using the Planck law and the OBSERVATE routine from the Python package SEDPY for spectral energy distributions (SEDs) to generate synthetic photometry through the

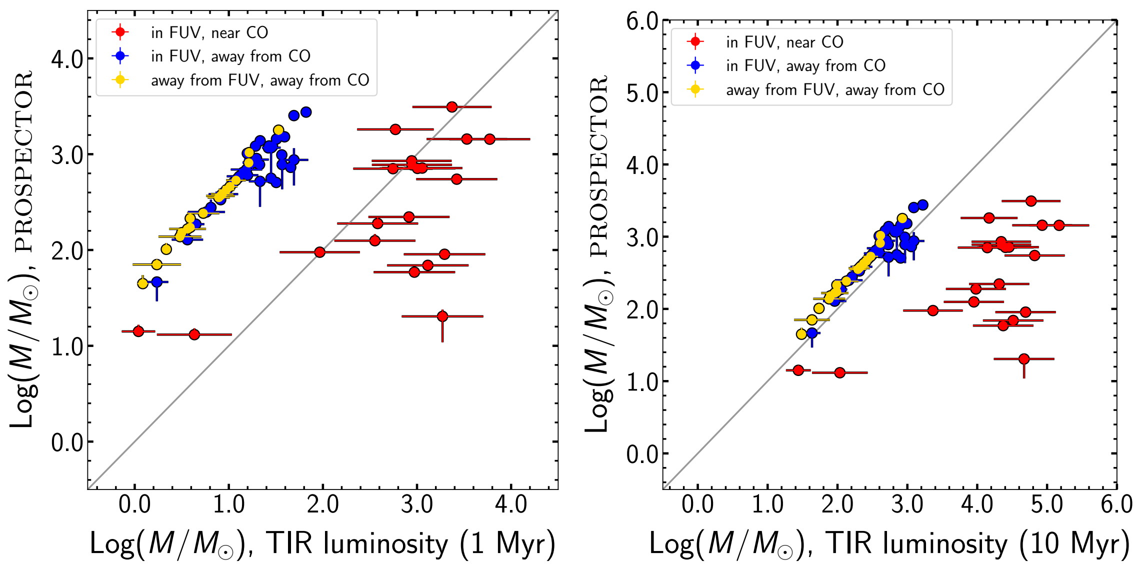

Figure 40. Comparison of object masses computed using PROSPECTOR versus the TIR luminosity for all three object types, where the TIR luminsoity method assumes an age of 1 Myr (left) or an age of 10 Myr (right). The gray line shows where the masses computed using both methods are the same.

four *JWST* filters (Johnson 2019). For each object we found the blackbody temperature corresponding to the F090W–F150W and F250M–F430M colors separately.

Assuming our objects are embedded star clusters, we found the luminosity of each object using the SEDs from Table 2 of Xu *et al.* (2001), which gives the flux density versus wavelength for six normal galaxies with 24 μm luminosities ranging from 10^7 to $10^{10.6}$ $L_\odot$, two AGNs with 24 μm luminosities of 10^8 $L_\odot$ and 10^{11} $L_\odot$, and eight starburst galaxies with 24 μm luminosities ranging from 10^7 to $10^{11.5}$ $L_\odot$. For the eight starburst galaxy luminosity bins, we integrated over both the entire SED and a subset of the SED the width of the four *JWST* bands, and found the ratio of the full SED to the JWST-width SED for each. We converted the summed flux of our objects in the four *JWST* filters to luminosity. We then took the average full SED-to-JWST SED ratio of the eight luminosity bins, which we found to be approximately 4, to convert the summed luminosities in the four *JWST* bands to total IR (TIR) luminosities. We

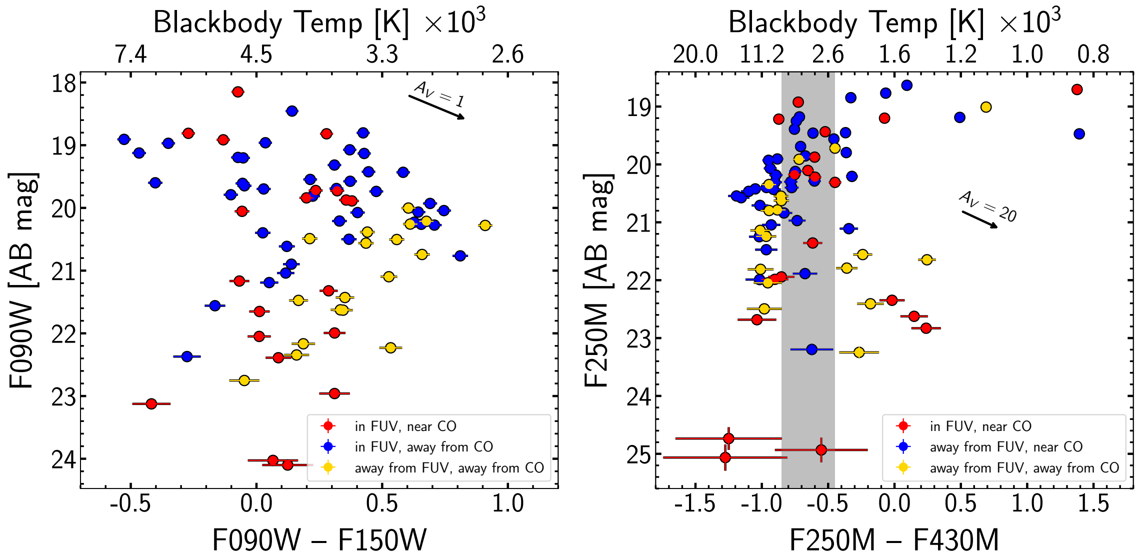

Figure 41. Left: F090W versus F090W–F150W CMD for all objects (red: in FUV knots and near CO, blue: in FUV knots and away from CO, and yellow: away from FUV knots and away from CO). The blackbody temperature corresponding to the F090W–F150W color is shown on the top x-axis, and the reddening vector $A_V = 1$ assuming SMC-like extinction is included in the upper right of the plot. Right: F250M versus F250M–F430M CMD for all objects. The blackbody temperature corresponding to the F250M–F430M color is shown on the top x-axis and the temperature range from the F090W versus F090W–F150W CMD is shaded in gray. The reddening vector $A_V = 20$ assuming SMC-like extinction is included in the upper right of the plot.

note that the higher metallicity of the Xu *et al.* (2001) galaxies compared to WLM may have an effect on the luminosities.

We then converted the TIR luminosities to total mass. Taking the bolometric magnitude of a young stellar population at less than 1 Myr age to be -2.69 for Small Magellanic Cloud (SMC) metallicity of 20% solar (Bruzual and Charlot 2003) and 4.74 mag as the bolometric magnitude of the Sun, the bolometric luminosity per solar mass of young stars is then $3.01 \times 10^{35} \times 10^{0.4 \times 2.69}$ (Elmegreen *et al.* 2018). We then took the TIR luminosity divided by this conversion for bolometric luminosity per solar mass of young stars at 1 Myr to get the mass of our objects.

We also computed the masses of our objects using the SED fitting toolbox PROSPEC-

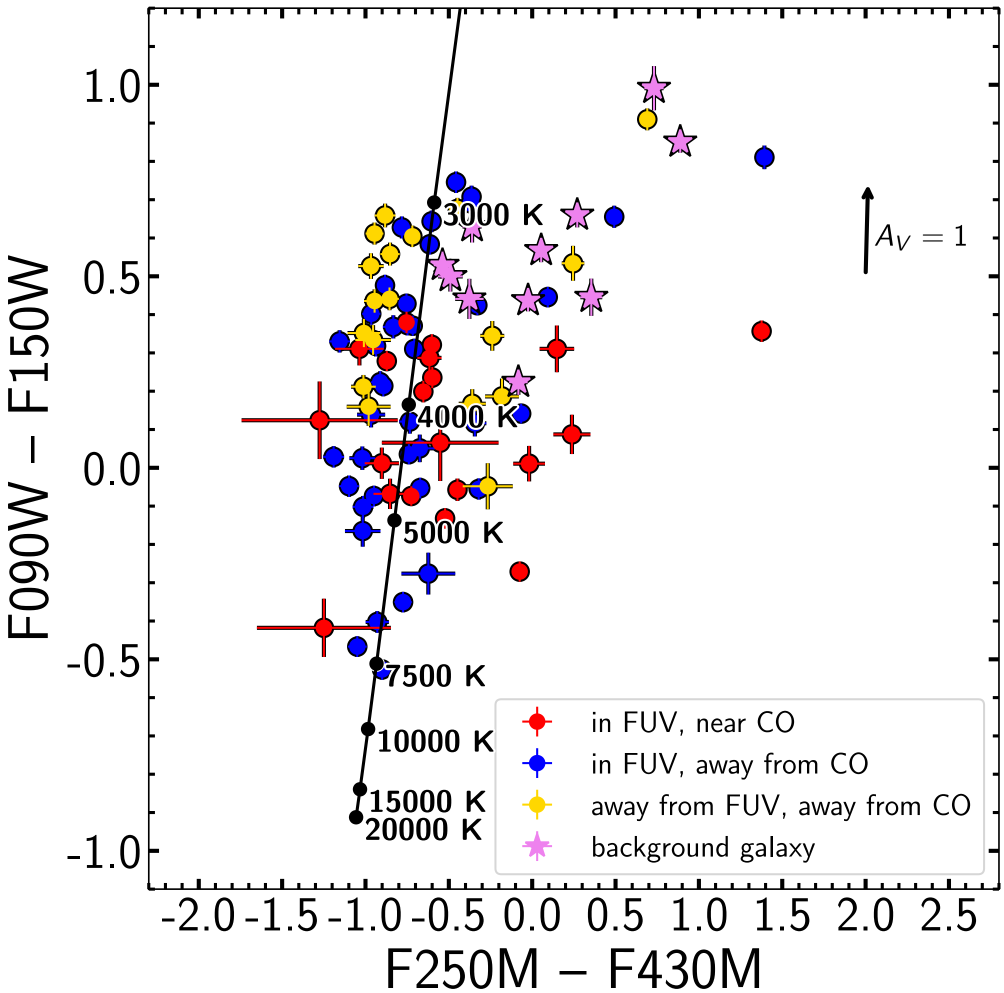

Figure 42. Color-color diagram of F090W–F150W versus F250M–F430M for all objects (red circles: in FUV knots and near CO, blue circles: in FUV knots and away from CO, and yellow circles: away from FUV knots and away from CO) including seven resolved background galaxies (light purple stars). A reddening vector of $A_V = 1$ assuming SMC-like extinction is included in the upper left of the plot, and the black line shows the effective temperature of a blackbody.

TOR (Leja *et al.* 2017; Johnson *et al.* 2021, 2022) for comparison with the masses derived from the TIR luminosities. We used dynamic nested sampling with the Python package DYNESTY (Conroy *et al.* 2009; Conroy and Gunn 2010; Speagle 2020; Koposov *et al.* 2022) assuming a single stellar population and fixed metallicity. The mass, diffuse dust V-band optical depth, and age were free parameters. We found that the optical depths and ages derived from this method were not reasonable for our objects, with most objects having ages in the highest age bin independent of the parameter priors used. As such, we opted to use the masses computed with the TIR method for this work. Comparing the masses between the two methods, we find that type 1 objects are similar between methods within the larger uncertainties of the TIR luminosity method, while object types 2 and 3 have systematically higher masses using PROSPECTOR by about 1.5 dex (Figure 40, top). One reason for this may be because the TIR method assumes an age of 1 Myr. One reason for this may be because the TIR method assumes an age of 1 Myr, which is reasonable for embedded star clusters. Increasing the age to 10 Myr, which changes the bolometric magnitude of the stellar population from -2.69 to +0.81, increases the mass of the object and brings the masses of object types 2 and 3 computed with the TIR luminosity method closer to those computed using PROSPECTOR (Figure 40, bottom).

3.3 Results

3.3.1 Color-Magnitude and Color-Color Diagrams

Figure 41 shows color-magnitude diagrams (CMDs) of the F090W versus F090W–F150W filters and F250M versus F250M–F430M filters for all objects. Many uncertainties are smaller than the size of the plot markers for both colors (<0.05), but we see that uncertainties in the color increase as objects get fainter (up to 0.10 for

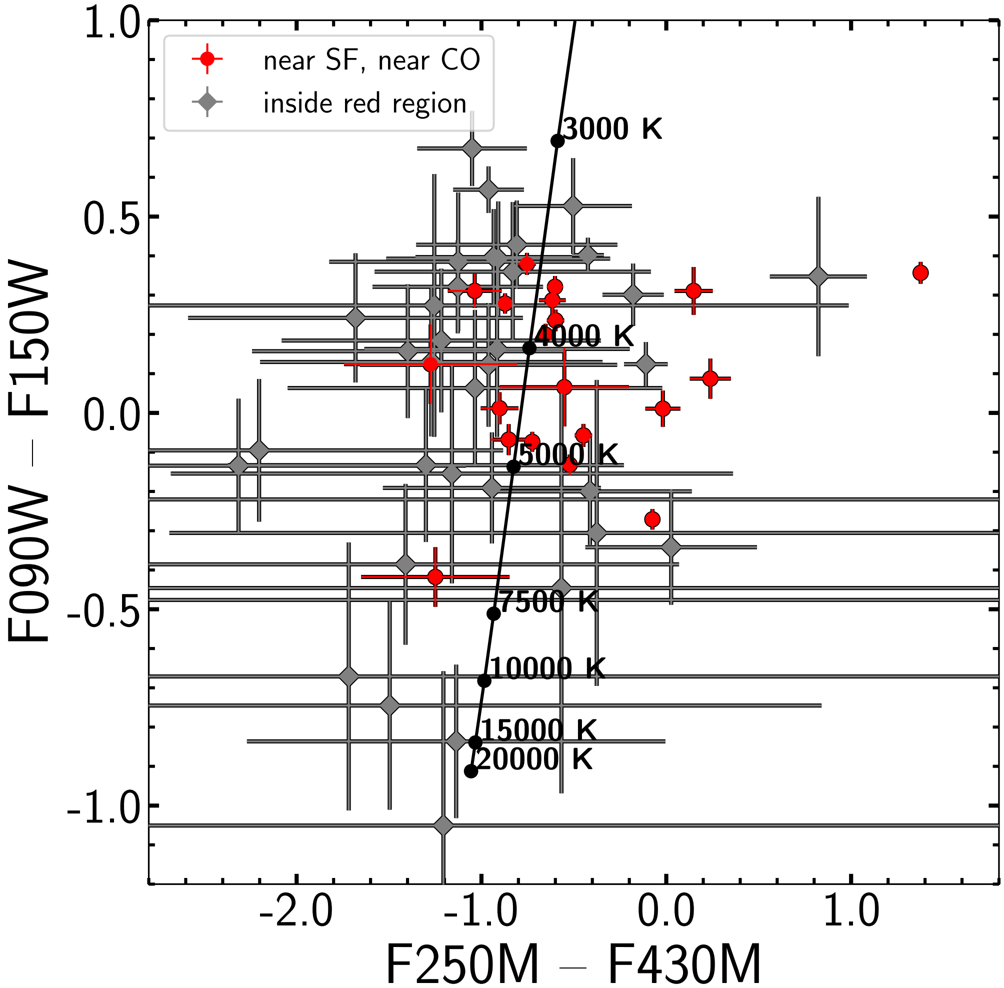

Figure 43. Color-color diagram of F090W–F150W versus F250M–F430M for type 1 objects (red circles) and resolved NIR sources within type 1 objects (gray diamonds). The black line corresponds to the effective temperature of a blackbody.

F090W–F150W and 0.47 for F250M–F430M). We include the blackbody temperatures corresponding to the color for the given filters on the opposing x-axis, with the temperature range from the F090W versus F090W–F150W CMD shown in gray on the F250M versus F250M–F430M CMD. Objects of all three types appear randomly distributed in the F090W versus F090W–F150W CMD, with the data centered around a color of 0.3. The data in the F250M versus F250M–F430M CMD appear clustered

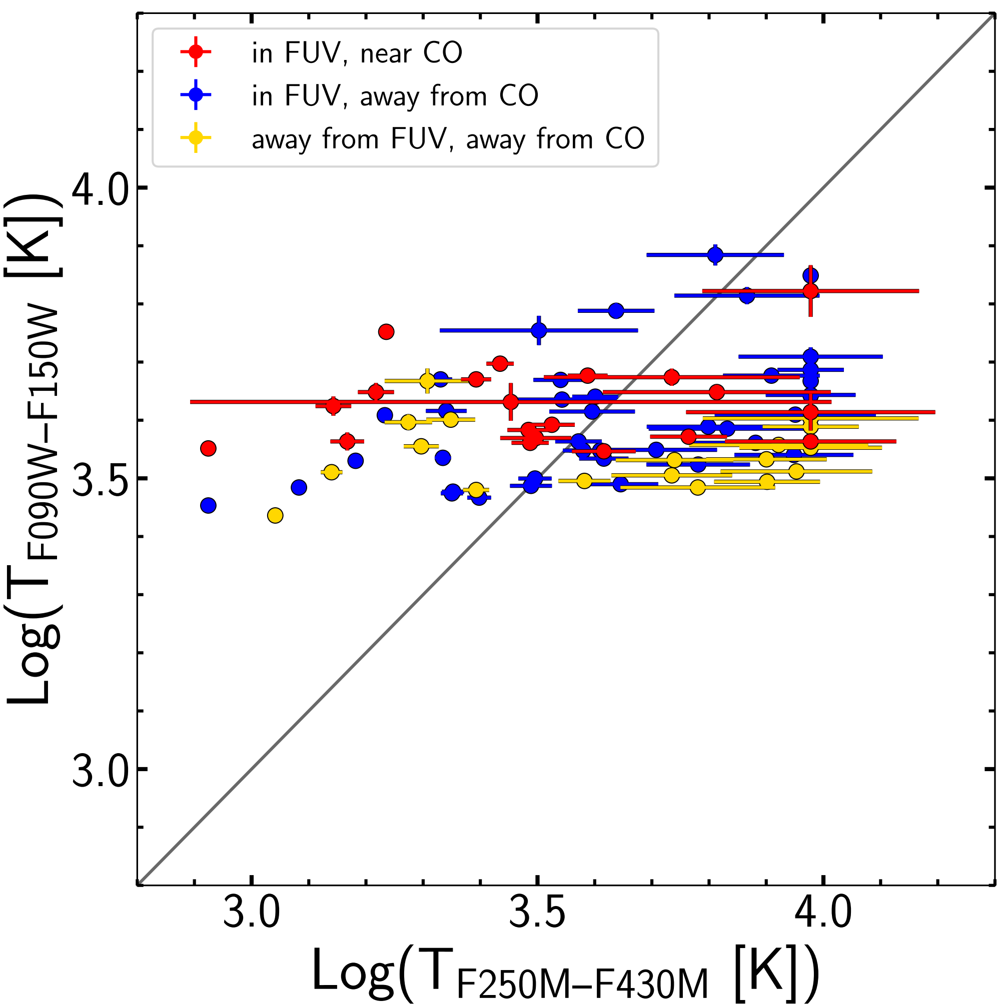

Figure 44. Log(temperature)-log(temperature) plot of F090W–F150W versus F250M–F430M for all objects (red: type 1 objects, blue: type 2 objects, and yellow: type 3 objects). The gray line shows where temperatures for both colors are the same to indicate how well the objects are represented by a blackbody. If our objects are embedded clusters, the infrared colors are affected by extinction and infrared excess of young stars and less sensitive to effective temperature, which may explain the larger F250M–F430M uncertainties at higher temperatures.

along a ridge from 23 to 18.5 in magnitude and -1.4 to 0 in color for objects of all three types, although several objects fall redward of this ridge.

Figure 42 shows a color-color diagram of F090W–F150W versus F250M–F430M for all objects, where many uncertainties are again smaller than the size of the plot

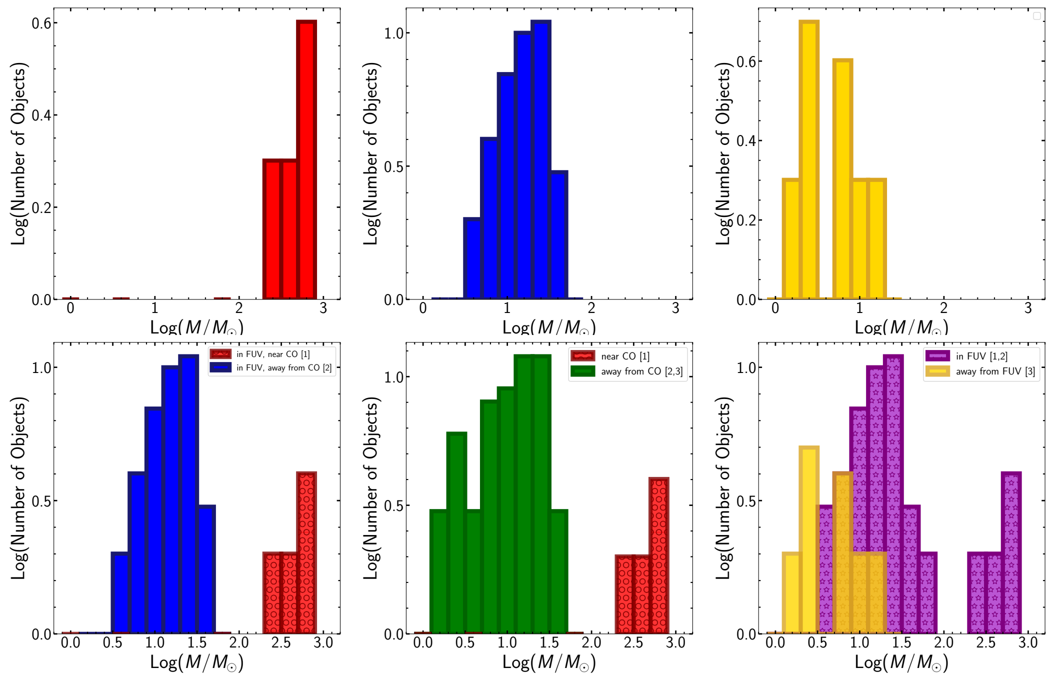

Figure 45. **Top:** *Left*- Mass distribution of type 1 objects (red). *Center*- Mass distribution of type 2 objects (blue). *Right*- Mass distribution of type 3 objects (yellow). **Bottom:** *Left*- Mass distribution comparing only objects in FUV knots – those near CO (red with circle hatches, type 1) and those away from CO (blue, type 2). *Center*- Mass distribution comparing objects near (red with circle hatches, type 1) and away from CO (green, types 2 and 3), independent of proximity to FUV. *Right*- Mass distribution comparing objects near (purple with star hatches, types 1 and 2) and away from (yellow, type 3) FUV, independent of proximity to CO. We note some bins contain one object and appear only as thicker lines at log(number of objects)=0. Mass is in units of $M_{\odot}$.

markers. A line indicating the effective temperature of a blackbody is overlaid on the plot. We find that most objects, regardless of their proximity to FUV or CO, are concentrated around the effective temperature line with blackbody temperatures between approximately 3000 to 7500 K, while some objects appear scattered to the right of the effective temperature line. We also include seven NIR sources that were obvious, resolved background galaxies (light purple stars in plot) to see if they displayed a preferential color, and find that they occupy a F090W–F150W color range

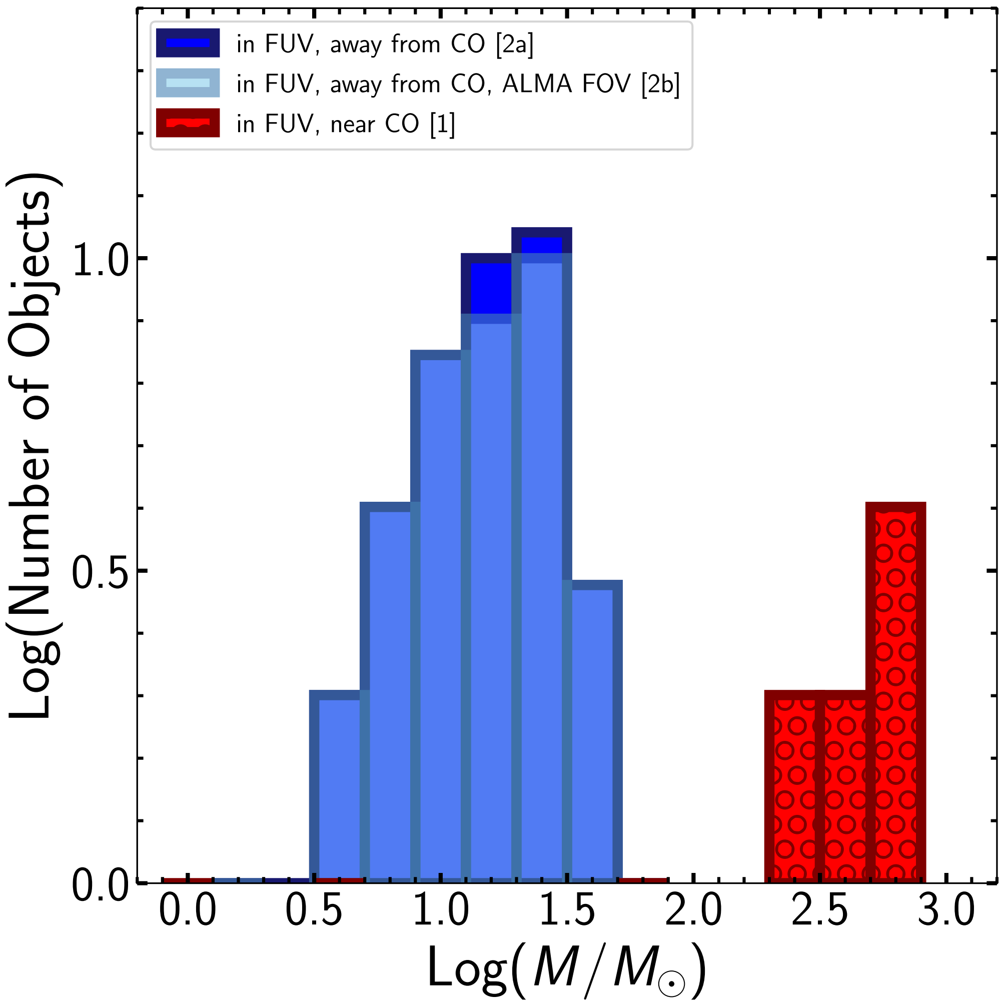

Figure 46. Mass histograms near star formation: type 1 (red with circle hatches) and a comparison of all type 2 objects (dark blue, 2a) to only type 2 objects in the ALMA FOV where CO was observed (light blue, 2b). Mass is in units of $M_\odot$.

from 0.2 to 1.0 and a F250M–F430M color range from -0.8 to 0.8. In Figure 43 we show a color-color diagram of F090W–F150W versus F250M–F430M for individual resolved NIR sources (gray) that comprise the type 1 objects (red) to compare the colors of the individual sources and larger clumps. We find that the larger uncertainties for the smaller sources place them in the same color ranges as the inclusive clumps.

We also show a log(temperature)-log(temperature) plot in Figure 44 of the effective temperatures corresponding to the F090W–F150W colors versus the effective temperatures corresponding to the F250M–F430M colors for all objects. If our objects were well represented by a black body, the best-match effective temperature would be the same for all colors, and the objects would fall along the gray diagonal line. We see that objects cover a much larger F250M–F430M effective temperature range compared to the F090W–F150W effective temperatures for all object types.

The table in Figure 36 contains the F090W and F250M AB magnitudes, along with the F090W–F150W and F250M–F430M colors and corresponding effective temperatures of type 1 objects. The same AB magnitudes, colors, and effective temperatures for objects of all three types are available in a table provided in the online materials. The RA, Dec, radius, F090W AB magnitude, F090W–F150W color, F250M AB magnitude, and F250M–F430M color of the background galaxies are listed in the table in Figure 39. Likewise, the RA, Dec, radius, F090W AB magnitude, F090W–F150W color, F250M AB magnitude, and F250M–F430M color for some of the individual sources inside type 1 objects we measured are listed in the table in Figure 38, with the full table of individual sources used in our sample included in a table in the online materials.

3.3.2 Mass

The top panel of Figure 45 shows histograms of the mass for each of the three object types. Type 1 objects range from approximately 1 to 5930 $M_{\odot}$ and span the largest range of masses of the three categories, with eight objects between 100 $M_{\odot}$ and 1000 $M_{\odot}$ and nine objects larger than 1000 $M_{\odot}$. Some of the mass bins contain one object and appear only as a thick line on the bottom x-axis at log(number of

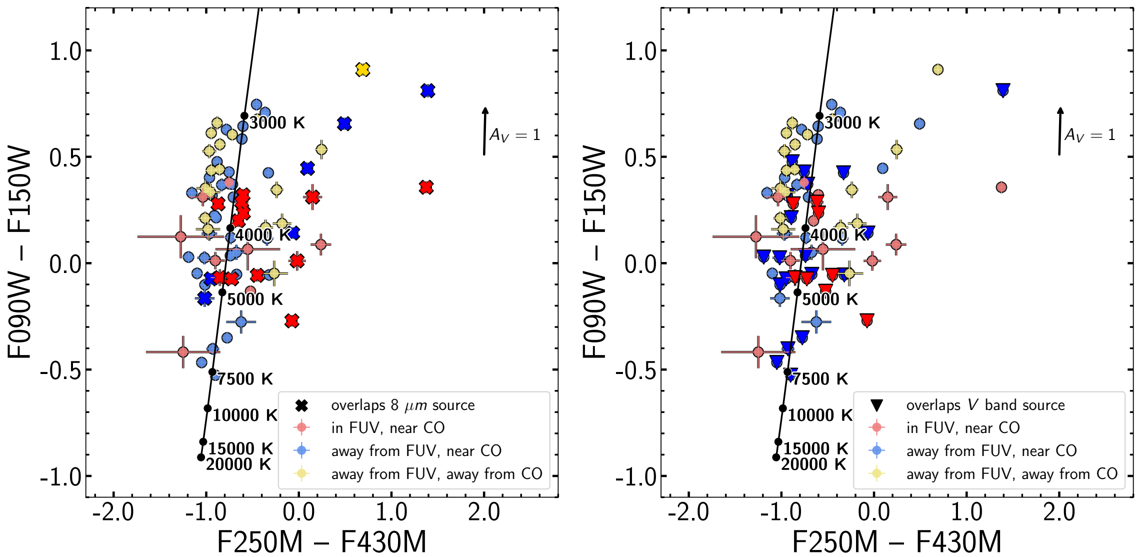

Figure 47. Color-color diagrams of F090W–F150W versus F250M–F430M for all objects (red circles: in FUV knots and near CO, blue circles: in FUV knots and away from CO, and yellow circles: away from FUV knots and away from CO). Objects that overlap 8μm sources are marked with a × instead of a circle (left), and objects that overlap V band sources are marked with a ∇ instead of a circle (right). A reddening vector of $A_V = 1$ assuming SMC-like extinction is included in the upper left of the plot, and the black line shows the effective temperature of a blackbody.

objects)=0. Type 2 objects comprise the largest number of objects and cover a range of masses approximately 1 to 66 $M_{\odot}$. Type 3 objects span the lowest range of masses from approximately 1 to 33 $M_{\odot}$. The masses of type 1 objects are listed in the table in Figure 36, and the masses of all objects are available in the table provided in the online materials.

The bottom panel of Figure 45 groups the objects differently to compare the mass. The histogram on the left compares only objects in FUV knots: type 1 (in FUV knots and near CO, red) and type 2 (in FUV knots and away from CO, blue). We see that objects near CO and FUV have higher masses than those in FUV and away from CO. The histogram in the center compares objects near and away from CO, independent of proximity to FUV. Object types 2 (blue) and 3 (yellow) are away from CO and combined into one category (green), while type 1 objects (red) are near CO and in their own category. We again see objects near CO have higher masses than those away from CO. The histogram on the right compares objects near and away from FUV knots, independent of proximity to CO. Here we combine objects 1 (red) and 2 (blue) into one category (purple) since they are both in FUV knots, while type 3 objects (yellow) are their own category. Objects away from FUV knots cover a smaller range of masses than those in FUV knots, but still appear to fall at the lower end of the mass range that objects in FUV knots span. We note that when the mass is measured using PROSPECTOR, the masses of all three types of objects cover the same mass range.

We also show histograms of type 1 objects, all type 2 objects, and only type 2 objects within the same area that CO was observed in Figure 46 to compare how the mass distributions are affected by the addition of type 2 objects that were not in the ALMA FOV and could contain CO that was not observed. We see that masses of type 2 objects appear to have similar distributions independent of whether the entire set or the ALMA FOV subset of type 2 objects are included.

3.4 Discussion

The effective temperatures from the F090W versus F090W–F150W CMD in Figure 41 match that of the color-color diagram in Figure 42, with most objects having effective temperatures ranging from ∼2600 K to 7400 K. However, the effective temperatures in the F250M versus F250M–F430M CMD cover a much wider range of <1000 K to 20000 K. We see in Figure 44 that the temperatures of our objects fall near the grey line delineating a perfect blackbody, albeit with large F250M–F430M uncertainties at temperatures above 3000 K. In the case that our objects are embedded clusters, the infrared colors of stars are considerably influenced by extinction and infrared excess associated with young stars, while not being inherently sensitive to effective temperature (Lada and Lada 2003). The small errors in the F250M–F430M color indicate that uncertainties in the color are not responsible for scatter of these objects, suggesting the scatter may be due to infrared excess. While we did not measure the extinction of our objects, we include reddening vectors assuming SMC-like extinction in the CMDs and color-color diagram (Figures 41 and 42) to indicate how our objects could be affected by extinction.

We examined our objects in a Spitzer Infrared Array Camera (IRAC) 8μm image of WLM and find several coincident with sources bright at 8μm, suggesting the regions are dominated by hot dust. We also examined our objects in a V band image of WLM from observations taken with the Lowell Observatory Hall 1.07-m Telescope (Hunter and Elmegreen 2006) and also find several coincident with sources bright in V. We cannot reliably measure the brightness of the objects in either the 8μm or V images due to the difference in angular resolution of 1.2$''$ in 8μm and 1.1$''$ in V compared to 0.063$''$ in F250M. However, we show in Figure 47 the F090W–F150W versus F250M–F430M color-color diagrams for the objects of all three types, this time noting which objects overlap the 8μm sources (top, marked with a $\times$) and V sources (bottom, marked with a ∇). We see most objects that overlap 8μm sources are also redward of the effective temperature line in F250M–F430M, which we would expect for clusters embedded in hot dust. Similarly, most objects that overlap V sources are along the effective temperature line, which we would expect from the photospheres of stars. For type 1 objects, 60% overlap 8μm sources and 40% overlap V sources, with 39% of the objects overlapping both. For type 2 objects, 15% overlap 8μm sources and

48% overlap V sources, with 11% of the objects overlapping both. For type 3 objects, 5% overlap 8μm sources and 0% overlap V sources, thus 0% of the objects overlapping both. The higher percentage of type 1 and 2 objects overlapping V sources than type 3 objects is expected due to type 1 and 2 objects being near FUV sources.

The difference in objects overlapping 8μm sources between types 1 and 2 may be the result of differing stages of star formation. We focused on a prominent FUV-bright region which we show in the top panel Figure 48. Archer *et al.* (2022b) also examined this region and estimated the age to be approximately 7 Myr. Jones *et al.* (2023) found hundreds of young stellar objects (YSOs) and pre-main sequence stars in NGC 346, a young star cluster in the SMC with an age of $\sim$3 Myr, so we do not expect the age of the FUV region to preclude younger embedded star formation. The Spitzer 8μm image of this region is shown in the bottom panel of Figure 48 with the CO cores, type 1 objects, and type 2 objects overlaid. We see that most type 1 objects appear to be associated with sources bright at 8μm, while no type 2 sources appear coincident with the 8μm sources. A possible explanation for this is that the type 1 objects are still embedded, while type 2 objects have already cleared their dust envelopes. This could also explain the comparable masses of type 1 objects between the PROSPECTOR and TIR luminosity methods when the TIR luminosity method assumes an age of 1 Myr, while the type 2 and type 3 objects have comparable masses between the two methods when the TIR luminosity method assumes an age of 10 Myr (Figure 40). However, we cannot be certain without accurate age estimates for the objects.

Embedded star clusters are associated with the most massive molecular cores in GMCs, with CO clump masses ranging from approximately 10^2 to 10^4 $M_\odot$ in the Milky Way and Large Magellanic Cloud (LMC) (Carpenter *et al.* 1995; Phelps and

Lada 1997; Nayak *et al.* 2016, 2018) and 10^2 to 10^5 in the SMC (Saldaño *et al.* 2023). A catalog of embedded star clusters within 2 kpc of the Sun compiled by Lada and Lada (2003) finds that the cluster masses range from approximately 10^1 to 10^4 $M_\odot$, and Elmegreen and Elmegreen (2019) find 8μm cores in dusty spirals on the order of 10^2 to 10^4 $M_\odot$. In the top panel of Figure 49, we find that the masses of our CO cores are comparable to the masses of CO clumps where embedded star clusters are found in the Milky Way, SMC, and LMC. Our objects associated with CO (type 1) have masses up to >5000 $M_\odot$, while embedded star clusters from Lada and Lada (2003) and Elmegreen and Elmegreen (2019) have higher upper mass limits. Figure 45 shows that type 1 objects do not appear to be sampled to the upper mass limit, so we cannot say whether the lower masses of our objects are the result of some physical constraint. However, the size of our objects, which have radii between 2 and 21 pc (Figure 49, bottom panel), are larger than the <2 pc radii embedded clusters from Lada and Lada (2003) and smaller on average than the ~25 pc radii 8μm cores in local spirals from Elmegreen *et al.* (2018). This may be a result of our grouping individual IR sources into larger objects compared to those in Lada and Lada (2003) while the resolution of the NIRCam images in this work are much higher than the IRAC images used in Elmegreen *et al.* (2018).

In the top panel of Figure 49, we also include lines delineating where the ratio of the type 1 object mass to CO core mass is 0.1%, 1%, and 10%. One possibility for objects in the 10% range is that the molecular gas has already been destroyed and the objects left behind are bound clusters. However, H_2 can be self-shielded from the photodissociation that results in the smaller CO cores seen in low-metallicity galaxies, leaving the cores surrounded by a potentially large reservoir of CO-dark H_2 gas (e.g. Wolfire *et al.* 2010; Planck Collaboration *et al.* 2011; Pineda *et al.* 2014; Cormier *et al.*

2017; Madden *et al.* 2020). If there is CO-dark H_2 gas present, then the ratios of type 1 object mass to molecular gas mass would be lower.

3.5 Summary and Conclusions

In this work we present an analysis of the relationship between CO and early star-forming regions seen as embedded IR sources in the low metallicity dIrr galaxy WLM. We use ALMA-detected CO data from Rubio *et al.* (2015) and Rubio et al. (in preparation), *GALEX* FUV data from Zhang *et al.* (2012), and *JWST* NIRCam data from Weisz *et al.* (2023). The IR sensitivity and high angular and spatial resolution of *JWST* allow us to probe embedded, early star-forming regions in WLM at an unprecedented depth and in regions of higher extinction.

We compare and contrast objects that are: near FUV knots and near CO (**type 1**), in FUV knots and away from CO (**type 2**), and away from FUV knots and away from CO (**type 3**) to identify whether the early star-forming regions have similar physical properties in different local environments and analyze the relationship between early star formation and CO in low metallicity environments. The objects in this work are clumps of NIR sources. A test analysis of the individual NIR sources inside a subset of our type 1 objects finds that the colors of the smaller individual sources and larger objects are consistent within the uncertainties.

We find that objects of all three types have comparable NIR colors and magnitudes. Likewise, the three object types also cover the same effective temperature range, although the infrared colors of young star-forming regions do not exhibit high sensitivity to effective temperature and are notably impacted by extinction and infrared excess. Type 1 objects appear to have higher masses than the other two object types when computed using the TIR luminosity. However, when the masses are measured using PROSPECTOR, all object types cover the same mass range.

We find IR sources associated with CO cores throughout WLM (type 1 objects). The masses of our objects associated with the CO, along with the masses of their corresponding CO cores, are in agreement with the masses of embedded clusters and their CO cores found elsewhere in the SMC, LMC, Milky Way, and other spirals. However, the sizes of our objects are larger than embedded clusters from Lada and Lada (2003) and smaller than those from Elmegreen *et al.* (2018). A possible explanation for this is that our objects are clumps of IR sources compared to individual sources in Lada and Lada (2003), while our *JWST* NIRCam images have a much higher resolution than the Spitzer IRAC images used in Elmegreen *et al.* (2018). Our type 1 objects also appear to coincide with bright 8μm sources at a higher frequency than the other two object types, which suggests young embedded star formation in these CO cores. These type 1 objects may be at an earlier evolutionary stage than the other object types, but we cannot confirm this without accurate age estimates.

3.6 Acknowledgements

This material is based upon work supported by the National Science Foundation under Grant AST-1907492 to D.A.H.

M.R. wishes to acknowledge support from ANID(CHILE) through Basal FB210003 and FONDECYT grant No1190684.

This paper makes use of the following ALMA data: ADS/JAO.ALMA#2012.1.00208.S and ADS/JAO.ALMA#2018.1.00337.S. ALMA is a partnership of ESO (representing its member states), NSF (USA) and NINS (Japan), together with NRC (Canada), MOST and ASIAA (Taiwan), and KASI (Republic of Korea), in cooperation with the Republic of Chile. The Joint ALMA Observatory is operated by ESO, AUI/NRAO and NAOJ. The National Radio Astronomy Observatory is a facility of the National Science Foundation operated under cooperative agreement by Associated Universities, Inc.

We would like to thank the referee for carefully reading our manuscript and for providing constructive comments which greatly enhanced the quality and clarity of this manuscript.

Lowell Observatory sits at the base of mountains sacred to tribes throughout the region. We honor their past, present, and future generations, who have lived here for millennia and will forever call this place home.

*Facilities:*ALMA, JWST(NIRCam)

*Software:*IRAF (Tody 1986), SEDpy (Johnson 2019), prospector (Leja *et al.* 2017; Johnson *et al.* 2021, 2022), dynesty (Conroy *et al.* 2009; Conroy and Gunn 2010; Speagle 2020; Koposov *et al.* 2022)

3.7 APPENDIX

Postage stamps showing the *JWST* three-color image of each individual object. Type 1 objects and their CO cores are shown in Figure 50, type 2 objects in Figure 51, type 3 objects in Figure 52, and select resolved background galaxies used in this work in Figure 53.

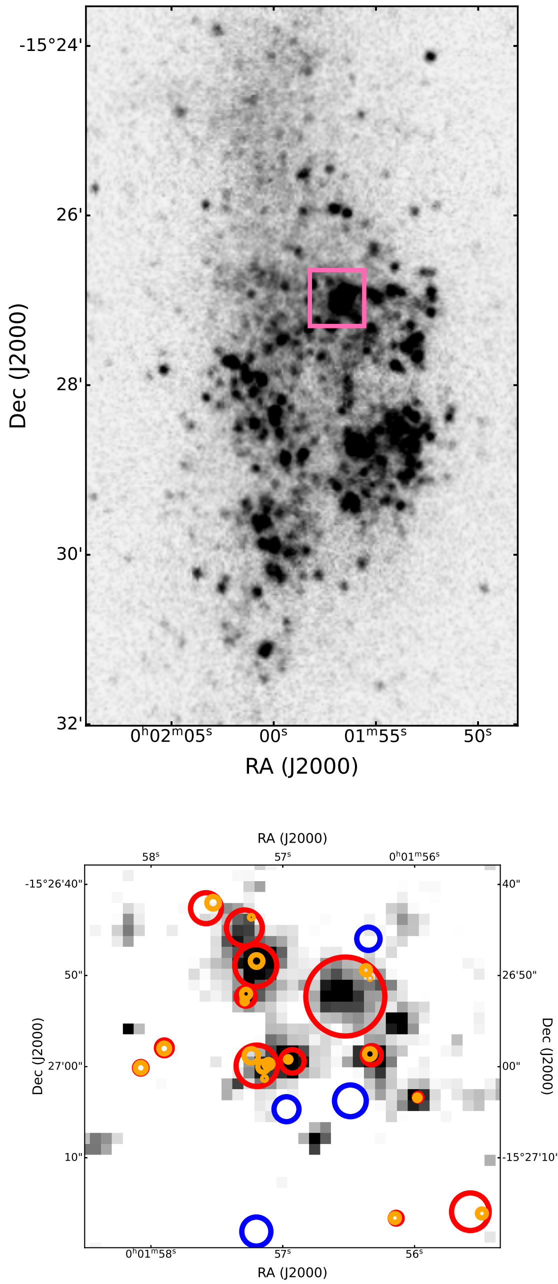

Figure 48. Top: *GALEX* FUV image of WLM showing FUV-bright star-forming region (pink box). Bottom: Close-up of the FUV-bright star-forming region in Spitzer 8μm showing that type 1 objects (red circles) are typically associated with 8μm sources while most type 2 objects (blue circles) do not overlap 8μm sources. The CO cores within the type 1 objects are also included (orange circles).

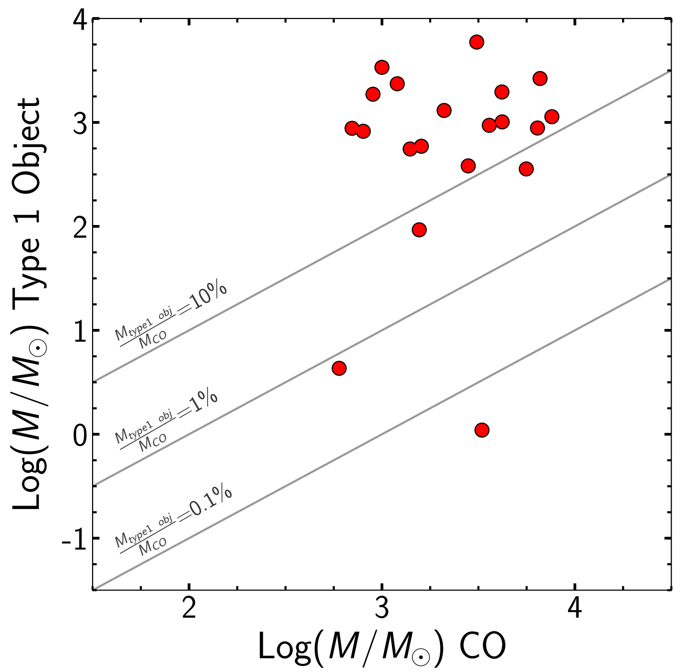

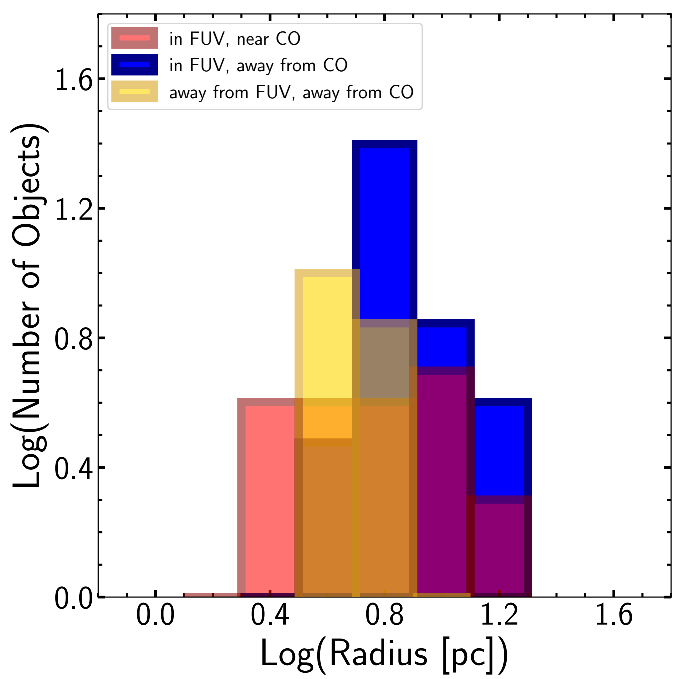

Figure 49. Top: Mass of type 1 objects versus the mass of the CO core that the object is associated with. Bottom: Histogram of object radii in pc for each of the three objects types.

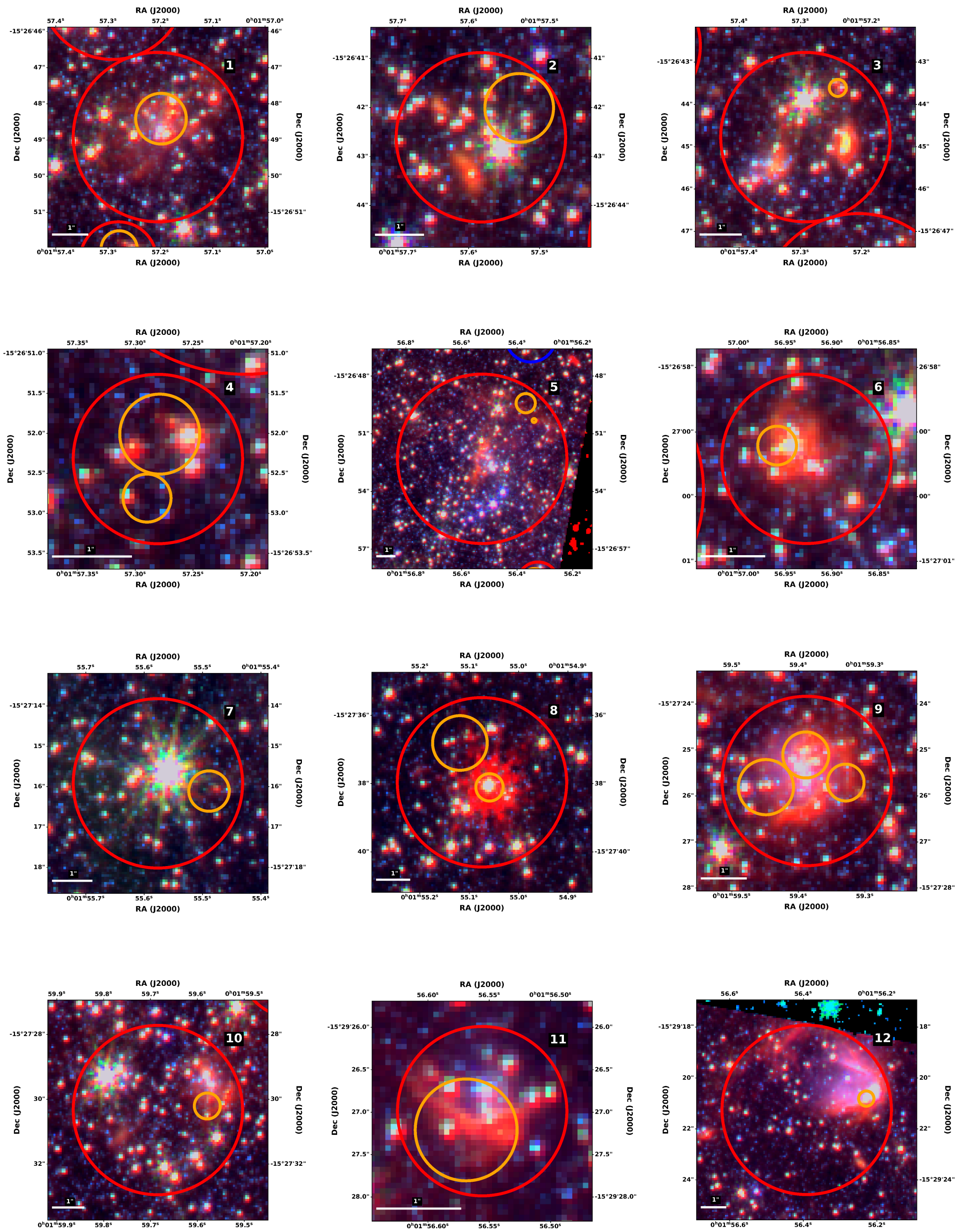

Figure 50. F250M (red), F150W (green), F090W (blue) three-color image of each type 1 object (in FUV and near CO, red circles) and the CO cores (orange circles) within them. The orientation of the image is such that North is up and East is to the left. The object number corresponding to the number in the table in Figure 36 is given in the upper right of the image.

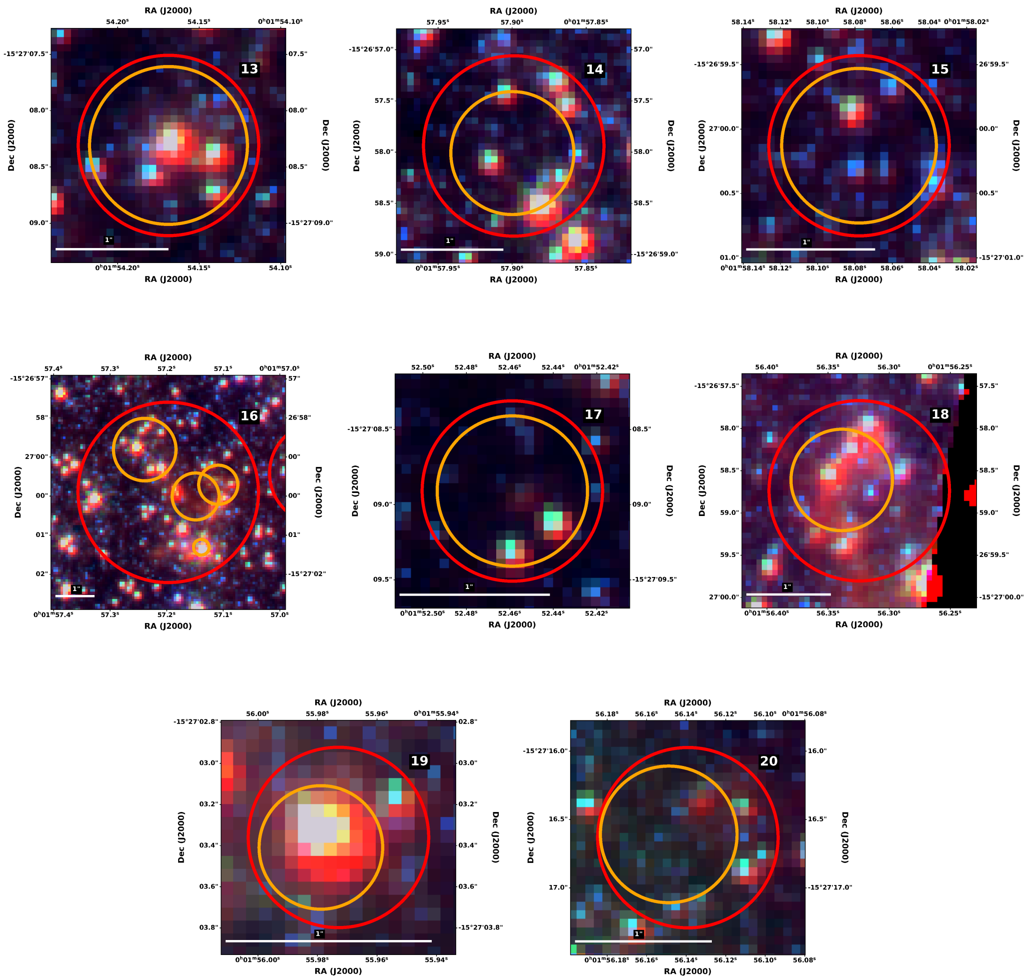

Figure 50. **cont.** F250M (red), F150W (green), F090W (blue) three-color image of each type 1 object (in FUV and near CO, red circles) and the CO cores (orange circles) within them. The orientation of the image is such that North is up and East is to the left. The object number corresponding to the number in the table in Figure 36 is given in the upper right of the image.

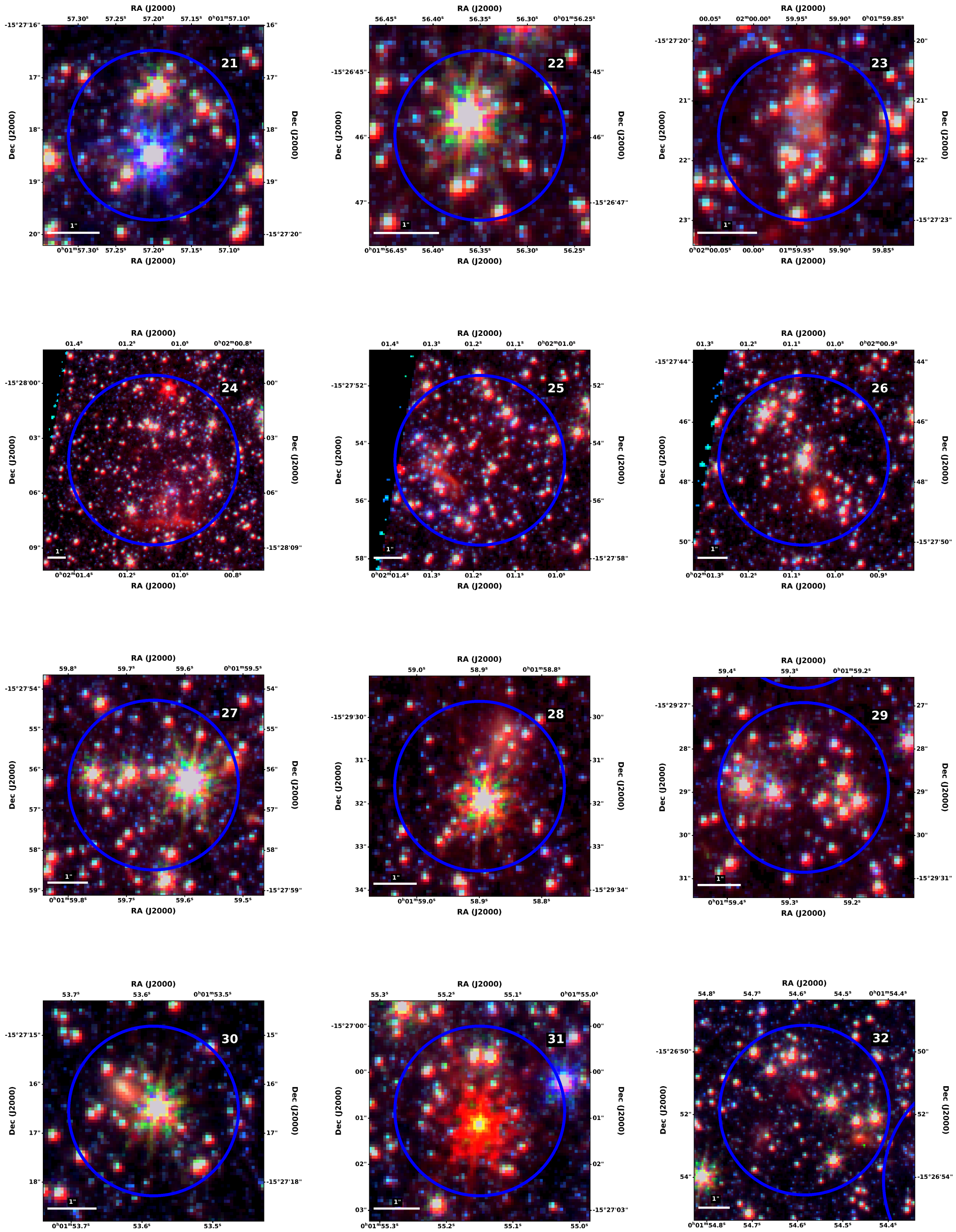

Figure 51. F250M (red), F150W (green), F090W (blue) three-color image of each type 2 object (in FUV and away from CO, blue circles). The orientation of the image is such that North is up and East is to the left. The object number corresponding to the number in the extended version of the table in Figure 36 provided in the online materials is given in the upper right of the image.

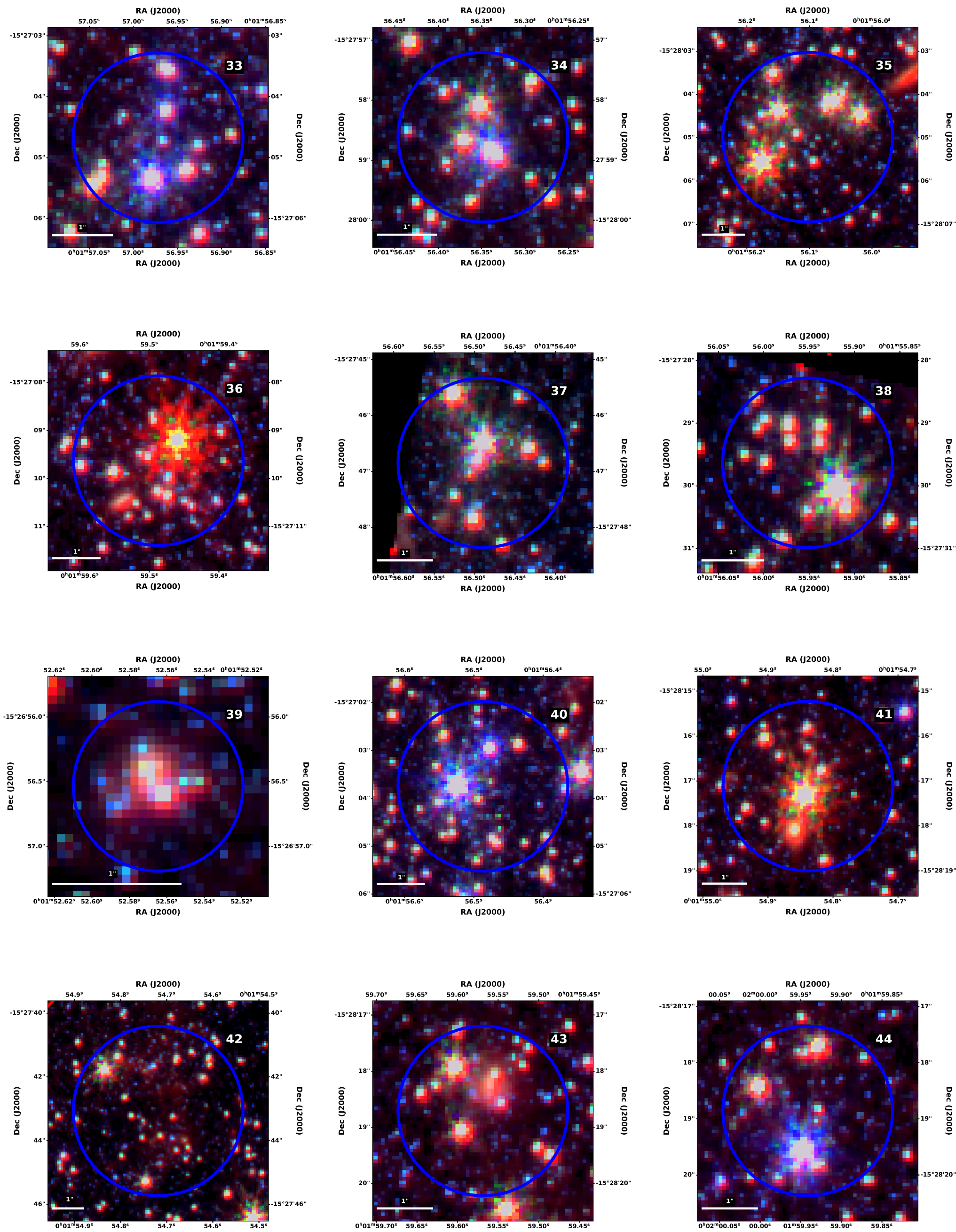

Figure 51. **cont.** F250M (red), F150W (green), F090W (blue) three-color image of each type 2 object (in FUV and away from CO, blue circles). The orientation of the image is such that North is up and East is to the left. The object number corresponding to the number in the extended version of the table in Figure 36 provided in the online materials is given in the upper right of the image.

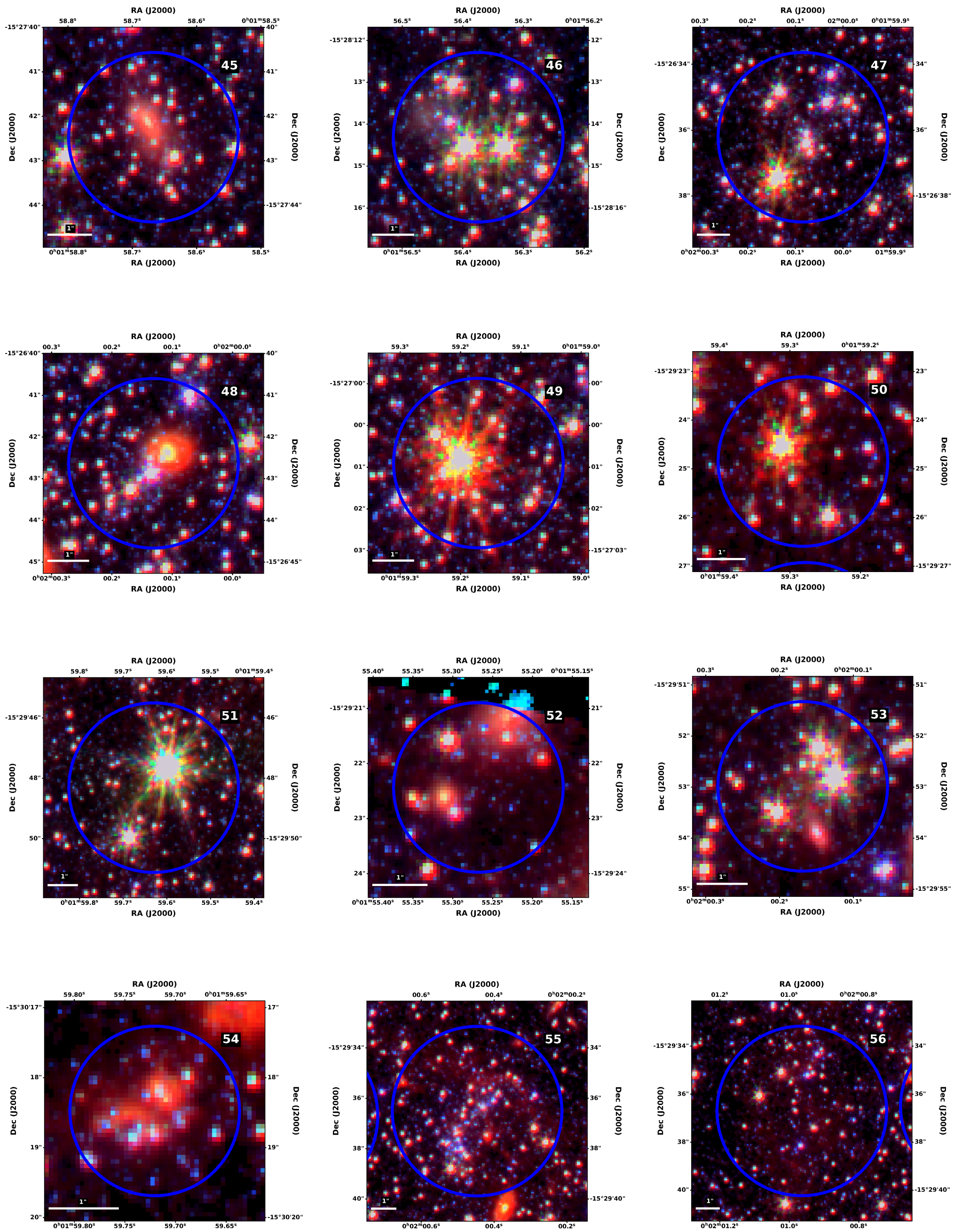

Figure 51. **cont.** F250M (red), F150W (green), F090W (blue) three-color image of each type 2 object (in FUV and away from CO, blue circles). The orientation of the image is such that North is up and East is to the left. The object number corresponding to the number in the extended version of the table in Figure 36 provided in the online materials is given in the upper right of the image.

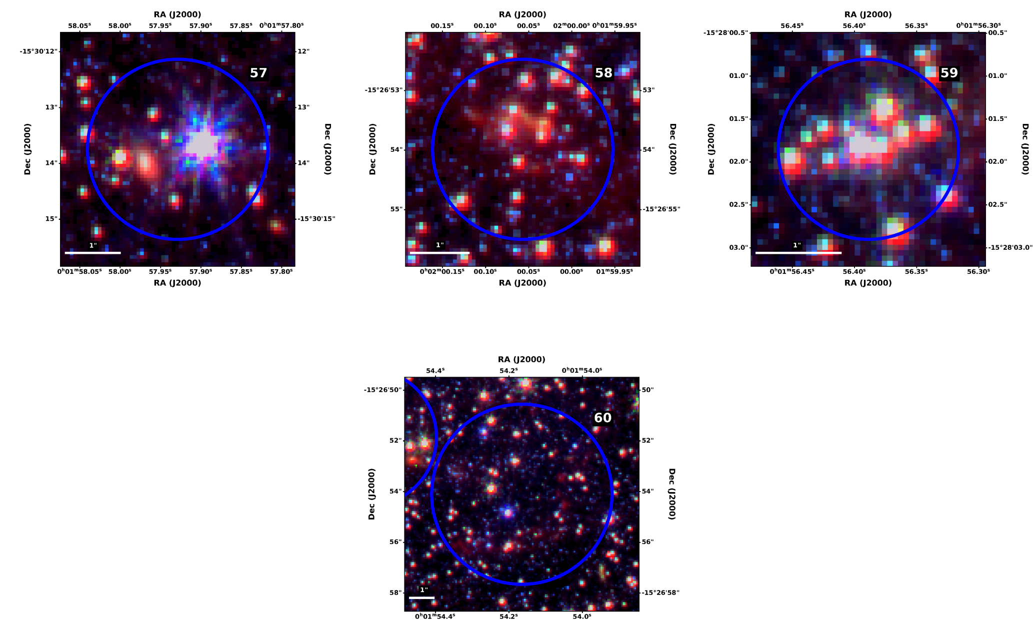

Figure 51. **cont.** F250M (red), F150W (green), F090W (blue) three-color image of each type 2 object (in FUV and away from CO, blue circles). The orientation of the image is such that North is up and East is to the left. The object number corresponding to the number in the extended version of the table in Figure 36 provided in the online materials is given in the upper right of the image.

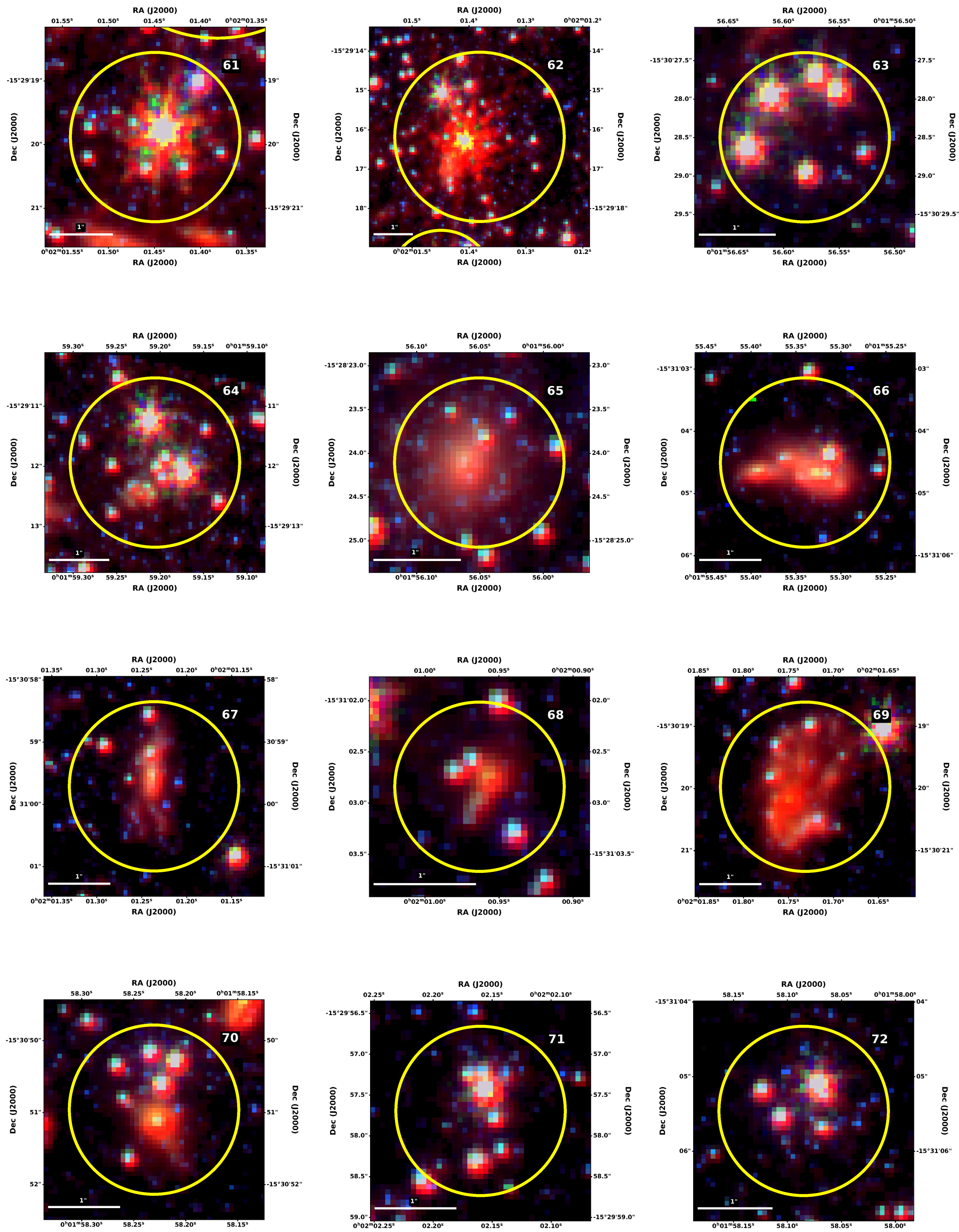

Figure 52. F250M (red), F150W (green), F090W (blue) three-color image of each type 3 object (away from FUV and away from CO, yellow circles). The orientation of the image is such that North is up and East is to the left. The object number corresponding to the number in the extended version of the table in Figure 36 provided in the online materials is given in the upper right of the image.

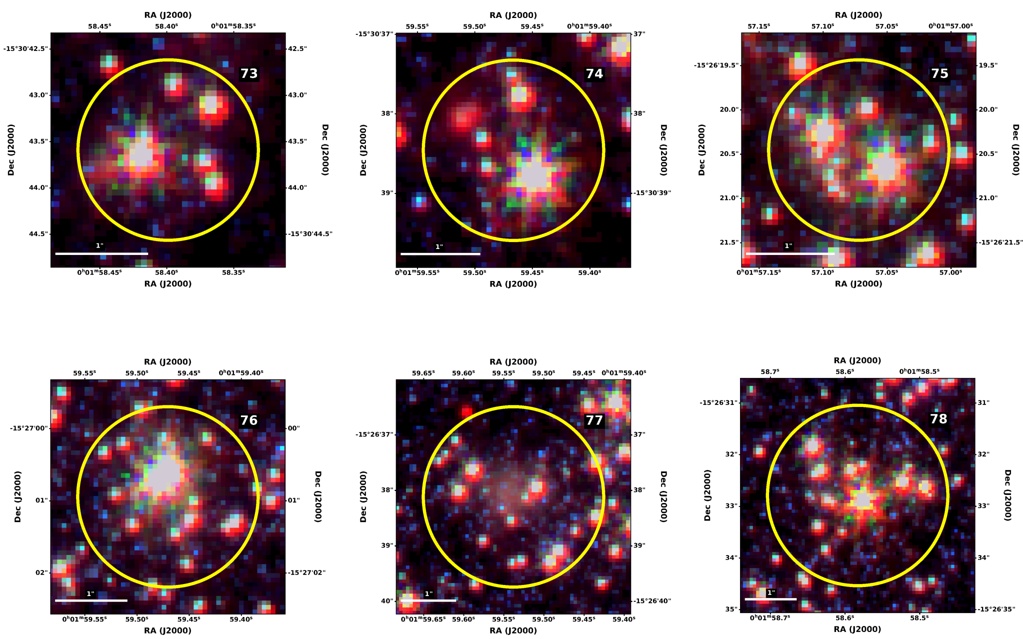

Figure 52. **cont.** F250M (red), F150W (green), F090W (blue) three-color image of each type 3 object (away from FUV and away from CO, yellow circles). The orientation of the image is such that North is up and East is to the left. The object number corresponding to the number in the extended version of the table in Figure 36 provided in the online materials is given in the upper right of the image.

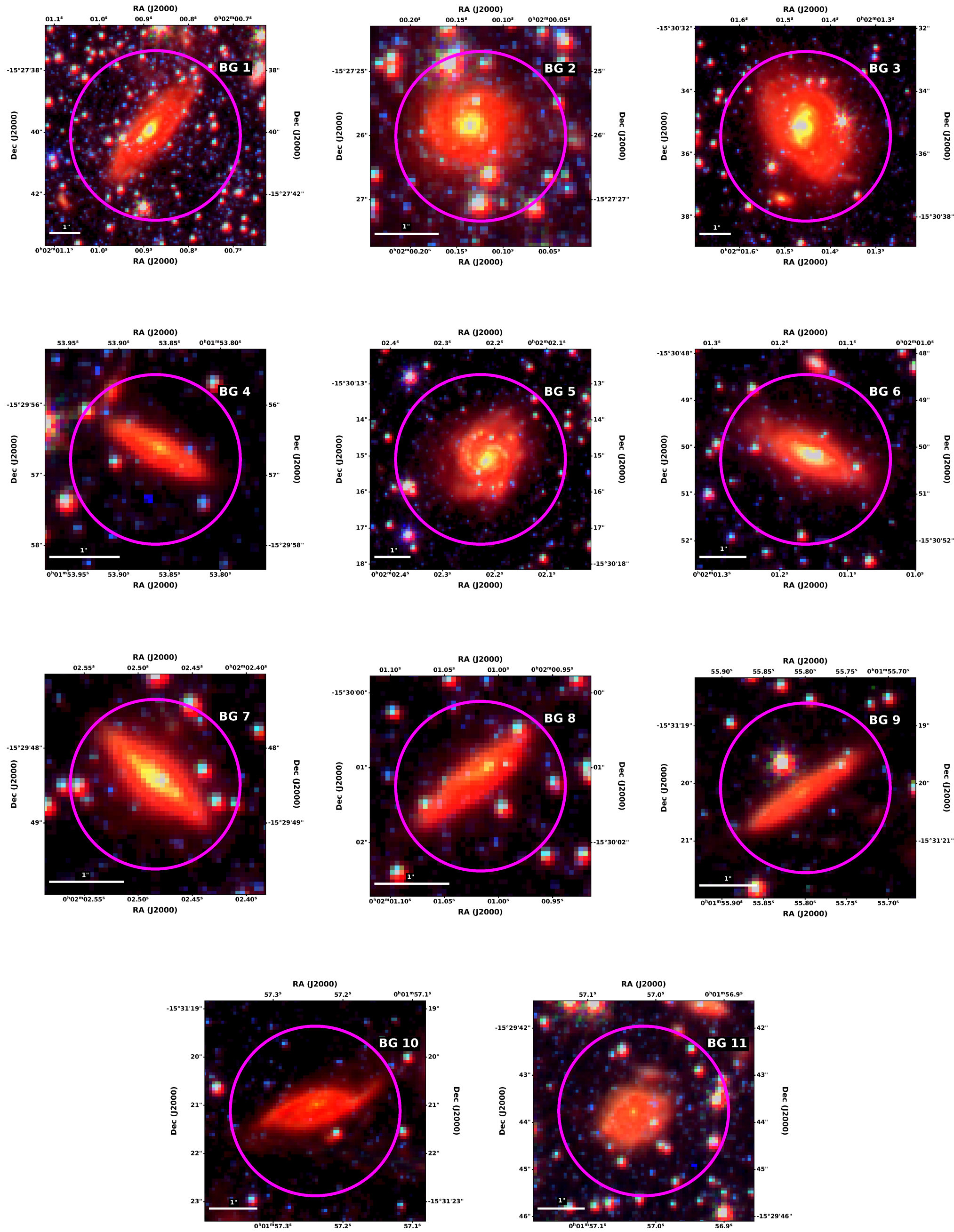

Figure 53. F250M (red), F150W (green), F090W (blue) three-color image of select obvious background galaxies (magenta circles). The orientation of the image is such that North is up and East is to the left. The object number corresponding to the number in the extended version of the table in Figure 36 provided in the online materials is given in the upper right of the image.

Chapter 4

STELLAR POPULATIONS AND MOLECULAR GAS COMPOSITION IN THE LOW-METALLICITY ENVIRONMENT OF WLM

[1,2]Haylee N. Archer, [2]Deidre A. Hunter, [3]Bruce G. Elmegreen, [4]Leslie K. Hunt, [1]Rosalia O'Brien, [5]Elias Brinks, [6]Phil Cigan, [7]Monica Rubio, [1]Rogier A. Windorst, [1]Rolf A. Jansen, [8,9,10]Elija P. Mathews

[1]School of Earth and Space Exploration, Arizona State University, Tempe, AZ, USA

[2]Lowell Observatory, Flagstaff, AZ, USA

[3]IBM T. J. Watson Research Center, Yorktown Heights, NY, USA

[4]INAF, Osservatorio Astrofisico di Arcetri, Firenze, Italy

[5]Centre for Astrophysics Research, University of Hertfordshire, Hatfield, UK

[6]United States Naval Observatory, Washington, DC, USA

[7]Departamento de Astronomía, Universidad de Chile, Santiago, Chile

[8]Department of Astronomy & Astrophysics, The Pennsylvania State University, University Park, PA, USA

[9]Institute for Computation & Data Sciences, The Pennsylvania State University, University Park, PA, USA

[10]Institute for Gravitation and the Cosmos, The Pennsylvania State University, University Park, PA, USA

In press in the Astronomical Journal

Abstract: We investigate the stellar populations and molecular gas properties of a star-forming region within the dwarf irregular (dIrr) galaxy WLM. Low-metallicity dIrrs like WLM offer a valuable window into star formation in environments that are unlike those of larger, metal-rich galaxies such as the Milky Way. In these conditions, carbon monoxide (CO), typically used to trace molecular clouds, is more easily photodissociated by ultraviolet (UV) radiation, leading to a larger fraction of CO-dark molecular gas, where H_2 exists without detectable CO emission, or CO-dark gas in the form of cold H I. Understanding the molecular gas content and the stellar populations in these star-forming regions provides important information about the role of CO-bright and CO-dark gas in forming stars.

4.1 Introduction

The study of star formation in low-metallicity dwarf galaxies provides valuable insights into the star-forming environments of the most numerous galaxy type in the universe. Wolf–Lundmark–Melotte (WLM) is a Local Group dwarf irregular (dIrr) galaxy located at a distance of approximately 980 kiloparsecs (kpc, Leaman *et al.* 2012; Albers *et al.* 2019; Lee *et al.* 2021; Newman *et al.* 2024). With a total stellar mass of 1.62×10^7 $M_\odot$ (Zhang *et al.* 2012) and a metallicity of 12 + log(O/H) = 7.8 (13% $Z_\odot$, Lee *et al.* 2005), WLM is characterized by low mass and low metallicity. The galaxy's isolation, with large separations from both the Milky Way and M31, implies a low likelihood of past interactions with these systems (Teyssier *et al.* 2012; Albers *et al.* 2019). This combination of low mass, low metallicity, distance, and isolation makes WLM an ideal laboratory for studying star formation in undisturbed dwarf galaxies, providing insight into star-forming processes in a metal-poor environment.

Metallicity plays a critical role in star formation processes, as metals enhance gas cooling and help shield molecular gas from dissociating radiation (e.g., Draine and Li 2007; Fukui and Kawamura 2010; Wakelam *et al.* 2017b; Osman *et al.* 2020). In low-metallicity environments, like those found in dwarf galaxies, the reduced metal content limits gas cooling efficiency and molecular cloud shielding, which can impact star formation rates, the initial mass function (IMF), and feedback mechanisms from young stars (e.g., Elmegreen 1989; Brosch *et al.* 1998; Hunter *et al.* 1998; Leroy *et al.* 2008; Chevance *et al.* 2020a; Hunter *et al.* 2024). These conditions may lead to different star formation dynamics, where molecular gas cooling, cloud collapse, and star formation proceed less efficiently compared to metal-rich environments.

One of the main challenges in studying molecular gas in low-metallicity environments is the detection of molecular hydrogen (H_2), the primary fuel for star formation. Unlike in higher-metallicity galaxies, where carbon monoxide (CO) serves as a reliable tracer for H_2, low-metallicity systems exhibit lower CO abundances due to a lack of shielding against photodissociating ultraviolet (UV) radiation (Elmegreen *et al.* 1980; Elmegreen 1989; Taylor *et al.* 1998). This results in a large fraction of CO-dark molecular gas, where H_2 is present without detectable CO emission (Wolfire *et al.* 2010). Consequently, accurate assessment of molecular gas content in these environments requires alternative approaches, such as dust-based methods or [C II] emission, to account for the significant CO-dark gas component (Planck Collaboration *et al.* 2011; Pineda *et al.* 2014; Cormier *et al.* 2017; Hunt *et al.* 2023).

This CO-dark gas may contribute extensively to the star-forming material, even though it is invisible in traditional CO surveys (Madden *et al.* 2020; Madden 2022).

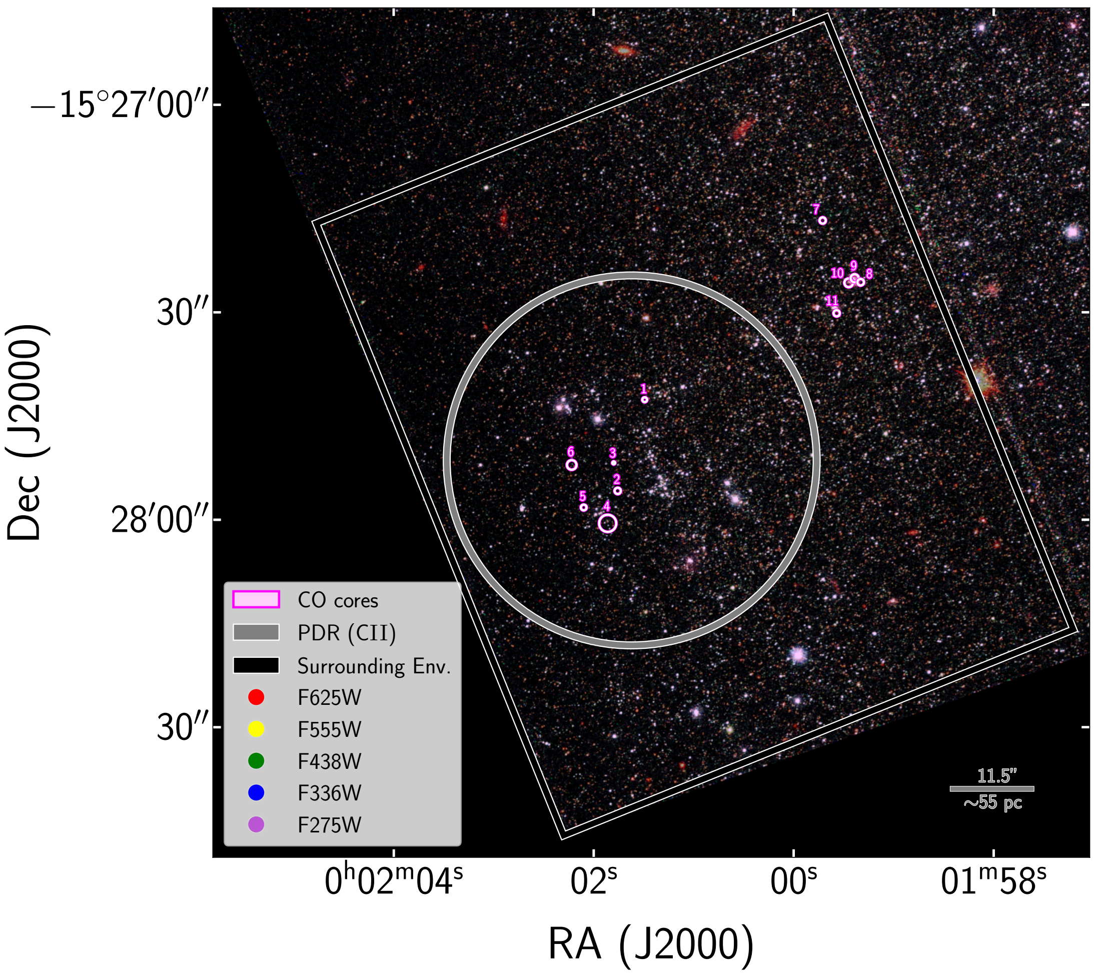

Figure 54. Multicolor image combining the five *HST* filters, with the outline of the PACS [C II]-detected PDR from Cigan *et al.* (2016) (large gray circle) and CO cores (smaller magenta circles) overlaid (Rubio *et al.* 2015). The large black rectangle outlines the environment outside the PDR considered in this work. The legend shows the color assigned to each filter. We also include the 11.5″ (55 pc) PACS beam size, which is the resolution of the PDR, in the bottom right corner.

By studying the stellar populations in and around these regions, we can gain insight into how star formation proceeds in areas with varying molecular gas visibility and density. The characteristics of these populations – such as their ages, masses, and spatial distribution – provide valuable clues about the role of CO-bright and CO-dark

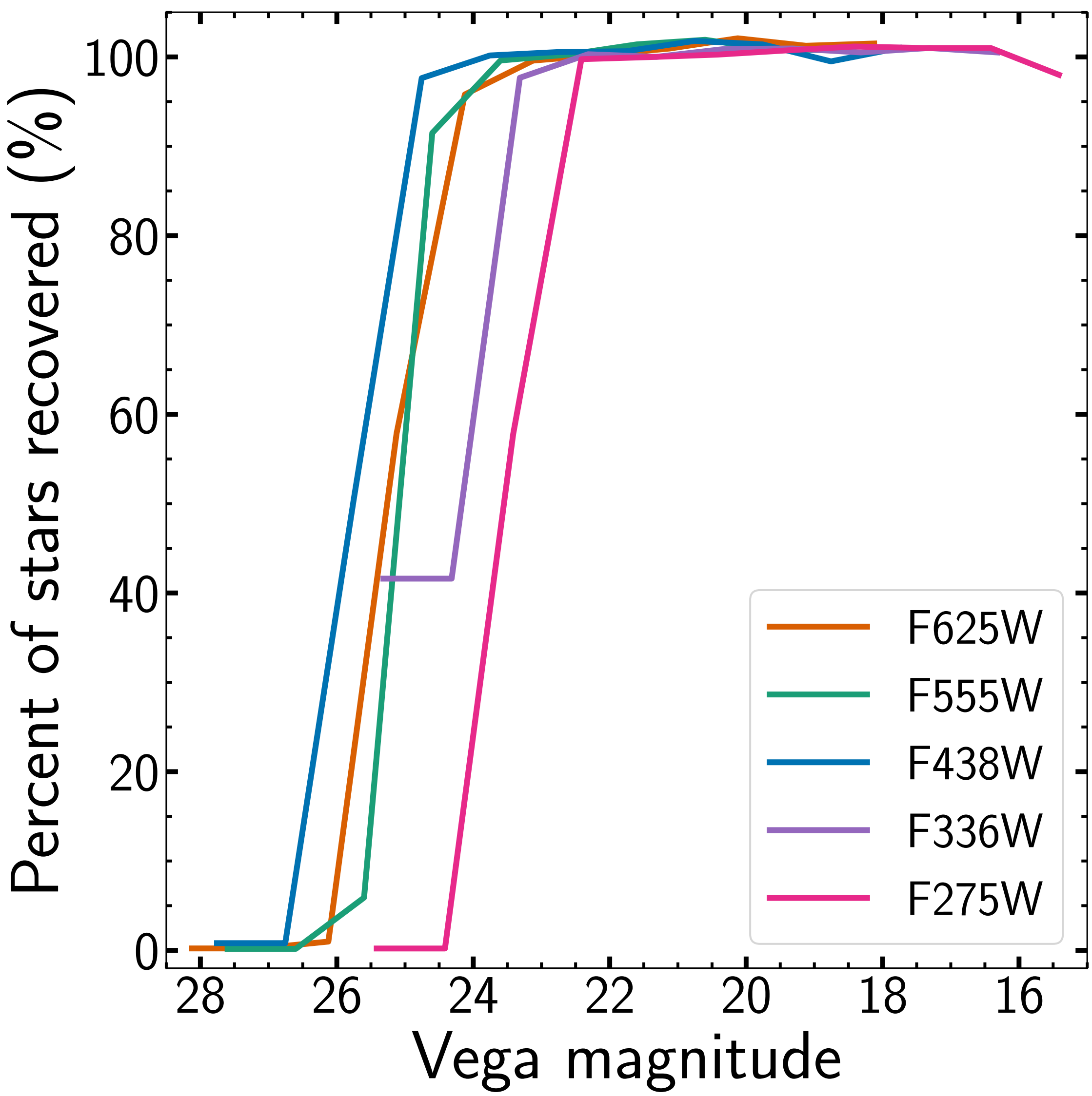

Figure 55. Percent of fake stars recovered using DAOPHOT as a function of Vega magnitude for the F625W (orange), F555W (green), F438W (blue), F336W (purple), and F275W (pink) *HST* filters.

gas in forming stars and how the local environment influences star formation efficiency in metal-poor galaxies.

Following the discovery of CO(3–2) emission in two star-forming regions of WLM by Elmegreen *et al.* (2013) using the Atacama Pathfinder Experiment (APEX) telescope,

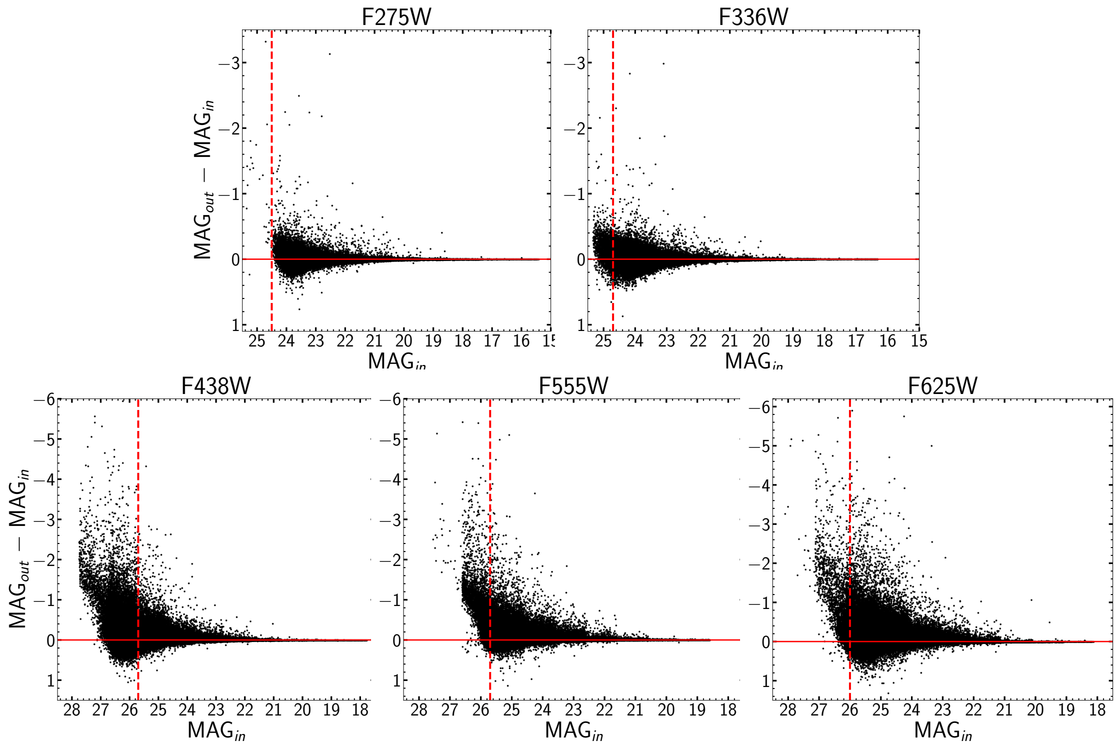

Figure 56. The difference between output and input magnitudes as a function of input magnitude for all artificial stars generated in the artificial star tests for each filter. The solid red horizontal line represents where input and output magnitudes are identical, while the dashed red vertical line marks the faintest magnitude in that filter observed in the final matched catalog of stars.

Rubio *et al.* (2015) conducted pointed CO(1–0) observations of these regions with the Atacama Large Millimeter Array (ALMA). Their work produced the first detailed map of 10 CO cores in WLM, and Rubio et al. (in preparation) have since mapped most of the star forming area of WLM with ALMA CO(2–1) observations and detected an additional 35 cores. Surrounding six of the original 10 detected cores, [C II] observations traced a photodissociation region (PDR) with a width five times larger than the cluster of CO cores, suggesting that molecular clouds at lower metallicities contain [C II] that doesn't correspond to visible CO or H I and more compact CO cores compared to those observed in the Milky Way (Rubio *et al.* 2015; Cigan *et al.* 2016).

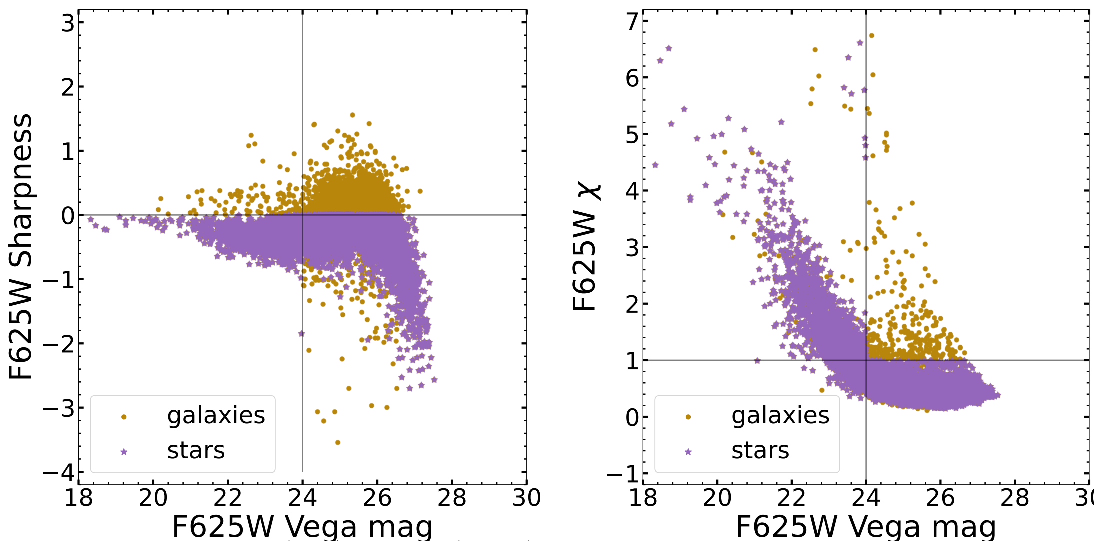

Figure 57. Sharpness (left) and χ (right) values as a function of Vega magnitude for all sources detected in the F625W filter. Gray vertical and horizontal lines are shown to demarcate which sources were stars or galaxies. Sources with a Vega magnitude brighter than 24 were determined to be stars if their sharpness was less than zero (bottom left quadrant in the sharpness plot), while sources with a Vega magnitude fainter than 24 were determined to be stars if both their sharpness was less than zero and their χ was less than one (bottom right quadrant in both plots). Sources determined to be galaxies are shown as gold points, while sources determined to be stars are shown as purple stars.

In this work, we focus on the region defined by the PDR–the only area in WLM with [C II] imaging–which contains six of the CO cores identified by (Rubio *et al.* 2015). Studies of other low-metallicity dwarf galaxies have shown that most of the molecular gas reservoir is not well-traced by CO(1-0) but can instead be tracked using the [C II] 158μm line (e.g., Requena-Torres *et al.* 2016; Madden *et al.* 2020; Ramambason *et al.* 2024). This motivated our choice to use the PDR to define the star-forming region. We compare the stellar populations within that region to those in the surrounding environment, which also contains five additional CO cores detected by Rubio et al. (in preparation), to understand their relationship to the CO cores and the PDR.

This paper is organized as follows. In Section 4.2, we describe our data sources and processing techniques. Section 4.3 presents the results of our photometric analysis, stellar isochrone fitting, and molecular gas assessment, while Section 4.4 discusses the implications of these findings for understanding star formation and molecular gas in WLM and similar galaxies. Finally, Section 4.5 provides a summary and conclusions of our study.

Table 1. *HST* **filter wavelengths and exposure times**

HST Filter Name	Effective Wavelength (Å)	Exp Time (s)
F275W	2709.7	2220
F336W	3354.5	1230
F438W	4326.2	1760
F555W	5308.4	1125
F625W	6242.6	1050

Figure 58. Table 1 from Stellar Populations and Molecular Gas Composition in the Low Metallicity Environment of WLM by Archer et al. (2025) in press in the Astronomical Journal.

4.2 Data

4.2.1 HST GO #17068

We obtained near-ultraviolet (NUV) images covering most of the star-forming area of WLM through the *HST* GO program #17068 (Archer *et al.* 2022a). Focusing on the star-forming region constrained by the [C II]-detected PDR, this project acquired the WFC3/UVIS F275W, F336W, F438W, F555W, and F625W images of the region for detecting and analyzing the stellar population. The F275W and

F336W ultraviolet (UV) filters were post-flashed with 20 e^- to account for the charge transfer efficiency (CTE) degradation of the UVIS detector, and the calwfc3 pipeline implements the CTE-correction code of Anderson *et al.* (2021). We include the effective wavelength and exposure times for each filter in the table in Figure 58. The *HST* images were processed to align the exposures, remove cosmic rays, subtract the background, and correct for geometric distortion using the DrizzlePac tasks TweakReg and AstroDrizzle (Hoffmann *et al.* 2021). We utilized the standard calibrated flc files for WFC3/UVIS, and the pixel scales were kept at their default values of 0.04″. Figure 54 shows a multicolor image combining all five WFC3/UVIS filters, with the PDR, surrounding environment, and CO cores overlaid. All *HST* data can be found in MAST: http://dx.doi.org/10.17909/xyhn-3z68.

Table 2. SED Free Parameters

Parameter	Symbol	Unit	Prior Distribution
Initial mass	$\log_{10} M_{\rm ini}$	$M_\odot$	Kroupa[a] IMF prior (see Equation 3)
Stellar age	$\log_{10} t$	yr	Constant SFH prior (see Equation 4)
Optical dust attenuation	A_V	mag	Normal ($\mu = 0.3, \sigma = 1.0$), truncated to the range$(0, 4)$
Luminosity distance	$\log_{10} d_{\rm L}$	pc	Normal ($\mu = 5.9934, \sigma = 0.0132$), truncated to the range $(5.9273, 6.0598)$

[a]Kroupa (2002)

Figure 59. Table 2 from Stellar Populations and Molecular Gas Composition in the Low Metallicity Environment of WLM by Archer et al. (2025) in press in the Astronomical Journal.

4.2.1.1 Photometry

Crowded field photometry was performed individually on all five *HST* UVIS images using the Image Reduction and Analysis Facility (IRAF) (Tody 1986) routine Daophot, derived from the Stetson (1987) version. To determine the completeness limit for star detection in our crowded field photometry, we conducted a series of artificial star tests on a band-by-band basis using DAOPHOT. First, we took the total number of stars detected in the image and divided them into magnitude bins. For each bin, we generated a set of artificial (or fake) stars with magnitudes corresponding to that bin and random positions distributed across the entire field, excluding the edges. The number of fake stars inserted in each bin was set to 10% of the total stars originally detected in that magnitude range. These fake stars were then added to the image, and we assessed whether DAOPHOT could retrieve them. This process was repeated 200 times for each of the five images, allowing us to build robust statistics on the detection efficiency at different magnitudes for the different filters. From this, we determined the percentages of stars recovered as a function of magnitude for each filter on a band-by-band basis, shown in Figure 55. The scatter in the artificial star tests is for each filter is shown in Figure 56.

To remove background galaxies, we used the DAOPHOT output parameters: SHARPNESS, a goodness-of-fit statistic indicating how much broader the object's profile appears compared to the PSF, and chi (χ), the ratio of observed pixel-to-pixel deviation from the profile fit to the expected noise based on Poisson and readout noise. Annunziatella *et al.* (2013) found that plotting sharpness and χ against magnitude clearly separates stars and galaxies, with stars having a sharpness below zero and galaxies showing higher χ values at fainter magnitudes. Due to the overlap of stars and galaxies in sharpness and χ at fainter magnitudes, we applied different criteria for sources with Vega magnitudes brighter and fainter than 24. Sources brighter than 24 were classified as stars if their sharpness is less than zero, while sources fainter than 24 were classified as stars if both their sharpness is less than zero and χ is less than one. Although sharpness and χ were obtained for all five filters, we used F625W values for their clearer population separation. Figure 57 illustrates sharpness and χ values as a function of Vega magnitude for sources detected in the F625W filter. We do not observe a distinct separation between the populations in color and, therefore, do not use color as a criterion for star-galaxy classification. Using single filters to accomplish star-galaxy separation is justified based on a comparison between our Figure 56 and the deeper data of Windhorst *et al.* (2011, panels 2-5 in their Figure 10a) in WFC3 and ACS filters very similar to ours. Our Figure 56 suggests approximate completeness limits of ∼24-26 mag in F275W to F625W, respectively. To the equivalent depth in the filters from the deeper images of Windhorst *et al.* (2011), the large majority of unresolved objects are stars, while almost all galaxies to our shallower depths will be resolved with FWHM>0.1–$0.2''$. In addition, the stellar density in our WLM fields is far higher than the star counts in the Windhorst *et al.* (2011) GOODS-S field at high galactic latitude. The fraction of truly compact galaxies with FWHM$<0.2''$ to our shallower detection limits is therefore very small. Hence, we do not need to use color for reliable star-galaxy separation.

We first created individual catalogs of stars detected in each of the five filters. To construct a combined catalog of stars detected across all five filters, we performed step-by-step matching, beginning with the UV filters (F275W and F336W), as these are expected to have the shallowest detection limits. Next, we sequentially matched this initial catalog with detections in the F438W, F555W, and F625W filters, combining results at each step. The matching process was carried out using the KDTree.query_radius function from the scikit-learn Python library. A matching radius of $0.018''$ was adopted, which was determined by measuring the positional offsets of a small sample of stars identified by eye across multiple filters. The stars in the resulting catalog were examined to ensure there were no spurious detections on diffraction spikes included in the sample. The same methodology was used to create a combined catalog of stars detected across all but the F275W filter.

4.2.2 SED Fitting

To relate physical stellar properties to observed filter magnitudes and photometric uncertainties, we use the CMD 3.8[1] tool, which collects the PARSEC 1.2S (Bressan *et al.* 2012; Chen *et al.* 2014; Tang *et al.* 2014; Chen *et al.* 2015), and COLIBRI S_37 (Marigo *et al.* 2017; Pastorelli *et al.* 2019, 2020) stellar evolutionary tracks onto a mass/age grid, fixing stellar metallicity to $Z_{\rm ini} = 0.0026$. For each mass/age grid point, CMD provides model fluxes for each of the HST filters used in this work. To generate model fluxes between grid points, we interpolate the model fluxes linearly in $M_{\rm ini}$ and $\log_{10} t$, allowing flux to be generated for any arbitrary mass or age within the range given by CMD. For stellar masses above the maximum mass present in the grid for a given stellar age, we set the flux to $M_{\rm Vega} = 999.99$ as we do not model stellar remnants. Finally, we apply dust attenuation using an SMC extinction curve (Gordon *et al.* 2003) in addition to luminosity distance, as follows,

$$m_{\rm predict}(\theta) = m_{\rm interp}(M_{\rm ini}, t) + 5 \log_{10} d_L + A_V k_\lambda, \tag{4.1}$$

where $m_{\rm interp}$ is the flux[2] predicted by the isochrone table interpolation, d_L is the luminosity distance, A_V is the dust attenuation, and k_λ specifies the dust curve and

[1] Available at http://stev.oapd.inaf.it/cgi-bin/cmd.

[2] All magnitudes given in this work are Vega magnitudes.

varies by filter,

$$k_\lambda = \begin{cases} 3.625 & \text{F275W}, \\ 1.672 & \text{F336W}, \\ 1.374 & \text{F438W}, \\ 1.000 & \text{F555W}, \\ 0.801 & \text{F625W}. \end{cases} \tag{4.2}$$

Our four free parameters and their priors are listed in Table 59. For the initial stellar mass, we assume a Kroupa (2002) IMF prior, with prior probability given as

$$\ln p_{\mathrm{M}}(M_{\mathrm{ini}}) = \begin{cases} (1-\alpha_0)\ln 10 \log_{10} M_{\mathrm{ini}} & M_{\mathrm{ini}} \leq M_1, \\ \Psi_2 + (1-\alpha_1)\ln 10 \log_{10} M_{\mathrm{ini}} & M_1 < M_{\mathrm{ini}} \leq M_2, \\ \Psi_3 + (1-\alpha_2)\ln 10 \log_{10} M_{\mathrm{ini}} & M_{\mathrm{ini}} > M_2, \end{cases} \tag{4.3}$$

where $\Psi_2 = (\alpha_1 - \alpha_0)\ln 10 \log_{10} M_1$ and $\Psi_3 = Q_2 + (\alpha_2 - \alpha_1)\ln 10 \log_{10} M_2$, and the α_i and M_i values are adopted from Kroupa (2002). Additionally, we assume a uniform prior in stellar age t,

$$\ln p_t(\log_{10} t) = (\ln 10)\log_{10} t, \tag{4.4}$$

which is equivalent to assuming a constant SFH prior, consistent with the choice made by Gordon *et al.* (2016), who also employed Bayesian inference for SED fitting of stars in M31. It should be noted that neither of these two priors are normalized, since Markov Chain Monte Carlo (MCMC) samplers generally only require a probability function that is *proportional* to the true posterior probability. For the optical dust attenuation A_V, we adopt the Normal distribution prior from the Prospector-α physical model (Leja *et al.* 2019). Finally, we adopt a Normal distribution prior for the luminosity distance, with mean $\sim$985 kpc and standard deviation of $\sim$30 kpc to account for the varying distance estimates found in the literature (e.g. Leaman *et al.* 2012; Albers *et al.* 2019; Lee *et al.* 2021; Newman *et al.* 2024), and truncated to $\pm 5\sigma$.

Using the flux predicted by the interpolation scheme, we compute the likelihood of the observed fluxes μ_i and their uncertainties σ_i for each filter i given the model θ using a multivariate normal distribution,

$$\ln p(\mu, \sigma | \theta) = -\frac{1}{2} \sum_i \left(\frac{m_{\mathrm{predict},i}(\theta) - \mu_i}{\sigma_i} \right)^2 . \tag{4.5}$$

Finally, we compute the non-normalized posterior likelihood as

$$\begin{aligned} \ln p(\theta | \mu, \sigma) = & \ln p(\mu, \sigma | \theta) + \ln p_M(M_{\mathrm{ini}}) + \\ & \ln p_t(t) + \ln p_d(d_L) + \ln p_{A_V}(A_V). \end{aligned} \tag{4.6}$$

We set the initial position for the sampler at the *maximum a posteriori* (MAP) location, which is estimated using the Adam optimizer (Kingma and Ba 2017) with $\alpha = 10^{-2}$, run for 10^5 iterations with the Optim.jl Julia package (Mogensen and Riseth 2018). Compared to providing a random or zero initial position vector, the MAP location helps the sampler explore the primary mode in the posterior and avoid getting stuck proposing stellar remnant solutions, which may provide a zero gradient since those solutions are fixed at $M_{\mathrm{Vega}} = 999.99$ without varying. Once the MAP location is found, we then adapt the step size and mass matrix for the No-U-Turn sampler (NUTS, Hoffman and Gelman 2011) as implemented in the AdvancedHMC.jl package (Xu *et al.* 2020) using the windowed adaptation scheme from Stan (Stan Development Team 2024), assuming a dense mass matrix and a target acceptance rate of 80%. We run the sampler for 4000 adaptation iterations, after which the mass matrix and step size are frozen. Finally, after adaptation, we use NUTS to draw 4000 samples from the posterior. We estimate each parameter's value as the median (50th percentile) of the parameter's marginalized posterior distribution. The associated uncertainty is quantified as half the difference between the 84th and 16th percentiles: $(\mathrm{P}_{84} - \mathrm{P}_{16})/2$.

Table 3. Locations, radii, and masses of the CO cores

CO Core	RA (deg)	DEC (deg)	Radius (pc)	M_{vir} ($M_\odot$)
1[a]	0.5062	−15.462	1.7	1000 +/− 700
2[a]	0.5073	−15.466	<1	<400 +/− 300
3[a]	0.5075	−15.464	2.2	1100 +/− 700
4[a]	0.5078	−15.467	6.0	10900 +/− 3200
5[a]	0.5086	−15.466	2.0	6900 +/− 5400
6[a]	0.5092	−15.464	3.4	1400 +/− 800
7	0.4988	−15.455	1.9	2100 +/− 1300
8	0.4972	−15.457	1.9	900 +/− 600
9	0.4975	−15.457	2.5	3900 +/− 1300
10	0.4977	−15.457	3.0	1800 +/− 1000
11	0.4983	−15.458	1.7	1600 +/− 1200

[a]From Table 1 of Rubio et al. (2015).

Figure 60. Table 3 from Stellar Populations and Molecular Gas Composition in the Low Metallicity Environment of WLM by Archer et al. (2025) in press in the Astronomical Journal.

Table 4. Right ascension, declination, and Vega magnitudes for the five *HST* filters for stars inside the PDR and projected inside the CO cores

	RA (deg)	DEC (deg)	F275W (Vega mag)	F336W (Vega mag)	F438W (Vega mag)	F555W (Vega mag)	F625W (Vega mag)
1	0.5077	-15.467	23.07 +/− 0.07	23.10 +/− 0.05	24.04 +/− 0.04	24.04 +/− 0.04	23.84 +/− 0.06
2	0.5079	-15.467	22.86 +/− 0.06	23.23 +/− 0.06	24.26 +/− 0.04	24.38 +/− 0.04	24.30 +/− 0.05

Figure 61. Table 4 from Stellar Populations and Molecular Gas Composition in the Low Metallicity Environment of WLM by Archer et al. (2025) in press in the Astronomical Journal.

Table 5. Right ascension, declination, and Vega magnitudes for the five *HST* filters for sources inside the PDR and outside the CO cores

	RA (deg)	DEC (deg)	F275W (Vega mag)	F336W (Vega mag)	F438W (Vega mag)	F555W (Vega mag)	F625W (Vega mag)
1	0.5122	-15.468	23.09 +/− 0.08	23.43 +/− 0.07	24.03 +/− 0.05	23.99 +/− 0.05	23.95 +/− 0.06
2	0.5131	-15.465	23.66 +/− 0.07	23.35 +/− 0.06	23.42 +/− 0.05	22.68 +/− 0.05	21.91 +/− 0.05
3	0.5130	-15.464	20.43 +/− 0.04	20.86 +/− 0.04	22.29 +/− 0.05	22.45 +/− 0.04	22.25 +/− 0.05
4	0.5113	-15.466	20.99 +/− 0.04	21.44 +/− 0.05	22.89 +/− 0.04	23.04 +/− 0.05	23.06 +/− 0.07
5	0.5109	-15.467	21.70 +/− 0.04	22.04 +/− 0.05	22.63 +/− 0.04	22.71 +/− 0.04	22.61 +/− 0.06
6	0.5095	-15.471	22.24 +/− 0.05	22.65 +/− 0.05	23.66 +/− 0.04	23.86 +/− 0.04	23.74 +/− 0.06
7	0.5097	-15.470	22.60 +/− 0.05	22.90 +/− 0.05	24.08 +/− 0.06	24.14 +/− 0.05	24.00 +/− 0.05
8	0.5121	-15.461	22.93 +/− 0.06	22.26 +/− 0.05	21.72 +/− 0.04	21.55 +/− 0.04	21.26 +/− 0.06
9	0.5111	-15.463	21.46 +/− 0.05	21.35 +/− 0.05	21.44 +/− 0.06	21.6 +/− 0.05	21.32 +/− 0.06
10	0.5100	-15.466	22.28 +/− 0.05	22.60 +/− 0.06	23.82 +/− 0.05	24.02 +/− 0.05	23.83 +/− 0.06

NOTE—Only a portion of this table is shown here to demonstrate its form and content. A machine-readable version is available for all 443 sources detected inside the PDR and outside the CO cores.

Figure 62. Table 5 from Stellar Populations and Molecular Gas Composition in the Low Metallicity Environment of WLM by Archer et al. (2025) in press in the Astronomical Journal.

Table 6. Right ascension, declination, and Vega magnitudes for the five *HST* filters for sources outside the PDR and projected inside the CO cores

	RA (deg)	DEC (deg)	F275W (Vega mag)	F336W (Vega mag)	F438W (Vega mag)	F555W (Vega mag)	F625W (Vega mag)
1	0.4975	-15.457	21.51 +/− 0.05	21.43 +/− 0.04	22.59 +/− 0.04	22.31 +/− 0.07	22.24 +/− 0.04
2	0.4976	-15.457	22.88 +/− 0.08	23.38 +/− 0.07	24.45 +/− 0.07	24.24 +/− 0.06	24.13 +/− 0.06

Figure 63. Table 6 from Stellar Populations and Molecular Gas Composition in the Low Metallicity Environment of WLM by Archer et al. (2025) in press in the Astronomical Journal.

4.2.3 CO Cores and [C II]

In Cycle 1, Rubio *et al.* (2015) used ALMA to image two star-forming regions in WLM, focusing on CO(1-0) emissions, and detected 10 CO cores. The beam size for these observations was $0.9'' \times 1.3''$. Of the 10 detected cores, six were located in the PDR, referred to as Region B in Elmegreen *et al.* (2013), WLM-SE region in (Rubio *et al.* 2015), and Region 1 in Archer *et al.* (2022b), which is the primary focus of this paper. The masses and locations of these six CO cores, labeled as 1 through 6 in

Table 7. Right ascension, declination, and Vega magnitudes for the five *HST* filters for sources outside the PDR and outside the CO cores

	RA	DEC	F275W	F336W	F438W	F555W	F625W
	(deg)	(deg)	(Vega mag)	(Vega mag)	(Vega mag)	(Vega mag)	(Vega mag)
1	0.5151	-15.464	22.55 +/− 0.05	22.93 +/− 0.06	23.95 +/− 0.04	24.04 +/− 0.04	23.79 +/− 0.05
2	0.5124	-15.471	22.68 +/− 0.06	22.85 +/− 0.05	23.89 +/− 0.04	24.05 +/− 0.04	23.86 +/− 0.09
3	0.5128	-15.470	23.39 +/− 0.06	23.29 +/− 0.05	24.07 +/− 0.05	23.98 +/− 0.04	23.92 +/− 0.07
4	0.5123	-15.470	23.81 +/− 0.09	23.29 +/− 0.07	23.57 +/− 0.08	23.08 +/− 0.06	22.70 +/− 0.06
5	0.5123	-15.471	22.74 +/− 0.06	22.95 +/− 0.06	23.97 +/− 0.04	24.00 +/− 0.04	23.81 +/− 0.05
6	0.5102	-15.476	21.77 +/− 0.04	22.07 +/− 0.04	23.46 +/− 0.05	23.47 +/− 0.04	23.22 +/− 0.06
7	0.5103	-15.474	24.51 +/− 0.18	23.93 +/− 0.09	23.69 +/− 0.04	23.49 +/− 0.04	23.24 +/− 0.05
8	0.5095	-15.476	23.87 +/− 0.11	23.13 +/− 0.07	22.89 +/− 0.05	22.61 +/− 0.04	22.17 +/− 0.06
9	0.5111	-15.471	20.76 +/− 0.04	21.13 +/− 0.04	22.35 +/− 0.04	22.44 +/− 0.04	22.53 +/− 0.04
10	0.5103	-15.473	22.67 +/− 0.05	22.8 +/− 0.05	23.36 +/− 0.05	23.40 +/− 0.04	23.18 +/− 0.05

Note—Only a portion of this table is shown here to demonstrate its form and content. A machine-readable version is available for all 566 sources detected outside the PDR and outside the CO cores.

Figure 64. Table 7 from Stellar Populations and Molecular Gas Composition in the Low Metallicity Environment of WLM by Archer et al. (2025) in press in the Astronomical Journal.

Figure 54, can be found in Table 1 of Rubio *et al.* (2015) as regions SE-1 through SE-6. An additional 35 CO cores were detected using CO(2-1) observations at 1″resolution (4.8 pc at WLM distance) with ALMA Cycle 6 (Rubio et al. in prep), all of which were detected outside the PDR as the survey did not include it. Five of these 35 CO cores were included when examining the environment surrounding the PDR to compare stellar populations inside the CO cores and outside the PDR to stellar populations inside the CO cores and inside the PDR. The locations, radii, and virial masses of the 11 CO cores included in this work can be found in the table in Figure 60.

The [C II] 158μm image was obtained using the PACS spectrometer aboard Herschel for LITTLE THINGS (Cigan *et al.* 2016). The beam size for the PACS [C II] was 11.5″(shown in Figure 54), which imaged the targeted region in WLM with a diameter of 54″, and showed [C II] filling the entire region. We acknowledge that any clouds smaller than 11.5″ would be unresolved in our analysis. Additionally, since the PACS pointing was the only one available for WLM, the [C II] may extend beyond the region defined as the PDR boundary in this study.

Table 8. Right ascension, declination, and Vega magnitudes for the four *HST* filters for the star inside the PDR and projected inside the CO cores not detected in the F275W filter

	RA (deg)	DEC (deg)	F336W (Vega mag)	F438W (Vega mag)	F555W (Vega mag)	F625W (Vega mag)
1	0.5062	-15.462	24.08 +/− 0.10	25.09 +/− 0.06	25.35 +/− 0.07	24.89 +/− 0.08

Figure 65. Table 8 from Stellar Populations and Molecular Gas Composition in the Low Metallicity Environment of WLM by Archer et al. (2025) in press in the Astronomical Journal.

Table 9. Right ascension, declination, and Vega magnitudes for the four *HST* filters for sources inside the PDR and outside the CO cores not detected in the F275W filter

	RA (deg)	DEC (deg)	F336W (Vega mag)	F438W (Vega mag)	F555W (Vega mag)	F625W (Vega mag)
1	0.5128	-15.470	23.18 +/− 0.05	23.98 +/− 0.05	23.91 +/− 0.04	23.86 +/− 0.07
2	0.5123	-15.470	23.18 +/− 0.07	23.48 +/− 0.08	23.01 +/− 0.06	22.65 +/− 0.06
3	0.5150	-15.462	22.52 +/− 0.05	23.49 +/− 0.04	23.65 +/− 0.04	23.31 +/− 0.05
4	0.5111	-15.471	21.01 +/− 0.04	22.26 +/− 0.04	22.37 +/− 0.04	22.47 +/− 0.04
5	0.5110	-15.471	19.97 +/− 0.07	21.41 +/− 0.04	21.50 +/− 0.04	21.62 +/− 0.06
6	0.5101	-15.472	22.79 +/− 0.05	23.81 +/− 0.04	23.83 +/− 0.04	23.80 +/− 0.06
7	0.5134	-15.462	23.90 +/− 0.09	23.67 +/− 0.04	23.48 +/− 0.04	23.22 +/− 0.07
8	0.5095	-15.472	23.26 +/− 0.07	23.10 +/− 0.04	23.05 +/− 0.04	22.88 +/− 0.05
9	0.5103	-15.466	23.78 +/− 0.09	23.61 +/− 0.04	23.57 +/− 0.04	23.25 +/− 0.05
10	0.5113	-15.463	23.89 +/− 0.09	23.36 +/− 0.04	22.47 +/− 0.04	21.95 +/− 0.07

Note—Only a portion of this table is shown here to demonstrate its form and content. A machine-readable version is available for all 144 sources detected inside the PDR and outside the CO cores.

Figure 66. Table 9 from Stellar Populations and Molecular Gas Composition in the Low Metallicity Environment of WLM by Archer et al. (2025) in press in the Astronomical Journal.

Table 10. Right ascension, declination, and Vega magnitudes for the four *HST* filters for sources outside the PDR and outside the CO cores not detected in the F275W filter

	RA (deg)	DEC (deg)	F336W (Vega mag)	F438W (Vega mag)	F555W (Vega mag)	F625W (Vega mag)
1	0.5112	-15.473	24.06 +/− 0.09	23.72 +/− 0.04	22.90 +/− 0.04	22.35 +/− 0.06
2	0.5166	-15.456	23.83 +/− 0.09	23.71 +/− 0.04	23.07 +/− 0.04	22.40 +/− 0.05
3	0.5094	-15.476	23.70 +/− 0.08	22.91 +/− 0.05	21.87 +/− 0.07	21.12 +/− 0.06
4	0.5086	-15.476	23.51 +/− 0.08	23.10 +/− 0.04	22.27 +/− 0.05	21.70 +/− 0.07
5	0.5094	-15.474	23.79 +/− 0.09	23.67 +/− 0.05	23.21 +/− 0.04	22.94 +/− 0.05
6	0.5132	-15.455	24.33 +/− 0.13	24.46 +/− 0.06	23.86 +/− 0.04	23.24 +/− 0.06
7	0.5128	-15.454	23.66 +/− 0.07	23.58 +/− 0.04	22.91 +/− 0.04	22.30 +/− 0.04
8	0.5046	-15.477	22.92 +/− 0.06	21.17 +/− 0.05	19.52 +/− 0.04	18.70 +/− 0.05
9	0.5107	-15.454	23.79 +/− 0.08	23.33 +/− 0.04	22.81 +/− 0.04	22.08 +/− 0.05
10	0.5094	-15.455	24.08 +/− 0.08	23.12 +/− 0.04	22.01 +/− 0.04	21.24 +/− 0.05

Note—Only a portion of this table is shown here to demonstrate its form and content. A machine-readable version is available for all 78 sources detected outside the PDR and outside the CO cores.

Figure 67. Table 10 from Stellar Populations and Molecular Gas Composition in the Low Metallicity Environment of WLM by Archer et al. (2025) in press in the Astronomical Journal.

4.3 Results

4.3.1 Photometry

We separated the stars into four categories based on their coincidence with the PDR and CO cores: (1) stars inside the PDR and projected inside the CO cores, (2) stars inside the PDR and outside the CO cores, (3) stars outside the PDR and projected inside the CO cores, and (4) stars outside the the PDR and outside the CO cores. Only four stars are spatially coincident with the CO cores. To better constrain the SED, we include only stars detected in all five filters and in all but the F275W filter. Consequently, there may be stars within the CO that are excluded, as these stars would be embedded and not appear in the bluest filters. This limitation reduces

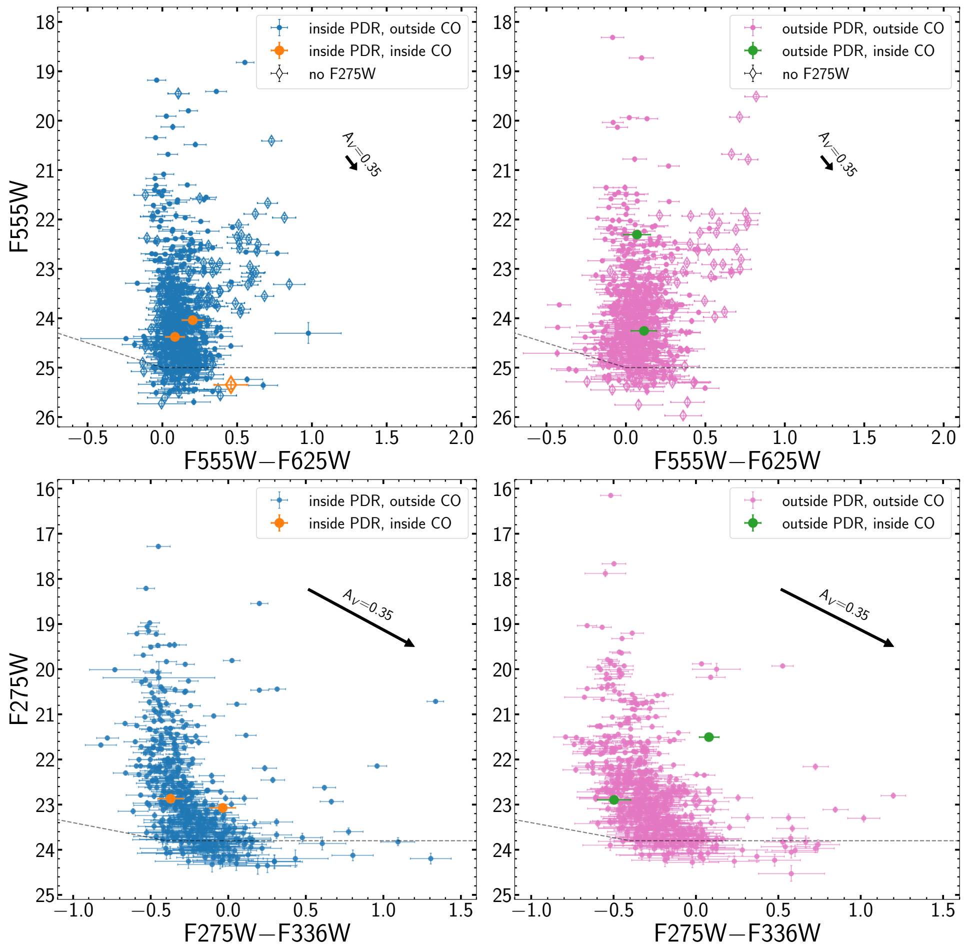

Figure 68. Top left: F555W vs F555W–F625W color-magnitude diagram for stars inside the PDR and outside the CO cores (blue) and stars inside the PDR and projected inside the CO cores (orange). Top right: F555W vs F555W–F625W color-magnitude diagram for stars outside the PDR and outside the CO cores (pink) and stars outside the PDR and projected inside the CO cores (green). Bottom left: F275W vs F275W–F6336W color-magnitude diagram for stars inside the PDR and outside the CO cores (blue) and stars inside the PDR and projected inside the CO cores (orange). Bottom right: F275W vs F275W–F336W color-magnitude diagram for stars outside the PDR and outside the CO cores (pink) and stars outside the PDR and projected inside the CO cores (green). Stars detected in all filters are represented by circles (○), while stars that were not detected in the F275W filter are represented by diamonds (◇). The black arrow in each plot shows the reddening vector for A_V=0.35, the mean A_V of stars in WLM measured by Wang *et al.* (2022), assuming SMC-like extinction. The errorbars in the upper left corner of each plot demonstrate the mean uncertainty associated with the data shown. The gray dashed line shows the 5σ point source detection limit for the given filters and exposure times (Windhorst *et al.* 2022).

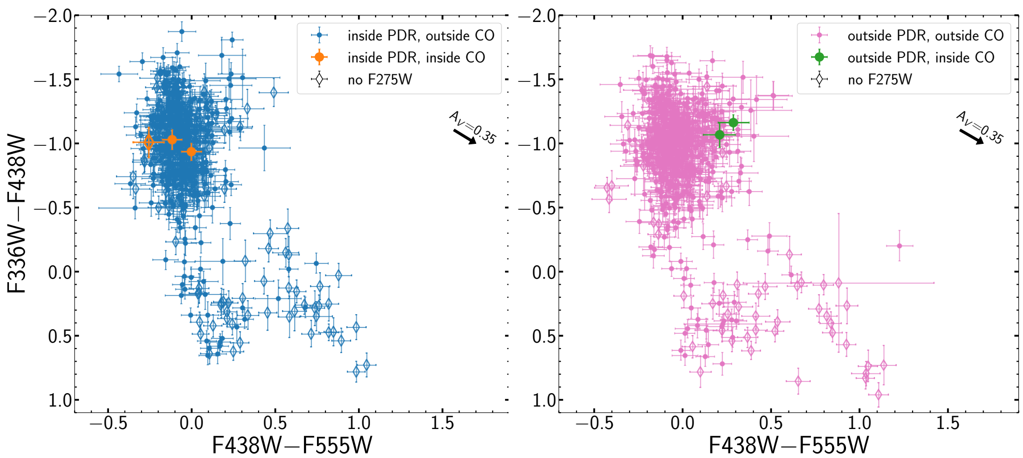

Figure 69. Left: F336W–F438W vs F438W–F555W color-color diagram for stars inside the PDR and outside the CO cores (blue) and stars inside the PDR and projected inside the CO cores (orange). Right: F336W–F438W vs F438W–F555W color-color diagram for stars outside the PDR and outside the CO cores (pink), and stars outside the PDR and projected inside the CO cores (green). Stars detected in all filters are represented by circles (○), while stars that were not detected in the F275W filter are represented by diamonds (◇). The black arrow in each plot shows the reddening vector for A_V=0.35, the mean A_V of stars in WLM measured by Wang *et al.* (2022), assuming SMC-like extinction. The errorbars in the upper left corner of each plot demonstrate the mean uncertainty associated with the data shown.

the number of stars available for analysis in these regions. Additionally, some stars coincident with the CO cores may be located in front of the CO rather than within the cores themselves. Stars visible in the reddest *HST* filter (F625W) but absent from the bluest filters are also detected in the F555W filter, further suggesting that the UVIS dataset does not capture embedded stars. Identifying such stars would require the unique high-resolution infrared capabilities of *JWST*, particularly that of the Mid-Infrared Instrument (MIRI), as the MIRI filters are found to play a crucial role in distinguishing young stellar objects from cool, evolved red stars and background galaxies (Peltonen *et al.* 2024). The JWST Resolved Stellar Populations Early Release Science Program (e.g. Weisz *et al.* 2023; McQuinn *et al.* 2024; Boyer *et al.* 2024; Newman *et al.* 2024) provide publicly available NIR photometric catalogs for WLM

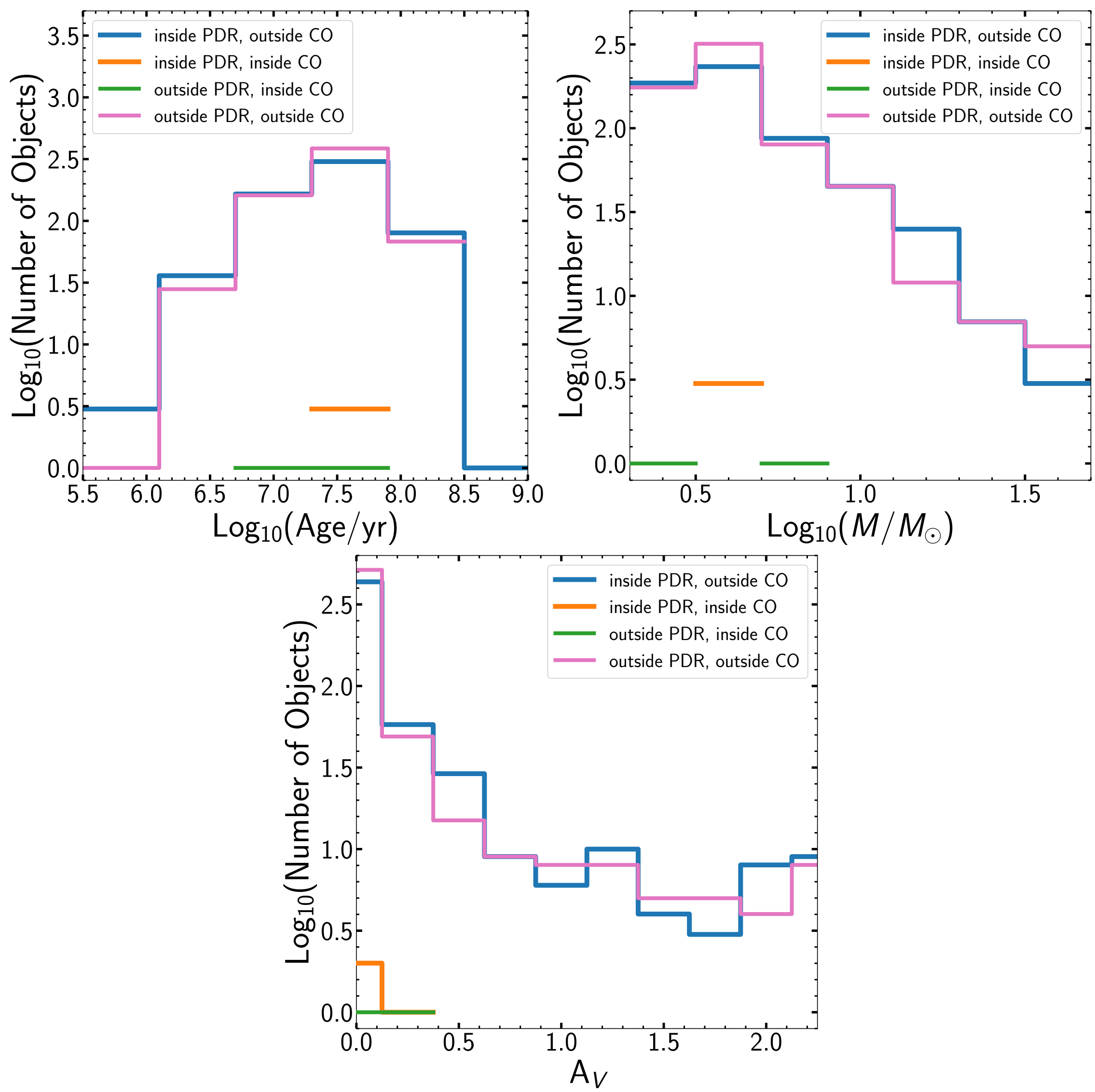

Figure 70. Histograms of the ages (top left), masses (top right), and A_V (bottom) for stars inside the PDR and outside the CO cores (blue), stars inside the PDR and projected inside the CO cores (orange), stars outside the PDR and projected inside the CO cores (green), and stars outside the PDR and outside the CO cores (pink). Clusters of closely packed stars may not be resolved into individual components.

as part of the JWST Resolved Stellar Populations Early Release Science Program. However, the fields they targeted do not overlap with the region analyzed in this study.

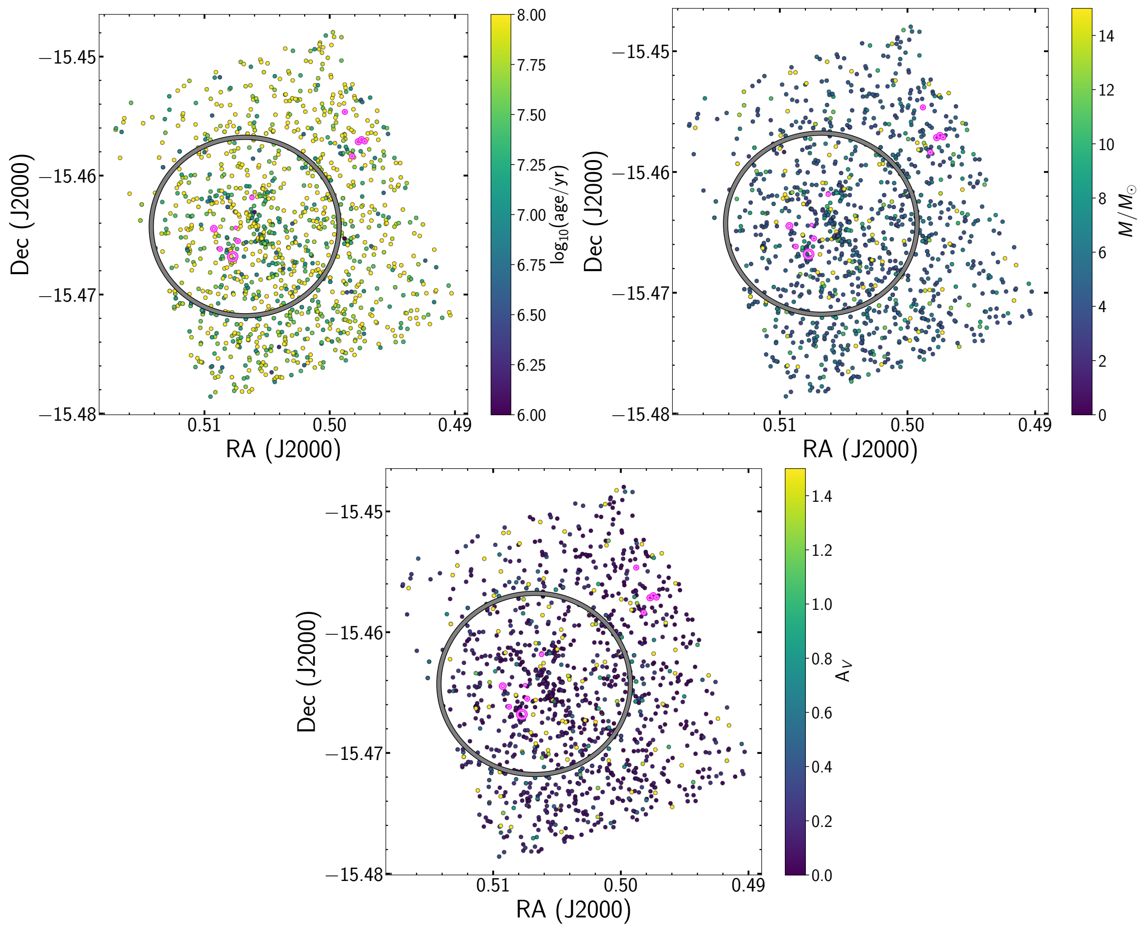

Figure 71. Plots showing the spatial distribution of stars, color-coded by their ages (top left), masses (top right), and A_V (bottom). The large gray circle demarcates the PDR, while the smaller magenta circles show the locations and sizes of the CO cores.

Because the requirement of a detection in the F275W/F336W filters, a larger number of stars detected in the reddest filter, F625W, were excluded. After separating stars from galaxies using the sharpness and χ parameters, the total number of stars detected in F625W was 11,732, while the total number of detected stars in the F275W filter was 1,946. The resulting catalog after matching all five filters contains 1,013 stars, or around 10% of the stars found in F625W, while the resulting catalog after matching all but the F275W filter includes an additional 223 stars more than the full five-filter catalog.

The right ascension (RA), declination (DEC), and apparent Vega magnitudes corresponding to the five *HST* filters for stars in each of the four categories are included in the tables shown in Figures 61, 62, 63, 64, with the full tables from Figures 62 and 64 available in machine-readable format in the online materials. For stars not detected in the F275W filter, the right ascension (RA), declination (DEC), and apparent Vega magnitudes corresponding to the other four *HST* filters are included in the table shown in Figure 65 for stars inside the PDR and projected inside the CO cores, the table shown in Figure 66 for stars inside the PDR and outside the CO cores, and the table shown in Figure 67 for stars outside the PDR and outside the CO cores. The full the tables from Figures 66 and 67 are available in machine-readable format in the online materials. No additional stars outside the PDR and projected inside the CO cores were detected after excluding the F275W filter. The sharpness and χ values for all detected filters of the sources determined to be stars are included in the appendix. We find that all stars, irrespective of proximity to the PDR or CO cores, occupy the same color and magnitude ranges, which can be seen in the F555W vs F555W–F625W and F275W vs F275W–F336W color-magnitude diagrams (CMDs) in Figure 68, and the F336W–F438W vs F438W–F555W color-color diagrams in Figure 69. The scatter in color observed in the CMDs appears to be primarily due to color uncertainties. However, we also find that stars not detected in the F275W filter tend to appear redder in the F555W vs F555W–F625W CMDs, as expected. The redward shift of fainter objects in the F275W vs F275W–F336W color-magnitude diagram may be attributed to reddening or to undercorrected faint object fluxes resulting from the Anderson *et al.* (2021) CTE correction applied in the pipeline, as demonstrated by Windhorst *et al.* (2022). The positions of stars on the color-color diagram in Figure 69 are also consistent with the U–B vs. B–V color indices of main-sequence stars (Nicolet 1980;

Bressan *et al.* 2012; Choi *et al.* 2016). Additionally, stars not detected in the F275W filter are more frequently found in the redder region of the color-color diagrams in Figure 69, aligning with the expected location of cooler main-sequence stars.

Table 11. Mass and age for stars inside the PDR and projected inside CO cores.

	$\log_{10}(M/M_\odot)$	$\log_{10}$(age/yr)	A_V/mag
1	0.62 +/− 0.03	8.07 +/− 0.07	0.20 +/− 0.06
2	0.63 +/− 0.03	7.96 +/− 0.11	0.05 +/− 0.04

Figure 72. Table 11 from Stellar Populations and Molecular Gas Composition in the Low Metallicity Environment of WLM by Archer et al. (2025) in press in the Astronomical Journal.

4.3.2 Masses, Ages, and A_V

The table in Figures 72, 73, 74, 75, 77, 78, and 79 contain the masses, ages, and A_V found using PARSEC for stars in each of the four categories, along with stars not detected in the F275W filter, with the full tables shown in Figures 73, 75, 78, and 79 included as machine-readable tables in the online materials. The small uncertainties in the inferred physical properties may result from the SED fitting process rather than reflecting genuinely low uncertainties. We include a corner plot illustrating the SED fit for a representative star from each category in the appendix. Figure 70 shows the histograms of the masses, ages, and A_V of the stars, where we find that stars across all four categories exhibit similar mass, age, and A_V distributions. The mean

Table 12. Mass and age for stars inside the PDR and outside CO cores.

	$\log_{10}(M/M_{\odot})$	$\log_{10}(\mathrm{age/yr})$	A_V/mag
1	0.56 +/− 0.01	8.24 +/− 0.03	0.09 +/− 0.05
2	0.90 +/− 0.01	7.56 +/− 0.01	0.69 +/− 0.02
3	0.95 +/− 0.04	7.40 +/− 0.10	0.09 +/− 0.04
4	0.95 +/− 0.05	7.12 +/− 0.34	0.07 +/− 0.03
5	0.88 +/− 0.01	7.55 +/− 0.01	0.18 +/− 0.04
6	0.67 +/− 0.02	7.93 +/− 0.06	0.03 +/− 0.03
7	0.68 +/− 0.04	7.85 +/− 0.13	0.10 +/− 0.05
8	1.00 +/− 0.01	7.37 +/− 0.01	0.17 +/− 0.03
9	1.13 +/− 0.01	7.16 +/− 0.01	0.41 +/− 0.04
10	0.75 +/− 0.05	7.62 +/− 0.22	0.10 +/− 0.05

Note—Only a portion of this table is shown here to demonstrate its form and content. A machine-readable version is available for all 433 sources detected inside the PDR and outside the CO cores.

Figure 73. Table 12 from Stellar Populations and Molecular Gas Composition in the Low Metallicity Environment of WLM by Archer et al. (2025) in press in the Astronomical Journal.

Table 13. Mass and age for stars outside the PDR and projected inside CO cores.

	$\log_{10}(M/M_{\odot})$	$\log_{10}(\mathrm{age/yr})$	A_V/mag
1	0.97 +/− 0.01	7.40 +/− 0.01	0.32 +/− 0.04
2	0.58 +/− 0.02	8.15 +/− 0.07	0.04 +/− 0.04

Figure 74. Table 13 from Stellar Populations and Molecular Gas Composition in the Low Metallicity Environment of WLM by Archer et al. (2025) in press in the Astronomical Journal.

Table 14. Mass and age for stars outside the PDR and outside CO cores.

	$\log_{10}(M/M_\odot)$	$\log_{10}(\mathrm{age/yr})$	A_V/mag
1	0.64 +/− 0.03	8.02 +/− 0.07	0.06 +/− 0.04
2	0.68 +/− 0.03	7.90 +/− 0.10	0.13 +/− 0.05
3	0.59 +/− 0.02	8.18 +/− 0.05	0.26 +/− 0.04
4	0.97 +/− 0.01	7.40 +/− 0.01	1.00 +/− 0.03
5	0.65 +/− 0.03	8.00 +/− 0.09	0.14 +/− 0.05
6	0.82 +/− 0.04	7.56 +/− 0.14	0.14 +/− 0.04
7	0.91 +/− 0.01	7.50 +/− 0.01	1.18 +/− 0.05
8	0.91 +/− 0.01	7.51 +/− 0.01	0.61 +/− 0.04
9	0.82 +/− 0.01	7.69 +/− 0.01	0.04 +/− 0.02
10	0.78 +/− 0.01	7.75 +/− 0.01	0.26 +/− 0.04

NOTE—Only a portion of this table is shown here to demonstrate its form and content. A machine-readable version is available for all 566 sources detected outside the PDR and outside the CO cores.

Figure 75. Table 14 from Stellar Populations and Molecular Gas Composition in the Low Metallicity Environment of WLM by Archer et al. (2025) in press in the Astronomical Journal.

A_V of all the stars detected is $\sim$0.34$\pm$0.06 mag, which is similar to the mean A_V of stars in WLM measured by Wang *et al.* (2022) found to be 0.35 mag. This mean extinction value is similar across the different categories. Stellar ages typically range from $\sim$1-100 Myr, with older stars likely belonging to the underlying disk population. We note that clusters of closely packed stars may not be fully resolved into individual components.

We also find no correlation is observed between the spatial locations of stars and their respective masses, ages, or A_V as shown in Figure 71. However, we identify some structure and clusters of younger stars near the center of the PDR, which align with regions bright in the far-ultraviolet (FUV). A three-color image of the region is shown in Figure 76, where red corresponds to the *HST* F336W image, green corresponds to the *HST* F275W image, and blue corresponds to the FUV image from the NASA Galaxy Evolution Explorer (GALEX[1]) satellite (Martin *et al.* 2005a; Zhang *et al.* 2012).

The mean velocity dispersion in the region is approximately 8 km/s (Iorio *et al.* 2017), indicating that stars could have been dispersed by nearly 82 pc over 10 Myr. This dispersion may explain the scattering of young stars observed outside the PDR, which has a radius of ∼130 pc. Additionally, Figure 76 highlights ongoing star formation beyond the PDR, which may not be directly linked to the same star-forming event and could account for the young stars seen outside the PDR.

4.3.3 Gas Mass

To get a comprehensive view of the gas in our targeted region, we combined our *HST* and CO data with extant H I masses of the region. The H I mass comes from converting the H I surface density ($\Sigma_{\mathrm{H\,I}}$) in Table 2 of Archer *et al.* (2022b) to mass. The robust-weighted $\Sigma_{\mathrm{H\,I}}$ map was acquired with the Karl G. Jansky Very Large Array (VLA) for Local Irregulars That Trace Luminosity Extremes, The H I Nearby Galaxy Survey (LITTLE THINGS), a multiwavelength survey of 37 nearby dIrr galaxies and 4 nearby Blue Compact Dwarf (BCD) galaxies (Hunter *et al.* 2012). We include the mass of the H I atomic gas for this region in the table in Figure 80.

To determine the amount of CO-dark molecular gas in the region, we first found the

[1]GALEX was operated for NASA by the California Institute of Technology under NASA contract NAS5-98034.

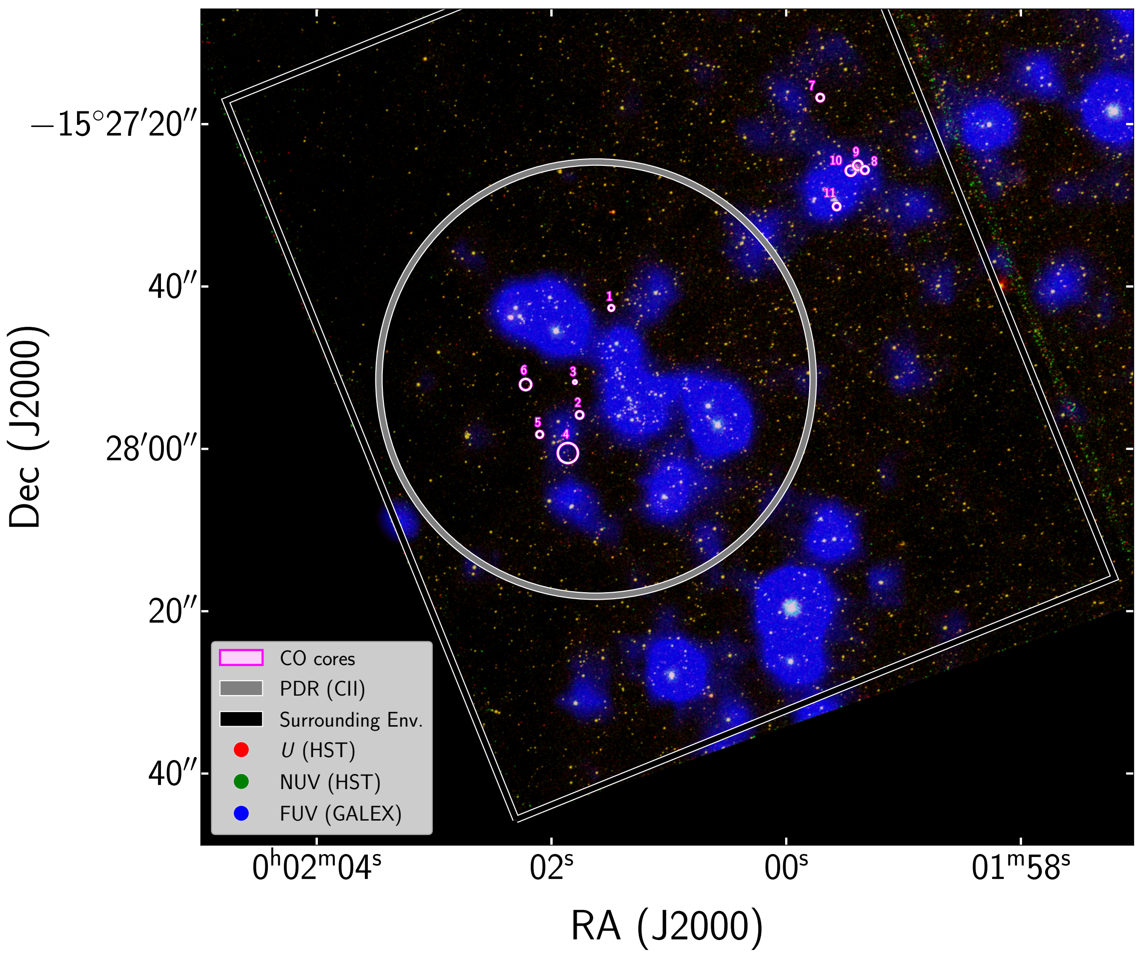

Figure 76. Three-color composite image combining the *HST* 336W (red), *HST* 275W (green), and GALEX FUV (blue) images of the region, highlighting how the ultraviolet clumps of star formation correspond to the structures and clusters of younger stars within the PDR shown in Figure 71.

total mass of young stars detected in our region. We estimated the number of detected disk stars in the PDR to be approximately 400. This number also approximately corresponds to the number of stars with ages greater 30 Myr. Only including stars younger than 30 Myr–the more recent star formation–we estimate the total stellar mass of young stars in our sample to be $\sim$2,000 $M_\odot$. The absence of low-mass stars in our sample due to completeness suggests that the total stellar mass is likely much greater than this estimate by a factor of 2 or 3, considering a standard IMF. Krumholz *et al.* (2012) find that approximately 1% $\pm$ 2% of the molecular gas is converted to stars per local free-fall time. For our region, spanning 260 pc in diameter and assuming a velocity dispersion comparable to the stellar dispersion of 8 km/s, the turbulence crossing time is 32 Myr, which is comparable to the selected age window for our stellar mass. The timescale is also comparable to that of large-scale star formation in the LMC, which is $\sim$20 Myr on this scale from Figure 1 in Elmegreen (2000). Taking these timescales as the effective free fall time over the large PDR region considered here, and a conservative estimate of 2% of the gas mass converting to stars in this time. Taking a conservative estimate of 2%, we find the total star-forming gas mass in the PDR using our estimated stellar mass is then:

$$2 \times 10^3 \ M_\odot \ / \ 0.02 \approx 1 \times 10^5 \ M_\odot. \tag{4.7}$$

Accounting for the total virial mass of the six CO cores in the region, $\sim$20,000 $M_\odot$, we find the CO-dark molecular gas mass to be

$$1 \times 10^5 \ M_\odot - 2 \times 10^4 \ M_\odot = 8 \times 10^4 \ M_\odot, \tag{4.8}$$

suggesting that approximately 80% of the molecular gas mass is CO-dark. Assuming 1% or 3% of the molecular gas is converted to stars instead yields a CO-dark gas percentage of 90% or 70% respectively. The total CO virial mass, total stellar mass, total estimated molecular gas mass, and total estimated CO-dark gas mass, along with their associated uncertainties, are included in the table in Figure 80.

Table 15. Mass and age for the star inside the PDR and projected inside CO cores not detected in the F275W filter.

	$\log_{10}(M/M_{\odot})$	$\log_{10}(\mathrm{age/yr})$	A_V/mag
1	0.62 +/− 0.06	7.71 +/− 0.41	0.34 +/− 0.17

Figure 77. Table 15 from Stellar Populations and Molecular Gas Composition in the Low Metallicity Environment of WLM by Archer et al. (2025) in press in the Astronomical Journal.

Table 16. Mass and age for stars inside the PDR and outside CO cores not detected in the F275W filter.

	$\log_{10}(M/M_{\odot})$	$\log_{10}(\mathrm{age/yr})$	A_V/mag
1	0.61 +/− 0.01	8.13 +/− 0.03	0.33 +/− 0.10
2	1.20 +/− 0.03	7.09 +/− 0.04	2.55 +/− 0.09
3	0.79 +/− 0.05	7.72 +/− 0.11	0.55 +/− 0.13
4	0.90 +/− 0.04	7.52 +/− 0.08	0.14 +/− 0.10
5	1.24 +/− 0.09	6.87 +/− 0.28	0.33 +/− 0.10
6	0.72 +/− 0.05	7.83 +/− 0.14	0.36 +/− 0.15
7	1.04 +/− 0.01	7.31 +/− 0.01	2.11 +/− 0.06
8	1.07 +/− 0.01	7.26 +/− 0.01	1.88 +/− 0.05
9	0.95 +/− 0.01	7.45 +/− 0.01	1.65 +/− 0.08
10	0.91 +/− 0.01	7.52 +/− 0.01	1.15 +/− 0.07

Note—Only a portion of this table is shown here to demonstrate its form and content. A machine-readable version is available for all 144 sources detected inside the PDR and outside the CO cores.

Figure 78. Table 16 from Stellar Populations and Molecular Gas Composition in the Low Metallicity Environment of WLM by Archer et al. (2025) in press in the Astronomical Journal.

Table 17. Mass and age for stars outside the PDR and outside CO cores not detected in the F275W filter.

	$\log_{10}(M/M_\odot)$	$\log_{10}$(age/yr)	A_V/mag
1	1.06 +/− 0.01	7.30 +/− 0.01	2.26 +/− 0.03
2	1.29 +/− 0.01	6.96 +/− 0.01	3.07 +/− 0.06
3	1.52 +/− 0.01	6.77 +/− 0.01	3.89 +/− 0.06
4	1.52 +/− 0.01	6.76 +/− 0.01	3.61 +/− 0.06
5	1.13 +/− 0.01	7.16 +/− 0.01	2.44 +/− 0.08
6	1.12 +/− 0.05	7.17 +/− 0.09	2.70 +/− 0.13
7	1.10 +/− 0.01	7.21 +/− 0.01	2.60 +/− 0.09
8	2.02 +/− 0.01	6.44 +/− 0.01	4.00 +/− 0.01
9	1.03 +/− 0.01	7.35 +/− 0.01	1.93 +/− 0.02
10	1.63 +/− 0.01	6.66 +/− 0.01	3.99 +/− 0.01

Note—Only a portion of this table is shown here to demonstrate its form and content. A machine-readable version is available for all 78 sources detected outside the PDR and outside the CO cores.

Figure 79. Table 17 from Stellar Populations and Molecular Gas Composition in the Low Metallicity Environment of WLM by Archer et al. (2025) in press in the Astronomical Journal.

4.4 Discussion

Estimating molecular gas mass in low-metallicity galaxies like WLM remains a significant challenge due to the high fraction of CO-dark gas. Elmegreen *et al.* (2013) estimated α_{CO} for WLM using dust mass inferred from 160μm emission from the Spitzer Local Volume Survey (Dale *et al.* 2009) and 870μm emission from the APEX telescope. By adjusting the dust-to-gas ratio for WLM's lower metallicity, they determined a dust-derived α_{CO} of 124 ± 60 $M_\odot$ pc^{-2} K^{-1} km^{-1} s. Using this α_{CO}

value and the CO core luminosity in our region, the total H_2 mass would be:

$$\begin{aligned} M_{gas} &= \alpha_{CO} \times L_{CO} \\ &= (124 \pm 60\ M_\odot\ \text{pc}^{-2}\ \text{K}^{-1}\ \text{km}^{-1}\ \text{s}) \\ &\quad\ \times (935 \pm 60\ \text{K km s}^{-1}\ \text{pc}^2) \\ &\approx 115{,}900 \pm 5{,}700\ M_\odot, \end{aligned} \tag{4.9}$$

where L_{CO} is the summed L_{CO} values for the six CO cores in the region from Rubio *et al.* (2015, Table 1). Alternatively, computing the α_{CO} from our total molecular gas mass of $1 \times 10^5\ M_\odot$, we find:

$$\begin{aligned} \alpha_{\text{CO}} &= M_{gas}/L_{CO} \\ &= \frac{(1 \times 10^5 \pm 5 \times 10^4\ M_\odot)}{(935 \pm 60\ \text{K km s}^{-1}\ \text{pc}^2)} \\ &\approx 100 \pm 50\ M_\odot\ \text{pc}^{-2}\ \text{K}^{-1}\ \text{km}^{-1}\ \text{s}, \end{aligned} \tag{4.10}$$

which is consistent with the dust-derived α_{CO} found by Elmegreen *et al.* (2013).

The high fraction of CO-dark gas in WLM indicates that a substantial portion of the molecular gas available for star formation exists in a state not directly detectable via CO emission. Studies of other low metallicity galaxies such as the SMC, LMC, and the Dwarf Galaxy Survey (DGS) find 70% to 100% of the molecular hydrogen in low-metallicity galaxies ($Z = 0.02$ to $0.6\ Z_\odot$) is CO-dark, increasing with lower metallicity (e.g. Requena-Torres *et al.* 2016; Chevance *et al.* 2020b; Madden *et al.* 2020; Ramambason *et al.* 2024), which is consistent with our estimated CO-dark gas percentage. Similar to the tiny CO cores detected in WLM, Saldaño *et al.* (2023) find that the molecular mass associated with CO clouds in the SMC is primarily concentrated in low-mass clouds distributed throughout the galaxy. This reinforces the understanding that CO-bright regions correspond to the densest, most shielded parts of molecular clouds in low-metallicity environments, while CO-dark regions constitute a diffuse and widespread reservoir of H_2 (Wolfire *et al.* 2010; Krumholz *et al.* 2012; Bolatto *et al.* 2013) or cold H I (Hu *et al.* 2021, 2022, 2023). These findings underscore the necessity of accounting for CO-dark gas when evaluating the star formation potential of galaxies, particularly in low-metallicity conditions. The agreement between the molecular gas mass inferred from dust measurements (Elmegreen *et al.* 2013) and that estimated by combining stellar mass with an assumed 2% star formation efficiency is encouraging. If the dust-related total gas mass is assumed to be the most reliable, then the missing low mass stars suggest that the product of the efficiency per unit free fall time and the number of free fall times for star formation could be low by a factor of $\sim$2, which is the likely correction for stellar mass given a standard IMF. For example, the 30 Myr window for our evaluation of young stellar mass could represent two free fall times on this large scale, rather than one as assumed.

4.5 Summary and Conclusions

In this study, we explored the stellar and gas characteristics within the nearby galaxy WLM using multi-wavelength *HST* imaging and ALMA CO(1–0) and CO(2-1) observations. By employing photometry across five *HST* filters ranging from 2709.7 to 6242.6 Å, we classified stars and distinguished them from background galaxies, allowing us to analyze stellar masses, ages, and A_V using the PARSEC isochrone models. Our results demonstrate that stars located within the PDR and the CO cores, as well as those outside these regions, exhibit similar distributions in age, mass, and optical depth, indicating a uniform stellar population across the observed area.

To provide a comprehensive assessment of the gas content, we incorporated existing

Table 18. Gas masses in the targeted region

Type	Mass ($M_\odot$)
H I	1,620,000 ± 600
Stars	2,000 ± 300
CO_{vir}	20,000 ± 6,000
Total (molecular)[a]	100,000 ± 5,000
CO-dark [a]	80,000 ± 5,000

[a] Assuming 2% ± 1% of molecular gas is converted to stars (Krumholz et al. 2012)

Figure 80. Table 18 from Stellar Populations and Molecular Gas Composition in the Low Metallicity Environment of WLM by Archer et al. (2025) in press in the Astronomical Journal.

H I data and estimated the total molecular gas mass, including contributions from CO-dark molecular gas. Our analysis revealed a significant fraction of CO-dark gas, emphasizing its critical role in molecular gas mass estimates that cannot rely solely on CO observations. Additionally, the dust-derived $\alpha_{\rm CO}$ for WLM from Elmegreen *et al.* (2013) yields a total molecular gas mass consistent with our estimate based on stellar mass and an assumed star formation efficiency of 2%. However, the stellar mass estimate excludes lower-mass stars that were not detected in our sample. This agreement suggests that combining stellar mass with a 2% star formation efficiency provides an alternative for estimating total molecular gas mass in star-forming regions when dust and CO data are unavailable, though both methods likely underestimate the actual molecular gas mass.

This work examines the molecular gas composition and star formation processes in low-metallicity environments. The results highlight the critical role of CO-dark gas in these systems. Expanding this analysis to a larger sample of star-forming regions within WLM and other low-metallicity galaxies could determine whether the high CO-dark gas content observed in this region is a common characteristic or a unique feature. Such investigations would enhance our understanding of the gas reservoirs that fuel star formation across diverse galactic environments and contribute to a more comprehensive framework for star formation in the local universe.

4.6 Acknowledgements

This research is based on observations made with the NASA/ESA Hubble Space Telescope obtained from the Space Telescope Science Institute, which is operated by the Association of Universities for Research in Astronomy, Inc., under NASA contract NAS 5–26555. These observations are associated with program HST-GO-17068.

M.R. wishes to acknowledge support from ANID(CHILE) through Basal FB210003.

This paper makes use of the following ALMA data: ADS/JAO.ALMA#2012.1.00208.S. ALMA is a partnership of ESO (representing its member states), NSF (USA), and NINS (Japan), together with NRC (Canada), MOST and ASIAA (Taiwan), and KASI (Republic of Korea), in cooperation with the Republic of Chile. The Joint ALMA Observatory is operated by ESO, AUI/NRAO and NAOJ. The National Radio Astronomy Observatory is a facility of the National Science Foundation operated under cooperative agreement by Associated Universities, Inc.

We thank the referee for their thorough review and constructive feedback, which significantly improved the quality and clarity of this manuscript.

Lowell Observatory sits at the base of mountains sacred to tribes throughout the

region. We honor their past, present, and future generations, who have lived here for millennia and will forever call this place home.

*Facilities:*ALMA, HST(WFC3/UVIS) *Software:*IRAF (Tody 1986), scikit-learn (Pedregosa *et al.* 2011), AdvancedHMC.jl (Xu *et al.* 2020), CMD (Bressan *et al.* 2012; Chen *et al.* 2014, 2015; Tang *et al.* 2014; Marigo *et al.* 2017; Pastorelli *et al.* 2019, 2020), Julia (Bezanson *et al.* 2017), Matplotlib (Hunter 2007), NumPy (Harris *et al.* 2020), Optim.jl (Mogensen and Riseth 2018)

4.7 APPENDIX

4.7.1 Sharpness and Chi Parameters

The sharpness and chi parameters for all objects determined to be stars are included in tables shown in Figures 81, 82, 83, 84, 85, 86, and 87. The full tables from Figures 82, 84, 86, and 87 are available in machine-readable format in the online materials.

4.7.2 SED fits

Corner plots of the SED fits for a representative star from each of the seven categories based on their proximity to the PDR and CO cores, along with whether or not they were detected in the F275W filter, are show in Figures 88, 92, 89, 93, 90, 91, and 94. No additional stars were detected away from the PDR and projected inside the CO cores when excluding the F275W filter. The values shown in the plots are the posterior median (50th percentile) along with the 84th and 16th percentiles as the upper and lower errors respectively for each parameter. Figure 93 in particular shows how degeneracies between mass and age can result in multiple solutions.

Table 19. The sharpness and chi parameters for the five *HST* filters for sources inside the PDR and projected inside the CO cores

	F275W Sharpness	F275W χ	F336W Sharpness	F336W χ	F438W Sharpness	F438W χ	F555W Sharpness	F555W χ	F625W Sharpness	F625W χ
1	0.12	0.25	−0.07	0.23	−0.06	0.5	−0.06	0.57	−0.43	0.89
2	0.01	0.21	−0.03	0.34	0.01	0.37	0.02	0.38	−0.08	0.54

Figure 81. Table 19 from Stellar Populations and Molecular Gas Composition in the Low Metallicity Environment of WLM by Archer et al. (2025) in press in the Astronomical Journal.

Table 20. The sharpness and chi parameters for the five *HST* filters for sources inside the PDR and outside the CO cores

	F275W Sharpness	F275W χ	F336W Sharpness	F336W χ	F438W Sharpness	F438W χ	F555W Sharpness	F555W χ	F625W Sharpness	F625W χ
1	−0.07	0.33	−0.21	0.35	−0.18	0.70	−0.11	0.82	−0.32	0.85
2	−0.01	0.11	−0.16	0.26	−0.18	0.96	−0.10	1.08	−0.35	2.75
3	−0.09	1.19	0.09	0.86	−0.09	1.14	−0.21	0.89	−0.07	1.92
4	−0.07	0.64	−0.22	0.86	−0.01	0.75	−0.09	1.40	−0.56	1.69
5	−0.16	0.53	−0.34	0.76	−0.22	1.20	−0.12	1.22	−0.37	2.17
6	−0.16	0.44	0.11	0.41	−0.04	0.48	−0.09	0.63	−0.44	1.08
7	−0.16	0.28	−0.11	0.33	−0.33	0.62	−0.30	0.63	−0.21	0.62
8	0.01	0.20	−0.17	0.54	−0.14	1.93	−0.04	2.09	−0.31	3.81
9	0.10	0.77	0.23	1.09	0.24	3.10	0.25	2.52	−0.44	3.44
10	−0.08	0.43	−0.28	0.49	−0.18	0.59	−0.42	0.68	−0.28	1.03

NOTE—Only a portion of this table is shown here to demonstrate its form and content. A machine-readable version is available for all 443 sources detected inside the PDR and outside the CO cores.

Figure 82. Table 20 from Stellar Populations and Molecular Gas Composition in the Low Metallicity Environment of WLM by Archer et al. (2025) in press in the Astronomical Journal.

Table 21. The sharpness and chi parameters for the five *HST* filters for sources outside the PDR and projected inside the CO cores

	F275W Sharpness	F275W χ	F336W Sharpness	F336W χ	F438W Sharpness	F438W χ	F555W Sharpness	F555W χ	F625W Sharpness	F625W χ
1	0.11	0.70	0.05	0.83	0.14	1.41	0.77	4.14	−0.02	1.15
2	0.19	0.41	0.24	0.34	0.41	0.62	0.24	1.16	−0.13	0.63

Figure 83. Table 21 from Stellar Populations and Molecular Gas Composition in the Low Metallicity Environment of WLM by Archer et al. (2025) in press in the Astronomical Journal.

Table 22. The sharpness and chi parameters for the five *HST* filters for sources outside the PDR and outside the CO cores

	F275W Sharpness	F275W χ	F336W Sharpness	F336W χ	F438W Sharpness	F438W χ	F555W Sharpness	F555W χ	F625W Sharpness	F625W χ
1	−0.07	0.25	−0.22	0.31	0.02	0.32	0.01	0.49	−0.17	0.63
2	−0.11	0.32	−0.01	0.33	−0.11	0.50	−0.02	0.52	−0.43	1.62
3	0.08	0.11	−0.05	0.22	−0.01	0.40	0.05	0.51	−0.49	0.96
4	0.09	0.13	−0.11	0.34	0.57	2.00	0.65	2.02	−0.56	2.19
5	−0.05	0.26	−0.21	0.42	−0.01	0.46	−0.03	0.57	−0.14	0.65
6	0.01	0.26	−0.01	0.58	0.28	1.03	−0.11	0.63	−0.38	1.44
7	−0.62	0.17	−0.21	0.27	0.05	0.51	−0.04	0.85	−0.38	1.15
8	−0.25	0.20	−0.18	0.44	−0.10	1.51	−0.06	1.72	−0.38	2.86
9	−0.12	0.93	−0.06	0.92	0.10	1.34	0.16	1.08	−0.06	1.15
10	−0.05	0.17	−0.02	0.29	0.14	0.86	0.14	0.71	−0.22	1.24

Note—Only a portion of this table is shown here to demonstrate its form and content. A machine-readable version is available for all 566 sources detected outside the PDR and outside the CO cores.

Figure 84. Table 22 from Stellar Populations and Molecular Gas Composition in the Low Metallicity Environment of WLM by Archer et al. (2025) in press in the Astronomical Journal.

Table 23. The sharpness and chi parameters for the four *HST* filters for the source inside the PDR and projected inside the CO cores not detected in the F275W filter

	F336W Sharpness	F336W χ	F438W Sharpness	F438W χ	F555W Sharpness	F555W χ	F625W Sharpness	F625W χ
1	−0.23	0.27	0.04	0.24	0.46	0.60	−0.24	0.61

Figure 85. Table 23 from Stellar Populations and Molecular Gas Composition in the Low Metallicity Environment of WLM by Archer et al. (2025) in press in the Astronomical Journal.

Table 24. The sharpness and chi parameters for the four *HST* filters for sources inside the PDR and outside the CO cores not detected in the F275W filter

	F336W Sharpness	F336W χ	F438W Sharpness	F438W χ	F555W Sharpness	F555W χ	F625W Sharpness	F625W χ
1	−0.05	0.22	−0.00	0.40	0.05	0.51	−0.49	0.95
2	−0.11	0.34	0.57	2.00	0.65	2.02	−0.56	2.19
3	−0.16	0.49	−0.14	0.61	−0.27	0.85	−0.28	0.98
4	−0.06	0.92	0.10	1.34	0.16	1.07	−0.06	1.15
5	−0.19	2.60	0.28	2.31	0.14	2.12	−0.51	3.68
6	0.03	0.35	0.04	0.47	0.10	0.80	−0.16	0.83
7	−0.29	0.21	0.10	0.53	0.13	0.53	−0.56	1.57
8	−0.18	0.34	0.07	0.94	0.05	0.96	−0.42	1.37
9	−0.38	0.29	−0.03	0.49	−0.02	0.54	−0.31	1.28
10	−0.13	0.20	−0.14	0.55	−0.05	1.23	−0.62	3.40

NOTE—Only a portion of this table is shown here to demonstrate its form and content. A machine-readable version is available for all 144 sources detected inside the PDR and outside the CO cores.

Figure 86. Table 24 from Stellar Populations and Molecular Gas Composition in the Low Metallicity Environment of WLM by Archer et al. (2025) in press in the Astronomical Journal.

Table 25. The sharpness and chi parameters for the four *HST* filters for sources outside the PDR and outside the CO cores not detected in the F275W filter

	F336W Sharpness	F336W χ	F438W Sharpness	F438W χ	F555W Sharpness	F555W χ	F625W Sharpness	F625W χ
1	0.16	0.20	−0.01	0.63	0.05	1.00	−0.44	2.84
2	−0.30	0.30	−0.10	0.51	0.09	0.77	−0.28	1.88
3	−0.10	0.30	−0.05	1.27	−0.13	1.76	−0.21	4.00
4	−0.03	0.38	0.09	0.72	−0.04	1.25	−0.35	3.83
5	−0.13	0.29	0.28	0.90	0.17	1.08	−0.37	1.32
6	−0.37	0.28	−0.20	0.40	−0.10	0.50	−0.13	0.93
7	−0.07	0.21	−0.05	0.63	0.07	0.68	−0.13	1.55
8	−0.05	0.49	0.29	3.19	0.05	4.45	−0.23	5.18
9	−0.09	0.23	−0.02	0.55	0.06	0.68	−0.13	2.05
10	0.17	0.18	−0.13	0.78	0.05	1.35	−0.09	3.05

Note—Only a portion of this table is shown here to demonstrate its form and content. A machine-readable version is available for all 78 sources detected outside the PDR and outside the CO cores.

Figure 87. Table 25 from Stellar Populations and Molecular Gas Composition in the Low Metallicity Environment of WLM by Archer et al. (2025) in press in the Astronomical Journal.

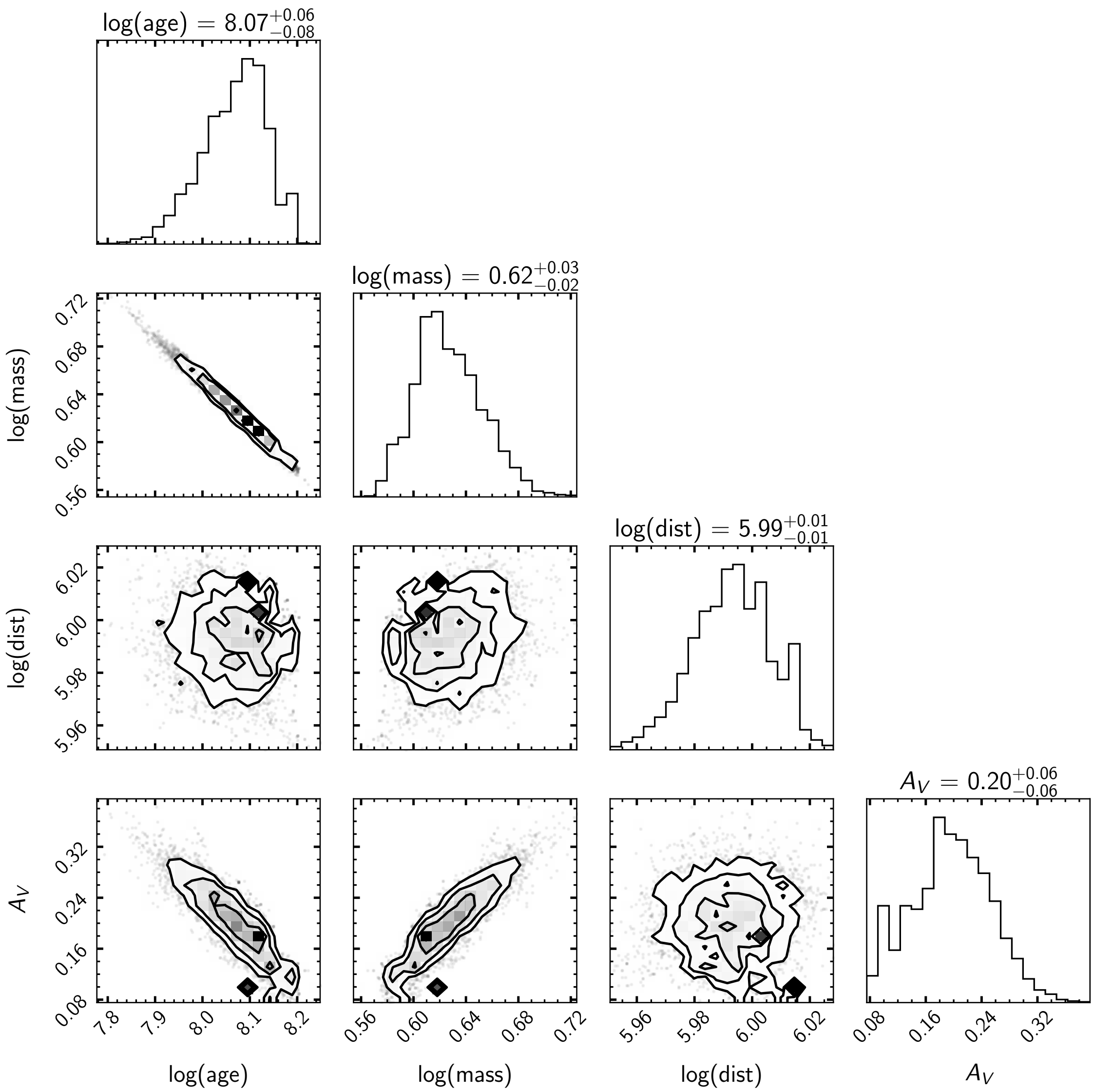

Figure 88. Corner plot of samples drawn from the posterior distribution for Star 1 in the table shown in Figure 72 of stars inside the PDR and projected inside the CO cores demonstrating the degeneracies between mass, age, distance, and dust.

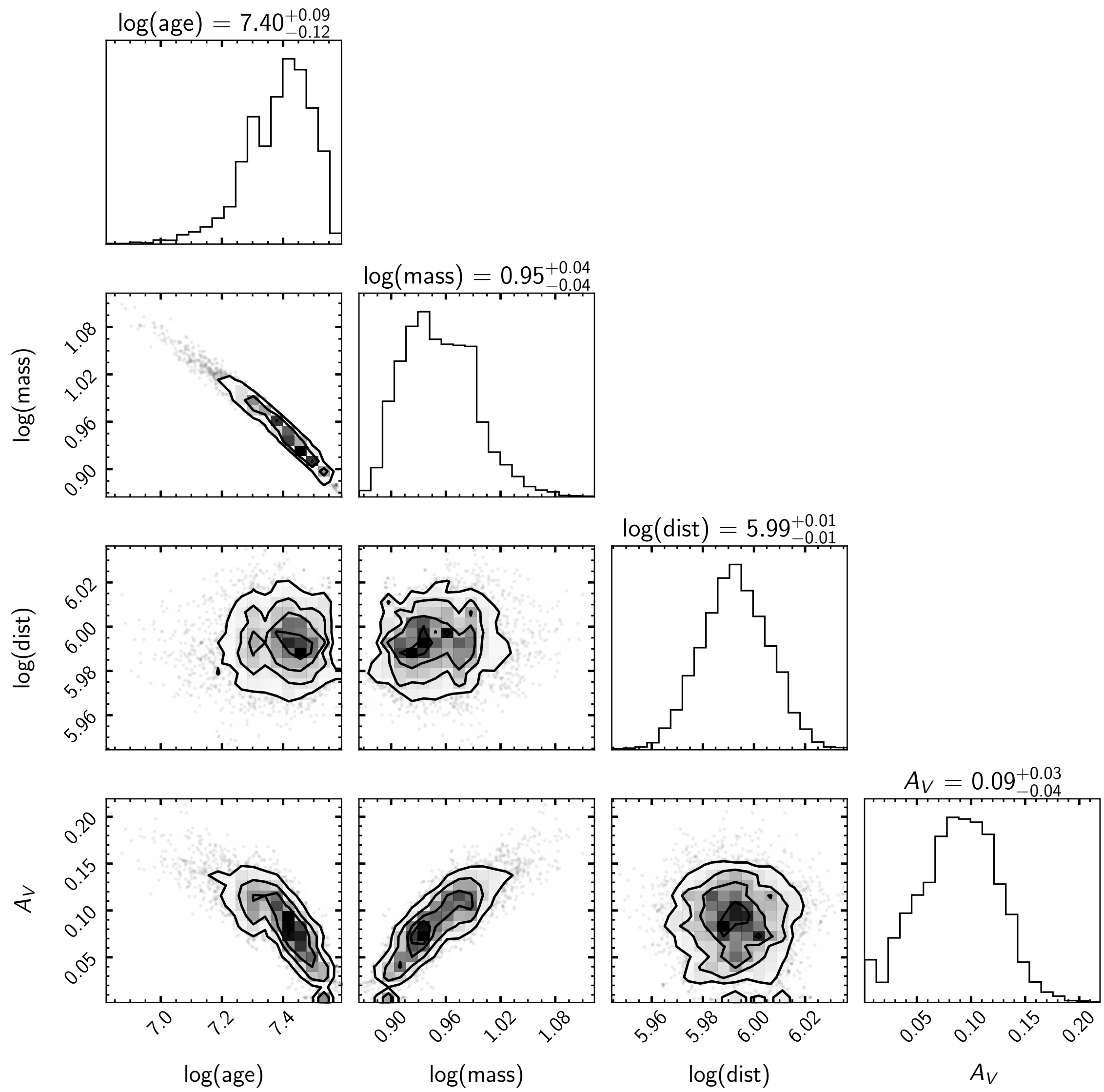

Figure 89. Corner plot of samples drawn from the posterior distribution for Star 3 in the table shown in Figure 73 of stars inside the PDR and away from the CO cores demonstrating the degeneracies between mass, age, distance, and dust.

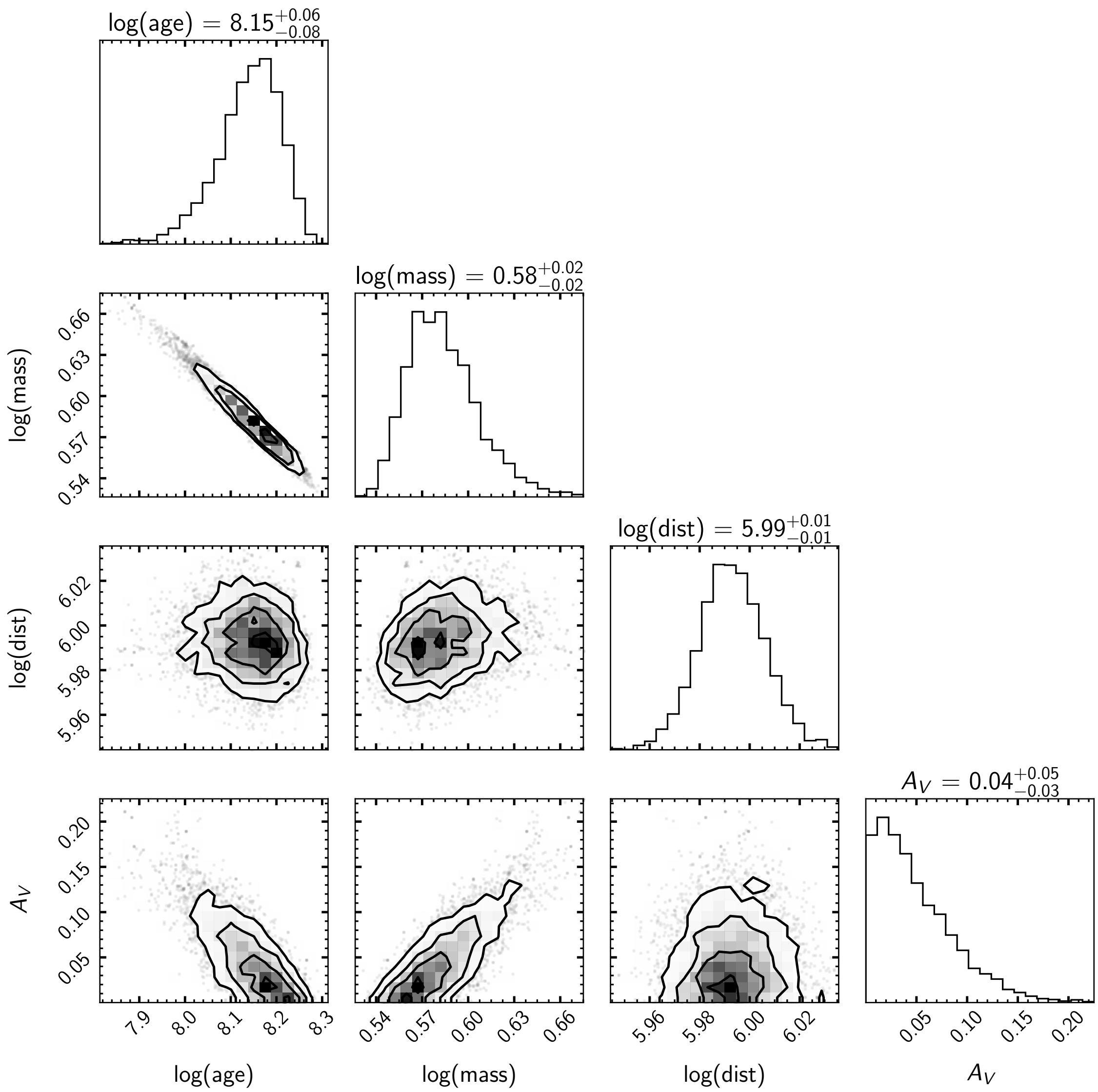

Figure 90. Corner plot of samples drawn from the posterior distribution for Star 2 in the table shown in Figure 74 of stars away from the PDR and projected inside the CO cores demonstrating the degeneracies between mass, age, distance, and dust.

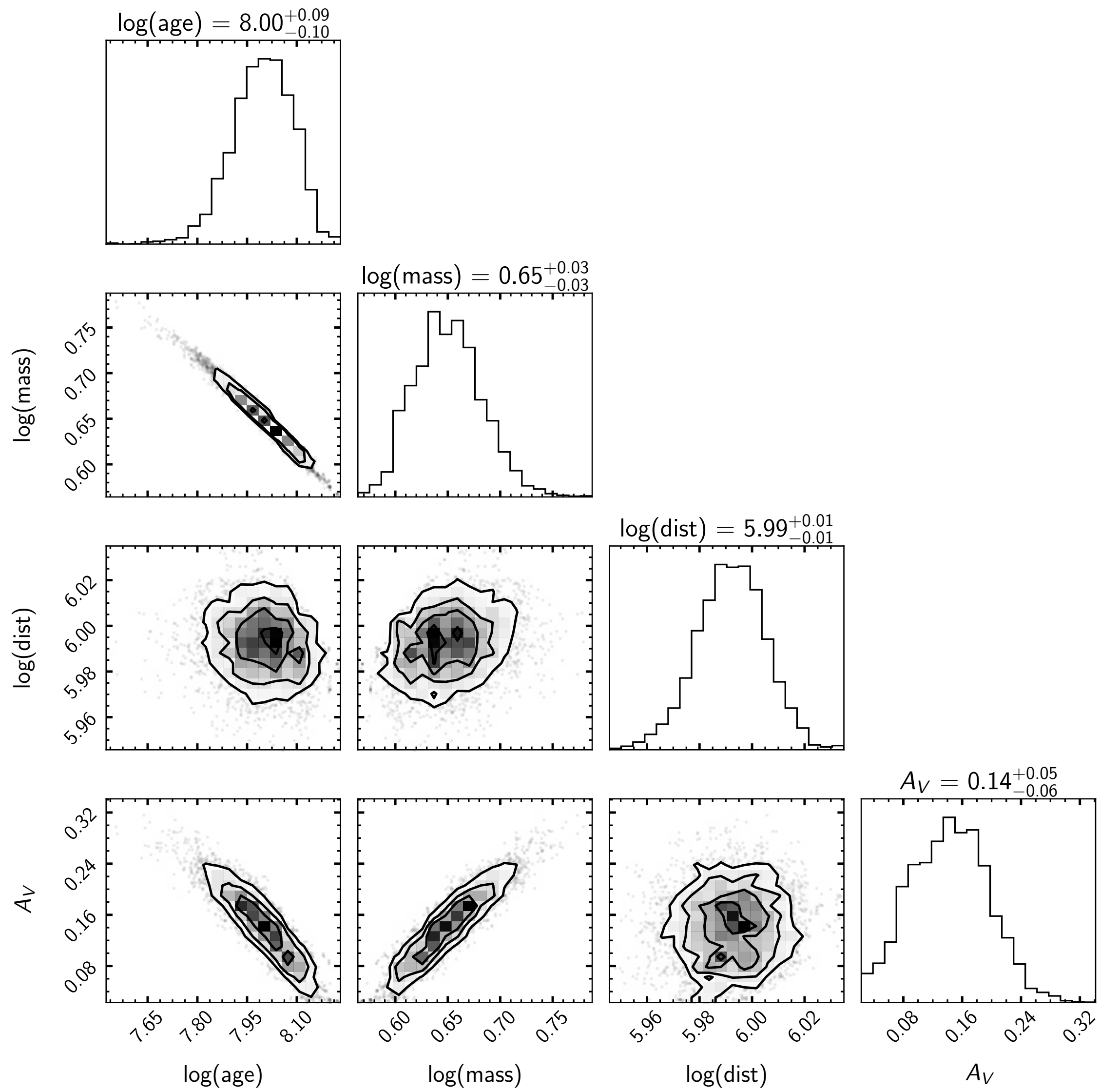

Figure 91. Corner plot of samples drawn from the posterior distribution for Star 5 in the table shown in Figure 75 of stars away from the PDR and away from the CO cores demonstrating the degeneracies between mass, age, distance, and dust.

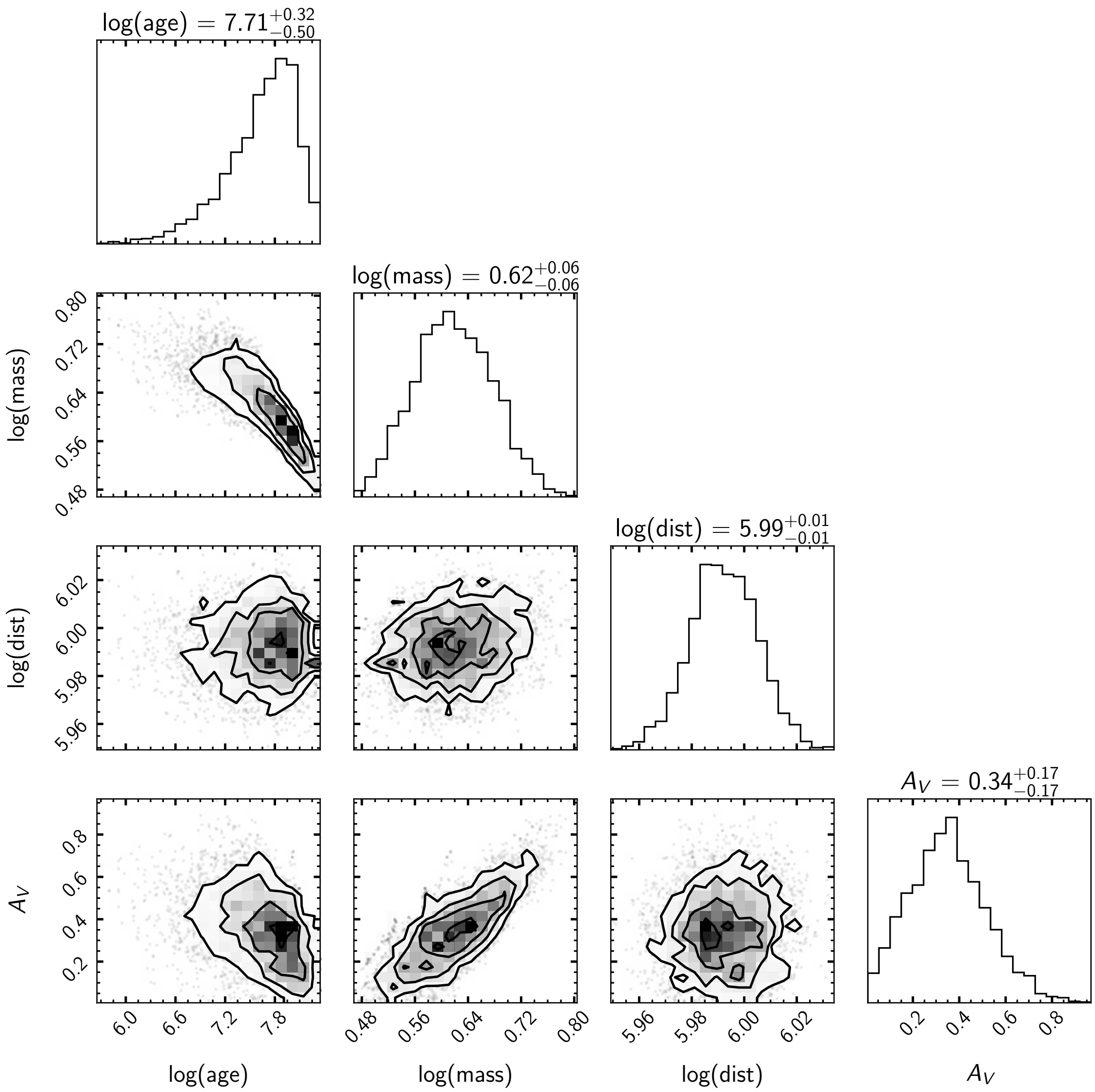

Figure 92. Corner plot of samples drawn from the posterior distribution for Star 1 in the table shown in Figure 77 of the star in the PDR and projected inside the CO cores not detected in the F275W filter demonstrating the degeneracies between mass, age, distance, and dust.

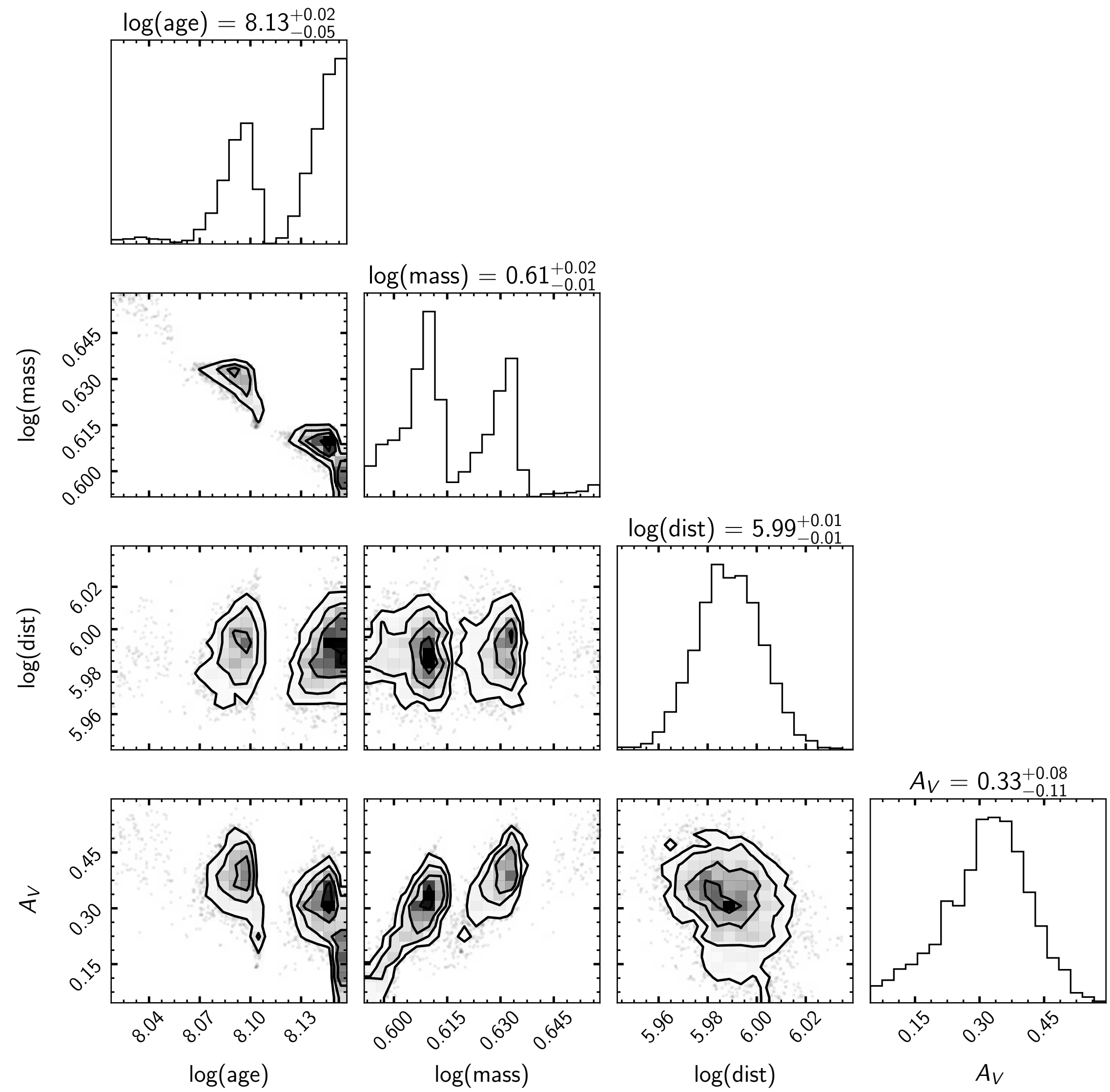

Figure 93. Corner plot of samples drawn from the posterior distribution for Star 1 in the table shown in Figure 78 of stars in the PDR and away from the CO cores not detected in the F275W filter demonstrating the degeneracies between mass, age, distance, and dust.

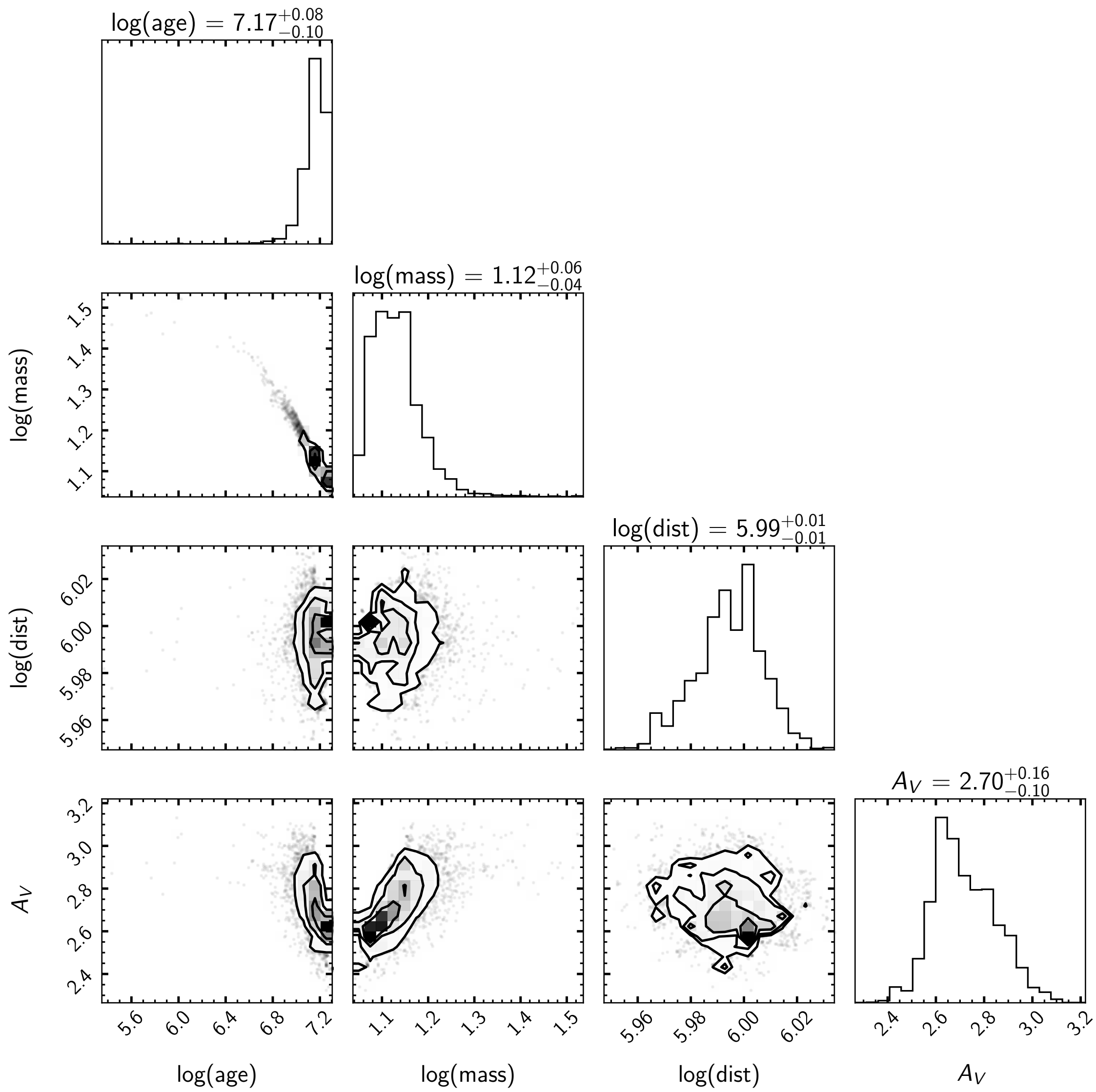

Figure 94. Corner plot of samples drawn from the posterior distribution for Star 6 in the table shown in Figure 79 of stars away from the PDR and away from the CO cores not detected in the F275W filter demonstrating the degeneracies between mass, age, distance, and dust.

Chapter 5

BRINGING LECTURE-TUTORIALS ONLINE: AN ANALYSIS OF A NEW STRATEGY TO TEACH PLANET FORMATION IN THE UNDERGRADUATE CLASSROOM

[1,2]Haylee N. Archer, [1]Molly N. Simon, [1]Chris Mead, [3]Edward E. Prather, [1]Mia Brunkhorst, [1]Diana Hunsley

[1]School of Earth and Space Exploration, Arizona State University, Tempe, AZ, USA

[2]Lowell Observatory, Flagstaff, AZ, USA

[3]Department of Astronomy, University of Arizona, Tucson, AZ, USA

Published in the Astronomy Education Journal at doi.org/10.32374/AEJ.2024.4.1.090ra (Archer *et al.* 2024b)

Abstract: Previous studies conclusively show that pencil-and-paper lecture-tutorials (LTs) are incredibly effective at increasing student engagement and learning gains on a variety of topics when compared to traditional lecture. LTs in astronomy are post-lecture activities developed with the intention of helping students engage with conceptual and reasoning difficulties around a specific topic with the end goal of them developing a more expert-like understanding of astrophysical concepts. To date, all astronomy LTs have been developed for undergraduate courses taught in-person. Increases in online course enrollments and the COVID-19 pandemic further highlighted the need for additional interactive, research-based, curricular materials designed for

online classrooms. To this end, we developed and assessed the efficacy of an innovative, interactive LT designed to teach planet formation in asynchronous, online, introductory astronomy courses for undergraduates. We utilized the Planet Formation Concept Inventory to compare learning outcomes between courses that implemented the new online, interactive LT, and those that used either a lecture-only approach or utilized a standard pencil-and-paper LT on the same topic. Overall, learning gains from the standard pencil-and-paper LT were statistically indistinguishable from the in-person implementation of the online LT and both of these conditions outperformed the lecture-only condition. However, when implemented asynchronously, learning gains from the online LT were lower and not significantly above the lecture-only condition. While improvements can be made to improve the online LT in the future, the current discipline ideas still outperform traditional lecture, and can be used as a tool to teach planet formation effectively.

5.1 Introduction

The United States requires all 4-year college students to complete at least one semester-long science course, enrolling hundreds of thousands of students in general education science courses every year (Rudolph *et al.* 2010). For non-science majors (students who do not intend to pursue an undergraduate science degree), these courses are often their last formal science instruction, which influences their personal viewpoints and civil engagement with scientific issues (Hobson 2008). In a world where the internet and other media offer conflicting information on scientific research, the importance of scientific and data literacy is at an all-time high. Developing classroom materials for these courses that address common preconceptions and increase student understanding is essential for creating "competent outsiders", non-scientists who understand how science relates to local or personal issues without relying on specific scientific concepts learned in the classroom (Feinstein *et al.* 2013). An introductory, semester-long, astronomy course for non-science majors, commonly referred to as ASTRO 101 is often taken as this general science elective. As such, it is especially important to ensure that students leave ASTRO 101 with a better understanding of our place in the Universe before becoming active members of society who will engage with broader scientific concepts outside of the classroom.

To date, traditional lecture is the dominant form of undergraduate instruction, but several cross-disciplinary studies have shown that the implementation of active learning strategies leads to higher student learning outcomes (Chi and Wylie 2014; Freeman *et al.* 2014). While the concept of active learning is broadly defined (Lombardi *et al.* 2021), we define active learning to mean requiring students to interact with and think deeply about classroom material in a meaningful way, as opposed to traditional lecture where students passively receive information. One well-researched active learning strategy in ASTRO 101 is the Lecture-Tutorial. Lecture-Tutorials (LTs) are worksheets designed to supplement lecture, and typically require that students work in small, collaborative groups. The LTs consist of a series of questions that build on one another, and address common conceptual and reasoning difficulties that arise as students learn about a variety of topics in astronomy. In the domain of ASTRO 101 courses, LTs have been used for decades, resulting in significant increases in student learning on a variety of topics (e.g. Prather *et al.* 2004; LoPresto and Murrell 2009; Wallace *et al.* 2012; Lombardi *et al.* 2021).

Far less research has been conducted on the use of active learning strategies like LTs in online astronomy courses, and there is a scarcity of learner-centered, research-based instructional materials designed for the online student population (Simon *et al.* 2022). This insufficiency was further highlighted when the COVID-19 pandemic required courses traditionally taught in-person to pivot online with little notice. Even prior to the COVID-19 pandemic, online course enrollments have increased exponentially due to online courses' accessibility and appeal (e.g. Allen and Seaman 2013; Cooper *et al.* 2019). Students benefit from the ability to enroll in courses without the need to commute to a physical classroom, expanding access to higher education to students who may otherwise have difficulty attending courses in-person (e.g. caretakers, active military personnel, and full-time employees). Increases in online ASTRO 101 enrollments coupled with limited active learning-based curricular materials accessible in the online format motivated the development of an online LT, and a research effort to assess whether an online LT will lead to student learning that is consistent with what has been seen with the pencil-and-paper LTs.

We created an online LT specifically for ASTRO 101 courses that was designed to actively engage students in learning about the topic of planet formation. We modeled the online LT after the Planet Formation Lecture-Tutorial (PFLT), a version of which is published in *Lecture-Tutorials for Introductory Astronomy, 4th Edition* (Prather *et al.* 2021). The discovery and characterization of over 5,000 planets outside of our Solar System (exoplanets) highlights the importance of integrating planet formation into the ASTRO 101 curriculum. By learning about how planets and planetary systems form, students gain a better understanding of the origin and evolution of both our own Solar System and the discovered planetary systems beyond. Exoplanet discovery and characterization is one of the most active areas of research in astronomy, and it is important that ASTRO 101 students have a preliminary understanding of planet formation in order to make comparisons between exoplanetary systems and our own planetary neighborhood.

Through this online LT development work we explored the following questions: 1. Is the pedagogical approach employed for pencil-and-paper LTs enhanced when converted to a digital version (which includes additional interactive elements)? 2. How do student learning gains compare between the new online LT and the traditional LT, especially when considering the extent of student learning in online asynchronous courses? This paper is organized as follows: we present an overview of the PFLT in Section 5.2 and the translation of the PFLT to our Planet Formation Online Lecture-Tutorial (PFOLT) in Section 5.3. In Section 5.4 we introduce our study participants and describe the assessment used in the study, along with our analysis methods. We present our results and discuss our findings in Section 5.5 and Section 5.6 respectively. Finally, our conclusions and opportunities for future work are presented in Section 5.7.

5.2 Overview of the Planet Formation Lecture-Tutorial (PFLT)

The format and question sequence of the PFLT was modeled after the process used to develop LTs on other disciplinary topics (e.g. Prather *et al.* 2004; Wallace *et al.* 2016, 2021).

The activity employs a variety of representations (graphs, data tables, drawings, etc.) paired with carefully sequenced, questions and tasks intended to engage students in disciplinary discernment and increase their fluency with the topic of planet formation (French and Prather 2020; Simon *et al.* 2022). The PFLT is intended to be administered as a 25-30 minute, small-group (2-3 student per group) activity following a lecture on the topic of planet formation and relevant sub-topics (e.g. gravity, angular momentum, and condensation of the elements). After completing the PFLT, students should be able to:

- Distinguish the formation of out Solar System from the formation of the Universe

- Apply the relationship between distance from the Sun and condensation temperature to predict the composition of planets at a variety of locations
- Identify the location of the frost/snow line and its relationship to planetary composition
- Explain how it could be possible for a gas/ice giant planet to be found inside the frost/snow line of a hypothetical exoplanetary system

These learning outcomes and the overall content presented in the PFLT were informed by prior work investigating ASTRO 101 students' conceptual and reasoning difficulties on the topic of planet formation (Simon *et al.* 2018). Most notably was ASTRO 101 students' inability to distinguish the formation of the Solar System from the formation of the Universe, despite the events being separated by more than nine billion years. To this end, the PFLT begins with a question sequence that culminates with a hypothetical student debate aimed to challenge students' understanding of cosmological time. Hypothetical student debates are prevalent amongst LTs and model conversations free of science jargon between 2-3 students where one student presents a common reasoning difficulty and the other student challenges this reasoning difficulty in favor of a more scientifically accurate explanatory model. An example from the PFLT is below:

Student 1: I think the formation of the Universe and the formation of the

Solar System are totally different events. The Universe formed billions of years before our Solar System.

Student 2: I don't think so. All of the material in the Universe was created during the Big Bang, so our Solar System must have formed when the Universe did, nearly 14 billion years ago.

Do you agree or disagree with either or both of the students? Explain your reasoning.

In this particular example, learners are presented with an opportunity to challenge Student 2, who conflates the formation of the Universe with the formation of our Solar System. Requiring students to confront their own conceptual and reasoning difficulties head-on is an exceptionally valuable tool in promoting a metacognitive approach to

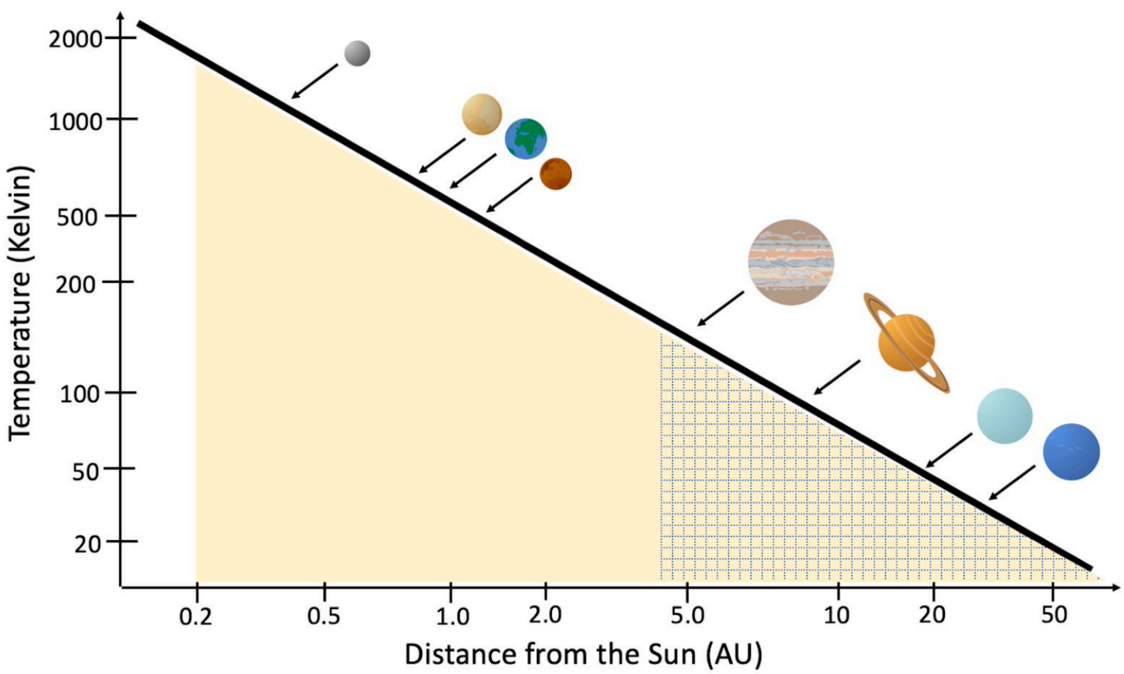

Figure 95. Temperature in the protoplanetary disk at the time of planet formation versus distance from the Sun for our Solar System. The region (and temperature range) where rock and metals condense is shaded in pale yellow, and where hydrogen compounds condense to form ice is overlaid by a blue grid pattern. The relative locations of the planets are indicated by arrows.

learning (in which students cultivate an awareness of their thinking processes and how they learn) leading to more persisting conceptual change (Posner *et al.* 1982; Prather *et al.* 2004).

Students then learn about the timeline of Solar System formation from cloud collapse to the formation of the Sun, the protoplanetary disk, planetesimals, and ultimately, planets. After a short question sequence highlighting the role of gravity in planet formation, the PFLT introduces the concept of condensation temperature, which is a focal point of the remainder of the LT. The condensation temperature component of the PFLT begins with a table consisting of the condensation temperature and relative abundances (mass %) of hydrogen and helium gas, silicates (hereafter referred to as rock) and metals, and hydrogen compounds (e.g. water, methane, and ammonia) in the protoplanetary disk. Students are then shown a graph of the relationship between temperature in the disk at the time of planet formation (y-axis) and distance from the Sun (x-axis) for the planets in our Solar System (Figure 95). The variables represented on the x and y-axes can be approximately represented with a power law for the early solar system. Although the relationship between temperature and distance in actuality is more complex, it is important that introductory students are able to understand at the most fundamental level that temperature in the disk decreases with distance from the central star. Purposefully displaying data in an accessible way is common for pedagogical discipline representations or PDRs. PDRs "depict stylized physical scenarios and highlight discipline relationships that, while invaluable pedagogically, have little to no value to experts and professionals working in that field" (French and Prather 2020, p. 2). PDRs are often included in LTs due to their ability to assist students in developing stronger representational competence surrounding a given topic (French and Prather 2020; Volkwyn *et al.* 2020; Simon *et al.* 2022).

Students use Figure 95 (and the condensation temperature values presented in a corresponding table) to determine the range of distances in the protoplanetary disk over which rock and metals and hydrogen compounds condense during our Solar System's formation. Students are then required to input the solid materials present at the location of each of the planets into a table where a column containing this information is intentionally left blank.

At this point in the PFLT, students are presented with a choice of three diagrams, one of which most accurately represents the distribution of solid material in our Solar System at the time of planet formation (Figure 96).

Through analyzing Figure 96, students integrate the information from multiple data representations (graph and table) to demonstrate an understanding that rocks and metals are able to condense throughout the protoplanetary disk, whereas hydrogen compounds condense only in the outer Solar System beyond the frost line. Next, students engage with a student debate intended to address any reasoning difficulties learners may still have with the relationship between condensation temperature, the frost line, and planetary composition. The student debate is structured as follows:

> Student 1: I think drawing "C" is correct because we know the Terrestrial planets are made of rock and Neptune and Uranus are ice giants so they will be the only planets made of just ice.
>
> Student 2: I agree with you, but I think you need to include Jupiter and Saturn as having some ice too, and based on the graph the blue frost line should be drawn closer to the Sun than Jupiter, so I think it's drawing "B".
>
> Student 3: I think you're right that the frost line should be drawn closer to the Sun, but I think drawing "A" is correct because there were rocks

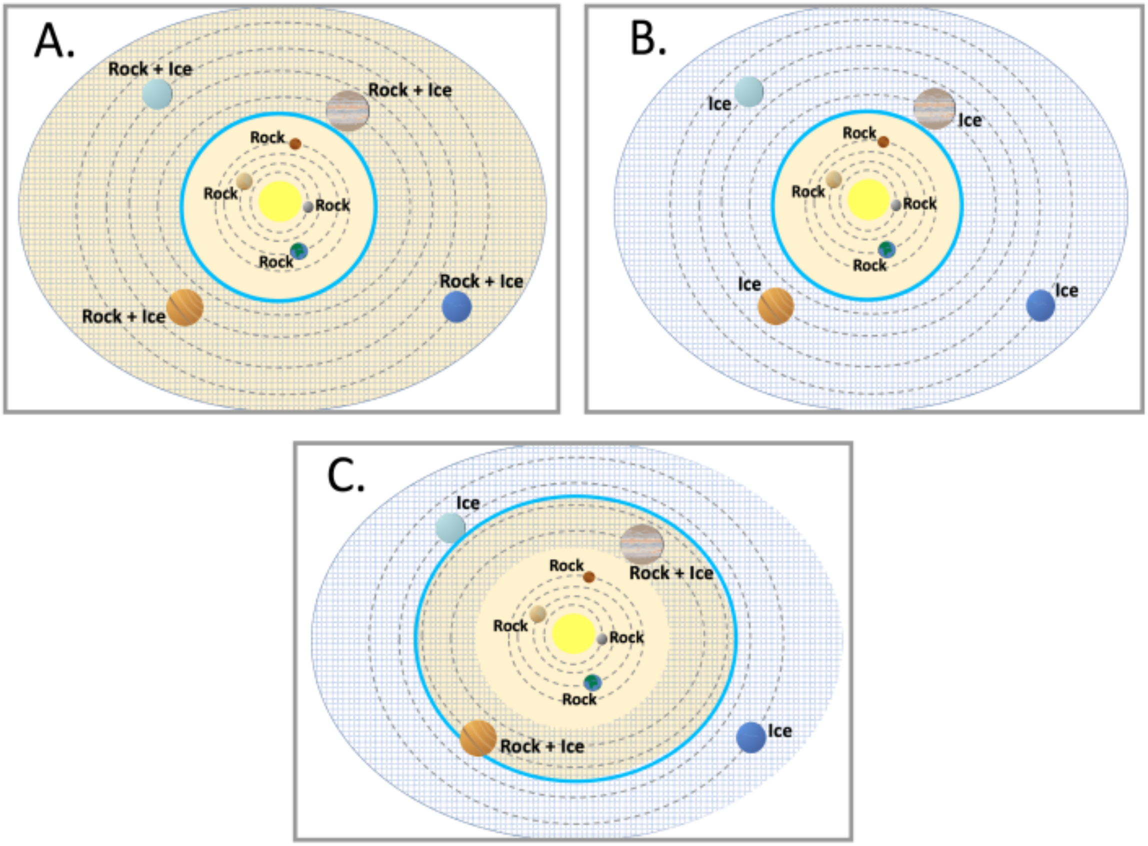

Figure 96. Students are required to select which of the three diagrams (A, B, or C) most accurately represents the solid materials available to each of the planets in our Solar System during formation. Pale yellow corresponds to the region where solid rocks and metals condense, and the blue grid pattern is used to identify the region where hydrogen compounds condense into ice. A thick blue line (known as the snow line or frost line) is drawn to represent the location in the Solar System nearest the Sun where ices can begin to form.

> and metals throughout the early Solar System but ice only formed past the frost line where we find the gas giant planets.
>
> Which student do you agree with? Which do you disagree with? Explain your reasoning.

Through their peer discussions of the range of ideas presented in this student debate, learners have an opportunity to address the most prevalent reasoning difficulties on the topic of condensation temperature, namely that the frost line acts as a barrier between solid rocks/metals and ices, and that rocks and metals are only able to condense

Table 1. Planetary parameters for three planets in a hypothetical exoplanetary system, sorted by planet mass.

Planet Name	Mass (Earth = 1)	Distance from star (AU)	Atmosphere (Large/Small)
A	0.643	1.774	Small
B	11.34	6.482	Large
C	12.01	0.031	Large

Figure 97. Table 1 from Bringing Lecture-Tutorials Online: An Analysis of A New Strategy to Teach Planet Formation in the Undergraduate Classroom by Archer *et al.* (2024b), published in the Astronomy Education Journal.

at distances inward of the frost line (Simon *et al.* 2018). Next, students complete a short fill-in-the-blank section that helps learners develop the relationship between the availability of solids for a particular planet location and the differences in mass between the inner and outer planets in our Solar System.

The PFLT concludes with a section that requires students to apply their knowledge of the relationship between condensation temperature, planet mass, and distance from the central star to a hypothetical exoplanetary system with three planets. Relevant properties for each of the planets in this system are listed in the table shown in Figure 97.

The goal of this part of the activity is to identify which (if any) of the planets in the hypothetical exoplanetary system are at locations (relative to their host star) we would expect based on what they have learned about planet formation in our Solar System. Once students identify that Planet C is much closer to its host star than what would be expected of a giant planet, we introduce the final student debate of the PFLT.

Student 1: I think that the physics that explains where rock, ice, and gas would exist during the planet formation process doesn't apply when we're dealing with planets in other solar systems.

Student 2: I disagree. I think that the locations where we'd expect to find rock, ice, and gas would be pretty much the same in every solar system. What I think happens is that the star gets way more massive after the solar system forms, and this pulls planets closer in towards the star.

Student 3: We learned that essentially all the mass of a solar system is in the star already, and if it did get more massive it would pull all the planets inward, not just this one gas giant. I think these planets must be interacting with other objects in the solar system and that eventually causes the planet to move out of the position where it was originally forming.

Which student do you agree with? Which do you disagree with? Explain your reasoning.

This final debate introduces the concept that planets may move from the original locations in which they formed. Instructors are encouraged to use this final debate as a launching point to discuss Hot Jupiters, a class of giant exoplanet discovered at distances typically less than 0.1 AU from their host star.

5.3 Translation of the PFLT to the Planet Formation Online Lecture-Tutorial (PFOLT)

The PFOLT is analogous to the PFLT in its learning outcomes, concepts covered, and question sequence. The PFOLT differs from the pencil-and-paper PFLT in the tasks being asked of students at various places in the activity. For example, in the PFOLT, students discover where different materials (e.g. rocks/metals, hydrogen compounds, hydrogen/helium gas) condense in the Solar System by using an interactive simulation to place each material at different distances from the Sun and generating

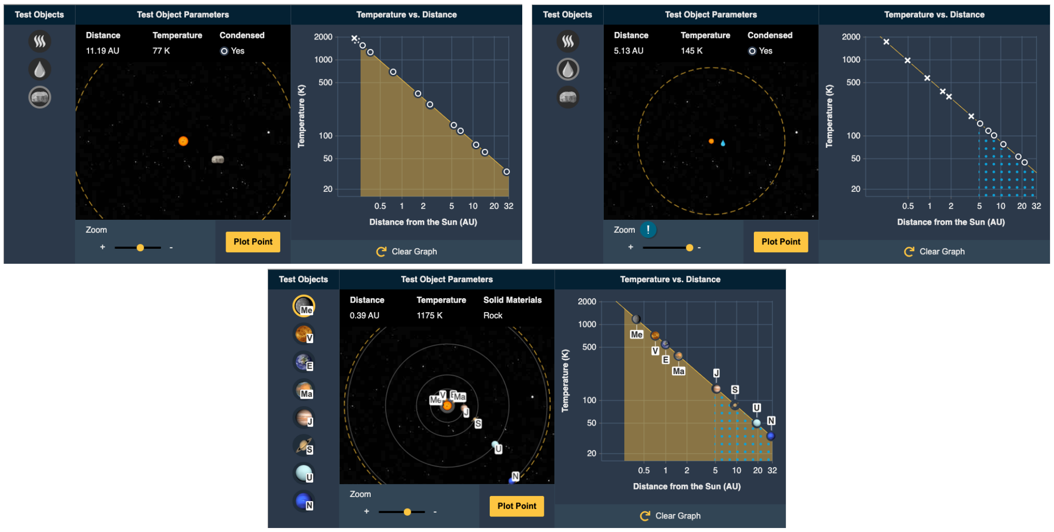

Figure 98. (Top left) PFOLT simulation screenshot illustrating how students place different materials such as rocks and (top right) hydrogen compounds at different locations in the Solar System. When students click “Plot Point”, a circle or “X” appears on the plot indicating whether the material does or does not condense at that location. After plotting enough points, the area below the graph automatically fills in to show the region (and temperature range) over which each material condenses. Yellow corresponds to the region where rocks and metals condense, and the region where hydrogen compounds condense to form ice is overlaid by a blue dot pattern. Bottom: PFOLT simulation screenshot illustrating how students can place the planets in our Solar System at their current locations. As students drag each planet to its correct location, the planet will appear atop the plots generated in the top two panels. This allows students to visualize why the terrestrial planets and gas/ice giants have different compositions. The three panels can be compared to the static version from the PFLT presented in Figure. 95

a plot to visualize whether or not each material condenses at that specific location (Figures 98A and 98B). Students are then taken to a simulation where they can drag each planet in our Solar System to its specific location to better understand which solid materials are available at each location (Figure 98C). This introduces a level of interactivity the pencil-and-paper PFLT cannot afford, as the PFLT asks students to make interpretations about the relationship between condensation temperature and

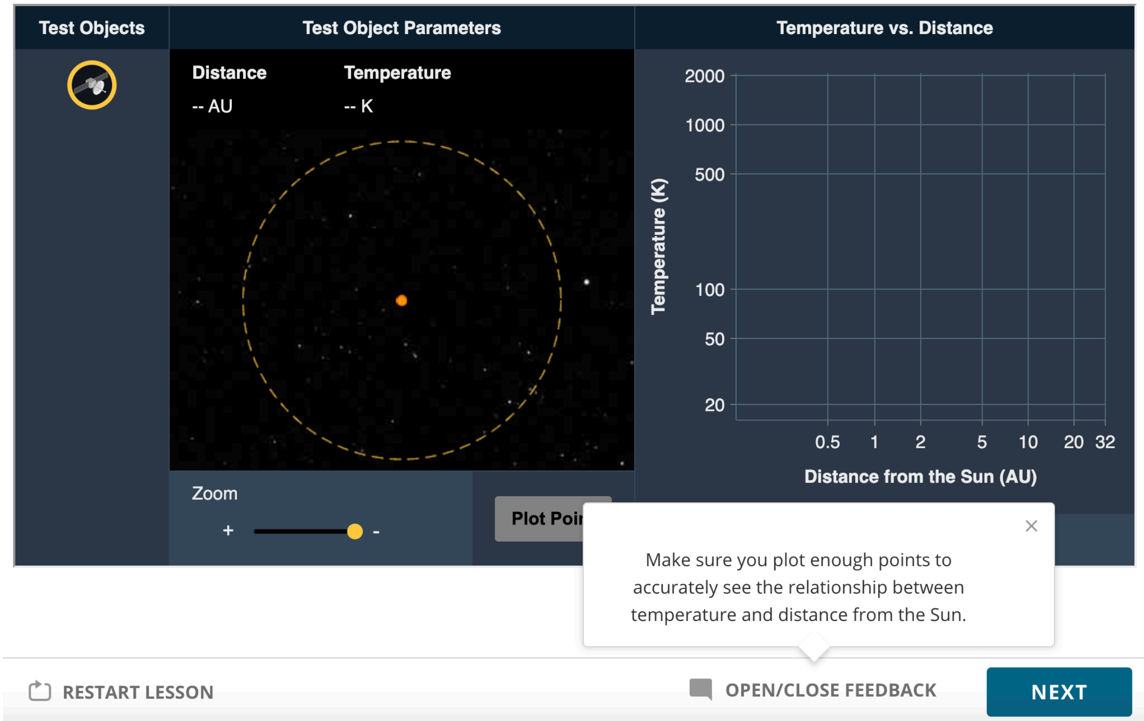

Figure 99. PFOLT simulation screenshot showing feedback that appears after students input an incorrect response. In the case shown above, this feedback appears if the student has not plotted enough points to determine the relationship between temperature in the protoplanetary disk and distance from the Sun.

distance from the Sun using a plot that has already been generated for them (Figure 95).

Due to the slightly more interactive nature of the PFOLT, the online LT takes students approximately 40 minutes to complete. The PFOLT is also intended to supplement a short lecture on the topic of planet formation, and it can be completed by students either collaboratively or independently as long as they have access to the internet. The PFOLT was developed over the Summer and Fall of 2021 in collaboration with Arizona State University's (ASU) Center for Education Through eXploration (ETX Center).

Learning designers at the ETX center have experience outfitting online curriculum with adaptive learning technology. Adaptive learning designs use predetermined rules to provide a learning experience that is tailored to each student's specific sequence of choices and responses. Prior research has shown this approach to learning design to be very effective, rivaling even human tutoring (Vanlehn 2011; Kulik and Fletcher 2016). The key to this effectiveness, as demonstrated by Vanlehn (2011), is a system that provides feedback to students within the problem solving process, not merely at the end. As students progress through the PFOLT, they receive feedback intended to help them reason through challenges until they reach the correct response, as shown in Figure 99. This adaptive feedback allows students in fully asynchronous (i.e. those where instruction is provided solely through pre-recorded material) courses to work through the PFOLT independently, as these students do not have the ability to seek help from their peers or course instructors as they progress through the activity. A complete version of the PFOLT can be accessed free of charge through the NASA Infiniscope website (https://infiniscope.org/) with the lesson title "Solar System Formation".

5.4 Methods

5.4.1 Settings & Participants

We implemented either the PFLT or PFOLT with students enrolled in eleven different astronomy courses at ten institutions of higher education, between January 2022–December 2022. Instructors (and their corresponding institutions) were recruited for this study via email correspondence through an astronomy education listserv called 'astrolrner.' The listserv is hosted by the Center for Astronomy Education based

Table 2. Testing Institution Information

Institution	# of Courses	Institution Type	Course Modality	Activity Implemented
		Spring 2022		
University of Alabama at Birmingham	1	Public University	Online Asynchronous	PFOLT
Glendale Community College[1]	1	Public Community College	Online Asynchronous	PFOLT
Califonia Polytechnic State University, San Luis Obispo	1	Public University	Online Asynchronous	PFOLT
University of Colorado Boulder	1	Public University	In-Person	PFLT
University of Arizona	1	Public University	In-Person	PFLT
University of Alaska	1	Public University	In-Person	PFLT
		Fall 2022		
University of Michigan	1	Public University	Online Asynchronous	PFOLT
New Mexico State University	1	Public University	In-Person	PFOLT
Albion College	1	Private Liberal Arts College	In-Person	PFOLT
Arizona State University	2	Public University	1 Online Asynchronous, 1 In-Person	PFOLT

[1] Located in Glendale, Arizona

Figure 100. Table 2 from Bringing Lecture-Tutorials Online: An Analysis of A New Strategy to Teach Planet Formation in the Undergraduate Classroom by Archer *et al.* (2024b), published in the Astronomy Education Journal.

out of Steward Observatory at the University of Arizona, but anyone who teaches astronomy or is interested in astronomy education research is able to subscribe. Due to the relatively small nature of the astronomy education community, several of the participating instructors were known to the authors personally, but that was not a requirement for the study. The distribution of institutions in terms of geographic location and institution-type (e.g. private versus public) was random, as any instructor who indicated their intent to participate in the study through the listserv was selected.

The implementation sites included one community college and nine four-year colleges and universities with varying degrees of research emphasis. The course modalities were split between in-person and online asynchronous. Originally, we collected data from two additional community colleges with online synchronous and hybrid courses, but they were excluded from the final data set due to low numbers of participants in each category. A complete list of participating institutions from the final data set is provided in the table shown in Figure 100.

The students enrolled in ten of the aforementioned courses were predominantly undergraduate non-science majors in the first two years of their undergraduate tenure. The eleventh course in the final data set was an introductory level earth and space science course that enrolled ∼70% (predominantly students in their first year of university) science majors, and ∼30% non-majors. Enrollments in these courses ranged from 8 to upwards of 200 students. This study was approved by Arizona State University's institutional review board and classified as "exempt," meaning the project did not pose any harm to the study participants and was not subject to further review unless there were significant changes made to the study protocol[3].

5.4.2 Assessments

To evaluate the impact of the PFLT/PFOLT on student learning, participants were given the Planet Formation Concept Inventory (PFCI), a previously validated assessment developed by Simon *et al.* (2019). A concept inventory is a multiple-choice style instrument that addresses a single topic or closely related set of topics and is written in a way that minimizes scientific jargon and maximizes students' natural language. Concept inventories differ from traditional multiple-choice assessments in that they use research-based preconceptions as the basis for the incorrect answer choices (Bailey 2009). We removed 5 questions from the full PFCI that did not cover content presented in either the PFLT or PFOLT. It is important to note that none of the questions from the PFCI were removed in the original analysis conducted by Simon *et al.* (2019), of which we compare one course's lecture-only learning gains to those from our study. Because of our item removals from the PFCI, we calculated a

[3] Planet Formation Activity Study, Arizona State University (IRB of Record) ID: STUDY00014402

Cronbach's alpha on the shortened assessment to verify that it retained satisfactory reliability. Cronbach's alpha is defined as:

$$\alpha = \frac{K}{K-1}\left(1 - \frac{\Sigma\sigma_i^2}{\sigma_x^2}\right) \tag{5.1}$$

where K is the number of test items, σ_i^2 is the variance of each individual item, and σ_x^2 is the variance of the full test (Bardar *et al.* 2006), with $\alpha \geq 0.70$ considered an acceptable reliability coefficient (Nunnally 1978). Using the post-test data from all courses, alpha was 0.736. This is comparable to the original instrument reliability (Simon *et al.* 2019, Section 3.4).

The abbreviated PFCI was administered as a pre/post assessment online via QuestionPro. Students completed the PFCI pre-test within the first two weeks of their ASTRO 101 in order to assess their knowledge of planet formation before the instructor covered any related material. They took the PFCI again within a few days of completing either the PFLT or PFOLT. We removed any course section from the final data set where fewer than 50% of students who took the pre-test were represented in the post-test data. Additionally, to determine how instructors implemented either the PFLT or PFOLT in their respective courses, we developed an instructor implementation survey which was administered via Google Forms at the conclusion of each course. This survey included a series of questions regarding course modality, activity implementation, and the use of other active learning strategies. Responses to the instructor implementation survey informed several of the topics discussed in Section 5.6 as well as the information provided in column 4 of the table in Figure 100. The survey questions can be found in the appendix.

5.4.3 Normalized Gain Scores

The data reported throughout the remainder of the paper are student responses to the abbreviated PFCI before and after completion of the respective learning activities. Before computing potential learning gains, we removed any students from our sample who completed the PFCI in less than two minutes to avoid the data being skewed by students who did not seriously attempt to answer the questions. To avoid early question bias, we also removed any students who did not answer the last three questions of the PFCI. We also matched students via unique identifiers to ensure that the final data set only included students who took the pre-test, completed either the PFLT or PFOLT, and then took the post-test, hereafter referred to as matched pairs. It also allowed us to more directly compare any potential learning gains that resulted from completion of the PFLT or PFOLT to those derived from a lecture-only comparison course presented in Simon *et al.* (2019, Tables 3 and 4) where learning gains were calculated exclusively with matched pairs data.

Following the procedure outlined in Simon *et al.* (2019), we computed normalized gain scores for each of the students in the matched pairs data set using the formula:

$$g_{student} = \frac{post\% - pre\%}{100 - pre\%}. \tag{5.2}$$

Additionally, we calculated the average normalized gain score for each of the eleven ASTRO 101 classes in our sample:

$$g_{class} = \frac{<M>post\% - <M>pre\%}{100 - <M>pre\%} \tag{5.3}$$

where <M> is the mean pre-/post-test score. We used student-level (rather than course-level) gain calculations when employing an analysis of variance as described in Section 5.4.4 to look for statistical significance between modalities and between the activity types. Because g is undefined for students with perfect pre-test scores, these students were excluded and our number of students differ very slightly depending on whether we are using g_{class} or $g_{student}$ for our analysis.

5.4.4 Inferential Statistics

There are two key questions in our analysis. First, are student learning gains following the PFOLT comparable to those from the in-person implementation of the pencil-and-paper PFLT? Second, do student learning gains from classes that used the PFOLT exceed those of traditional lecture classes, which used no additional active learning activities? To answer these questions, we employed a one-way between group analysis of variance (ANOVA) with post hoc testing using Tukey's HSD (honestly significant difference) to identify statistically significant paired comparisons (Toothaker 1993). Because the PFOLT was tested in both in-person and asynchronous modalities (see the table in Figure 100), we treat these two course instructional modalities as distinctly different in our analysis. Finally, our lecture comparison data come from a previously published study (Simon *et al.* 2019, Table 3). Thus, we only had access to course-level summary data (i.e. mean, standard deviation, and number of students). An ANOVA requires student-level data. Therefore, we simulated student-level data with these characteristics using the `rnorm()` function in R before performing the ANOVA.

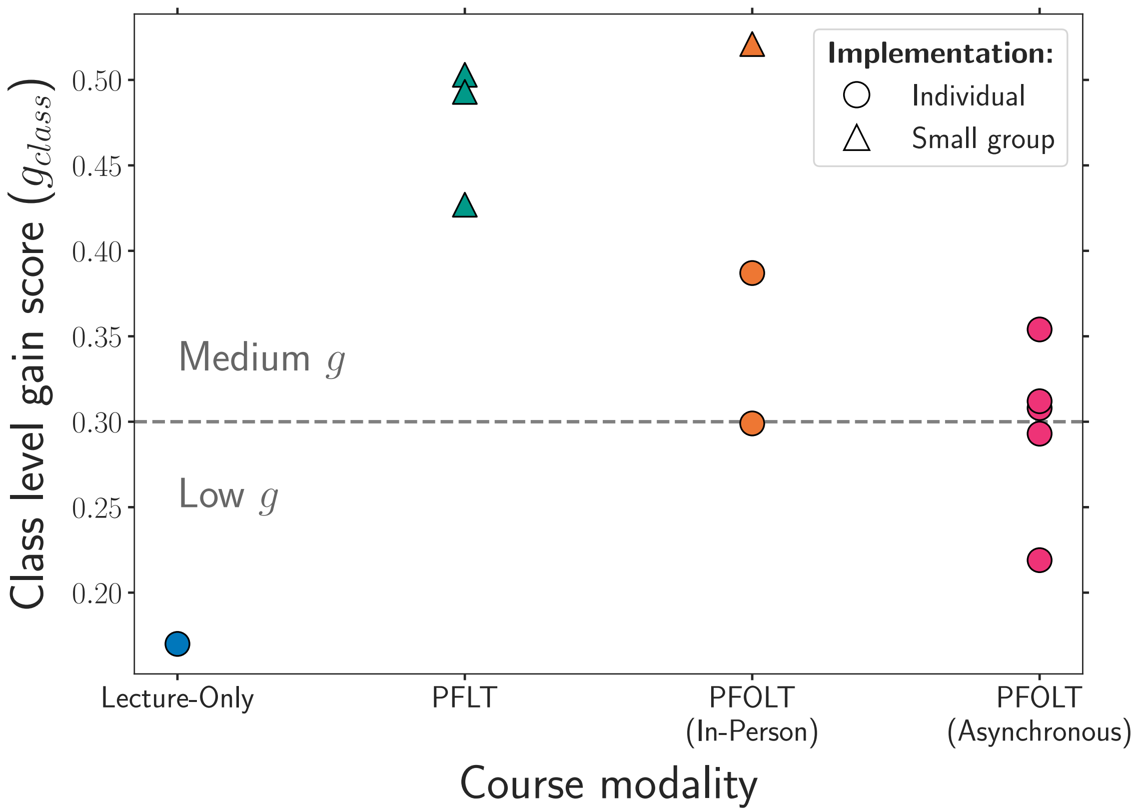

Figure 101. Class level gain score (g_{class}) for each instructional method. g_{class} for the lecture-only condition was taken from Simon *et al.* (2019, Table 3). The lecture-only course and the courses that utilized the traditional PFLT were all taught in-person. PFOLT g_{class} results are split into two categories: in-person and asynchronous to denote online asynchronous. Whether the intervention was conducted individually or in small groups is marked by either circles or triangles (the lecture-only course is also marked with a circle). The gray, dashed line separates low normalized gain ($g_{class} < 0.3$) from medium normalized gain ($0.3 < g_{class} < 0.7$).

5.5 Results

5.5.1 Learning Gains

The table in Figure 102 provides a summary of learning gains data by class. This includes mean <M> and standard deviation <SD> values for pre- and post-tests and

Table 3. Matched-pairs measured learning gains

Institution	Modality	Activity Implemented	# of Matched Pairs[1]	Pre-test <M> (%)	Pre-test <SD> (%)	Post-test <M> (%)	Post-test <SD> (%)	g_{class}
University of Alaska	In-Person	PFLT	15	63.6	15.9	79.1	18.4	0.427
University of Colorado Boulder	In-Person	PFLT	84	49.8	18.4	75.1	18.9	0.503
University of Arizona 1	In-Person	PFLT	198	48.8	17.5	74.0	17.5	0.493
University of Alabama at Birmingham	Asynchronous	PFOLT	34	45.9	16.6	62.5	23.1	0.308
California Polytechnic State University, San Luis Obisbo	Asynchronous	PFOLT	64	48.5	16.7	66.8	17.7	0.354
Glendale Community College[2]	Asynchronous	PFOLT	12	48.9	14.7	63.9	25.7	0.293
New Mexico State University	In-Person	PFOLT	14	53.8	13.2	67.6	20.0	0.299
Albion College	In-Person	PFOLT	14	41.0	15.7	63.8	16.5	0.387
University of Michigan	Asynchronous	PFOLT	21	49.2	20.0	65.1	23.8	0.312
Arizona State University 1	In-Person	PFOLT	149	58.7	19.1	80.2	16.9	0.521
Arizona State University 2	Asynchronous	PFOLT	150	57.2	17.1	66.6	20.7	0.219
University of Arizona 2[3]	In-Person	Lecture-Only	40	51.0	14.9	60.1	20.2	0.170

[1] Number of students where we were able to match pre and post-tests
[2] Located in Glendale, Arizona
[3] Data based on Simon et al. (2019)

Figure 102. Table 3 from Bringing Lecture-Tutorials Online: An Analysis of A New Strategy to Teach Planet Formation in the Undergraduate Classroom by Archer *et al.* (2024b), published in the Astronomy Education Journal.

the normalized gain score for each class, g_{class}. The table also includes course modality, activity implemented, and number of matched pairs. In Figure 101 we show g_{class} for the different activity types (PFLT/PFOLT) while also highlighting implementation strategy (whether students completed the respective activity independently or in small groups). In both the table shown in Figure 102, along with Figure 101, we include the lecture-only learning gains reported in Simon *et al.* (2019), where students took the full PFCI in an ASTRO 101 course with no active learning interventions. Note that learning gains in this lecture-only condition were measured using the full PFCI, in contrast to the other classes which were measured using a 15-question subset of the same assessment. Three categories of normalized gain scores are defined by Hake (1998) and Prather *et al.* (2009): low ($g < 0.3$), medium ($0.3 < g < 0.7$), and high ($g > 0.7$). A dashed line in Figure 101 denotes the separation between low and medium normalized gain scores.

Table 4. Descriptive condition-level learning gain statistics[1]

Activity Implemented	# of Matched Pairs[2]	$g_{student}$ <M>	$g_{student}$ <SD>	$g_{student}$ Min	$g_{student}$ Max	$g_{student}$ <SE[3]>
PFLT	297	0.480	0.360	-1.750	1.000	0.021
PFOLT (In-Person)	175	0.506	0.350	-1.000	1.000	0.026
PFOLT (Asynchronous)	280	0.256	0.448	-2.000	1.000	0.027
Lecture-Only[4]	40	0.170	0.245	-0.362	0.577	0.039

[1] Values shown are averages of student-level data
[2] Number of students where we were able to match pre and post-tests
[3] Standard error
[4] Data based on Simon et al. (2019)

Figure 103. Table 4 from Bringing Lecture-Tutorials Online: An Analysis of A New Strategy to Teach Planet Formation in the Undergraduate Classroom by Archer *et al.* (2024b), published in the Astronomy Education Journal.

Table 5. One-way ANOVA summary

	Sum of Squares	df[1]	Mean Square	F[2]	Significance
Between Groups	11.734	3	3.911	26.11	$< .001$
Within Groups	118.059	788	0.150		
Total	129.793	791			

[1] Degrees of freedom
[2] F statistic

Figure 104. Table 5 from Bringing Lecture-Tutorials Online: An Analysis of A New Strategy to Teach Planet Formation in the Undergraduate Classroom by Archer *et al.* (2024b), published in the Astronomy Education Journal.

5.5.2 ANOVA Results

A comparison of student-level learning gains across instructional methods was significant overall with the F statistic, F(3, 788) = 26.11; $p < .001$. Speaking to our first question of interest (how does student learning compare when using the PFLOT versus using the PFLT), post hoc testing shows the PFLT to have significantly higher learning gains ($p < .001$) than the asynchronous implementation of the PFOLT, but there is

Table 6. Pairwise comparisons

Activity Implemented			95% Confidence Interval		
Condition 1	Condition 2	Mean Difference (Condition 1 - Condition 2)	Lower Bound	Upper Bound	Significance
PFLT	PFOLT (In-Person)	–0.026	0.069	–0.121	0.892
PFLT	PFOLT (Asynchronous)	0.224	0.307	0.141	<0.001
PFLT	Lecture-Only	0.310	0.477	0.142	<0.001
PFOLT (In-Person)	PFOLT (Asynchronous)	0.250	0.346	0.154	<0.001
PFOLT (In-Person)	Lecture-Only	0.336	0.511	0.161	<0.001
PFOLT (Asynchronous)	Lecture-Only	0.086	0.254	–0.083	0.558

Figure 105. Table 6 from Bringing Lecture-Tutorials Online: An Analysis of A New Strategy to Teach Planet Formation in the Undergraduate Classroom by Archer *et al.* (2024b), published in the Astronomy Education Journal.

virtually no difference ($p = .89$) between the PFLT and the in-person implementation of the PFOLT. Regarding our second question (how does the PFOLT compare to lecture-only instruction), post hoc testing shows that the in-person PFOLT had significantly higher learning gains ($p < .001$) than lecture. However, the asynchronous PFOLT was not significantly different from lecture ($p = .56$). Finally, testing also indicates that the in-person implementation of the PFOLT was significantly more effective than the asynchronous implementation ($p < .001$). The complete ANOVA results and relevant descriptive statistics are presented in the tables shown in Figures 103-105.

5.6 Discussion

5.6.1 Exploration of Learning Gains

When the PFOLT was implemented in-person, the learning gains were comparable to the PFLT. However, when implemented asynchronously, the learning gains were comparable to the lecture-only group. One likely explanation for this pattern can be attributed to the value of small group learning. Studies find that students who work in small groups showed significantly greater gains on conceptual questions than students who worked individually (Gokhale 1995; Adams and Slater 2002). When working together in small groups, ASTRO 101 students, who are often at varying levels of discipline knowledge and ability, are better able to reason through a problem when presented with other perspectives or interpretations of their peers. The higher learning gains among courses implementing the PFLT/PFOLT in small groups further highlights the importance of collaborative learning. In addition to underscoring one of the fundamental pedagogical tenets of LTs, this finding is also consistent with findings from other research in active learning, particularly the ICAP (Interactive, Constructive, Active, and Passive) framework (Chi and Wylie 2014) which found "interactive" learning, i.e. co-construction of knowledge, to be the most effective form of active learning.

In the case of the PFOLT, however, the single course that implemented the activity both in small groups and in-person was the only course in the final data set that enrolled predominantly science majors (see Section 5.4.1). Despite being a majors-dominant course, the course was still at the introductory level and did not have any science prerequisite. It is expected that science majors will out-perform non-majors and, indeed, Simon *et al.* (2019) found that science majors' normalized gain scores were significantly higher than those of non-science majors on the PFCI. Had the course been made up of entirely non-science majors, we predict the gain scores would be lower to some extent. To this end, we likely cannot attribute this class' high gain score ($g_{class} = 0.521$) to small group collaboration alone.

Additionally, prior research indicates that the quality of instructor implementation can be the most crucial factor in determining gain scores (Prather *et al.* 2009; Wallace *et al.* 2012). This factor impacted our results in two distinct ways. First, the highest learning gains were found in classes where instructors facilitated small group collaboration (Figure 101). Second, the presence and quality of prior instruction likely played a role in the lower-than-expected learning gains for the asynchronous PFOLT courses. Lecture-tutorials, conventionally, supplement lecture instruction on a given topic. In contrast to the PFLT classes and most in-person PFOLT classes, not all of the asynchronous classes included instruction on planet formation prior to the PFOLT. Of the five asynchronous courses in our final data set, one preceded the PFOLT with a separate interactive digital tutorial. The other four had lower quality prior instruction, one providing no prior instruction at all, and the other three providing asynchronous videos or readings that were recommended but not required. Although not all of these videos and readings were trackable, from the data that were available, less than half of students viewed these materials, thus beginning the PFOLT without any pre-activity engagement.

Both of these variations in quality of implementation complicate the interpretation of our results. For example, since all of the PFLT data come from in-person classes that implemented that activity after a lecture on the topic, and with small groups, and, conversely, no fully online class employed small group instruction (e.g. through webinar break out groups) we cannot fully disentangle implementation and activity-type. Similarly, because the measured learning gains reflect gains from *both* the lecture and the LT, in classes without any required prior instruction, the LT itself is responsible for relatively greater learning (i.e. some portion of what would otherwise have been learned in the lecture portion). Not to mention the value found from repetition and reinforcement of concepts when a LT is preceded by a lecture or other instruction.

In summary, while this study does not find clear, statistically significant differences between lecture only and the PFOLT in all implementations, the higher gain scores observed for the online asynchronous condition when compared to traditional lecture (despite limited pre-instruction) indicate that the PFOLT is worthy of being used as a tool to teach planet formation in ASTRO 101 courses online. Finally, our results also underscore the value of small group learning and highlight a recurring challenge in asynchronous online learning settings to find ways to build in opportunities for peer-learning.

5.6.2 Activity Improvements

In our instructor implementation survey, we requested feedback on the implementation of either the PFLT or PFOLT in their classes. Two instructors suggested that the redundancy of plotting points on the graphs in the PFOLT caused students to lose interest. In future versions of the PFOLT, we will program the activity such that the graphs automatically fill in earlier than they currently do, immediately after students demonstrate an understanding of the relationship they are intended to plot.

Even though we typically observed higher PFOLT learning gains in in-person courses, we anticipate the PFOLT will be used predominantly in ASTRO 101 courses online. Since the PFOLT is designed to be used in asynchronous courses where students often work independently, outfitting the activity with a more complex, intelligent tutoring system (ITS) would likely lead to more profound student learning than what we currently observe. Unlike human tutoring, computer-based tutoring is traditionally separated into two technological types: answer-based and step-based (Vanlehn 2011). As it stands, the PFOLT falls under the answer-based category, which gives students immediate feedback and hints based on their answer choices. Adding a step-based ITS would provide students with feedback and hints along each step of the problem-solving process, similar to conversing directly with a peer. Alternatively, the inconsistency of prior instruction could be addressed by building in a standardized pre-recorded lecture.

Furthermore, a meta-analysis (Wisniewski *et al.* 2020) of more than 400 research studies looking at the effects of feedback on student learning found that the "cognitive complexity" of adaptive feedback directly relates to the effectiveness of the feedback. The three categories of complexity ranging from least to most complex are: task level feedback, process level feedback, and self-regulation feedback. Currently, the PFOLT utilizes task-level feedback, providing students with responses regarding whether a task was done correctly rather than presenting students with suggestions and strategies concerning how to complete each task. We plan to work with the ETX center at ASU to integrate an ITS into the PFOLT specifically designed to offer more process and/or self-regulation based feedback with the goal of further increasing student learning.

5.7 Summary & Conclusions

An uptick in online course enrollments coupled with the COVID-19 pandemic put a spotlight on the need for additional effective, research-based, curricular materials that lead to more lasting conceptual change. As one contribution toward this overarching objective, we developed and explored the efficacy of a novel, digital LT intended to teach planet formation in online ASTRO 101 courses. We utilized the previously validated PFCI to compare student and course-level learning gains between lecture-only courses, courses that implemented the PFOLT, and those that implemented the traditional pencil-and-paper PFLT. Several previous efforts conclusively demonstrate that LTs are incredibly effective at increasing student learning on a myriad of topics when compared to lecture alone. To date, however, all available LTs for ASTRO 101 are pencil-and-paper based, having been developed exclusively for courses taught in-person.

Overall, our results show learning gains from these pencil-and-paper LT (PFLT) to be statistically indistinguishable from the in-person implementation of the PFOLT and show that both of these conditions exceed gains from lecture-only instruction. However, when implemented asynchronously, learning gains from the PFOLT were lower and not statistically distinct from the lecture-only condition. These results are qualified by important differences in instructor implementation, including learning in small groups versus individual work and the presence and quality of pre-LT instruction. The highest learning gains for the PFOLT were also found in an introductory course primarily intended for science majors, whereas all other data came from courses for non-science majors. While improvements can be made to improve the online LT in the future, the current version still outperforms traditional lecture (for in-person, small group implementations), and can be used as a tool to teach planet formation effectively.

In a future research study, we plan to revisit the question of whether LTs can be effective in online, asynchronous classes. This work will be done following revisions to the PFOLT and with tighter controls on pre-activity instruction. We will update the PFOLT as described in Section 5.6.2, including addressing plotting redundancies and improving automatic feedback. To better ensure similar pre-activity instruction across testing sites, we will embed a pre-recorded lecture video that will precede the interactive component of the activity. The potential benefits from LT-style instruction in asynchronous online classes are compelling, but the inherent differences in that modality raise real concerns about how to effectively translate a proven in-person active learning strategy.

5.8 Declarations

Data from this study can be obtained from the authors upon reasonable request.

5.8.1 List of Abbreviations

- ANOVA: Analysis of Variance
- ASU: Arizona State University
- ETX: Education Through eXploration
- g: Normalized Learning Gain
- HSD: Honestly significant difference
- ICAP: Interactive, Constructive, Active, and Passive
- ITS: Intelligent Tutoring System
- LT: Lecture-Tutorial
- M: Mean
- PDR: Pedagogical Discipline Representation
- PFCI: Planet Formation Concept Inventory
- PFLT: Planet Formation Lecture-Tutorial
- PFOLT: Planet Formation Online Lecture-Tutorial
- SD: Standard Deviation
- SE: Standard Error

5.8.2 Ethical Approval (Optional)

This study was approved by Arizona State University's institutional review board and classified as "exempt" under IRB of Record ID: STUDY00014402.

5.8.3 Consent for Publication

Not applicable.

5.8.4 Competing Interests

The author(s) declare that they have no competing interests.

5.8.5 Funding

This material is based upon work supported by the NASA SMD Exploration Connection under Award Number: NNX16AD79A.

5.8.6 Author's Contributions

H. N. Archer: Data curation, formal analysis, investigation, methodology, resources, software, validation, visualization, writing – original draft.

M. N. Simon: Conceptualization, data curation, funding acquisition, investigation, methodology, project administration, resources, supervision, validation, writing – original draft.

C. Mead: Conceptualization, methodology, formal analysis, software, validation, visualization, writing – original draft.

E. E. Prather: Resources, writing – review and editing.

M. Brunkhorst: Data curation, resources, software, visualization.

D. Hunsley: Data curation, resources, software, visualization.

5.9 Acknowledgements

The authors would like to acknowledge each of the instructors who allowed us to implement either the PFLT or PFOLT in their courses, along with the students who contributed their efforts to this work.

5.10 APPENDIX

5.10.1 Instructor Implementation Survey

Instructor Information

1. Instructor Name
2. Instructor Email
3. Instructor Institution
4. How many students were enrolled in your course(s)?
    - ○ <25
    - ○ 25-50
    - ○ 50-100
    - ○ >100
5. What was the course modality?

- Asynchronous online
- Synchronous online
- In-person
- Hybrid
- Other [please explain]

6. Which activity did you implement?
    - Online lecture-tutorial
    - Pencil-and-paper lecture-tutorial
    - Both

Pencil-and-paper lecture-tutorial

1. Please describe how you implemented the lecture-tutorial (e.g. student groups, students working individually, students working in zoom breakout rooms). Did you implement it all at once? Break it into sections?
2. Please provide feedback regarding how the lecture-tutorial could be improved (or what you liked about it).

Online lecture-tutorial

1. Please describe how you implemented the online lesson in your course.
2. Would you use this online lesson again in your course?
    - Yes
    - No
3. Please provide feedback regarding how the online lecture-tutorial could be improved (or what you liked about it).

General Planet Formation Teaching Questions

1. In your course, do you implement any active learning activities beyond the in-person tutorial or online lesson (e.g. think-pair-share questions, additional tutorials)?
    - Yes
    - No, lecture-only

2. If yes, please briefly explain.
3. When teaching planet formation, did you implement any active learning strategies beyond the pencil-and-paper/online lecture-tutorial?
   - ○ Yes
   - ○ No, lecture-only
   - ○ I did not cover planet formation beyond what was in the lecture-tutorial
4. If yes, please briefly explain.
5. By the time my students have taken the post-test, they have learned the following concepts in my class: SELECT ALL THAT APPLY.
   - ☐ The definition of an exoplanet
   - ☐ The definition of a solar system
   - ☐ The definition of a star
   - ☐ The definition of a planet
   - ☐ The definition of a dwarf planet
   - ☐ Planetary motion/orbits
   - ☐ The nebular theory
   - ☐ Accretion: planetesimals into planets
   - ☐ The composition of the rocky planets and gas giant planets
   - ☐ Condensation temperature and/or the snowline
   - ☐ Basic concept of planetary migration
   - ☐ The formation of the Universe – the Big Bang
   - ☐ The size and scale of the Universe (e.g. what is a galaxy versus a solar system)

Chapter 6

SUMMARY & CONCLUSIONS

6.1 Summary

6.1.1 Star Formation in Low-Metallicity Environments

This dissertation has investigated star formation in low-metallicity environments by studying the dwarf irregular galaxy WLM. By analyzing multi-wavelength observational data from ALMA, JWST, and HST, as well as other ancillary ground- and space-based data, we have conducted a thorough investigation into the interplay between molecular gas and star formation at low metallicities.

Through our analyses, we found that CO emission is not exclusively associated with very young star-forming regions; instead, it appears across regions of various ages. This suggests that the small CO cores are not products of fragmentation over time, but rather represent the typical sizes that molecular clouds can achieve in low-metallicity environments. Additionally, although star-forming regions with higher total CO core masses tend to coincide with areas of elevated H I surface density, the relationship is complicated by the presence of regions with minimal CO along the high-H I density ridge, as well as regions containing CO but located away from this dense ridge.

We also find that young star-forming regions detected in the NIR with JWST that coincide with CO cores overlap more frequently with Spitzer 8μm sources compared to those without associated CO emission. This suggests that regions associated with

CO cores are likely younger, consistent with expectations for sources still embedded and not yet having cleared their surrounding gas and dust.

Finally, we do not identify clear differences between the stellar populations within the [C II]-demarcated photodissociation region (PDR) in WLM and its surrounding area. However, since the [C II] observation was limited to a single pointing in WLM, it is possible that the PDR extends beyond our defined region. By estimating the molecular gas content within the PDR under the assumption that 2% of molecular gas is converted into stars, we find that nearly 80% of this molecular gas resides in a phase not traced by the small CO cores detected in the star-forming region. This underscores the significance of accounting for CO-dark gas when examining star formation processes at low metallicities.

6.1.2 The Planet Formation Online Lecture-Tutorial

We adapted a traditional Planet Formation Lecture-Tutorial (PFLT) into an online format—the Planet Formation Online Lecture-Tutorial (PFOLT)—to provide active learning for online introductory astronomy students. By translating the established in-class activities into a digital environment, this approach aimed to address prevalent student preconceptions about planet formation in a more interactive way.

In this study, we analyzed the effectiveness of adapting traditional lecture-tutorials into an online format by examining student learning outcomes across multiple institutions. Using pre- and post-instruction assessments from several undergraduate astronomy classes across the US, we found that students who completed the PFOLT demonstrated learning gains similar to who used the tradition PFLT when the PFOLT was implemented in-person. In these classes, the instructor often provided a short lecture before assigning the lecture-tutorial, and students often worked on the PFOLT in groups. These results highlight the importance of group work and pre-lecture-tutorial instruction. We analyzed the effectiveness of adapting the traditional Planet Formation Lecture-Tutorial into an online format by examining student learning outcomes across multiple institutions. When implemented asynchronously online, the PFOLT yielded student learning gains comparable to or exceeding those of students who received only lecture-based instruction without a lecture-tutorial. This suggests that interactive online tools like the PFOLT can effectively enhance students' understanding of complex concepts, such as planet formation, while addressing common preconceptions.

6.2 Conclusions

The integration of ALMA, JWST, and HST observational data has been instrumental in clarifying the connections between early-stage star formation and molecular gas in the low-metallicity dwarf galaxy WLM. Our multi-wavelength approach has identified clear signatures of star-forming activity associated with molecular gas regions, advancing our ability to detect and characterize star-forming areas where these observations have been historically challenging. These results help us better pinpoint where and how star formation occurs in low-metallicity environments, contributing valuable insights that can refine theoretical models of star formation, especially those relevant to conditions in the early universe.

Adapting lecture-tutorials to an online format proved successful in addressing common preconceptions about planet formation among undergraduate astronomy students. Our results indicate that online pedagogical tools can offer equal or superior educational outcomes compared to traditional lecture and further highlights the importance of active learning. This work thus provides an important contribution to astronomy education research, advocating for the continued development and assessment of interactive, student-centered online educational practices.

Overall, this dissertation emphasizes the critical importance of explicitly considering environmental factors in low-metallicity star formation and supports continued innovation in astronomy education. Future research should extend these findings by investigating a broader range of galaxies across various metallicity regimes and by further refining online educational tools by including pre-recording lectures with the PFOLT or developing online lecture-tutorials for other astronomical topics such as star formation, galaxy evolution, and dwarf galaxies. Such efforts promise to enhance scientific knowledge of galaxy evolution and star formation processes, as well as improve educational outcomes for students.

REFERENCES

Adams, J. and T. Slater, "Learning through Sharing: Supplementing the Astronomy Lecture with Collaborative-Learning Group Activities", Journal of College Science Teaching **31**, 6, 384–87, URL https://eric.ed.gov/?id=EJ661703, eRIC Number: EJ661703 (2002).

Albers, S. M., D. R. Weisz, A. A. Cole, A. E. Dolphin, E. D. Skillman, B. F. Williams, M. Boylan-Kolchin, J. S. Bullock, J. J. Dalcanton, P. F. Hopkins, R. Leaman, A. W. McConnachie, M. Vogelsberger and A. Wetzel, "Star formation at the edge of the Local Group: a rising star formation history in the isolated galaxy WLM", MNRAS **490**, 4, 5538–5550 (2019).

Allen, I. E. and J. Seaman, "Changing Course: Ten Years of Tracking Online Education in the United States", Tech. rep., Sloan Consortium, URL https://eric.ed.gov/?id=ED541571 (2013).

Anderson, J., S. Baggett and B. Kuhn, "Updating the WFC3/UVIS CTE model and Mitigation Strategies", Instrument Science Report 2021-9, 44 pages (2021).

Annunziatella, M., A. Mercurio, M. Brescia, S. Cavuoti and G. Longo, "Inside Catalogs: A Comparison of Source Extraction Software", PASP **125**, 923, 68 (2013).

Archer, H. N., P. Cigan, B. Elmegreen, L. Hunt, D. A. Hunter, R. A. Jansen, M. Rubio and R. A. Windhorst, "Young Stars and Gas Structure within the ALMA Coverage of Dwarf Irregular Galaxy WLM", HST Proposal. Cycle 30, ID. #17068 (2022a).

Archer, H. N., D. A. Hunter, B. G. Elmegreen, P. Cigan, R. A. Jansen, R. A. Windhorst, L. K. Hunt and M. Rubio, "The Environments of CO Cores and Star Formation in the Dwarf Irregular Galaxy WLM", AJ **163**, 3, 141 (2022b).

Archer, H. N., D. A. Hunter, B. G. Elmegreen, M. Rubio, P. Cigan, R. A. Windhorst, J. R. Cortés and R. A. Jansen, "Probing the Relationship Between Early Star Formation and CO in the Dwarf Irregular Galaxy WLM with JWST", AJ **167**, 6, 274 (2024a).

Archer, H. N., M. N. Simon, C. Mead, E. E. Prather, M. Brunkhorst and D. Hunsley, "Bringing Lecture-Tutorials Online: An Analysis of A New Strategy to Teach Planet Formation in the Undergraduate Classroom", AEJ **04**, 1 (2024b).

Asplund, M., N. Grevesse, A. J. Sauval and P. Scott, "The Chemical Composition of the Sun", ARA&A **47**, 1, 481–522 (2009).

Bailey, J. M., "Concept Inventories for ASTRO 101", The Physics Teacher **47**, 7, 439–441 (2009).

Bardar, E., E. E. Prather and T. Slater, "Development and validation of the light and spectroscopy concept inventory", Astronomy Education Review **5** (2006).

Bastian, N. and S. P. Goodwin, "Evidence for the strong effect of gas removal on the internal dynamics of young stellar clusters", MNRAS **369**, 1, L9–L13 (2006).

Bertelli, G., A. Bressan, C. Chiosi, F. Fagotto and E. Nasi, "Theoretical isochrones from models with new radiative opacities.", A&AS **106**, 275–302 (1994).

Bertin, E. and S. Arnouts, "SExtractor: Software for source extraction.", A&AS **117**, 393–404 (1996).

Bezanson, J., A. Edelman, S. Karpinski and V. B. Shah, "Julia: A fresh approach to numerical computing", SIAM Review **59**, 1, 65–98, URL https://epubs.siam.org/doi/10.1137/141000671 (2017).

Bialy, S. and A. Sternberg, "Thermal Phases of the Neutral Atomic Interstellar Medium from Solar Metallicity to Primordial Gas", ApJ **881**, 2, 160 (2019).

Bigiel, F., A. K. Leroy, F. Walter, E. Brinks, W. J. G. de Blok, C. Kramer, H. W. Rix, A. Schruba, K. F. Schuster, A. Usero and H. W. Wiesemeyer, "A Constant Molecular Gas Depletion Time in Nearby Disk Galaxies", ApJ **730**, 2, L13 (2011).

Bolatto, A. D., J. M. Jackson and J. G. Ingalls, "A Semianalytical Model for the Observational Properties of the Dominant Carbon Species at Different Metallicities", ApJ **513**, 1, 275–286 (1999).

Bolatto, A. D., M. Wolfire and A. K. Leroy, "The CO-to-H_2 Conversion Factor", ARA&A **51**, 1, 207–268 (2013).

Boyer, M. L., G. Pastorelli, L. Girardi, P. Marigo, A. E. Dolphin, K. B. W. McQuinn, M. J. B. Newman, A. Savino, D. R. Weisz, B. F. Williams, J. Anderson, R. E. Cohen, M. Correnti, A. A. Cole, M. C. Geha, M. Gennaro, N. Kallivayalil, E. N. Kirby, K. M. Sandstrom, E. D. Skillman, C. T. Garling, H. Richstein and J. T. Warfield, "The JWST Resolved Stellar Populations Early Release Science Program. VI. Identifying Evolved Stars in Nearby Galaxies", ApJ **973**, 2, 120 (2024).

Bressan, A., P. Marigo, L. Girardi, B. Salasnich, C. Dal Cero, S. Rubele and A. Nanni, "PARSEC: stellar tracks and isochrones with the PAdova and TRieste Stellar Evolution Code", MNRAS **427**, 1, 127–145 (2012).

Brosch, N., A. Heller and E. Almoznino, "Star Formation in Dwarf Galaxies", ApJ **504**, 2, 720–724 (1998).

Bruzual, G. and S. Charlot, "Stellar population synthesis at the resolution of 2003", MNRAS **344**, 4, 1000–1028 (2003).

Calzetti, D., "Star Formation Rate Indicators", in "Secular Evolution of Galaxies", edited by J. Falcón-Barroso and J. H. Knapen, p. 419 (Cambridge University Press, 2013).

Cardelli, J. A., G. C. Clayton and J. S. Mathis, "The Relationship between Infrared, Optical, and Ultraviolet Extinction", ApJ **345**, 245 (1989).

Carpenter, J. M., R. L. Snell and F. P. Schloerb, "Star Formation in the Gemini OB1 Molecular Cloud Complex", ApJ **450**, 201 (1995).

Chabrier, G., "Galactic Stellar and Substellar Initial Mass Function", PASP **115**, 809, 763–795 (2003).

Chen, Y., A. Bressan, L. Girardi, P. Marigo, X. Kong and A. Lanza, "PARSEC evolutionary tracks of massive stars up to 350 $M_\odot$ at metallicities $0.0001 \leq Z \leq 0.04$", MNRAS **452**, 1, 1068–1080 (2015).

Chen, Y., L. Girardi, A. Bressan, P. Marigo, M. Barbieri and X. Kong, "Improving PARSEC models for very low mass stars", MNRAS **444**, 3, 2525–2543 (2014).

Chevance, M., J. M. D. Kruijssen, A. Hygate, A. Schruba, S. Longmore, B. Groves, J. D. Henshaw, C. N. Herrera, A. Hughes, S. Jeffreson, P. Lang, A. K. Leroy, S. E. Meidt, J. Pety, A. Razza, E. Rosolowsky, E. Schinnerer, F. Bigiel, G. A. Blanc, E. Emsellem, C. M. Faesi, S. Glover, D. Haydon, I. Ho, K. Kreckel, J. C. Lee, D. Liu, M. Querejeta, T. Saito, J. Sun, A. Usero and D. Utomo, "The lifecycle of molecular clouds in nearby star-forming disc galaxies", MNRAS **493**, 2, 2872–2909 (2020a).

Chevance, M., M. R. Krumholz, A. F. McLeod, E. C. Ostriker, E. W. Rosolowsky and A. Sternberg, "The Life and Times of Giant Molecular Clouds", in "Protostars and Planets VII", edited by S. Inutsuka, Y. Aikawa, T. Muto, K. Tomida and M. Tamura, vol. 534 of *Astronomical Society of the Pacific Conference Series*, p. 1 (2023).

Chevance, M., S. C. Madden, C. Fischer, W. D. Vacca, V. Lebouteiller, D. Fadda, F. Galliano, R. Indebetouw, J. M. D. Kruijssen, M.-Y. Lee, A. Poglitsch, F. L. Polles, D. Cormier, S. Hony, C. Iserlohe, A. Krabbe, M. Meixner, E. Sabbi and H. Zinnecker, "The CO-dark molecular gas mass in 30 Doradus", MNRAS **494**, 4, 5279–5292 (2020b).

Chi, M. T. H. and R. Wylie, "The ICAP Framework: Linking Cognitive Engagement to Active Learning Outcomes", Educational Psychologist **49**, 4, 219–243, URL https://doi.org/10.1080/00461520.2014.965823 (2014).

Choi, J., A. Dotter, C. Conroy, M. Cantiello, B. Paxton and B. D. Johnson, "Mesa Isochrones and Stellar Tracks (MIST). I. Solar-scaled Models", ApJ **823**, 2, 102 (2016).

Cigan, P., L. Young, D. Cormier, V. Lebouteiller, S. Madden, D. Hunter, E. Brinks, B. Elmegreen, A. Schruba, V. Heesen and the <SPAN CLASS="sml">Little Things</SPAN> Team, "Herschel Spectroscopic Observations of Little Things Dwarf Galaxies", AJ **151**, 1, 14 (2016).

Cohen, R. E., K. B. W. McQuinn, A. Savino, M. J. B. Newman, D. R. Weisz, A. E. Dolphin, M. L. Boyer, M. Correnti, M. C. Geha, M. Gennaro, K. M. Gilbert, N. Kallivayalil, J. T. Warfield, B. F. Williams, A. M. Brooks, A. A. Cole, E. D. Skillman, C. T. Garling, J. S. Kalirai and J. Anderson, "The JWST Resolved Stellar Populations Early Release Science Program. VIII. The Spatially Resolved Star Formation History of WLM", arXiv e-prints p. arXiv:2502.13887 (2025).

Conroy, C. and J. E. Gunn, "The Propagation of Uncertainties in Stellar Population Synthesis Modeling. III. Model Calibration, Comparison, and Evaluation", ApJ **712**, 2, 833–857 (2010).

Conroy, C., J. E. Gunn and M. White, "The Propagation of Uncertainties in Stellar Population Synthesis Modeling. I. The Relevance of Uncertain Aspects of Stellar Evolution and the Initial Mass Function to the Derived Physical Properties of Galaxies", ApJ **699**, 1, 486–506 (2009).

Cooper, K. M., L. E. Gin and S. E. Brownell, "Diagnosing differences in what Introductory Biology students in a fully online and an in-person biology degree program know and do regarding medical school admission", Advances in Physiology Education **43**, 2, 221–232 (2019).

Cormier, D., G. J. Bendo, S. Hony, V. Lebouteiller, S. C. Madden, F. Galliano, S. C. O. Glover, R. S. Klessen, N. P. Abel, F. Bigiel and P. C. Clark, "New ALMA constraints on the star-forming interstellar medium at low metallicity: a 50 pc view of the blue compact dwarf galaxy SBS 0335-052", MNRAS **468**, 1, L87–L91 (2017).

Dale, D. A., S. A. Cohen, L. C. Johnson, M. D. Schuster, D. Calzetti, C. W. Engelbracht, A. Gil de Paz, R. C. Kennicutt, J. C. Lee, A. Begum, M. Block, J. J. Dalcanton, J. G. Funes, K. D. Gordon, B. D. Johnson, A. R. Marble, S. Sakai, E. D. Skillman, L. van Zee, F. Walter, D. R. Weisz, B. Williams, S. Y. Wu and Y. Wu, "The Spitzer Local Volume Legacy: Survey Description and Infrared Photometry", ApJ **703**, 1, 517–556 (2009).

Dale, J. E., B. Ercolano and I. A. Bonnell, "Early evolution of embedded clusters", MNRAS **451**, 1, 987–1003 (2015).

Dolphin, A. E., "Hubble Space Telescope Studies of the WLM Galaxy. II. The Star Formation History from Field Stars", ApJ **531**, 2, 804–812 (2000).

Draine, B. T. and A. Li, "Infrared Emission from Interstellar Dust. IV. The Silicate-Graphite-PAH Model in the Post-Spitzer Era", ApJ **657**, 2, 810–837 (2007).

Efremov, Y. N. and B. G. Elmegreen, "Hierarchical star formation from the time-space distribution of star clusters in the Large Magellanic Cloud", MNRAS **299**, 2, 588–594 (1998).

El-Badry, K., J. Bradford, E. Quataert, M. Geha, M. Boylan-Kolchin, D. R. Weisz, A. Wetzel, P. F. Hopkins, T. K. Chan, A. Fitts, D. Kereš and C.-A. Faucher-Giguère, "Gas kinematics in FIRE simulated galaxies compared to spatially unresolved H I observations", MNRAS **477**, 2, 1536–1548 (2018).

Elmegreen, B. G., "A Pressure and Metallicity Dependence for Molecular Cloud Correlations and the Calibration of Mass", ApJ **338**, 178 (1989).

Elmegreen, B. G., "Star Formation in a Crossing Time", ApJ **530**, 1, 277–281 (2000).

Elmegreen, B. G. and D. M. Elmegreen, "Highly Embedded 8 μm cores of Star Formation in the Spiral Arms and Filaments of 15 Nearby Disk Galaxies", ApJS **245**, 1, 14 (2019).

Elmegreen, B. G. and D. M. Elmegreen, "Observing the Earliest Stages of Star Formation in Galaxies: 8 μm Cores in Three Edge-on Disks", ApJ **895**, 1, 71 (2020).

Elmegreen, B. G., D. M. Elmegreen and Y. N. Efremov, "Regularly Spaced Infrared Peaks in the Dusty Spirals of Messier 100", ApJ **863**, 1, 59 (2018).

Elmegreen, B. G., M. Morris and D. M. Elmegreen, "On the abundance of carbon monoxide in galaxies - A comparison of spiral and Magellanic irregular galaxies", ApJ **240**, 455–463 (1980).

Elmegreen, B. G., M. Rubio, D. A. Hunter, C. Verdugo, E. Brinks and A. Schruba, "Carbon monoxide in clouds at low metallicity in the dwarf irregular galaxy WLM", Nature **495**, 7442, 487–489 (2013).

Ester, M., H.-P. Kriegel, J. Sander and X. Xu, "A density-based algorithm for discovering clusters in large spatial databases with noise", in "KDD", pp. 226–231 (1996), URL http://www.aaai.org/Library/KDD/1996/kdd96-037.php.

Feinstein, N. W., S. Allen and E. Jenkins, "Outside the Pipeline: Reimagining Science Education for Nonscientists", Science **340**, 6130, 314–317, URL https://www.science.org/doi/abs/10.1126/science.1230855 (2013).

Freeman, S., S. L. Eddy, M. McDonough, M. K. Smith, N. Okoroafor, H. Jordt and M. P. Wenderoth, "Active learning increases student performance in science, engineering, and mathematics", Proceedings of the National Academy of Sciences **111**, 23, 8410–8415, URL https://www.pnas.org/doi/10.1073/pnas.1319030111 (2014).

French, R. S. and E. E. Prather, “From a systematic investigation of faculty-produced Think-Pair-Share questions to frameworks for characterizing and developing fluency-inspiring activities”, Physical Review Physics Education Research **16**, 2, 020138, URL https://link.aps.org/doi/10.1103/PhysRevPhysEducRes.16.020138 (2020).

Fukui, Y. and A. Kawamura, “Molecular Clouds in Nearby Galaxies”, AARA **48**, 547–580 (2010).

Glover, S. C. O. and P. C. Clark, “Is molecular gas necessary for star formation?”, MNRAS **421**, 1, 9–19 (2012).

Glover, S. C. O. and M. M. Mac Low, “On the relationship between molecular hydrogen and carbon monoxide abundances in molecular clouds”, MNRAS **412**, 1, 337–350 (2011).

Gokhale, A. A., “Collaborative Learning Enhances Critical Thinking”, in “Journal of Technology Education”, vol. 7 (1995), URL http://scholar.lib.vt.edu/ejournals/JTE/v7n1/gokhale.jte-v7n1.html.

Gordon, K. D., G. C. Clayton, K. A. Misselt, A. U. Landolt and M. J. Wolff, “A Quantitative Comparison of the Small Magellanic Cloud, Large Magellanic Cloud, and Milky Way Ultraviolet to Near-Infrared Extinction Curves”, ApJ **594**, 1, 279–293 (2003).

Gordon, K. D., M. Fouesneau, H. Arab, K. Tchernyshyov, D. R. Weisz, J. J. Dalcanton, B. F. Williams, E. F. Bell, L. Bianchi, M. Boyer, Y. Choi, A. Dolphin, L. Girardi, D. W. Hogg, J. S. Kalirai, M. Kapala, A. R. Lewis, H.-W. Rix, K. Sandstrom and E. D. Skillman, “The Panchromatic Hubble Andromeda Treasury. XV. The BEAST: Bayesian Extinction and Stellar Tool”, ApJ **826**, 2, 104 (2016).

Grasha, K., D. Calzetti, A. Adamo, R. C. Kennicutt, B. G. Elmegreen, M. Messa, D. A. Dale, K. Fedorenko, S. Mahadevan, E. K. Grebel, M. Fumagalli, H. Kim, C. L. Dobbs, D. A. Gouliermis, G. Ashworth, J. S. Gallagher, L. J. Smith, M. Tosi, B. C. Whitmore, E. Schinnerer, D. Colombo, A. Hughes, A. K. Leroy and S. E. Meidt, “The spatial relation between young star clusters and molecular clouds in M51 with LEGUS”, MNRAS **483**, 4, 4707–4723 (2019).

Grasha, K., D. Calzetti, L. Bittle, K. E. Johnson, J. Donovan Meyer, R. C. Kennicutt, B. G. Elmegreen, A. Adamo, M. R. Krumholz, M. Fumagalli, E. K. Grebel, D. A. Gouliermis, D. O. Cook, J. S. Gallagher, A. Aloisi, D. A. Dale, S. Linden, E. Sacchi, D. A. Thilker, R. A. M. Walterbos, M. Messa, A. Wofford and L. J. Smith, “Connecting young star clusters to CO molecular gas in NGC 7793 with ALMA-LEGUS”, MNRAS **481**, 1, 1016–1027 (2018).

Grisdale, K., O. Agertz, A. B. Romeo, F. Renaud and J. I. Read, "The impact of stellar feedback on the density and velocity structure of the interstellar medium", MNRAS **466**, 1, 1093–1110 (2017).

Hake, R. R., "Interactive-engagement versus traditional methods: A six-thousand-student survey of mechanics test data for introductory physics courses", American Journal of Physics **66**, 1, 64–74, URL https://aapt.scitation.org/doi/abs/10.1119/1.18809 (1998).

Harris, C. R., K. J. Millman, S. J. van der Walt, R. Gommers, P. Virtanen, D. Cournapeau, E. Wieser, J. Taylor, S. Berg, N. J. Smith, R. Kern, M. Picus, S. Hoyer, M. H. van Kerkwijk, M. Brett, A. Haldane, J. F. del Río, M. Wiebe, P. Peterson, P. Gérard-Marchant, K. Sheppard, T. Reddy, W. Weckesser, H. Abbasi, C. Gohlke and T. E. Oliphant, "Array programming with NumPy", Nature **585**, 7825, 357–362, URL https://doi.org/10.1038/s41586-020-2649-2 (2020).

Heiles, C., "H I shells and supershells", ApJ **229**, 533–537 (1979).

Heiles, C., "Magnetic Fields, Pressures, and Thermally Unstable Gas in Prominent H i Shells", ApJ **336**, 808 (1989).

Herrmann, K. A., D. A. Hunter, H.-X. Zhang and B. G. Elmegreen, "Mass-to-light versus Color relations for Dwarf Irregular Galaxies", AJ **152**, 177–181 (2016).

Heyer, M., C. Krawczyk, J. Duval and J. M. Jackson, "Re-Examining Larson's Scaling Relationships in Galactic Molecular Clouds", ApJ **699**, 2, 1092–1103 (2009).

Hobson, A., "The Surprising Effectiveness of College Scientific Literacy Courses", Physics Teacher **46**, 7, 404–406 (2008).

Hoffman, M. D. and A. Gelman, "The no-u-turn sampler: Adaptively setting path lengths in hamiltonian monte carlo", URL https://arxiv.org/abs/1111.4246 (2011).

Hoffmann, S. L., J. Mack, R. Avila, C. Martlin, Y. Cohen and V. Bajaj, "New Drizzlepac Handbook Version 2.0 Released In Hdox: Updated Documentation For HST Image Analysis", in "American Astronomical Society Meeting Abstracts", vol. 53 of *American Astronomical Society Meeting Abstracts*, p. 216.02 (2021).

Hopkins, P. F., N. Murray, E. Quataert and T. A. Thompson, "A maximum stellar surface density in dense stellar systems", MNRAS **401**, 1, L19–L23 (2010).

Hu, C.-Y., A. Schruba, A. Sternberg and E. F. van Dishoeck, "Dependence of X $_{CO}$ on Metallicity, Intensity, and Spatial Scale in a Self-regulated Interstellar Medium", ApJ **931**, 1, 28 (2022).

Hu, C.-Y., A. Sternberg and E. F. van Dishoeck, “Metallicity Dependence of the H/H_2 and C^+/C/CO Distributions in a Resolved Self-regulating Interstellar Medium”, ApJ **920**, 1, 44 (2021).

Hu, C.-Y., A. Sternberg and E. F. van Dishoeck, “Coevolution of Dust and Chemistry in Galaxy Simulations with a Resolved Interstellar Medium”, ApJ **952**, 2, 140 (2023).

Hunt, L. K., F. Belfiore, F. Lelli, B. T. Draine, A. Marasco, S. García-Burillo, G. Venturi, F. Combes, A. Weiß, C. Henkel, K. M. Menten, F. Annibali, V. Casasola, M. Cignoni, A. McLeod, M. Tosi, M. Beltrán, A. Concas, G. Cresci, M. Ginolfi, N. Kumari and F. Mannucci, “Gas, dust, and the CO-to-molecular gas conversion factor in low-metallicity starbursts”, A&A **675**, A64 (2023).

Hunter, D. A., A. Adamo, B. G. Elmegreen, S. Gallardo, J. C. Lee, D. O. Cook, D. Thilker, B. Kayitesi, H. Kim, L. Kahre, L. Ubeda, S. N. Bright, J. E. Ryon, D. Calzetti, M. Tosi, K. Grasha, M. Messa, M. Fumagalli, D. A. Dale, E. Sabbi, M. Cignoni, L. J. Smith, D. M. Gouliermis, E. K. Grebel, A. Aloisi, B. C. Whitmore, R. Chandar and K. E. Johnson, “A Comparison of Young Star Properties with Local Galactic Environment for LEGUS/LITTLE THINGS Dwarf Irregular Galaxies”, AJ **156**, 1, 21 (2018).

Hunter, D. A. and B. G. Elmegreen, “Broadband Imaging of a Large Sample of Irregular Galaxies”, ApJS **162**, 1, 49–79 (2006).

Hunter, D. A., B. G. Elmegreen, H. Archer, C. E. Simpson and P. Cigan, “A Search for Correlations between Turbulence and Star Formation in LITTLE THINGS Dwarf Irregular Galaxies”, AJ **161**, 4, 175 (2021).

Hunter, D. A., B. G. Elmegreen and C. L. Berger, “H I Clouds in LITTLE THINGS Dwarf Irregular Galaxies”, AJ **157**, 6, 241 (2019).

Hunter, D. A., B. G. Elmegreen and S. C. Madden, “The Interstellar Medium in Dwarf Irregular Galaxies”, AARA **62**, 1, 113–155 (2024).

Hunter, D. A., B. G. Elmegreen and H. van Woerden, “Neutral Hydrogen and Star Formation in the Irregular Galaxy NGC 2366”, ApJ **556**, 2, 773–800 (2001).

Hunter, D. A., D. Ficut-Vicas, T. Ashley, E. Brinks, P. Cigan, B. G. Elmegreen, V. Heesen, K. A. Herrmann, M. Johnson, S.-H. Oh, M. P. Rupen, A. Schruba, C. E. Simpson, F. Walter, D. J. Westpfahl, L. M. Young and H.-X. Zhang, “Little Things”, AJ **144**, 5, 134 (2012).

Hunter, D. A., E. M. Wilcots, H. van Woerden, J. S. Gallagher and S. Kohle, “The Nature of the Extended H I Gas around NGC 4449: The Dr. Jekyll/Mr. Hyde of Irregular Galaxies”, ApJL **495**, 1, L47–L50 (1998).

Hunter, J. D., "Matplotlib: A 2d graphics environment", Computing in Science & Engineering **9**, 3, 90–95 (2007).

Iorio, G., F. Fraternali, C. Nipoti, E. Di Teodoro, J. I. Read and G. Battaglia, "LITTLE THINGS in 3D: robust determination of the circular velocity of dwarf irregular galaxies", MNRAS **466**, 4, 4159–4192 (2017).

Israel, F. P., T. de Graauw, H. van de Stadt and C. P. de Vries, "Carbon Monoxide in the Magellanic Clouds", ApJ **303**, 186 (1986).

Johnson, B., D. Foreman-Mackey, J. Sick, J. Leja, N. Byler, M. Walmsley, E. Tollerud, H. Leung and S. Scott, "dfm/python-fsps: python-fsps v0.4.2rc1", (2022).

Johnson, B. D., "SEDPY: Modules for storing and operating on astronomical source spectral energy distribution", Astrophysics Source Code Library, record ascl:1905.026 (2019).

Johnson, B. D., J. Leja, C. Conroy and J. S. Speagle, "Stellar Population Inference with Prospector", ApJS **254**, 2, 22 (2021).

Jones, O. C., C. Nally, N. Habel, L. Lenkić, K. Fahrion, A. S. Hirschauer, L. E. U. Chu, M. Meixner, G. De Marchi, O. Nayak, M. Robberto, E. Sabbi, P. Zeidler, C. Alves de Oliveira, T. Beck, K. Biazzo, B. Brandl, G. Giardino, T. Jerabkova, C. Keyes, J. Muzerolle, N. Panagia, K. Pontoppidan, C. Rogers, B. A. Sargent and D. Soderblom, "JWST/NIRCam detections of dusty subsolar-mass young stellar objects in the Small Magellanic Cloud", Nature Astronomy **7**, 694–701 (2023).

Kalberla, P. M. W., U. J. Schwarz and W. M. Goss, "High resolution mapping of galactic HI in the direction of 3C 147.", A&A **144**, 27–36 (1985).

Kennicutt, R. C. and N. J. Evans, "Star Formation in the Milky Way and Nearby Galaxies", ARA&A **50**, 531–608 (2012).

Kennicutt, R. C., Jr., "The Global Schmidt Law in Star-forming Galaxies", ApJ **498**, 2, 541–552 (1998).

Kepley, A. A., E. M. Wilcots, D. A. Hunter and T. Nordgren, "A High-Resolution Study of the H I Content of Local Group Dwarf Irregular Galaxy WLM", AJ **133**, 5, 2242–2257 (2007).

Kim, J.-G., W.-T. Kim and E. C. Ostriker, "Modeling UV Radiation Feedback from Massive Stars. II. Dispersal of Star-forming Giant Molecular Clouds by Photoionization and Radiation Pressure", ApJ **859**, 1, 68 (2018).

Kingma, D. P. and J. Ba, "Adam: A method for stochastic optimization", URL https://arxiv.org/abs/1412.6980 (2017).

Koposov, S., J. Speagle, K. Barbary, G. Ashton, E. Bennett, J. Buchner, C. Scheffler, B. Cook, C. Talbot, J. Guillochon, P. Cubillos, A. Asensio Ramos, B. Johnson, D. Lang, Ilya, M. Dartiailh, A. Nitz, A. McCluskey, A. Archibald, C. Deil, D. Foreman-Mackey, D. Goldstein, E. Tollerud, J. Leja, M. Kirk, M. Pitkin, P. Sheehan, P. Cargile, Ruskin23 and R. Angus, "joshspeagle/dynesty: v2.0.3", (2022).

Kroupa, P., "The Initial Mass Function of Stars: Evidence for Uniformity in Variable Systems", Science **295**, 5552, 82–91 (2002).

Kruijssen, J. M. D., A. Schruba, M. Chevance, S. N. Longmore, A. P. S. Hygate, D. T. Haydon, A. F. McLeod, J. J. Dalcanton, L. J. Tacconi and E. F. van Dishoeck, "Fast and inefficient star formation due to short-lived molecular clouds and rapid feedback", Nature **569**, 7757, 519–522 (2019).

Krumholz, M. R., A. Dekel and C. F. McKee, "A Universal, Local Star Formation Law in Galactic Clouds, nearby Galaxies, High-redshift Disks, and Starbursts", ApJ **745**, 1, 69 (2012).

Krumholz, M. R., M. Fumagalli, R. L. da Silva, T. Rendahl and J. Parra, "SLUG - stochastically lighting up galaxies - III. A suite of tools for simulated photometry, spectroscopy, and Bayesian inference with stochastic stellar populations", MNRAS **452**, 2, 1447–1467 (2015).

Krumholz, M. R. and J. C. Tan, "Slow Star Formation in Dense Gas: Evidence and Implications", ApJ **654**, 1, 304–315 (2007).

Kulik, J. A. and J. D. Fletcher, "Effectiveness of Intelligent Tutoring Systems: A Meta-Analytic Review", Review of Educational Research **86**, 1, 42–78, URL https://doi.org/10.3102/0034654315581420 (2016).

Lada, C. J. and E. A. Lada, "Embedded Clusters in Molecular Clouds", ARA&A **41**, 57–115 (2003).

Larson, R. B., "Turbulence and star formation in molecular clouds.", MNRAS **194**, 809–826 (1981).

Leaman, R., K. A. Venn, A. M. Brooks, G. Battaglia, A. A. Cole, R. A. Ibata, M. J. Irwin, A. W. McConnachie, J. T. Mendel and E. Tolstoy, "The Resolved Structure and Dynamics of an Isolated Dwarf Galaxy: A VLT and Keck Spectroscopic Survey of WLM", ApJ **750**, 1, 33 (2012).

Lee, A. J., W. L. Freedman, B. F. Madore, K. A. Owens, A. J. Monson and T. J. Hoyt, "The Astrophysical Distance Scale. III. Distance to the Local Group Galaxy WLM Using Multiwavelength Observations of the Tip of the Red Giant Branch, Cepheids, and JAGB Stars", ApJ **907**, 2, 112 (2021).

Lee, C., A. K. Leroy, A. D. Bolatto, S. C. O. Glover, R. Indebetouw, K. Sandstrom and A. Schruba, “The parsec-scale relationship between I_{CO} and A_V in local molecular clouds”, MNRAS **474**, 4, 4672–4708 (2018).

Lee, H., E. D. Skillman and K. A. Venn, “Investigating the Possible Anomaly between Nebular and Stellar Oxygen Abundances in the Dwarf Irregular Galaxy WLM”, ApJ **620**, 1, 223–237 (2005).

Leja, J., B. D. Johnson, C. Conroy, P. van Dokkum, J. S. Speagle, G. Brammer, I. Momcheva, R. Skelton, K. E. Whitaker, M. Franx and E. J. Nelson, “An Older, More Quiescent Universe from Panchromatic SED Fitting of the 3D-HST Survey”, ApJ **877**, 2, 140 (2019).

Leja, J., B. D. Johnson, C. Conroy, P. G. van Dokkum and N. Byler, “Deriving Physical Properties from Broadband Photometry with Prospector: Description of the Model and a Demonstration of its Accuracy Using 129 Galaxies in the Local Universe”, ApJ **837**, 2, 170 (2017).

Leroy, A. K., A. Bolatto, C. Bot, C. W. Engelbracht, K. Gordon, F. P. Israel, M. Rubio, K. Sandstrom and S. Stanimirović, “The Structure of a Low-metallicity Giant Molecular Cloud Complex”, ApJ **702**, 1, 352–367 (2009).

Leroy, A. K., F. Walter, E. Brinks, F. Bigiel, W. J. G. de Blok, B. Madore and M. D. Thornley, “The Star Formation Efficiency in Nearby Galaxies: Measuring Where Gas Forms Stars Effectively”, AJ **136**, 6, 2782–2845 (2008).

Levesque, E. M. and P. Massey, “Spectral Types of Red Supergiants in NGC 6822 and the Wolf-Lundmark-Melotte Galaxy”, AJ **144**, 1, 2 (2012).

Lombardi, D., T. F. Shipley, J. M. Bailey, P. S. Bretones, E. E. Prather, C. J. Ballen, J. K. Knight, M. K. Smith, R. L. Stowe, M. M. Cooper, M. Prince, K. Atit, D. H. Uttal, N. D. LaDue, P. M. McNeal, K. Ryker, K. St. John, K. J. van der Hoeven Kraft and J. L. Docktor, “The Curious Construct of Active Learning”, Psychological Science in the Public Interest **22**, 1, 8–43, URL https://doi.org/10.1177/1529100620973974 (2021).

LoPresto, M. and T. Slater, “A New Comparison Of Active Learning Strategies To Traditional Lectures For Teaching College Astronomy”, Journal of Astronomy & Earth Sciences Education (JAESE) **3**, 59 (2016).

LoPresto, M. C. and S. R. Murrell, “Using the Star Properties Concept Inventory to Compare Instruction with Lecture Tutorials to Traditional Lectures”, Astronomy Education Review **8**, 1, 010105 (2009).

Madden, S. C., "CO-dark gas: What fuels the star formation in low metallicity dwarf galaxies?", in "European Physical Journal Web of Conferences", vol. 265 of *European Physical Journal Web of Conferences*, p. 00011 (2022).

Madden, S. C. and D. Cormier, "Dwarf Galaxies: Their Low Metallicity Interstellar Medium", in "Dwarf Galaxies: From the Deep Universe to the Present", edited by K. B. W. McQuinn and S. Stierwalt, vol. 344, pp. 240–254 (2019).

Madden, S. C., D. Cormier, S. Hony, V. Lebouteiller, N. Abel, M. Galametz, I. De Looze, M. Chevance, F. L. Polles, M. Y. Lee, F. Galliano, A. Lambert-Huyghe, D. Hu and L. Ramambason, "Tracing the total molecular gas in galaxies: [CII] and the CO-dark gas", A&A **643**, A141 (2020).

Marigo, P., L. Girardi, A. Bressan, P. Rosenfield, B. Aringer, Y. Chen, M. Dussin, A. Nanni, G. Pastorelli, T. S. Rodrigues, M. Trabucchi, S. Bladh, J. Dalcanton, M. A. T. Groenewegen, J. Montalbán and P. R. Wood, "A New Generation of PARSEC-COLIBRI Stellar Isochrones Including the TP-AGB Phase", ApJ **835**, 1, 77 (2017).

Martin, D. C., J. Fanson, D. Schiminovich, P. Morrissey, P. G. Friedman, T. A. Barlow, T. Conrow, R. Grange, P. N. Jelinsky, B. Milliard, O. H. W. Siegmund, L. Bianchi, Y.-I. Byun, J. Donas, K. Forster, T. M. Heckman, Y.-W. Lee, B. F. Madore, R. F. Malina, S. G. Neff, R. M. Rich, T. Small, F. Surber, A. S. Szalay, B. Welsh and T. K. Wyder, "The Galaxy Evolution Explorer: A Space Ultraviolet Survey Mission", ApJ **619**, 1, L1–L6 (2005a).

Martin, D. C., J. Fanson, D. Schiminovich, P. Morrissey, P. G. Friedman, T. A. Barlow, T. Conrow, R. Grange, P. N. Jelinsky, B. Milliard, O. H. W. Siegmund, L. Bianchi, Y.-I. Byun, J. Donas, K. Forster, T. M. Heckman, Y.-W. Lee, B. F. Madore, R. F. Malina, S. G. Neff, R. M. Rich, T. Small, F. Surber, A. S. Szalay, B. Welsh and T. K. Wyder, "The Galaxy Evolution Explorer: A Space Ultraviolet Survey Mission", ApJ **619**, 1, L1–L6 (2005b).

Massey, P., R. T. McNeill, K. A. G. Olsen, P. W. Hodge, C. Blaha, G. H. Jacoby, R. C. Smith and S. B. Strong, "A Survey of Local Group Galaxies Currently Forming Stars. III. A Search for Luminous Blue Variables and Other Hα Emission-Line Stars", AJ **134**, 6, 2474–2503 (2007).

McKee, C. F. and E. C. Ostriker, "Theory of Star Formation", ARA&A **45**, 1, 565–687 (2007).

McKee, C. F. and J. P. Ostriker, "A theory of the interstellar medium: three components regulated by supernova explosions in an inhomogeneous substrate.", ApJ **218**, 148–169 (1977).

McQuinn, K. B. W., M. J. B. Newman, A. Savino, A. E. Dolphin, D. R. Weisz, B. F. Williams, M. L. Boyer, R. E. Cohen, M. Correnti, A. A. Cole, M. C. Geha, M. Gennaro, N. Kallivayalil, K. M. Sandstrom, E. D. Skillman, J. Anderson, A. Bolatto, M. Boylan-Kolchin, C. T. Garling, K. M. Gilbert, L. Girardi, J. S. Kalirai, A. Mazzi, G. Pastorelli, H. Richstein and J. T. Warfield, "The JWST Resolved Stellar Populations Early Release Science Program. IV. The Star Formation History of the Local Group Galaxy WLM", ApJ **961**, 1, 16 (2024).

Meaburn, J., "The giant and supergiant shells of the Magellanic Clouds.", MNRAS **192**, 365–375 (1980).

Mebold, U., "On the Intercloud Hi-Gas", A&A **19**, 13 (1972).

Melotte, P. J., "New nebulæ shown on Franklin-Adams chart plates", MNRAS **86**, 636–638 (1926).

Mogensen, P. K. and A. N. Riseth, "Optim: A mathematical optimization package for Julia", Journal of Open Source Software **3**, 24, 615 (2018).

Nayak, O., M. Meixner, Y. Fukui, K. Tachihara, T. Onishi, K. Saigo, K. Tokuda and R. Harada, "Molecular Cloud Structures and Massive Star Formation in N159", ApJ **854**, 2, 154 (2018).

Nayak, O., M. Meixner, R. Indebetouw, G. De Marchi, A. Koekemoer, N. Panagia and E. Sabbi, "A Study of the Relation between Star Formation and Molecular Clumps on Subparsec Scales in 30 Doradus", ApJ **831**, 1, 32 (2016).

Newman, M. J. B., K. B. W. McQuinn, E. D. Skillman, M. L. Boyer, R. E. Cohen, A. E. Dolphin and O. G. Telford, "An Empirical Calibration of the Tip of the Red Giant Branch Distance Method in the Near Infrared. II. JWST NIRCam Wide Filters", ApJ **975**, 2, 195 (2024).

Nicolet, B., "A Plot of UBV Diagram", A&AS **42**, 283 (1980).

Nunnally, J., *Psychometric Theory*, McGraw-Hill series in psychology (McGraw-Hill, 1978).

Osman, O., K. Bekki and L. Cortese, "The role of dust destruction and dust growth in the evolution of the interstellar medium", MNRAS **497**, 2, 2002–2017 (2020).

Ostriker, E. C., C. F. McKee and A. K. Leroy, "Regulation of Star Formation Rates in Multiphase Galactic Disks: A Thermal/Dynamical Equilibrium Model", ApJ **721**, 2, 975–994 (2010).

Pastorelli, G., P. Marigo, L. Girardi, B. Aringer, Y. Chen, S. Rubele, M. Trabucchi, S. Bladh, M. L. Boyer, A. Bressan, J. J. Dalcanton, M. A. T. Groenewegen, T. Lebzelter, N. Mowlavi, K. L. Chubb, M.-R. L. Cioni, R. de Grijs, V. D. Ivanov, A. Nanni, J. T. van Loon and S. Zaggia, "Constraining the thermally pulsing asymptotic giant branch phase with resolved stellar populations in the Large Magellanic Cloud", MNRAS **498**, 3, 3283–3301 (2020).

Pastorelli, G., P. Marigo, L. Girardi, Y. Chen, S. Rubele, M. Trabucchi, B. Aringer, S. Bladh, A. Bressan, J. Montalbán, M. L. Boyer, J. J. Dalcanton, K. Eriksson, M. A. T. Groenewegen, S. Höfner, T. Lebzelter, A. Nanni, P. Rosenfield, P. R. Wood and M.-R. L. Cioni, "Constraining the thermally pulsing asymptotic giant branch phase with resolved stellar populations in the Small Magellanic Cloud", MNRAS **485**, 4, 5666–5692 (2019).

Pedregosa, F., G. Varoquaux, A. Gramfort, V. Michel, B. Thirion, O. Grisel, M. Blondel, A. Müller, J. Nothman, G. Louppe, P. Prettenhofer, R. Weiss, V. Dubourg, J. Vanderplas, A. Passos, D. Cournapeau, M. Brucher, M. Perrot and É. Duchesnay, "Scikit-learn: Machine Learning in Python", Journal of Machine Learning Research **12**, 2825–2830 (2011).

Peltonen, J., E. Rosolowsky, T. G. Williams, E. W. Koch, A. Dolphin, J. Chastenet, J. J. Dalcanton, A. Ginsburg, L. C. Johnson, A. K. Leroy, T. Richardson, K. M. Sandstrom, S. K. Sarbadhicary, A. Smercina, T. Wainer and B. F. Williams, "JWST reveals star formation across a spiral arm in M33", MNRAS **527**, 4, 10668–10679 (2024).

Phelps, R. L. and E. A. Lada, "Spatial Distribution of Embedded Clusters in the Rosette Molecular Cloud: Implications for Cluster Formation", ApJ **477**, 1, 176–182 (1997).

Pineda, J. L., W. D. Langer and P. F. Goldsmith, "A Herschel [C II] Galactic plane survey. III. [C II] as a tracer of star formation", A&A **570**, A121 (2014).

Planck Collaboration, P. A. R. Ade, N. Aghanim, M. Arnaud, M. Ashdown, J. Aumont, C. Baccigalupi, A. Balbi, A. J. Banday, R. B. Barreiro, J. G. Bartlett, E. Battaner, K. Benabed, A. Benoît, J. P. Bernard, M. Bersanelli, R. Bhatia, J. J. Bock, A. Bonaldi, J. R. Bond, J. Borrill, F. R. Bouchet, F. Boulanger, M. Bucher, C. Burigana, P. Cabella, J. F. Cardoso, A. Catalano, L. Cayón, A. Challinor, A. Chamballu, L. Y. Chiang, C. Chiang, P. R. Christensen, D. L. Clements, S. Colombi, F. Couchot, A. Coulais, B. P. Crill, F. Cuttaia, T. M. Dame, L. Danese, R. D. Davies, R. J. Davis, P. de Bernardis, G. de Gasperis, A. de Rosa, G. de Zotti, J. Delabrouille, J. M. Delouis, F. X. Désert, C. Dickinson, K. Dobashi, S. Donzelli, O. Doré, U. Dörl, M. Douspis, X. Dupac, G. Efstathiou, T. A. Enßlin, H. K. Eriksen, E. Falgarone, F. Finelli, O. Forni, P. Fosalba, M. Frailis, E. Franceschi, Y. Fukui, S. Galeotta, K. Ganga, M. Giard, G. Giardino, Y. Giraud-Héraud, J. González-Nuevo, K. M. Górski, S. Gratton, A. Gregorio, I. A. Grenier, A. Gruppuso, F. K. Hansen, D. Harrison, G. Helou, S. Henrot-Versillé, D. Herranz, S. R. Hildebrandt, E. Hivon, M. Hobson, W. A. Holmes, W. Hovest, R. J. Hoyland, K. M. Huffenberger, A. H. Jaffe, W. C. Jones, M. Juvela, A. Kawamura, E. Keihänen, R. Keskitalo, T. S. Kisner, R. Kneissl, L. Knox, H. Kurki-Suonio, G. Lagache, J. M. Lamarre, A. Lasenby, R. J. Laureijs, C. R. Lawrence, S. Leach, R. Leonardi, C. Leroy, P. B. Lilje, M. Linden-Vørnle, M. López-Caniego, P. M. Lubin, J. F. Macías-Pérez, C. J. MacTavish, B. Maffei, D. Maino, N. Mandolesi, R. Mann, M. Maris, P. Martin, E. Martínez-González, S. Masi, S. Matarrese, F. Matthai, P. Mazzotta, P. McGehee, P. R. Meinhold, A. Melchiorri, L. Mendes, A. Mennella, M. A. Miville-Deschênes, A. Moneti, L. Montier, G. Morgante, D. Mortlock, D. Munshi, A. Murphy, P. Naselsky, P. Natoli, C. B. Netterfield, H. U. Nørgaard-Nielsen, F. Noviello, D. Novikov, I. Novikov, I. J. O'Dwyer, T. Onishi, S. Osborne, F. Pajot, R. Paladini, D. Paradis, F. Pasian, G. Patanchon, O. Perdereau, L. Perotto, F. Perrotta, F. Piacentini, M. Piat, S. Plaszczynski, E. Pointecouteau, G. Polenta, N. Ponthieu, T. Poutanen, G. Prézeau, S. Prunet, J. L. Puget, W. T. Reach, M. Reinecke, C. Renault, S. Ricciardi, T. Riller, I. Ristorcelli, G. Rocha, C. Rosset, M. Rowan-Robinson, J. A. Rubiño-Martín, B. Rusholme, M. Sandri, D. Santos, G. Savini, D. Scott, M. D. Seiffert, P. Shellard, G. F. Smoot, J. L. Starck, F. Stivoli, V. Stolyarov, R. Stompor, R. Sudiwala, J. F. Sygnet, J. A. Tauber, L. Terenzi, L. Toffolatti, M. Tomasi, J. P. Torre, M. Tristram, J. Tuovinen, G. Umana, L. Valenziano, P. Vielva, F. Villa, N. Vittorio, L. A. Wade, B. D. Wandelt, A. Wilkinson, D. Yvon, A. Zacchei and A. Zonca, "Planck early results. XIX. All-sky temperature and dust optical depth from Planck and IRAS. Constraints on the "dark gas" in our Galaxy", A&A **536**, A19 (2011).

Posner, G. J., K. A. Strike, P. W. Hewson and W. A. Gertzog, "Accommodation of a scientific conception: Toward a theory of conceptual change", Science Education **66**, 2, 211–227, URL https://onlinelibrary.wiley.com/doi/abs/10.1002/sce.3730660207 (1982).

Prather, E. E., G. Brissenden, C. Wallace and J. Adams, *Lecture Tutorials for Introductory Astronomy* (Pearson Education, 2021), 4 edn., URL https://www.pearson.com/store/p/lecture-tutorials-for-introductory-astronomy/P200000006822/9780135807026.

Prather, E. E., A. L. Rudolph and G. Brissenden, "Teaching and learning astronomy in the 21st century", Physics Today **62**, 10, 41–47, URL https://physicstoday.scitation.org/doi/10.1063/1.3248478 (2009).

Prather, E. E., T. Slater, J. Adams, J. Bailey, L. Jones and J. Dostal, "Research on a Lecture-Tutorial Approach to Teaching Introductory Astronomy for Non–Science Majors", Astronomy Education Review **3** (2004).

Radhakrishnan, V., J. D. Murray, P. Lockhart and R. P. J. Whittle, "The Parkes Survey of 21-centimeter Absorption in Discrete-Source Spectra. II. Galactic 21-centimeter Observations in the Direction of 35 Extragalactic Sources", ApJS **24**, 15 (1972).

Ramambason, L., V. Lebouteiller, S. C. Madden, F. Galliano, C. T. Richardson, A. Saintonge, I. De Looze, M. Chevance, N. P. Abel, S. Hernandez and J. Braine, "Modeling the molecular gas content and CO-to-H_2 conversion factors in low-metallicity star-forming dwarf galaxies", A&A **681**, A14 (2024).

Rémy-Ruyer, A., S. C. Madden, F. Galliano, M. Galametz, T. T. Takeuchi, R. S. Asano, S. Zhukovska, V. Lebouteiller, D. Cormier, A. Jones, M. Bocchio, M. Baes, G. J. Bendo, M. Boquien, A. Boselli, I. DeLooze, V. Doublier-Pritchard, T. Hughes, O. Ł. Karczewski and L. Spinoglio, "Gas-to-dust mass ratios in local galaxies over a 2 dex metallicity range", A&A **563**, A31 (2014).

Requena-Torres, M. A., F. P. Israel, Y. Okada, R. Güsten, J. Stutzki, C. Risacher, R. Simon and H. Zinnecker, "Carbon gas in SMC low-metallicity star-forming regions", A&A **589**, A28 (2016).

Rosolowsky, E. and A. Leroy, "Bias-free Measurement of Giant Molecular Cloud Properties", PASP **118**, 842, 590–610 (2006).

Rubio, M., B. G. Elmegreen, D. A. Hunter, E. Brinks, J. R. Cortés and P. Cigan, "Dense cloud cores revealed by CO in the low metallicity dwarf galaxy WLM", Nature **525**, 7568, 218–221 (2015).

Rudolph, A. L., E. E. Prather, G. Brissenden and W. M. Schlingman, "A National Study Assessing the Teaching and Learning of Introductory Astronomy Part I: The Effect of Interactive Instruction", in "Science Education and Outreach: Forging a Path to the Future", edited by J. Barnes, D. A. Smith, M. G. Gibbs and J. G. Manning, vol. 431 of *Astronomical Society of the Pacific Conference Series*, p. 182 (2010).

Saintonge, A. and B. Catinella, “The Cold Interstellar Medium of Galaxies in the Local Universe”, ARA&A **60**, 319–361 (2022).

Saldaño, H. P., M. Rubio, A. D. Bolatto, C. Verdugo, K. E. Jameson and A. K. Leroy, “CO(2−1) survey at 9 pc resolution in the Small Magellanic Cloud”, A&A **672**, A153 (2023).

Salpeter, E. E., “The Luminosity Function and Stellar Evolution.”, ApJ **121**, 161 (1955).

Scalo, J. and B. G. Elmegreen, “Interstellar Turbulence II: Implications and Effects”, ARA&A **42**, 1, 275–316 (2004).

Schinnerer, E. and A. K. Leroy, “Molecular Gas and the Star-Formation Process on Cloud Scales in Nearby Galaxies”, ARA&A **62**, 1, 369–436 (2024).

Schlafly, E. F. and D. P. Finkbeiner, “Measuring Reddening with Sloan Digital Sky Survey Stellar Spectra and Recalibrating SFD”, ApJ **737**, 2, 103 (2011).

Schruba, A., A. K. Leroy, F. Walter, F. Bigiel, E. Brinks, W. J. G. de Blok, C. Kramer, E. Rosolowsky, K. Sandstrom, K. Schuster, A. Usero, A. Weiss and H. Wiesemeyer, “Low CO Luminosities in Dwarf Galaxies”, AJ **143**, 6, 138 (2012).

Simon, M. N., S. Buxner and C. Impey, “A Survey and Analysis of College Students’ Understanding of Planet Formation Before Instruction”, Astrobiology (2018).

Simon, M. N., E. E. Prather, S. R. Buxner and C. D. Impey, “The development and validation of the Planet Formation Concept Inventory”, International Journal of Science Education **41**, 17, 2448–2464, URL https://doi.org/10.1080/09500693.2019.1685140 (2019).

Simon, M. N., E. E. Prather, I. Rosenthal, M. Cassidy, J. Hammerman and L. Trouille, “A New Curriculum Development Model for Improving Undergraduate Students’ Data Literacy and Self-Efficacy in Online Astronomy Classrooms”, Astronomy Education Journal **2**, 1, URL https://astroedjournal.org/index.php/ijae/article/view/43 (2022).

Solomon, P. M., A. R. Rivolo, J. Barrett and A. Yahil, “Mass, Luminosity, and Line Width Relations of Galactic Molecular Clouds”, ApJ **319**, 730 (1987).

Speagle, J. S., “DYNESTY: a dynamic nested sampling package for estimating Bayesian posteriors and evidences”, MNRAS **493**, 3, 3132–3158 (2020).

Stan Development Team, “RStan: the R interface to Stan”, URL https://mc-stan.org/, r package version 2.32.6 (2024).

Stetson, P. B., "DAOPHOT: A Computer Program for Crowded-Field Stellar Photometry", PASP **99**, 191 (1987).

Tang, J., A. Bressan, P. Rosenfield, A. Slemer, P. Marigo, L. Girardi and L. Bianchi, "New PARSEC evolutionary tracks of massive stars at low metallicity: testing canonical stellar evolution in nearby star-forming dwarf galaxies", MNRAS **445**, 4, 4287–4305 (2014).

Taylor, C. L. and U. Klein, "A search for CO in the Local Group dwarf irregular galaxy WLM", A&A **366**, 811–816 (2001).

Taylor, C. L., H. A. Kobulnicky and E. D. Skillman, "CO Emission in Low-Luminosity, H I-rich Galaxies", AJ **116**, 6, 2746–2756 (1998).

Tenorio-Tagle, G. and P. Bodenheimer, "Large-scale expanding superstructures in galaxies.", ARAA **26**, 145–197 (1988).

Tenorio-Tagle, G., M. Prieto and F. Sanchez, eds., *Star formation in stellar systems* (1992).

Teyssier, M., K. V. Johnston and M. Kuhlen, "Identifying Local Group field galaxies that have interacted with the Milky Way", MNRAS **426**, 3, 1808–1818 (2012).

Tody, D., "The IRAF Data Reduction and Analysis System", in "Instrumentation in astronomy VI", edited by D. L. Crawford, vol. 627 of *Society of Photo-Optical Instrumentation Engineers (SPIE) Conference Series*, p. 733 (1986).

Tolstoy, E., V. Hill and M. Tosi, "Star-Formation Histories, Abundances, and Kinematics of Dwarf Galaxies in the Local Group", ARA&A **47**, 1, 371–425 (2009).

Toothaker, L. E., *Multiple Comparison Procedures* (SAGE Publications, Inc., Thousand Oaks, California, 1993), URL https://methods.sagepub.com/book/multiple-comparison-procedures.

Vanlehn, K., "The Relative Effectiveness of Human Tutoring, Intelligent Tutoring Systems, and Other Tutoring Systems", Educational Psychologist **46**, 197–221 (2011).

Volkwyn, T. S., J. Airey, B. Gregorcic and C. Linder, "Developing representational competence: linking real-world motion to physics concepts through graphs", Learning: Research and Practice **6**, 1, 88–107, URL https://doi.org/10.1080/23735082.2020.1750670 (2020).

Vorobyov, E. I. and S. Basu, "The Origin of Episodic Accretion Bursts in the Early Stages of Star Formation", ApJL **633**, 2, L137–L140 (2005).

Wakelam, V., E. Bron, S. Cazaux, F. Dulieu, C. Gry, P. Guillard, E. Habart, L. Hornekær, S. Morisset, G. Nyman, V. Pirronello, S. D. Price, V. Valdivia, G. Vidali and N. Watanabe, "H_2 formation on interstellar dust grains: The viewpoints of theory, experiments, models and observations", Molecular Astrophysics **9**, 1–36 (2017a).

Wakelam, V., E. Bron, S. Cazaux, F. Dulieu, C. Gry, P. Guillard, E. Habart, L. Hornekær, S. Morisset, G. Nyman, V. Pirronello, S. D. Price, V. Valdivia, G. Vidali and N. Watanabe, "H_2 formation on interstellar dust grains: The viewpoints of theory, experiments, models and observations", Molecular Astrophysics **9**, 1–36 (2017b).

Wallace, C., E. E. Prather and D. Duncan, "A Study of General Education Astronomy Students' Understandings of Cosmology. Part V. The Effects of a New Suite of Cosmology Lecture-Tutorials on Students' Conceptual Knowledge", International Journal of Science Education - INT J SCI EDUC **34**, 1–18 (2012).

Wallace, C. S., T. G. Chambers, E. E. Prather and G. Brissenden, "Using graphical and pictorial representations to teach introductory astronomy students about the detection of extrasolar planets via gravitational microlensing", American Journal of Physics **84**, 5, 335–343, URL https://doi.org/10.1119/1.4943035 (2016).

Wallace, C. S., C. Hatcher, T. G. Chambers, S. D. Hornstein, J. Kamenetzky and E. E. Prather, "A New *Lecture-Tutorial* for Teaching Interferometry to Astro 101 Students", The Physics Teacher **59**, 6, 440–444, URL https://pubs.aip.org/pte/article/59/6/440/153066/A-New-Lecture-Tutorial-for-Teaching-Interferometry (2021).

Wang, Y., J. Gao, Y. Ren and B. Chen, "Dust Extinction Law in Nearby Star-resolved Galaxies. II. M33 Traced by Supergiants", ApJS **260**, 2, 41 (2022).

Weisz, D., "Completing the Census of Isolated Dwarf Galaxy Star Formation Histories", HST Proposal ID 13768. Cycle 22 (2014).

Weisz, D. R., K. B. W. McQuinn, A. Savino, N. Kallivayalil, J. Anderson, M. L. Boyer, M. Correnti, M. C. Geha, A. E. Dolphin, K. M. Sandstrom, A. A. Cole, B. F. Williams, E. D. Skillman, R. E. Cohen, M. J. B. Newman, R. Beaton, A. Bressan, A. Bolatto, M. Boylan-Kolchin, A. M. Brooks, J. S. Bullock, C. Conroy, M. C. Cooper, J. J. Dalcanton, A. L. Dotter, T. K. Fritz, C. T. Garling, M. Gennaro, K. M. Gilbert, L. Girardi, B. D. Johnson, L. C. Johnson, J. S. Kalirai, E. N. Kirby, D. Lang, P. Marigo, H. Richstein, E. F. Schlafly, J. Schmidt, E. J. Tollerud, J. T. Warfield and A. Wetzel, "The JWST Resolved Stellar Populations Early Release Science Program. II. Survey Overview", ApJS **268**, 1, 15 (2023).

Williams, J. P., L. Blitz and C. F. McKee, "The Structure and Evolution of Molecular Clouds: from Clumps to Cores to the IMF", in "Protostars and Planets IV", edited by V. Mannings, A. P. Boss and S. S. Russell, p. 97 (2000).

Windhorst, R. A., T. Carleton, R. O'Brien, S. H. Cohen, D. Carter, R. Jansen, S. Tompkins, R. G. Arendt, S. Caddy, N. Grogin, A. Koekemoer, J. MacKenty, S. Casertano, L. J. M. Davies, S. P. Driver, E. Dwek, A. Kashlinsky, S. J. Kenyon, N. Miles, N. Pirzkal, A. Robotham, R. Ryan, H. Abate, H. Andras-Letanovszky, J. Berkheimer, J. Chambers, C. Gelb, Z. Goisman, D. Henningsen, I. Huckabee, D. Kramer, T. Patel, R. Pawnikar, E. Pringle, C. Rogers, S. Sherman, A. Swirbul and K. Webber, "SKYSURF: Constraints on Zodiacal Light and Extragalactic Background Light through Panchromatic HST All-sky Surface-brightness Measurements. I. Survey Overview and Methods", AJ **164**, 4, 141 (2022).

Windhorst, R. A., S. H. Cohen, N. P. Hathi, P. J. McCarthy, R. E. Ryan, Jr., H. Yan, I. K. Baldry, S. P. Driver, J. A. Frogel, D. T. Hill, L. S. Kelvin, A. M. Koekemoer, M. Mechtley, R. W. O'Connell, A. S. G. Robotham, M. J. Rutkowski, M. Seibert, A. N. Straughn, R. J. Tuffs, B. Balick, H. E. Bond, H. Bushouse, D. Calzetti, M. Crockett, M. J. Disney, M. A. Dopita, D. N. B. Hall, J. A. Holtzman, S. Kaviraj, R. A. Kimble, J. W. MacKenty, M. Mutchler, F. Paresce, A. Saha, J. I. Silk, J. T. Trauger, A. R. Walker, B. C. Whitmore and E. T. Young, "The Hubble Space Telescope Wide Field Camera 3 Early Release Science Data: Panchromatic Faint Object Counts for 0.2-2 μm Wavelength", ApJS **193**, 2, 27 (2011).

Windhorst, R. A., S. H. Cohen, R. A. Jansen, J. Summers, S. Tompkins, C. J. Conselice, S. P. Driver, H. Yan, D. Coe, B. Frye, N. Grogin, A. Koekemoer, M. A. Marshall, R. O'Brien, N. Pirzkal, A. Robotham, R. E. Ryan, C. N. A. Willmer, T. Carleton, J. M. Diego, W. C. Keel, P. Porto, C. Redshaw, S. Scheller, S. M. Wilkins, S. P. Willner, A. Zitrin, N. J. Adams, D. Austin, R. G. Arendt, J. F. Beacom, R. A. Bhatawdekar, L. D. Bradley, T. Broadhurst, C. Cheng, F. Civano, L. Dai, H. Dole, J. C. J. D'Silva, K. J. Duncan, G. G. Fazio, G. Ferrami, L. Ferreira, S. L. Finkelstein, L. J. Furtak, H. B. Gim, A. Griffiths, H. B. Hammel, K. C. Harrington, N. P. Hathi, B. W. Holwerda, R. Honor, J.-S. Huang, M. Hyun, M. Im, B. A. Joshi, P. S. Kamieneski, P. Kelly, R. L. Larson, J. Li, J. Lim, Z. Ma, P. Maksym, G. Manzoni, A. K. Meena, S. N. Milam, M. Nonino, M. Pascale, A. Petric, J. D. R. Pierel, M. del Carmen Polletta, H. J. A. Röttgering, M. J. Rutkowski, I. Smail, A. N. Straughn, L.-G. Strolger, A. Swirbul, J. A. A. Trussler, L. Wang, B. Welch, J. S. B. Wyithe, M. Yun, E. Zackrisson, J. Zhang and X. Zhao, "JWST PEARLS. Prime Extragalactic Areas for Reionization and Lensing Science: Project Overview and First Results", AJ **165**, 1, 13 (2023).

Wisniewski, B., K. Zierer and J. Hattie, “The Power of Feedback Revisited: A Meta-Analysis of Educational Feedback Research”, Frontiers in Psychology **10**, URL https://www.frontiersin.org/articles/10.3389/fpsyg.2019.03087 (2020).

Wolf, M., “Über einen größeren Nebelfleck in Cetus”, Astronomische Nachrichten **183**, 12, 187 (1909).

Wolfire, M. G., D. Hollenbach and C. F. McKee, “The Dark Molecular Gas”, ApJ **716**, 2, 1191–1207 (2010).

Xu, C., C. J. Lonsdale, D. L. Shupe, J. O’Linger and F. Masci, “Models for Multiband Infrared Surveys”, ApJ **562**, 1, 179–207 (2001).

Xu, K., H. Ge, W. Tebbutt, M. Tarek, M. Trapp and Z. Ghahramani, “Advancedhmc. jl: A robust, modular and efficient implementation of advanced hmc algorithms”, in “Symposium on Advances in Approximate Bayesian Inference”, pp. 1–10 (PMLR, 2020).

Yang, Y., R. Ianjamasimanana, F. Hammer, C. Higgs, B. Namumba, C. Carignan, G. I. G. Józsa and A. W. McConnachie, “Evidence of ram-pressure stripping of WLM, a dwarf galaxy far away from any large host galaxy”, A&A **660**, L11 (2022).

Zhang, H.-X., D. A. Hunter, B. G. Elmegreen, Y. Gao and A. Schruba, “Outside-in Shrinking of the Star-forming Disk of Dwarf Irregular Galaxies”, AJ **143**, 2, 47 (2012).

APPENDIX A

CO-AUTHOR PERMISSIONS

The papers published in this dissertation have the full acknowledgment and approval of the co-authors.